AUTOMOTIVE ELECTRIC ACTUATOR MODELLING AND DESIGN METHODOLOGIES

A thesis submitted to The University of Manchester
for the degree of Doctor of Philosophy (PhD)
in the faculty of Engineering and Physical Sciences

JOHN WELFORD

SCHOOL OF ELECTRICAL AND ELECTRONIC ENGINEERING
2014

Contents

44860 words.

Compiled on October 5, 2014, using version control revision 416.

List of Figures

List of Tables

Abstract

Electromechanical position actuation systems typically consist of an electric motor, driven by a set of power electronics, effecting output through a mechanical transmission. Whilst an optimal fully integrated actuator design from first principles could be considered, this is often not a cost-effective option. It is common to construct designs utilising commercially available subcomponents – the *Cummins* variable geometry turbocharging application detailed in this thesis provides a typical example. The design problem studied in this work is therefore one of meeting requirements through careful subcomponent selection.

Electromagnetic, mechanical and thermal equations are developed to model actuator performance. These may be parameterised based on datasheet values or sample component test data. A set of tests is proposed to extract the required information from example motors; this is demonstrated using five different sample motors. Validation is performed to assess the accuracy of the parameterised models for the sample motors. A process is then developed to use the validated models to assess actuator design performance against a set of requirements.

A key contribution of this work is the derivation of a computationally efficient motor model, which may be used with an integrated low-order lumped-parameter thermal model to investigate actuator performance at elevated temperatures – since this is often the limiting factor in machine rating. This allows a user to select the appropriate modelling fidelity, allowing accuracy to be traded against simulation performance. The overall process is demonstrated through the assessment of a full actuator design.

The models and design process developed in this work allow a candidate actuator design to be appraised through calculations and simulations at a range of different fidelities, and using only a minimal set of subcomponent parameters. This allows designs that cannot meet the performance requirements to be quickly identified and excluded. Satisfactory designs may then be modelled and evaluated in detail to optimise other requirements, such as cost or volume.

Declaration

No portion of the work referred to in this thesis has been submitted in support of an application for another degree or qualification, of this or any other university or institute of learning.

Copyright Statement

The author of this thesis (and appendices to this thesis) owns certain copyright or related rights in it (the 'Copyright'), and has given *The University of Manchester* certain rights to use such Copyright, including for administrative purposes.

Copies of this thesis, either in full or in extracts, and whether in hard or electronic copy, may be made only in accordance with the Copyright, Designs and Patents Act 1988 (as amended) and regulations issued under it or, where appropriate, in accordance with licensing agreements. This page must form part of any such copies made.

The ownership of certain Copyright, patents, designs, trademarks and other intellectual property (the 'Intellectual Property') and any reproductions of copyright works in the thesis, for example graphs and tables ('Reproductions'), which may be described in this thesis, may not be owned by the author and may be owned by third parties. Such Intellectual Property and Reproductions cannot and must not be made available for use without the prior written permission of the owner(s) of the relevant Intellectual Property and/or Reproductions.

Further information on the conditions under which disclosure, publication and commercialisation of this thesis, the Copyright (and any Intellectual Property and/or Reproductions described in it) may take place, is available in the university IP policy (see `http://documents.manchester.ac.uk/DocuInfo.aspx?DocID=487`), in any relevant thesis restriction declarations deposited in the university library, the university library's regulations (see `http://www.manchester.ac.uk/library/aboutus/regulations`) and in the university's policy on Presentation of Theses.

Acknowledgements

I would like to thank my supervisors at Manchester University, Judith Apsley and Andrew Forsyth, for their support and guidance throughout the work. Equal thanks go to my industrial sponsors and supervisors, Ali Sophian, Bushra Khan and Jeff Carter. Support, discussion and encouragement from both the wider Power Conversion Group in Manchester and the Mechatronics team at *Cummins Turbo Technologies* have been much appreciated.

I am also grateful to my family and friends, who have supported, encouraged, distracted and amused me throughout. Thank you for putting up with me over the last few years!

This work has been jointly funded by the Engineering and Physical Sciences Research Council (EPSRC) and *Cummins Turbo Technologies*.

Abbreviations

2DOF Two Degree Of Freedom

AC Alternating Current

back-EMF back Electro-Motive Force

CAN Controller Area Network

CFD Computational Fluid Dynamics

CVT Continuously Variable Transmission

DC Direct Current

ECU Engine Control Unit

EMF Electro-Motive Force

EMI Electromagnetic Interference

EPSRC Engineering and Physical Sciences Research Council

FE Finite Element

IGBT Insulated-Gate Bipolar Transistor

IP Integral Proportional

LCR Inductance Capacitance Resistance

LVDT Linear Variable Differential Transformer

MOSFET Metal-Oxide-Semiconductor Field-Effect Transistor

MMT Moving Magnet Technologies

NdFeB Neodymium Iron Boron

NEMA the National Electrical Manufacturers Association

PC Personal Computer

PDF Pseudo-Derivative Feedback

PDFF Pseudo-Derivative Feedback with Feedforward gain

PIC Programmable Integrated Circuit

PI Proportional-Integral

PID Proportional-Integral-Derivative

PWM Pulse Width Modulation

RMS Root Mean Square

SmCo Samarium Cobalt

THD Total Harmonic Distortion

UK United Kingdom

Notation

As this work covers a wide range of models, in a number of different physical domains, a large number of different parameters are required. In general, a standard italicised font has been used for electrical and mechanical parameters, e.g. R, C, B, T, whereas a cursive script is used for thermal and magnetic parameters, e.g. $\mathcal{R}, \mathcal{C}, \mathcal{B}, \mathcal{T}$. Conventional notation has been used as far as possible, however some variation has been necessary to avoid duplication. Scalar quantities are shown in a standard weight font, often with subscripts to denote the specific instance, as in v_1, i_2, vector quantities are shown in bold, such as $\boldsymbol{v}, \boldsymbol{i}$. Product names are identified through the use of italicised font, e.g. *Maxon*, *MMT*, *Simulink*. Where new concepts or terminology are introduced they are usually signified through the use of single quotation marks; after the first use they appear unquoted. A complete list of parameter notation is provided below.

α	Load acceleration
α_{fall}	Move profile deceleration
$\alpha_{r_{RMS}}$	RMS actuator output acceleration
α_{rise}	Move profile acceleration
$\widehat{\alpha}_r$	Maximum actuator output acceleration
β	Coefficient of cubical expansion
γ	Temperature coefficient of demagnetisation
ε	Emissivity of a surface
η_g	Gear efficiency
θ	Angular position
θ_b	Current mechanical backlash angle
$\widehat{\theta}_b$	Mechanical backlash angle limit
θ_e	Angular electrical position

θ_r	Actuator mechanical output rotation requirement
θ_{ef}	Motor electrical angle in which the current is falling to zero in a phase
θ_{in}	Mechanical input position
θ_{out}	Mechanical output position
θ_{pb}	Mechanical pre-backlash position
μ	Dynamic viscosity of dry air
π	Circle constant
ρ	Fluid density of air
σ	Stefan-Boltzmann constant
τ_d	PID derivative time constant
τ_i	PID integral time constant
τ_r	Move profile total period
τ_t	PID integral balance compensation time constant
τ_{const}	Move profile constant speed period
τ_{fall}	Move profile deceleration period
τ_{rise}	Move profile acceleration period
ϕ	Worm drive helix angle
ψ	Temperature coefficient of resistivity
ω	Angular speed
ω_b	Mechanical backlash speed
ω_e	Motor electrical angular speed
$\widehat{\omega}_l$	Maximum load mechanical angular speed
ω_m	Motor mechanical angular speed
$\widehat{\omega}_m$	Maximum motor mechanical angular speed
$\widehat{\omega}_r$	Maximum actuator output mechanical speed during move profile
ω_{in}	Mechanical input speed
ω_{out}	Mechanical output speed

ω_{pb}	Mechanical pre-backlash speed
$\widehat{\mathcal{B}}$	Peak stator magnetic flux
$\mathcal{C}_s$	Thermal capacitance of the motor stator
$\mathcal{C}_w$	Thermal capacitance of the motor windings
$\mathcal{R}_{sa}$	Motor stator to ambient thermal resistance
$\mathcal{R}_{ws}$	Motor winding-stator thermal resistance
$\mathcal{T}_{ref}$	Reference temperature, at which resistance and back-EMF constants are defined
$\mathcal{T}_r$	Motor rotor temperature
$\mathcal{T}_s$	Motor stator temperature
$\mathcal{T}_{w_1}$, $\mathcal{T}_{w_2}$, $\mathcal{T}_{w_3}$	Temperature of motor windings 1, 2 and 3
$\mathcal{T}_w$	Motor winding temperature
$\boldsymbol{\mathcal{T}}_w$	Vector of the motor winding temperatures
$\mathcal{U}_{con}$	Thermal conductance due to convection
$\mathcal{U}_{rad}$	Thermal conductance due to radiation
A	Stator surface area
B_c	Coulomb friction coefficient
B_e	Motor eddy current iron loss constant
B_h	Motor hysteresis iron loss constant
B_t	Gear tooth damping coefficient
B_v	Viscous friction coefficient
G_r	Grashof number
H_1, H_2, H_3	Motor hall sensor outputs 1, 2 and 3
$I_{\theta_{ef}}$	Electrical current at the end of the commutation period in an individual phase
$\overline{I}$	Average individual phase current over a full electrical cycle
$\widehat{I}_1$, $\widehat{I}_2$	Peak electrical current at the end of the first and second switching intervals in an individual phase
J	Mechanical inertia

J_g	Transmission mechanical inertia, referred to output
J_l	Load mechanical inertia
J_m	Motor mechanical inertia
J'_m	Motor mechanical inertia, referred through transmission
K_E	Motor individual phase back-EMF constant
K_{Eref}	Motor individual phase back-EMF constant, at reference temperature
K_T	Motor torque constant
K_p	PID position gain
K_t	Gear tooth stiffness
$\boldsymbol{K}_o$	Vector incorporating the peak back-EMF constant and the shape of the back-EMF
L	Motor individual phase electrical inductance
L_{11}, L_{22}, L_{33}	Motor individual phase electrical self-inductance in phases 1, 2 and 3
M	Motor individual phase electrical mutual-inductance
M_{12}, M_{21}, M_{31}, M_{13}, M_{23}, M_{32}	Motor individual phase electrical mutual-inductances between phases 1, 2 and 3
N_u	Nusselt number
$P_{\mathcal{C}_s}$	Power transferred into the thermal capacitance of the motor stator
$P_{\mathcal{C}_{w_1}}$, $P_{\mathcal{C}_{w_2}}$, $P_{\mathcal{C}_{w_3}}$	Power transferred into the thermal capacitance of motor windings 1, 2 and 3 as heat
P_r	Prandtl number
P_s	Power loss transferred to heat in the motor stator due to iron losses
P_{sa}	Power transferred from the motor stator to ambient
P_{w_1s}, P_{w_2s}, P_{w_3s}	Power transferred from motor windings 1, 2 and 3 to the motor stator as heat
P_{w_1}, P_{w_2}, P_{w_3}	Power losses (transferred to heat) in motor windings 1, 2 and 3
$\overline{P_w}$	Average winding power loss
$\boldsymbol{P}_w$	Vector of power losses in the motor windings
R_1, R_2, R_3	Motor individual phase electrical resistance in phases 1, 2 and 3

R_{ref}	Individual phase electrical resistance, at reference temperature
R_{s1}, R_{s2}, R_{s3}	Sense resistor values
$\boldsymbol{R}$	Vector of motor individual phase electrical resistances at operating temperature
S_1, S_2, S_3	Switch requests passed from software to the driver electronics for motor phases 1, 2 and 3
T	Motor torque output
$\overline{T}$	Average motor torque over a full electrical cycle
$\widehat{T}$	Peak motor torque
T_c	Coulomb friction torque
T_e	Theoretical ideal motor shaft torque, ignoring mechanical and iron losses
T_g	Gear mesh inefficiency torque
T_h	Motor torque loss, due to hysteresis in the stator
T_l	Load torque
T_l'	Load torque, including that required to accelerate the load
$T'_{l_{RMS}}$	Load maximum continuous (RMS) torque, including that required to accelerate the load
$\widehat{T}_l'$	Peak load torque, including that required to accelerate the load
T_v	Viscous friction torque
T_{RMS}	Motor maximum continuous (RMS) torque
T_{ed}	Motor torque loss, due to eddy currents in the stator
T_{in}	Mechanical input torque
T_{out}	Mechanical output torque
T_{pb}	Mechanical pre-backlash torque
V_s	Power supply voltage
W_e	Power loss per stator kilogram, due to eddy currents
W_h	Power loss per stator kilogram, due to hysteresis loops
a	Gear pair pinion diameter

b_d	PID derivative set-point weight
b_p	PID position set-point weight
c	Gear pair large gear diameter
c_e	Stator eddy current loss constant
$c_{e'}$	Stator eddy current loss constant, including frequency factors
c_h	Stator hysteresis loss constant
$c_{h'}$	Stator hysteresis loss constant, including frequency factors
d	Duty ratio
$\boldsymbol{e}$	Vector of motor individual phase back-EMF electrical voltages
e_1, e_2, e_3	Motor individual phase back-EMF electrical voltage in phases 1, 2 and 3
e_n	Scaled back-EMF
f	Motor frequency of commutation
$f_K(\theta_e)$	Motor torque/back-EMF shape
g	Acceleration due to gravity
$\boldsymbol{i}$	Vector of electrical current in motor phases
i_1, i_2, i_3	Electrical current in motor phases 1, 2 and 3
i_{sum0}	Sum of initial phase electrical currents
k	Fluid thermal conductivity
k_1, k_2, k_3	Terms influencing the load factor, based on the load and move profile
k_α	Motor accelerating factor
$\widehat{k}_\alpha$	Maximum motor accelerating factor
k_β	Load factor
$\widehat{k}_\beta$	Maximum load factor
m_s	Mass of the motor stator
n	Mechanical gear ratio
n_s	Steinmetz exponent of stator hysteresis loss

$n_{\tanh}$	Scaling constant for hyperbolic tangent functions used to smooth nonlinearities
n_{fall}	Move profile deceleration period proportion
n_{max}	Maximum mechanical gear ratio
n_{min}	Minimum mechanical gear ratio
n_{opt}	Optimum mechanical gear ratio
n_{pp}	Number of magnet pole-pairs on the rotor
n_{rise}	Move profile acceleration period proportion
s	Laplace operator
s_{1h}, s_{2h}, s_{3h}	Switch commands in the driver half-bridge high-side
s_{1l}, s_{2l}, s_{3l}	Switch commands in the driver half-bridge low-side
t	Time
$\boldsymbol{v}$	Vector of motor electrical voltages across individual phases
$\boldsymbol{v}_n$	Vector of motor electrical voltages across individual phases, relative to some (virtual) neutral point
v_1, v_2, v_3	Motor electrical voltage across individual phases 1, 2 and 3
v_{s1}, v_{s2}, v_{s3}	Voltage across sense resistors
x	Turbocharger required linear nozzle displacement

Chapter 1

Introduction

1.1 Background

This thesis investigates electric actuator specification techniques for use in variable geometry turbocharging applications. It is sponsored by *Cummins Turbo Technologies* and is motivated by their product line. Variable geometry turbocharging is a mature technology in use in many modern road vehicles. This thesis addresses the process for selecting and evaluating new designs to fulfil a specific set of requirements.

Cummins Turbo Technologies, previously *Holset Engineering Co.*, are a subsidiary of *Cummins Inc.*, that manufacture diesel engines, filtration and power generation products. *Cummins Turbo Technologies* are based in Huddersfield, United Kingdom (UK), with the main research, product development and manufacturing all being located there. The company also has major manufacturing sites in China, India and Brazil. *Cummins* turbocharger range is suitable for medium to heavy duty diesel engine applications, from 2 l to 92 l. This includes trucks, buses, trains, mining equipment and ships. Products include fixed, variable geometry and wastegated turbochargers, power turbines and two-stage systems. For variable geometry and wastegate designs some method of actuation is required; both electric and pneumatic actuators are used within *Cummins*.

Cummins actuators are sourced from external suppliers who design to meet a set of *Cummins* specified requirements. Increasingly, design evaluation within the *Cummins* mechatronics group has used actuator modelling techniques. These models aid in complete turbo performance assessment and allow potential design changes to be evaluated. This is typical of a general move towards model-based design in industry [1].

Models of brushless permanent magnet machines are well documented in the literature. Increasingly, Finite Element (FE) analysis in multiple domains (e.g. thermal and electromagnetic) is being brought together in professional modelling tools. This type of modelling requires a very detailed knowledge of the machine geometry and materials and is appropriate for the component manufacturer; however this thesis investigates actuators at the system level, rather than the machine design level. The focus is on developing models that can be executed with reasonable computational efficiency and appropriate fidelity to evaluate performance of the integrated system; these may be parameterised using readily available datasheet information or simple tests of a sample machine. Mechanical transmission, power electronics and control loop behaviour are all well understood in isolation; however their performance alongside a specific motor must be understood for complete actuator evaluation.

Due to the high temperature working environment of a turbocharger actuator it is important to take into account thermal performance within the models. This will exclude some actuator designs that would fulfil the requirements at ambient temperatures.

1.1.1 Variable geometry turbocharging

A turbocharger can be viewed as two separate components: a turbine driven from an engine's exhaust gas, and a compressor increasing the pressure of the air fed to the engine. These are mechanically connected by a shaft and high speed bearing system. The layout of a *Cummins* turbocharger is shown in Figure 1.1.

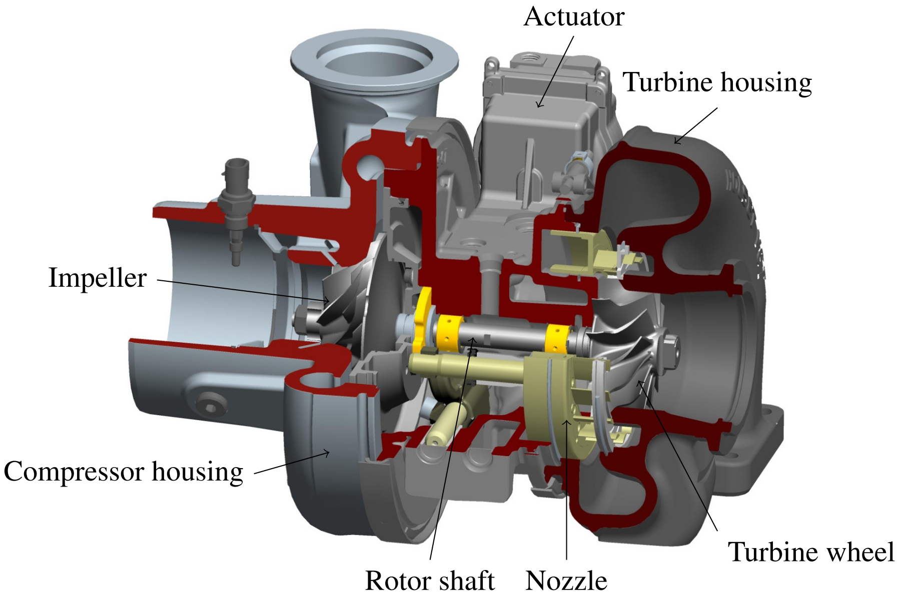

Figure 1.1: *Cummins* variable geometry turbocharger internals – Copyright *Cummins*

A standard normally-aspirated engine typically loses around a third of its energy down the exhaust, in heat and compression; the turbine exists to attempt to recover this energy. For example a $1000\,\mathrm{kW}$ engine might lose around $300\,\mathrm{kW}$, of which $50\,\mathrm{kW}$ could be recovered through the addition of a turbocharger. The turbine stage is typically around $75\,\%$ efficient at converting the energy in the hot compressed exhaust gas into rotation of the turbocharger shaft [2].

The power developed by an engine is directly related to the quantity of fuel burnt in its cylinders. For efficient combustion the fuel quantity must be in a precise ratio with the amount of air in the cylinders. By compressing the air entering a cylinder, more fuel may be injected, and therefore more power can be developed without increasing engine size. This is even more important in environments with a low ambient air pressure – such as operation at high altitude. Air entering the engine is compressed by the turbocharger compressor stage, driven by the turbine shaft. The compressor stage is typically around $80\,\%$ efficient at converting the shaft motion to air compression [2]. Airflow through the system increases with engine power output, and therefore turbocharger shaft speed also increases.

Output from a fixed geometry turbo is a design compromise over its speed range, and performance is likely to be poor during engine transients such as hard acceleration or braking; this can lead to characteristic 'turbo lag' or very high intake manifold boost pressures. In these cases a method of modifying the relationship between exhaust energy and intake compression is desirable.

Various solutions to this issue exist, for example wastegating allows some of the exhaust gas to bypass the turbine when intake boost pressures are high. Other solutions such as twin or sequential turbocharging are also in production by *Cummins* and their competitors. One of the best solutions currently available is variable geometry turbocharging. This allows dynamic variation of the turbine geometry during operation, increasing the efficiency of turbine operation over a range of speeds.

Two designs exist for turbine geometry variation; the most common is to have a ring of vanes around the inlet to the turbine wheel that are able to 'swing', thereby adjusting the area the exhaust gas passes through and the angle at which it hits the turbine wheel. The *Cummins* patented design uses a sliding nozzle over fixed vanes, or vice-versa, to vary the area the air passes through before reaching the turbine [3]. This design uses a reduced number of parts compared to a swing-vane design, leading to a more robust product. In both designs an actuator is required to vary the nozzle or vane position during use.

In use, a *Cummins* turbo shaft will typically be rotating between $80\,000\,\mathrm{rpm}$ and $200\,000\,\mathrm{rpm}$, depending on its size and the engine airflow. It has an oil feed from the engine which lubricates its bearings. Gas temperatures at the intake of the turbine can be up to $760\,^{\circ}\mathrm{C}$. Typically being mounted on the engine itself, the turbo will experience significant levels of vibration. In spite of this harsh environment, a *Cummins* turbo is typically be expected to last for $20\,000\,\mathrm{h}$ of service, or around $1\,000\,000\,\mathrm{miles}$ of road use.

1.2 Scope

This thesis is specifically focussed on the investigation of future generation electric actuator technologies for use on variable geometry turbochargers. The actuation process encompasses everything from the reception of a control signal to the movement of the turbocharger nozzle. Specific subsystems in this component are:

- Electronic control, including motor drivers and the closed-loop position control system.
- The electric motor.
- A gear train transmission to alter the torque/speed.

The process of receiving commands from an Engine Control Unit (ECU), or similar high level controller, and the specific system for moving the nozzle within the turbocharger are on the periphery of this research. They relate to the design of the actuation system, however they are also embedded within separate systems that are outside of this project's scope – overall vehicle control and turbocharger mechanical design respectively.

There are a number of measurable outcomes that may be used to assess an overall actuator design, including: power consumption, closed-loop performance, robustness, lifetime, cost, mass or volume. Current *Cummins* actuator designs achieve acceptable performance in most of these areas, however the volume (or 'space claim') of the these designs is noted as a particular area for potential improvement.

Although alternatives are discussed, this work focuses on a brushless Direct Current (DC) motor driven using standard half-bridge electronics and driving a set of spur gears. The primary focus is on developing models and processes to aid in actuator motor and gear specification, as this is where the widest range of options are available to a designer.

1.3 Aims and objectives

1.3.1 Aims

The overall aim of this work is to develop and test an actuator system design process for use in the variable geometry turbocharging application. The process should ensure that the actuator meets a user-specified set of requirements and also allow optimisation of measures such as volume, reliability, mass, precision, efficiency and cost.

The design process should include a formal actuator software modelling process to assist *Cummins* in quickly evaluating actuator designs and to form part of larger system simulations.

1.3.2 Objectives

Based on the overall aims of this work, the following objectives are specified:

- Develop, implement and validate actuator models to be populated based on physical component attributes. The actuator models will cover:
    - A control loop to accept a position demand.
    - A representation of the drive electronics.
    - A brushless DC motor.
    - A series of mechanical gears/linkages.
- Parameterise these models using simple motor tests or manufacturer supplied data.
- Allow investigation of actuator performance sensitivity to parameter variations.
- Develop a process for designing/evaluating an actuator against a set of requirements.
- Demonstrate the process using an appropriate prototype.

1.4 Significance of the work

Although actuator design and evaluation has been undertaken previously within *Cummins*, wider industry and academia, a key aspect of this work is the consideration of the integrated actuation system, focussing on the turbocharging application. The high temperature turbocharger environment and the actuator load profile present particularly challenging requirements that other studies have not addressed.

The closest similar work identified to date is [4], which investigated the optimal selection of a motor and gearhead combination for use in mechatronic applications, with a range of different optimisation criteria. This thesis builds upon this work, extending it with regard to investigations of the specific machine, driver and control scheme used.

Mathematical modelling of the physical aspects of motor operation is well documented in textbooks. Implementations in *Matlab Simulink* are frequently presented in the literature. Previous academic work has also investigated the joint specification of motor and transmission. Within this research, previous work is extended in a number of distinct areas, such that a joined-up process to work from a specific set of actuator requirements through to an evaluated design is formed.

Efficient simulation of actuator performance, based on physical component parameters, is critical to efficient design and development processes. This work allows models to be parameterised based on simple tests or using manufacturer-supplied data and derives computationally efficient versions of these models that significantly reduce simulation time. The models cover electromagnetic, mechanical and thermal aspects of the actuator and are validated against experimental test results.

The models are used within a design process to assess the suitability of specific actuator components for a particular positioning application. This enables the optimisation of the overall actuator system for the specification, whilst using commercially available components.

Although the focus of this work is on the turbocharging application, the models and processes developed are appropriate to most positioning actuator applications; particularly where operating conditions differ from the standards assumed in the manufacturer's datasheet, or where variability in some parameters is expected.

1.5 Thesis overview

This thesis is divided into several distinct sections, a review of relevant previous work, a description of models developed in this work, a summary of the experimental work undertaken and the formulation and demonstration of the design process. Chapter 2 provides an introduction to current technologies and previous research in this area. Further details of the *Cummins* actuation system are given in Section 2.2, before going into more detail on the actuator itself. The actuator is considered in three parts: a motor (Section 2.3), a set of drive electronics (Section 2.4) and a transmission (Section 2.5). Control schemes are considered as part the drive electronics. A range of different options for these components is presented, with the focus quickly narrowing to brushless permanent magnet motors and a spur gear train. Previous work investigating modelling of these components is reviewed in Section 2.6, and the theory of combined actuator component specification is introduced in Section 2.7. The summary in Section 2.8 details the specific actuator components and methods that are further investigated in the rest of the thesis.

A comprehensive description of the models developed under this work is given in Chapter 3. Several different domains are considered within these models, including electromagnetics (Section 3.2), thermodynamics (Section 3.3), power electronics (Section 3.4), control (Section 3.6) and mechanics (Section 3.7). Also described within the chapter is a more computationally efficient motor model (Section 3.5) that allows simulation using a far larger time-step, which is more appropriate for use in long duration thermal analysis. A summary detailing the relationship between various model components is given in Section 3.9. This also provides an overview of the effect of various model parameters on performance.

Chapter 4 describes a series of tests developed for measuring the motor parameters in order to populate the models. These are divided into testrig parameters (Section 4.2), motor electrical parameters (Section 4.3), and motor thermal parameters (Section 4.4). Transmission parameter measurement is beyond the scope of this work, instead parameters are taken from typical textbook or datasheet values, or experiments performed by *Cummins*.

The motor models developed in Chapter 3, and parameterised for the sample motors using the test from Chapter 4, are experimentally validated in Chapter 5. Steady-state performance in all domains is addressed using speed-torque curves in Section 5.2. Electromagnetic and mechanical dynamic response is investigated in the frequency domain in Section 5.3. Thermal transient performance is considered in Section 5.4 using long duration varying load and duty tests.

Chapters 2, 3, 4 and 5 lay a foundation for investigating actuator performance. This is built upon in Chapter 6 to construct and demonstrate a process for assessing actuator components and actuator design suitability. Initially a set of actuator requirements is defined in Section 6.2. These are developed by assuming a move profile in Section 6.3 to form a load profile requirement for the actuator in Section 6.4. A candidate actuator to be assessed against these requirements is introduced and parameterised in Section 6.5. It is shown how these parameters can be used to plot motor performance in speed-torque curves in Section 6.6, and against the actuator load curve to assess suitability in Section 6.7. The analysis in this section shows that the candidate actuator should be just capable of meeting the example requirement specification. A full model of the actuator is developed in Section 6.8 and an analysis of its performance against the requirements is performed in Section 6.9. This compares model simulated performance against the results of testing using a pneumatic load. Test results are compared for a range of loads, temperatures, and move requirements.

Conclusions are drawn in Chapter 7, along with a summary of the key contributions in this work. Possible extensions to this work are also suggested in a number of areas.

Appendices are presented to cover: full equations for the computationally efficient model (Appendix A); justification of the power loss approximation in the computationally efficient model (Appendix B); implementation of the model mathematics within *Matlab Simulink* (Appendix C); similar ‘acausal’ model implementations (Appendix D); alternative motor thermal models that were rejected during the work (Appendix E); details of the main test setup used throughout the work for motor testing (Appendix F); assessment of different switching schemes using the models (Appendix G); and details of the set of sample motors used throughout the work (Appendix H).

Chapter 2

Literature review

2.1 Introduction

The core focus of this work is on actuation mechanisms for variable geometry turbochargers, however within the automotive powertrain, electrical actuation is also applicable to turbocharger wastegates, throttle control valves, exhaust gas recirculation valves, electronic clutches and variable valve lift adjustment [5]. Electric machines in general are playing an increasing role in the automotive drivetrain, including water and fuel pumping and new developments in turbine-generators for waste heat recovery [6, 7]. Separating the turbocharger turbine and compressor and coupling them electrically, through a generator and a motor, rather than mechanically via a shaft, is also an area of active research [8, 9].

This chapter introduces the application for the actuator, with reference to *Cummins* variable geometry turbocharger designs, and evaluates the subcomponents that make up a typical actuator design – a motor, set of drive electronics and transmission system. Also provided is a review of previous work on actuator modelling and actuator specification techniques.

2.2 Variable geometry turbocharger actuation

Actuation in the context of this work refers to the transformation of a control signal into a movement at the turbocharger. The actuator position demand signal comes from the ECU and is sent over the vehicle wiring to the actuator using the Controller Area Network (CAN) protocol. These signals are typically received every $10\,\mathrm{ms}$, and a status message is returned from the actuator slightly less frequently.

The ultimate product of actuation is the movement of the nozzle in the variable geometry turbocharger. This is effected by a linkage mechanism that will depend on the design of the actuator and turbocharger. *Cummins* generally refer to the 'actuator' as the removable component that connects to the turbo to generate movement, however the full actuation system includes a series of linkages within the turbo that move the nozzle – as shown in Figure 2.1. In current *Cummins* variable geometry turbochargers this mechanism is contained within the central bearing housing. The nozzle is actuated from behind by two T-shaped ‘push-rods’. The push-rods are located either side of the main turbo shaft and are connected to a rotating yoke through a pair of ‘wear-blocks’. These translate the rotational movement of the yoke into linear movement in the push-rods. The yoke is connected via a ‘cross-shaft’ to a sector gear on the outside of the bearing housing. It is the sector gear that is driven by the external actuator. Due to the temperatures and pressures involved, the materials and sealing used in these moving parts is critical. Tolerances must allow for thermal expansion as well as part-to-part variation. This leads to a relatively large amount of friction in the seals and introduces some backlash in the mechanism.

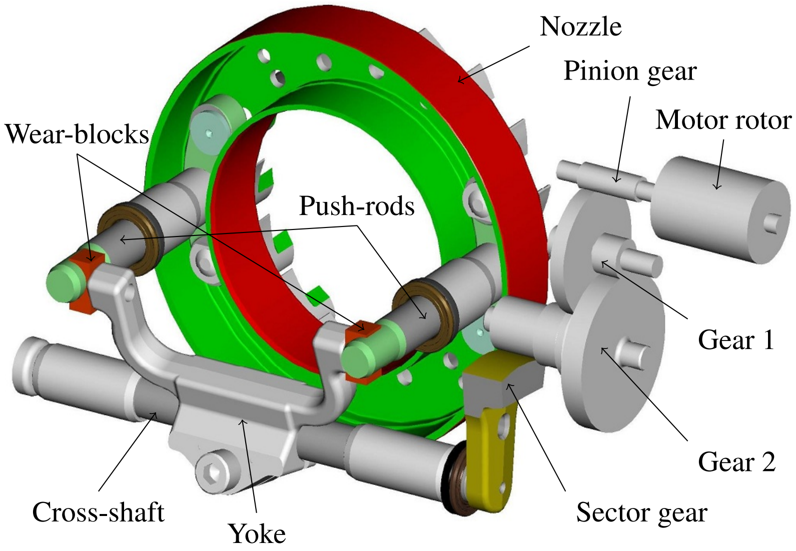

Figure 2.1: *Cummins* variable geometry nozzle actuation mechanism – Copyright *Cummins*

Nozzle movement can be up to 25 mm. In operation, the exhaust gas in the turbine produces a force against the nozzle that varies with exhaust gas pressure. Balancing holes in the nozzle reduce this force somewhat, however it still varies with exhaust gas pressure and nozzle position. The exhaust gas pressure will also pulsate due to engine valves opening and closing. Peak force on the nozzle during an exhaust pulse can be up to 900 N.

Whilst the nozzle, push-rods, wear-blocks, yoke assembly, cross-shaft and a sector gear are not considered as part of the ‘actuator’ from a sourcing perspective, they are specific to the actuator design and their performance is integral to actuator performance – therefore they are considered as part of this work.

Two main methods of actuation are currently in use within *Cummins*, pneumatic and electrical. *Cummins* pneumatic actuators use a piston to move a lever connected to the cross-shaft. The piston has a stroke of around 10 mm and can be mounted in a range of different positions depending on the customer’s engine requirements.

Pneumatic actuators are very robust and have a product life equal to, or better than, the turbocharger. The air supply to the piston acts against a spring, such that pressure in the supply specifies the position of the actuator. Compressed air is supplied from the vehicle's 'tank air' system and pressure is regulated by a controller. The controller and air supply can be mounted remotely from the turbo. Although pneumatic systems are quite reliable, they are unable to match electrically actuated systems in accuracy, controllability or response times.

Current generation *Cummins* electrical actuators utilise a brushless DC motor, controlled by an electronic drive circuit mounted in close proximity. The motor output drives a gearbox which then drives a sector gear on the turbo bearing housing. The motor, drive electronics and gearbox all mount on the outside of the turbo body, in between the turbine and compressor covers. Electrical actuation provides fast response times and accurate behaviour from a power source that is readily available in all vehicles. It is therefore highly likely that this will remain the favoured method for the foreseeable future. However there exist numerous different technology options within this area that could potentially perform the role of actuation.

Relatively little academic research has been published relating specifically to turbocharger actuator design. [10] describes one such design, utilising a lead screw driven from a brushless DC motor. Another design is presented in [11], where a pancake torque motor is used without a gear reducer to directly drive a load.

2.3 Motors

Although other options exist – solenoids and similar – electric motors are by far the most common mechanism for transferring electrical into kinetic energy. A brief overview of electric motors is given here in order to justify the focus of this work on brushless permanent-magnet machines. The structure of these is then discussed in order to provide a background to the more detailed analysis covered in the following chapters.

The majority of electric motors operate through the interaction of magnetic fields and current carrying conductors. Motor types differ in the way these fields and currents are created, positioned and varied. Depending on the design of motor, control of the generated torque is either through regulation of the current in its coils, or by switching which coils are connected, or some combination of these. Key parameters for comparison of motor designs are the torque they are capable of producing, and the speed at which they are able to operate. Suitability for actuator use may also consider torque or power per unit volume or mass, depending on the design criteria.

Piezoelectric [12], or 'ultrasonic', motor [13–18] technologies are one of the few options that do not rely on electromagnetics. These utilise the microscopic movement of piezoelectric elements in order to produce bulk motion. This type of motor is often used in the autofocus mechanism of modern cameras. Whilst these motors possess several benefits for an actuator application, such as compact size, high torque density and excellent positioning accuracy [19], there are potential issues with efficiency, cost and fatigue. There are also no motors of this type that are currently able to fulfil the power requirements of a turbocharger actuator; although the torque is generally sufficient, the speed of operation is too low [20].

Linear motors can be built in various designs, analogous to rotary motors [21–23]. Integrated into the turbocharger bearing housing, a linear motor could drive the push-rods or nozzle directly, eliminating several mechanical linkages. Unfortunately it is difficult to generate the required holding force on the nozzle with this type of motor and no gearing system, without producing an infeasibly large design. Previous work looking at linear reluctance actuators within the bearing housing [24–26] found that the force produced by an actuator of this type was unlikely to be sufficient.

Conventional rotary electromagnetic motors are available in a variety of different types. These include induction, reluctance and brushed or brushless permanent magnet machines. Induction motors produce a magnetic field in the rotor through interaction between its current paths and the stator field [27]. The stator field must therefore be varying at a higher frequency than the motor's rotation, for this reason they are often referred to as 'asynchronous' machines. Although torque is produced at all speeds, accurate torque control at zero speed is difficult with this type of machine. They are therefore unlikely to be suitable for use in a positioning application.

Reluctance motors utilise the reluctance, or alignment torque produced in a magnetically permeable material. They can be designed to synchronously follow a rotating magnetic field in the stator, or they can be 'switched' between several discrete alignment positions. They are capable of high speed, high torque and accurate low speed positioning [28]. They also do not use any permanent magnet material, allowing them to operate at very high temperatures. Their similar attributes to brushless permanent magnet machines has led to a recent renewed interest in their capabilities as the price of permanent magnet materials is increasing [29–32]. In many applications it is possible to achieve the same performance from both types of machine in a similar package size; however, the equivalent reluctance machine would require a considerably smaller minimum air-gap between the rotor and the stator. The level of vibration seen in the automotive environment is likely to be a problem for a small air-gap, without the use of expensive bearing designs. For this reason reluctance machines are not considered any further within this work, however it is noted that future technological advances and the cost and availability of rare-earth permanent magnet materials may make this design more viable in the future [33]. In this case much of the work in this thesis might be adapted to suit this type of design.

In a brushed motor, a stationary magnetic field is set up in the stator through either coils or permanent magnets; this interacts with a varying magnetic field in the rotor to produce torque. Current is carried to the rotor through stationary brushes touching moving rotor connections. This connection can be made with different windings at different points in the rotation, allowing the current to ‘commutate’ as rotor angle changes. This allows torque to be generated through a full rotation using only a DC source. The inherent mechanical commutation in the design makes brushed motors a cheap and effective option and they are therefore commonplace in a variety of different applications. Unfortunately the mechanical commutation also introduces extra friction into the design and the brushes are prone to wear. Depending on the application, sparking from the mechanical friction or Electromagnetic Interference (EMI) from the switching can also be an issue. Their suitability for use in an automotive actuator will depend upon the trade-off between service life and cost. For *Cummins*’ high durability, long service interval products, they are not expected to be suitable.

For accurate control and high torque applications, brushless permanent magnet motors are commonly used in a wide variety of industries. These provide a long lifespan, very efficient operation, and the ability to operate at a very high power [34]. A varying magnetic field is set up by electronically commutating current between coils in the stator. Permanent magnets on the rotor provide a constant high strength field that interacts with the stator field to produce torque. Electronic circuitry is required in order to vary current in the stator, along with information about the rotor position. There is considerable scope for variation in electronic commutation strategies for brushless motors, including sensorless control, electronic switching components and current waveforms. Design variation is also possible in the number of coils, magnet numbers, winding topology and motor geometry. The current supply can also be either a sinusoidal- or square-wave, often related to the shape of the back Electro-Motive Force (back-EMF) produced by the motor.

The remainder of this section briefly addresses some of the options available in brushless permanent magnet machine design. A basic introduction is provided in [35], whilst a detailed and comprehensive review is given in [34]. Although this thesis focuses on brushless motor equipped actuators, the detailed design process for this type of motor is outside the scope of the work.

2.3.1 Back-EMF

As the flux of the rotor permanent magnets links the stator windings during rotation, an Electro-Motive Force is induced within them. This is referred to as the motor back-EMF and is determined by the rotor magnetisation and the geometry of the magnetic circuit created. Typically the variation of back-EMF with rotor position, for a constant speed rotation, is either sinusoidal or trapezoidal. The number of pairs of magnet poles on the rotor will determine the number of back-EMF peaks seen during a full rotation of the motor. The magnitude of the back-EMF waveform varies linearly with the speed of motor rotation, and the constant of proportionality is referred to as the ‘back-EMF constant’. The energy conversion from electrical to mechanical by the machine means that the ratio of back-EMF to speed also determines the torque produced by a current in the windings. In this context it is usually referred to as the ‘torque constant’. When expressed in consistent units, and measured in the same manner, the back-EMF constant is equal to the torque constant. This is the ‘ideal’ torque, neglecting magnetic and mechanical losses in the machine. The manner in which these values are specified varies between manufacturers. However throughout this work the back-EMF constant is defined as the ratio of the peak of a single phase to the angular speed of rotor shaft rotation.

2.3.2 Rotor design

A wide variety of different rotor designs are possible, with variation in permanent magnet material, fixing method, shape, size (or ‘pole arc’), position (‘surface’ or ‘interior’ mounting) and number of poles [34]. Variation occurs for reasons of cost, robustness and ease of manufacture, however the primary impact is on the shape and magnitude of the back-EMF waveform, the inertia of the rotor and the losses during operation. Another impact of rotor design can be ‘saliency’, the variation in reluctance of the magnetic flux path – or ‘effective air-gap’ – with rotor position. This can be particularly significant if magnets are embedded within the rotor structure. Saliency is not addressed in this work as the majority of motors suitable for use in actuators utilise a continuous ring of ‘external’ permanent magnet material fixed to a cylindrical rotor, therefore exhibiting virtually no saliency.

Whilst internal rotor, radial flux, machines are the most common, both axial flux and external rotor designs are available. Axial flux machines can be produced with very short overall length, however they require very closely packed ‘end-turns’ at the axial end of the winding. This can lead to issues designing, constructing, and dealing with heat generation. For conventionally-mounted turbocharger actuators overall space-claim is generally more important than minimisation of a single dimension; therefore axial flux machines are not expected to offer significant benefits. An automotive actuator design based on an axial flux ‘pancake’ motor is modelled and assessed in [11].

External rotor designs locate the rotating permanent magnets on the outside of a stationary stator, requiring a cup type rotor design. This type of design can generally produce greater torque for their size, but at the expense of increased inertia. Heat generated within the motor windings can also be harder to dissipate when they are surrounded by the rotor. The benefits of this type of motor design for actuator use is likely to depend upon the specific requirements and is discussed further in Chapter 6. A recent discussion of the benefits for general positioning applications is given in [36].

Various different materials may be used for the permanent magnets. ‘Ferrite’ magnets were the first to receive significant attention for permanent magnet motor applications. The development of magnets using ‘rare earth’ metals, such as Samarium Cobalt (SmCo) and Neodymium Iron Boron (NdFeB), have extended power levels and increased cost-effectiveness [34]. Most modern high power brushless motors will use NdFeB magnets, with SmCo being used where high working temperatures require a compromise in power density. Ferrite magnets still find application where cost is a significant design driver.

Temperature increase will produce an approximately linear reduction in permanent magnet flux density and therefore torque. This reduction is reversible up to a fixed temperature, after which permanent demagnetisation will occur, with the magnetisation dropping sharply to zero at the ‘Curie’ temperature [37]. This sets a maximum temperature for the rotor that should not be exceeded during operation.

2.3.3 Stator design

Motor stators are typically constructed of a stack of laminated soft iron sections. The material is selected for its favourable magnetic properties and is axially laminated in thin sheets to minimise circulating currents induced by the changing magnetic field in the stator. These ‘eddy-currents’ can be a significant loss mechanism that contributes to inefficiency and stator heating. Another aspect of ‘core losses’ is ‘hysteresis’ loss; this occurs due to the hysteresis in the magnetisation curve of the stator steel [34].

Motor windings, generally copper wire, are usually inserted into slots in the stator, such that ‘teeth’ are created that carry the magnetic flux. The reluctance of these teeth can generate ‘detent’ or ‘cogging’ torque in the motor that is undesirable for some applications. A significant quantity of research has been devoted to the reduction of cogging torque in permanent magnet motor designs [38–43]; skew of either the stator teeth or the magnets axially, or careful shaping of the magnet profiles are frequently used. Toothless stator designs are possible, where the windings are located in the air-gap of the machine.

A wide variety of different stator designs and winding configurations are available, with variation in winding locations and stator geometries. Detailed FE, or generalised harmonic analysis, is used to determine the performance of variations in motor design. Optimisation methods have been proposed for automatic parameter optimisation of pre-determined designs, according to specified criteria [44–47]. Both stator and rotor geometries may be optimised, along with winding configurations.

In all designs a section of ‘end-winding’ is necessary to turn the wires. This portion of the winding will not generate torque and is ideally therefore minimised. This leads to designs where the windings no longer span the full diameter of the stator, these are referred to as a ‘short-pitched’, as opposed to a ‘fully-pitched’ winding. At the limit, the pitch of the winding is only a single stator tooth, in this case the winding is referred to as a ‘concentrated’ winding. There is also an interplay between the number of magnet pole-pairs on the rotor and the number of stator slots. Where a non-integer number of slots exist per pole, this is referred to as a ‘fractional slot’ winding [34].

Due to the low costs required in automotive components, motor assembly is an important consideration. Manual winding of coils around teeth may allow a compact, high torque design to be realised, however this is likely to be too expensive as a production technique. A straightforward and effective technique for mass production is to pre-wind concentrated windings on a bobbin, which is then fitted onto the stator teeth. The use of resin ‘potting’ compounds around windings can improve thermal conductivity, and is frequently used.

Even for a fixed stator design, there can still be significant variation in the windings. Generally it makes sense to fit as much copper into the cross-sectional area of the slot as possible, larger diameter wire will decrease resistive losses, but will reduce the number of possible turns in the coil. The optimum trade-off between turns and resistance will depend upon the intending operating voltage of the machine. Manufacturers typically produce a range of motors with similar stators and adjust the windings for operation from different voltage supplies [48]. Circular wire will also not pack perfectly into the stator slots, and therefore a ‘fill-factor’ or percentage area that can be filled with copper needs to be taken into account.

Typically stator windings consist of three phases, these can be connected in either ‘delta’, with two phases connected to each motor terminal, or ‘Y’, with phases connected at a central ‘star’ point, and each phase separately connected to a terminal. Equivalent delta-connected windings give a factor of $^1/_{\sqrt{3}}$ decrease in back-EMF constant [34] compared to Y-connected. This means that Y-connections will produce increased torque at low speeds, and they are therefore the natural choice for positioning applications.

Machines can theoretically be constructed with any number of phases and will require two or more conductors to carry current from their supply. Assuming that the area of conductors required to power the machine is to be minimised, three phase designs are found to be considerably more effective, as no return line is needed [34]. Single phase machines do find application, particularly for high-speed low-cost machines [49], however two and four phase designs confer no advantages over three. Five or greater phases are of interest in larger sizes, particularly as they can be constructed to be ‘fault-tolerant’, whereby they continue operation whilst one or more phases are faulty. Research in this area is extensive and ongoing [50]; however significant benefits are required in the application to justify the increase in power electronics and construction complexity required for more than three phases. With fault tolerance not being a significant concern in this application, and potential torque increases unlikely to be significant, it is not expected that multiphase machines will offer benefits for turbocharger actuators in the near-term.

Temperatures within the machine must be maintained below certain levels, as very high temperatures (above 180 °C) can cause instant failure due to either winding insulation breakdown or magnet demagnetisation [51, 52]. Even prolonged exposure to moderately high temperatures (above 115 °C to 155 °C for most machines [48, 52]) can cause winding degradation that significantly reduces expected lifespan [53]. Various grades of winding insulation are available for different applications, the main difference being their rated temperature specifications. Below these limits machine temperature still has a significant impact on performance. Winding resistance, and therefore resistive power losses for a given current, increase with temperature, whilst magnet flux reduces due to reversible thermal demagnetisation [34, 54]. These losses contribute to a reduction in efficiency at high temperatures.

2.3.4 Position sensing

A method of sensing rotor position is required in order to synchronise electronic commutation in a brushless motor. Several different options for position sensing exist, with variation in cost and performance [55]. For high precision, a rotary encoder may be added to the rotor shaft. An encoder uses electrical, magnetic or optical sensors to provide a digital electronic measure of position. Incremental encoders produce square wave outputs that may be counted to calculate position. Absolute encoders will directly report a position, however they require more digital channels to do so. These types are both available in a range of resolutions and may be interfaced directly to the motor control software. They add extra expense and size to the system and may suffer in a high vibration environment; therefore they are unlikely to be suitable for an automotive application.

The most common method of position sensing in brushless permanent magnet motors is the addition of ‘hall-effect’ sensors into the design. These are cheap, robust and operate over a wide range of temperatures. A hall sensor senses the magnetic flux of the rotor field to provide a digital signal indicating when the field is above a threshold value. Three correctly-positioned hall sensors allow sufficient determination of rotor position for three phase commutation. Incorrect hall sensor positioning can lead to increased torque ripple [56], however this is not generally an issue. They are also largely immune to vibration effects.

The cheapest and most compact motor designs do not include sensors at all. In this case ‘sensorless’ control must be used for commutation. A six-step controlled machine only has current flowing in two of its three phases, but a back-EMF voltage is present in the third phase; electronic sensing of this back-EMF will provide a measure of rotor position [57–59]. Noise on this signal may be compensated for by the addition of a position estimation algorithm [60]. This technique has been extended to sinusoidally excited machines through back-EMF sensing during the Pulse Width Modulation (PWM) off periods [61]. Sensorless control performance tends to degrade at low speed due to the low signal-to-noise ratio. Some research has attempted to address this [62, 63], however it is currently not considered to be a viable technique for stationary torque holding and positioning control.

Signal injection techniques may also be used for sensorless control. These exploit variation in saliency or magnetic circuit saturation to determine position and are reported to perform down to zero speed at high load [64–66]; however, neither of these effects are necessarily significant in the type of motor design commonly used in automotive actuators. For both sensorless control methods, extra analogue to digital conversion and processing power is required. This can increase the overall cost of the technique significantly.

2.3.5 Speed-torque curves

Motor performance is typically defined in terms of its speed-to-torque relationship at a given voltage [34, 48]. Under steady-state mechanical conditions, and discounting thermal and commutation effects, the speed-torque is virtually linear, its gradient depending on the back-EMF constant. Where the electrical time constant becomes similar to the commutation period of the machine, the rise time of the current can become a significant proportion of the commutation period, reducing average torque [48]. This effect is more pronounced in machines with high number of pole-pairs, due to the high electrical frequency for a given rotor speed. It causes a reduction in the middle of the speed-torque curve – this effect is seen for some of the motors examined in Chapter 5.

Motor manufacturer datasheets will generally supply a set of points on the speed-torque curve, as identified in Figure 2.2. ‘No-load’ parameters for speed and current indicate the performance without any external load applied. A ‘stall torque’ parameter indicates the torque at which speed will be reduced to zero. At full operating voltage a large current is typically required to sustain this torque, such that the motor heating from Joule losses in the windings would quickly raise the temperature above the maximum allowable. Manufacturers therefore also supply ‘continuous’ or ‘rated’ parameters. These define the point on the speed-torque curve where maximum operating temperature is reached during steady-state operation. It is generally acceptable to run the motor below the continuous torque rating indefinitely, however operation above this torque should be time limited to avoid exceeding temperature limits. A continuous stall torque may also be specified, this indicates the maximum torque that can be sustained at zero speed, and provides a boundary on the continuous operation region of the motor. The solid line in Figure 2.2 bounds the achievable speed-torque points for a specified voltage, whilst the shaded area shows the speed-torque combinations that may be used continuously without exceeding motor thermal limits.

The parameters and speed-torque curve are only valid for a given ambient temperature and mounting arrangement; 25 °C is typically used. Some basic thermal

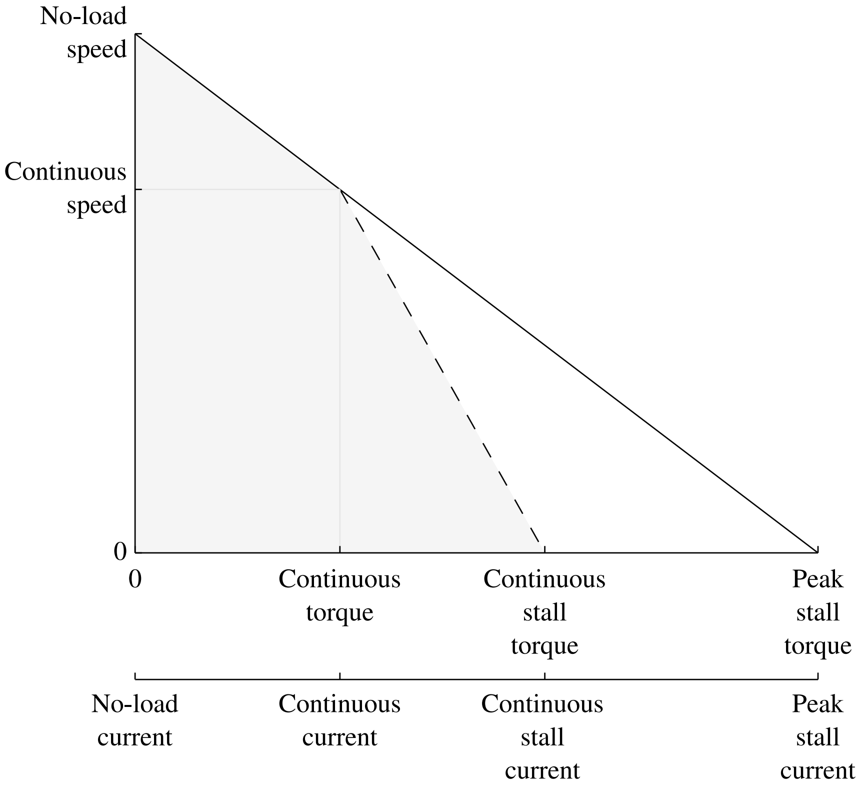

Figure 2.2: Example layout of a motor speed-torque plot, marking parameters that are commonly available in manufacturer datasheets; the shaded area is suitable for continuous operation

parameters, including the maximum permissible winding temperature, may also be included in the datasheet.

2.3.6 Discussion

Piezoelectric, ultrasonic and linear motors are not considered to be suitable for this application in the short term. Although brushed motors may be appropriate for some actuator applications, they are not expected to be robust enough for high reliability *Cummins* actuator applications. Induction motors are not appropriate due to difficulties in their control at low speed. Reluctance motors might be considered in the future if the small air-gap was acceptable. This might occur through a reduction in the typical engine vibration spectrum, or through improvements in motor bearing design. The most appropriate machine, and that most commonly used in this application, is the brushless permanent magnet motor. For low cost automotive actuators it is expected that hall sensors will remain the most viable position sensing method for the foreseeable future.

Motor design and optimisation have been the focus of a great deal of research, however this work is primarily interested in the performance of the integrated actuator system, where the focus is on selection of an appropriate commercially available motor. In this case the motor performance may be inferred from a few key electrical parameters, in particular the shape and magnitude of the back-EMF waveform.

2.4 Drive electronics and control

The purpose of the drive electronics is to control the mechanical movement of the actuator in order to respond to a position demand from a higher authority – most likely the ECU in an automotive context. The voltage and/or current must be controlled in order to achieve the demanded position and reject load disturbances. Additionally, in a three-phase brushless motor, the electronics are responsible for commutating current between the winding phases, according to a measurement of rotor position. The current should also be limited to protect the electronics and the power supply. Motor temperature may also be controlled through current regulation.

2.4.1 Power circuit

In order to switch between all three phases, allow operation in both directions, and potentially also provide regenerative braking, a three phase ‘half-bridge’ configuration is the industry standard for brushless motor control [34]. This uses two power electronic switches (usually Metal-Oxide-Semiconductor Field-Effect Transistors (MOSFETs)), with anti-parallel diodes, per phase. This is shown, along with the labelling convention that will be adopted throughout this work, in Figure 2.3, where the open connections 1, 2 and 3 refer to the motor coil connections, as indicated in Figure 3.1. Also shown in this diagram are additional current sense resistors R_{s1}, R_{s2} and R_{s3}. These are of low resistance, but will generate a voltage drop across them depending on the current flowing in the leg of the converter. These amplified voltage signals may be utilised in analogue control circuits, or converted to be used in a digital control loop. By positioning one sense resistor in the common supply return, the total current may be measured. The current in leg one may still be calculated by subtracting the currents in legs two and three from the total.

Alternative configurations have been proposed and are used in some specialist applications, often to reduce cost by reducing the number of switching components, or to increase the fault tolerance of the circuit [67, 68]. This can come at the expense of higher bus capacitance requirements or specific motor design requirements (such as bifilar windings). These alternative designs are not considered further in this work as they are not in widespread use and are likely to introduce extra control issues.

2.4.2 Commutation and current-shaping

Continuous rotation of a brushless rotor requires current to be switched between the coils of the stator to maintain positive torque. Where this switching is discrete it

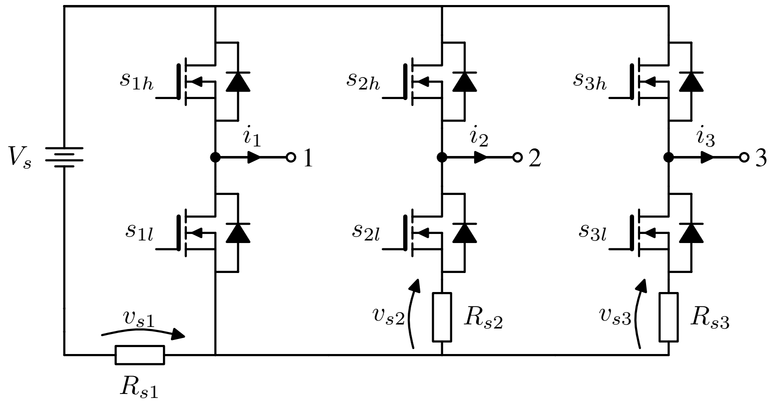

Figure 2.3: Three-phase half-bridge circuit

is referred to as commutation and is analogous to the operation of a brushed DC machine. More generally the current or voltage may be controlled to follow a specific shape. This is often a sinusoid, making the switching process similar to a DC:AC converter or ‘inverter’.

The exact shape of the current waveform depends on the structure of the motor, and the control scheme. It is often a trade-off between electrical and mechanical performance objectives. For smooth constant torque, the phase current shape should be matched to the back-EMF shape – usually either sinusoidal or trapezoidal – during the current supply period. Mismatches between the two will create torque variation with position, often referred to as ‘ripple’. Achieving an exact match may produce increased winding temperatures or require more frequent switching in the power electronics [34]. Combinations of current shape and back-EMF shape are investigated in more detail in Section 3.2.2. The waveform shaping should be viewed as separate from the current/voltage regulation used to control torque, speed or temperature.

A common approach is the use of ‘six-step’ commutation. This switches the current on or off to correspond with peaks in the phase-to-phase back-EMF. Three phases, with a positive and negative peak per electrical cycle, gives six ‘steps’ of commutation. Three hall sensor outputs provide sufficient positional information to commutate a motor in this sequence.

2.4.3 Voltage control

Brushless motors are typically controlled to achieve a specified speed or torque, often as part of a higher level control scheme. The applied voltage will determine the speed, and the current will determine torque. Control of voltage is achieved through high frequency switching or PWM. The effective voltage will be the line-to-line DC voltage scaled by the ratio of the ‘on’ to ‘off’ periods, neglecting losses and dead-time in the switching. The switches of the half-bridge circuit in Figure 3.1 may be used for PWM control of the voltage as well as for regulating current between phases [69].

There are a wide variety of different switching schemes that can be used to modulate the switches.

In this section a short summary of possible switching schemes to provide six-step commutation with a set duty ratio is given. If the PWM duty cycle is short compared to the motor winding electrical time constant, then a fixed duty ratio will approximate a fixed voltage supply to the winding. Switching schemes differ in the linearity of this duty ratio to voltage relationship, and also in: the current ripple seen at the supply and winding; the power losses produced in the switches; the division of losses between switches; and the ability to return power to the supply.

Six-step commutation is selected for discussion as it is the most likely choice for small cheap actuator-type motor controllers and it is in use in current *Cummins* products. This selection will be discussed further and justified in Chapter 3. A summary of different PWM schemes is given in Table 2.1. For brevity only the first two steps of the six-step control are given, the latter four follow from the first two by simple cyclic shifting. These may be used directly for voltage control, or indirectly for current control with the addition of a sensor and control loop. Although the overall structure of a sinusoidal scheme would be different, many of the features and trade-offs discussed here will remain relevant.

In the literature switching schemes are referred to by a variety of different names [34, 70] and therefore a simple letter is used here to designate the schemes (as given in the first column). The second column gives the switch states for each leg of the half-bridge for the first two steps of commutation. A '1' indicates that the high side of the leg is switched (phase connected to $+V_s$), '-1' indicates that the low side of the leg is switched (phase connected to $-V_s$), '0' shows that both high and low side switches are open – in this case current flow in the diodes will determine the voltage seen on the phase. If the current reaches zero, then the phase will be open circuit. There is no notation for both high and low switches of the same leg being active, as this would result in a short across the supply and should therefore never be allowed to occur. Where two switch states are given for a leg within a step, e.g. '1/0', this indicates that PWM switching is occurring – in this case in the high side switch. The third column shows the PWM switching sequence and relative ratio of on/off time for the two active phases during the first step, switching in subsequent steps is similar. The duty ratio is indicated by d and will be set by the control system. The switching period is not specified, but it is assumed to be considerably less than the time spent in each commutation step.

The terms 'two-quadrant' and 'four-quadrant' are sometimes used to refer to power flow in a motor. A motor operating in two quadrants can be driven forwards and backwards but it cannot provide torque in opposition to the direction it is turning. four-quadrant operation allows for regeneration of power back to the supply by providing torque against the rotation. The term 'unipolar' refers to the motor only being exposed to the supply voltage in one direction. A 'bipolar' scheme incorporates con-

Table 2.1: Six-step PWM switching schemes [34, 69, 70]

Scheme	Two steps of switching	PWM within first step	Unipolar/Bipolar
A1	1/0 -1 0 0 -1 1/0	1 -1 d 0 -1 $1-d$	Unipolar
A2	1 -1/0 0 0 -1/0 1	1 -1 d 1 0 $1-d$	Unipolar
B1	1/0 -1 0 0 -1/0 1	1 -1 d 0 -1 $1-d$	Unipolar
B2	1 -1/0 0 0 -1 1/0	1 -1 d 1 0 $1-d$	Unipolar
C1	1/-1 -1 0 0 -1 1/-1	1 -1 d -1 -1 $1-d$	Unipolar
C2	1 -1/1 0 0 -1/1 1	1 -1 d 1 1 $1-d$	Unipolar
D1	1/-1 -1 0 0 -1/1 1	1 -1 d -1 -1 $1-d$	Unipolar
D2	1 -1/1 0 0 -1 1/-1	1 -1 d 1 1 $1-d$	Unipolar
E	1/0 -1/0 0 0 -1/0 1/0	1 -1 d 0 0 $1-d$	Bipolar
F	1/-1 -1/1 0 0 -1/1 1/-1	1 -1 $0.5+0.5d$ -1 1 $0.5-0.5d$	Bipolar
G	1/0 -1/0 0 0 -1/0 1/0	1 0 d 0 0 $0.5-d$ 0 -1 d 0 0 $0.5-d$	Bipolar
H	1/-1 -1/1 0 0 -1/1 1/-1	1 1 $0.5-0.5d$ 1 -1 $0.5d$ -1 -1 $0.5-0.5d$ 1 -1 $0.5d$	Bipolar

nection of the motor to supply in both directions within a switching cycle. Although these are similar concepts, it is possible for a switching scheme to be unipolar whilst at the same time allowing four-quadrant operation – for this reason Table 2.1 specifies the schemes as either unipolar or bipolar.

The first eight schemes (A1 to D2) use unipolar switching – the phase voltage is switched between half the supply voltage and zero. During the inactive periods of the duty cycle any current still flowing, due to motor coil inductance, will circulate through the one switch that remains on and the diode opposite the inactive switch – for the first step, switch s_{2l} and diode s_{1l}. The difference between schemes A and B is where the PWM occurs. In the A schemes it is only in either the high (for A1) or low (for A2) side switches. This means that the non-PWM side switches only operate at the commutation frequency. This may allow the use of a lower specification device for these switches, however it may also lead to excessive heating in the PWM-side switches. There is also the possibility of 'overcurrent' during commutation with the two A schemes, as rising current in the 'incoming' switched phase combines with falling current in the 'outgoing' phase but is not controlled by either current sensor – assuming current sensors in the low side of the half-bridge. This is negated in the B schemes as the current sensor for the 'incoming' phase also sees the outgoing current [34]. In the B schemes the switching is spread between both the high and low side switches. This means that, as the phase becomes active for two contiguous steps, PWM is only active for one of them. The difference between schemes B1 and B2 is whether the PWM occurs during the incoming or outgoing step.

During the unipolar PWM off periods the current circulates and the motor will decelerate due to friction. Current is not usually returned to the supply and therefore the motor is not electrically decelerated. An exception to this can occur if commutation is demanded in the opposite direction to a load torque, in this case current will flow through either the switches or the diodes and return to the supply – the bridge will effectively be behaving as a passive rectifier.

Schemes C1, C2, D1 and D2 have the same motor current paths as A1, A2, B1 and B2 respectively, with the difference that switching in one leg is complementary, meaning that if the diode current drops to zero during the PWM off period it can then start to build in the opposite direction by flowing in the complementary switch; therefore current reversal is possible in the C and D schemes.

For all the unipolar schemes the bus capacitance requirements are lower and the switching losses are reduced. Equivalent bipolar schemes typically have twice the number of active devices and twice the voltage range, therefore producing up to four times the current ripple and losses.

In order to allow for regenerative braking of the motor within a PWM cycle, one of the bipolar switching schemes must be used (E, F, G, H). These all switch both the high and low side switches within a commutation period and therefore allow current to flow back to the supply. For this reason the DC bus must be capable of absorbing the returned power, in a large capacitor, dump-resistor, or the battery in an automotive actuator. The first two (E and F) switch the high and low sides at the same time; this is therefore referred to as either ‘simultaneous’ or ‘edge-aligned’ switching. This is easier to implement, but can lead to quite large current ripple, large bus capacitance requirements and also potentially high levels of EMI – due to the current spikes created [70]. An alternative is to switch the high and low sides at different times, this is done in schemes G and H, referred to as ‘centre-aligned’ or ‘symmetric ’ switching schemes. This more frequent switching can be harder to implement as it requires more complex PWM timing circuits, and can cause higher switching losses in the electronics, however it reduces current ripple and PWM noise.

A further option is switching between $+V_s$ and zero (schemes E and G), or switching between $+V_s$ and $-V_s$ (schemes F and H); these are referred to as ‘independent’ (or ‘non-complementary’) or ‘complementary’ respectively. In power electronic converters complementary switching is termed ‘synchronous rectification’. Although complementary operation requires more switching instances, the on-state conduction loss of the switches can be lower than diode conduction loss and therefore more efficient overall [70].

Due to the direct switching from high to low in the complementary schemes, there exists the possibility of ‘shoot through’ current shorting across the supply during switching. To prevent this a short period of ‘dead time’ is inserted between high and low switching, where neither switch is on; this allows for a short period of diode recovery. This can usually be short enough not to cause problems, however it should be considered in the design of a switching scheme [34].

The independent switching schemes (E and G) will give approximately the correct duty cycle (as shown in the third column of Table 2.1) for values above 0.5, however below 0.5 the duty is not well defined. During the ‘on’ period the current in the coil will rise and during the ‘off’ period it will fall towards zero but not below; the fall rate will depend upon the winding resistance and the conduction properties of the diodes. As with the two-quadrant schemes, the commutation sequence must be altered to reverse the motor rotation direction. In contrast, the complementary bipolar schemes reverse direction for duty ratios below 0.5. This allows finer current control around zero voltage.

The choice of switching scheme is important for a positioning actuator, and is investigated in more detail in Appendix G. Duty cycle linearity with respect to voltage, together with complementary switching operation, are shown to be of benefit in simplifying control design and achieving satisfactory positioning response.

2.4.4 Current control

Motor winding current determines output torque and also winding heating through resistive losses. Current therefore needs to be controlled, or at least monitored, in order to meet the actuator positioning and thermal requirements, and also to protect the drive electronics. Current measurement from sense resistors in the half-bridge circuit may be used in closed-loop control, setting the duty ratio of the PWM switching, and therefore the voltage. Alternatively, the current can be compared to a fixed threshold to disable or limit the PWM in the event of over-current [27, 34].

Due to the short time constants associated with the electrical system, a current control loop is usually constructed as the inner loop of a larger cascaded control system. This allows the current control to be tuned in isolation to provide a fast response. Outer position and velocity control loops operate in the mechanical domain and therefore with larger time constants.

If analogue-to-digital converters are available to process current measurements, and the control software is sufficiently faster than the time constants of the electrical system, or if it can be implemented directly in hardware, then the closed-loop current control will provide a superior response to voltage control; however, the cost associated with these improvements, relative to the performance gains, is too large for the automotive turbocharging application. A hardware comparator operating at a fixed current, driving a digital input to disable the PWM outputs during overcurrent, provides a cheap solution that can operate entirely in hardware, and therefore at very high speed.

2.4.5 Position and velocity control

The preceding discussion has considered motor performance as an open-loop system, with no position feedback, and indeed it could be effectively controlled as such if there were no external disturbances applied to the system; however, a load force is present on the variable geometry turbo nozzle due to the aerodynamics of the exhaust gases. This load varies with position and, although it is deterministic for a fixed position and engine state, the continuously changing nature of the engine during driving means that this load disturbance cannot be accurately predicted; it will vary with vehicle load, due to cargo, air resistance and gradient, and also engine demand, due to acceleration, emissions control measures and air density. A reasonable predictor of nozzle load is exhaust gas pressure, which is measured and may be available to the control system, but this will be subject to measurement sensor noise and possibly also communications delays.

The drive electronics for the motor require a direction and a voltage input or duty ratio. The maximum achievable voltage is the supply voltage. The control algorithms must achieve the positioning requirements by varying the voltage duty ratio and direction. Additionally it may be necessary to regulate the current drawn by the motor, to minimise motor temperature and protect the vehicle power supply and electronic devices.

A general structure for a positioning control system is shown in Figure 2.4. The actuator has been split into the motor and the mechanical aspects, in this case also including the linkage mechanisms up to the nozzle inside the turbo body. This highlights the load disturbance being fed back through the mechanics to interact with the torque supplied by the motor. In order to reject this disturbance, position feedback is supplied by the motor hall sensors, this may also be supplemented by a position sensor embedded within the mechanical linkages. Both of these sources of position measurement are subject to measurement noise and discretisation.

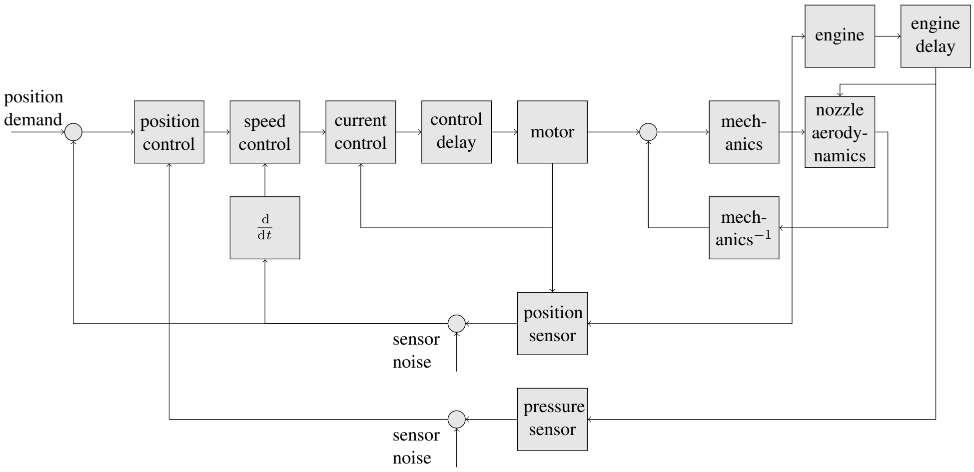

Figure 2.4: Complete control loop options

The left-hand side of Figure 2.4 shows a set of possible control loops that might be used to enable the system to follow a position demand in the presence of a load disturbance. This is based on a relatively standard cascaded control structure that is frequently used in industry. Although a wide variety of control structures are possible at each stage in the cascade, Proportional-Integral-Derivative (PID) type controllers are common [71]. This type of control is standard across industry, meaning that response and tuning processes are well understood. It is also straightforward and computationally efficient to implement in digital hardware.

It is common to cascade an outer position loop and a middle velocity loop around an inner current loop. This makes sense where a velocity measurement signal is available at a higher rate than position feedback. However, a brushless motor inherently requires positioning information for commutation, and separate velocity measurement is not typically available in this type of system. Where a derivative term is used in the controller, velocity – calculated from the position sensors – is inherently being used. Calculated acceleration using limited resolution position measurements, for use as a derivative term in an inner velocity control loop, introduces quantisation errors and high frequency noise .

In a classic PID control structure, all three terms are calculated based on the error signal. Where the parameters are tuned to reject disturbances, this can lead to large derivative outputs when the demand set-point changes. It is therefore common to apply the derivative term to the process variable only. A similar situation can occur with the proportional term. It has been shown that a Proportional-Integral (PI) motor controller provides an improved response if the proportional term is applied only to the feedback rather than the error term [72, 73]. This may be termed an Integral Proportional (IP) or a Pseudo-Derivative Feedback (PDF) control strategy.

An improvement on this scheme can be made by balancing the amount of error that is used in the proportional (and derivative) terms. This is referred to as 'set-point weighting' and includes an extra parameter to allow the user to set the amount of influence the error has on the proportional (or derivative) gains [74]. This appears equivalent to a feed-forward gain from the set-point to the controller output. The general term for this type of PID control is Two Degree Of Freedom (2DOF), however the equivalent PI controller may also be referred to as Pseudo-Derivative Feedback with Feedforward gain (PDFF) [75] or PI+ control [76]. Such a controller can behave as a standard PI controller or a IP controller if the set-point weight is adjusted to either extreme. A recent review of a 2DOF PI controller and an assessment of its robustness for speed control is given in [77]. This analysis suggests that classical control techniques still compete favourably with more recent control designs.

[75] and [76] discuss the lack of requirement for separate position and velocity loops and suggest that set-point weighting of the proportional and derivative terms of a standard PID controller is sufficient to achieve similar results. The resulting 5-term controller can be configured as a standard PID or an IP controller, or somewhere in between, through selection of the set-point weights. The derivative feed-forward term may be based on the change in desired position, or on a specific move profile.

The PID control loop is designed to reject load disturbances and track changes in position set-point. Although the integral term will provide a steady-state torque to hold against a load, its task is easier if this load is already rejected. If the load torque is known then this can be completely achieved using a feedforward signal. In most applications the load torque cannot be fully known, however even a rough estimate should provide better performance than not including it.

As indicated in Figure 2.4, the aerodynamics of the nozzle in the turbocharging application determine the load force. The aerodynamic load depends upon both the nozzle position and the pressure of the exhaust gas. If the relationship between these and the load force are available to the control system in the form of a lookup table, and measurements of the current position and exhaust gas pressure are available, then the control signal required to maintain a fixed position may be fed forward into the system. This reduces the demands on the PID controller, resulting in easier tuning and improved performance.

The integral term of the controller ensures zero steady-state error, however it can be susceptible to 'windup' where the the integrator value continues to increase during a period where it is unable to affect the system output. This will happen during system saturation, such as when the motor reaches maxium speed, or if the system is jammed or forced to an end-stop. The phenomenon can cause large overshoots in the system response, giving poor positioning performance and a large settling time.

Several techniques exist for dealing with integrator windup, the most common being back-calculation or conditional integration [74]. Back-calculation refers to techniques that introduce a correction at the input to the integrator when saturation is detected at the output. The detection usually takes the form of a difference calculation between the control signal and the achieved control performance. The difference is fed through a gain that influences the speed of the integral reset. Achieved control performance may be measured directly or provided by a software model; the signal fed back into the controller is sometimes referred to as a ‘tracking’ signal. Where feedforward control is also used, this must be subtracted from the tracking signal.

Conditional integration explicitly switches off the integrator when the controller is far from steady-state. Closeness to steady-state may be measured in a number of different ways, and control of the integral may also be handled in different manners; integrator clamping or resetting are both commonly used.

The two techniques provide different benefits depending on the system dynamics and tuning parameters chosen. Work has been done to combine the two techniques [78] and there are a wealth of modern techniques for assessing robustness and tuning [79]. In the turbo actuator application control saturation is a strong possibility, particularly during large step changes in position. The control output is limited to a PWM signal, which can provide a maximum of the supply voltage to the motor. This may be further modified based on the actions of the inner current control loop. The observation of the PID demand and the limited signal fed to the motor provide a difference suitable for using back-calculation to limit the integral.

2.4.6 Temperature regulation

Heating within the motor occurs during operation, due to Joule losses in the windings and iron losses in the stator. This heat passes through the motor thermal network and out through the motor casing, to be taken away by the actuator cooling system. Elevated temperature operation can produce significantly degraded motor performance, and at high temperatures permanent degradation or component failure can occur. Stator laminations, bearings and hall-sensors [80] generally have a higher temperature rating than windings and rotor permanent magnets; it is these that should therefore be the primary consideration when thermally sizing a machine for an application. It is expected that the winding temperature limit will be reached before the rotor magnet limit; this is typically around $125\,^{\circ}\mathrm{C}$ to $155\,^{\circ}\mathrm{C}$ depending on the type of winding insulation used [34]. Given that the windings are the most temperature sensitive part, and they generally also have the shortest thermal time constant, Joule losses must be minimised.

Temperature can be managed through the specification of conservative current limits, such that internal motor temperatures are incapable of reaching critical levels. Temporary excursions above the threshold may be allowed in specific circumstances, or for limited periods of time. An upper current limit is also required for the switching power electronics, and it will depend on the requirements and component specifications as to which is more strict – often it is the power electronics that set the absolute upper current/torque limit, with the continuous limit set by the winding temperatures. Setting a current limit inherently limits the torque available from the motor and is therefore a significant factor in motor specification for an actuator design.

Alternatively the internal temperatures may be monitored, and motor operation altered to actively control temperature. This may allow the specification to be met with a smaller, lower cost, motor in the majority of cases. Even more simply, it might be acceptable to occasionally exceed the maximum temperature limits and accept the reduction in motor lifetime, if a substantial reduction in size or cost were achievable. An accurate measure of internal motor temperature is required for active temperature control. This may be provided directly, by a thermocouple or resistive temperature probe inserted into the winding, or indirectly by estimation based on other motor measurements.

Estimation of the motor internal temperatures using model based techniques, based on motor performance, has been investigated for both permanent magnet and induction machines [81–89]. There has also been significant research looking into the use of winding resistance measurement for inferring winding temperature [83, 87, 90–92]. For most schemes this requires modification of the current levels in the motor, such that they no longer average to zero. This will have implications for both torque ripple and overall efficiency.

Increased computational power will be required to implement any form of active temperature management, especially if thermal models are used; however in an intermittent duty cycle application such as an actuator they may prove beneficial. The relative benefits of this approach will heavily depend on the application and design chosen. This approach would be complex and is not taken further in this work, however it is noted that the models developed in Chapter 3 would be well suited to investigating the benefits of active temperature regulation.

2.4.7 Other control considerations

A comprehensive review of all techniques and challenges associated with actuator control is beyond the scope of this thesis, however some secondary issues that affect implementation are noted below. These are are less relevant to actuator component specification and are noted as potential further work in Section 7.3.

Absolute position sensing

Due to the turbocharger actuator system being required to start from a zero power state and find a position, an absolute position sensor is sometimes included. This is a relatively low cost sensor, mounted on the output gear. It aids in coping with backlash and ensuring a smooth startup process. It might also be of use assisting the commutation process if backlash were taken into account.

Where an absolute position sensor is available it can also be used within the control scheme. It will be a more accurate measure of nozzle position than one derived from motor position due to reduced backlash at the measurement point. It should therefore replace the position derived from hall sensors in the positional error loop. Any significant divergence between these two position measurements during operation may be used to detect errors, such as slip in the gears.

If an absolute position sensor is not included then the actuator position can be determined through a startup routine that drives through the full range of movement, such that mechanical end-stops are encountered.

Gain scheduling

Gain scheduling is a technique commonly used in control to cope with nonlinearities in the system. The system is effectively treated as linear within a small region, and control gains are set accordingly. A scheduling variable is then used to determine what gains are used to control the system during operation, generally by interpolation between linearisation points [93].

For the actuator application nonlinearity is introduced in several places. The relationship between nozzle load, nozzle position and exhaust gas pressure is significantly nonlinear, however, as mentioned above, this may be better addressed through a feedforward control approach. Ambient or coolant temperature variations can produced significant changes in actuator behaviour, particularly if the increased viscosity of lubricants at low temperatures is considered. This may be a good candidate for gain scheduling of the PID control parameters, provided a temperature measurement is available to the controller as a scheduling variable.

Control parameter tuning

A number of control parameters have been proposed above. Whilst they all have defined limits, none have been given fixed values. They all require tuning depending upon the requirements and the hardware design chosen. The tuning of the control parameters is an important task, as they not only affect the ability of a design to achieve the requirements, but also the overall stability of the actuator system. A wide variety of standard formal tuning methods exist for PID controllers [74, 94, 95].

2.5 Transmission

Motor output is inherently limited to a bounded area below the speed-torque curve. Brushless permanent magnet motors will typically provide much larger maximum speed but significantly less torque than is required for an actuation application. The cost and size of a motor that could directly drive an actuator load would be very large, whilst the maximum speed may significantly exceed the requirements. A set of gears between the motor output and the actuator output/push-rod input increases the maximum torque output to an acceptable level, whilst also reducing the maximum speed by the same ratio. It is therefore likely that a gearbox will form part of any final actuator solution.

A spur gear pair can effect a change in speed and torque between the input and output shafts. For efficiency reasons the ratio is usually limited to a maximum of about 1:5 [96]. In order to achieve higher ratios a number of gear pairs may be combined in series. Current actuators use two internal gear-stages and a further third gear-stage in the interface to the output mechanism, to achieve a total ratio of around 1:100.

A review of gearing mechanisms is provided in this section, with a focus on their volume requirements, in order to reduce the volume of the overall actuator system. Implications for cost and performance are also identified.

2.5.1 Gear issues and design

Prior to discussing specific gear designs, some general issues often present in gear systems, along with different aspects of gear design, are outlined. This provides context for the discussion of overall transmission systems.

Backlash

This can be considered as the ‘lost motion’ in the system and is an effect by which input motion does not appear as output motion [97]. The total backlash in a gear system is due to a combination of tooth backlash, torsional stiffness and hysteresis [98]. In a continuously rotating system with a unidirectional load torque there are unlikely to be any problems, however for a positioning system with variable-direction load torques, such as a turbocharger actuator, backlash could be a major issue, affecting the precision of the output position and potentially causing stability issues in the control loop or excessive mechanical wear in achieving control. Techniques can be used to estimate the position within the backlash and compensate for this in the control [99].

Friction

As with all moving parts, there will be losses present in a gear system due to friction. Depending on the gear type used there will be either a rolling or a sliding contact between gears (or some combination of the two), as well as rolling friction at the bearings on the gear shaft, and 'windage' or churning losses caused by the rotation of the teeth in whatever fluid fills the gearbox [100]. Windage friction is significant in fluid filled gearboxes, however its effects are expected to be insignificant in the type of gearbox considered in this work. These are likely to be air filled, with thick grease as a lubricant rather than oil. Efficiency for a single spur gear pair is typically high, in the region of $98\,\%$ to $99\,\%$, however for large trains of gears this quickly reduces [96]. Most literature suggests that overall gear efficiency is dominated by sliding friction between gear teeth, especially at lower speeds [96, 100, 101].

Rolling friction in the bearings may be considered as two separate mechanisms, 'viscous' and 'Coulomb' friction. Viscous friction is a linear speed dependent friction. Coulomb friction in the bearings is a constant friction force opposing motion with a special case at stationary that prevents motion until the constant friction limit is reached, although this is sometimes omitted in simple models.

Inertia

The gears used will have an associated mass and therefore an inertia within the system. This may be significant in the overall system design and should be minimised. For sizing an actuator the inertia of the machine rotor and the transmission are generally referred to the output, for inclusion with the load torque and inertia when calculating the total load requirement.

Fatigue

Failures within gearboxes are often due to fatigue within their gears, axles or bearings. Fatigue is the degradation or failure of a component due to cyclic stress loading over a period, even when the magnitude of the stress is below the static strength of the material. Below a certain level of stress the number of load cycles can be considered effectively unlimited. If a range of different stress levels is expected, due to variation in drive cycles, as in the case of the turbocharger actuator, 'damage accumulation calculation' methods may be used, such as the Palmgren-Miner rule [102]. For the large number of stress cycles expected of the actuator, operation should be constrained to the unlimited load cycle case; this therefore sets a maximum level of stress that components should endure per cycle. The limiting stress within the gears can occur due to two mechanisms: either 'Hertzian' contact stress within the gear teeth as they mesh together; or bending stress at the root of a gear tooth. These limits will differ for a given material.

The conclusions from [103] are that:

- Hertzian stress is the limiting factor in the majority of cases (i.e. it requires the largest gear size);

- the root stress for the pinion gear is always higher than for the larger gear;
- root stress is dependent upon the number of teeth on the pinion;
- Hertzian stress is always greater between the sun/planets than it is between the planets/annulus;
- well known improvements in size and inertia through using planetary gears were verified.

The equations derived are also used by the authors in later work for optimisation of the complete drive system [4, 104, 105].

Tooth angle

The angle of the gear teeth impacts upon how the gear can be used, how it performs, and how much it costs. The cheapest option is 'spur', or 'straight cut', gears. In these the gear teeth are parallel to the axis of rotation. These are widely used due to being relatively cheap to manufacture and are sufficient for many purposes. They may only be used to connect between parallel shafts, and teeth engage and disengage between gears instantaneously, with a straight line load across a gear tooth. This can lead to noise and impact stress during use.

If the leading edges of a gear are not parallel to its axis, but set at an angle, then the tooth will form a helix shape – these are therefore referred to as 'helical' gears. These may be used to connect non-parallel shafts (when they are known as 'skew gears') and also have the advantage over spur gears that the contact point between teeth is a point that will move along the spiral as it rotates. This means that they are quieter and smoother during use.

A progression from helical gears is to combine two helical gears with opposing spirals on the same shaft. This is known as a 'double helical' or 'herringbone' gear and has the advantage that the axial thrusts from each separate helical gear are in opposition and therefore no net axial thrust is generated.

Tooth profile

The cross section through an individual gear tooth is the 'tooth profile'. Tooth profile is normally selected to ensure a constant velocity ratio between gears through a tooth's engagement; it also affects the friction and wear of the gear teeth. A wide range of tooth profiles are possible, however the 'involute' profile is by far the most common, especially in drivetrain applications.

Non-parallel shafts

Another use of gears, besides changing speed/torque ratios, is to transform motion into a different axis. Taking the helix angle of a helical gear close to 90° it resembles a screw, and is referred to as a ‘worm’ gear; these mesh with an ordinary helical gear called a ‘worm wheel’. Although ‘worm drives’ allow for very high gear ratios, they suffer from an increased amount of sliding friction and can be inefficient.

Similarly ‘bevel’ gears also allow for a change of motion axis. Bevel gears may have straight cut teeth like a spur gear or they may have teeth cut in a variety of other forms, for example ‘spiral bevel’ gear teeth are cut in a way analogous to helical gears. Other variations on this type of gear include ‘hypoid’ gears, that allow connection between shafts on non-intersecting axes, and ‘crown’ gears in which the teeth of the gear project at right angles to the plane of the gear.

Linear motion

Gears may also be used to transform between rotary and linear motion. Several of the gears discussed above have linear analogues formed by considering one of the gears in the pair to have an infinite radius. This means the larger of the gears becomes a ‘rack’ that moves with a linear motion when driven by a pinion.

Gear materials

Gear manufacture is possible from a wide variety of different materials, however practical gears are predominantly made from either metals or plastics. Steel is a popular choice due to its high strength and relatively low cost; however plastic gears are becoming increasingly popular, including within the automotive industry [106]. The choice of gear material will impact upon sheer strength, stiffness, inertia and expected lifetime.

2.5.2 Gearbox design

Although the design aspects considered above will affect performance and cost, many of them are independent of the specific gearbox design chosen. A gearbox may consist of a single pair of gears, or a number of gear stages to increase the overall ratio. Single stages are discussed in this section; multiple stages may be assembled by linking single stages, and the result will be a linear combination of the individual stage metrics.

A simplified comparison of gearbox volume is presented, by considering them to be of similar thickness. Stress calculations could be performed by adjusting radial size; or radial size may be kept constant and the depth may be altered to achieve the strength required. An overall comparison of different gear designs is presented in Table 2.2, including formulae for calculating the ratio and cross-sectional area of each gearbox. These are expressed in terms of the diameter of the pinion gear a and the large gear c. Individual gearbox designs are discussed in more detail below.

Table 2.2: Gearbox summary, where a and c are the diameters of the pinion gear and large gear respectively [98, 107–109]

Gearbox type	Ratio	Area	Efficiency	Backlash	Stiffness
Pinion and gear	$^{c}/_{a}$	$c+a, c$	98 %	<0.17°	High
Internal gear	$^{c}/_{a}$	c, c	98 %	<0.17°	High
Planetary	$1+{}^{c}/_{a}$	c, c	92 %	<0.05°	High
Cycloidal	$\frac{1}{^{c}/_{a}-1}$	c, c	70 %	<0.017°	Medium
Harmonic	$\frac{1}{^{c}/_{a}-1}$	c, c	80 %	<0.017°	Low
Worm drive (45° helix)	$0.5\pi{}^{c}/_{a}$	$c+a, c$	>90 %	No data	High
Worm drive (70° helix)	$1.38\pi{}^{c}/_{a}$	$c+a, c$	>84 %	No data	High

Pinion and gear

The simplest gear pair would consist of two parallel shafts connected by gears of differing size. If the input is to the pinion gear shaft, and the output from the larger gear shaft, then the torque will be increased and the speed reduced. The ratio will be equal to the ratio of the circumferences of the gears at their points of contact, or their 'pitch circle'. This is simply modelled by two cylinders rotating against one another with no slip between them. If the pinion diameter is a and the large gear diameter is c, such that $a < c$, then the gear ratio n is given by:

$$n = \frac{c}{a} \tag{2.1}$$

Internal gear

A modification of the above is to make the larger gear internally toothed, such that the pinion runs inside it. This allows the overall packaged area to be smaller for the same gear ratio – although the volume is not guaranteed to reduce, as a rear carrier for the internal gear will be required, increasing the depth and inertia of this system. Equation 2.1 is therefore also valid for this system, however the direction of rotation would be reversed.

Planetary

The internal gear above may be modified such that the input pinion is moved to the centre of the external gear, and connected to it through an 'idler' gear. This will not affect the ratio between the input and output, but will reverse the direction rotation between the two. Inserting several idler gears around the pinion will help to balance the forces and spread the load over more gear teeth. This is commonly known as a ‘planetary’ or ’epicyclic’ gearbox. The central pinion gear is referred to as the ‘sun’, the idlers are the ‘planets’, and the enclosing internal gear is the ‘ring’ or ‘annulus’ gear. With the planets fixed to a stationary carrier as detailed above, the gear ratio is the same as in Equation 2.1, where a is now the sun diameter and c the annulus.

If the planet rotational axes are all fixed to a carrier that is allowed to move, rotating about the same axis as the sun, then two other options become available. The annulus may be fixed and the planet carrier may be used as the output, in this case the gear ratio is given by:

$$n = 1 + \frac{c}{a} \tag{2.2}$$

With the sun fixed, the carrier used as the input and the annulus as the output, the gear ratio is given by:

$$n = \frac{1}{1 + \frac{a}{c}} \tag{2.3}$$

The maximum gear ratio is available from the second configuration, Equation 2.2. This provides a better ratio than can be achieved by a simple two gear arrangement, with very little increase in volume, well balanced forces through the gears, and the load spread between several planetary gears. For a fixed outer size it is apparent from Equation 2.2 that the maximum ratio will be achieved with the minimum size of sun gear permissible, or the largest planetary gears possible. As before, this will be limited by the stress in the teeth of the gears; a thorough analysis of this is given in [103] for both spur gear pairs and planetary gearboxes. The conclusions from this work are in line with conventional practice – that planetary gearboxes allow for a more compact drive train with a lower inertia. Compared to a single gear pair, a planetary system will typically be more expensive and less efficient due to the increased number of parts.

Cycloidal

Consider removing the sun gear from a planetary system and having only one planet, of a diameter considerably larger than the radius of the external gear, but still free to rotate. If the carrier for the planet is rotated, the planet will also rotate inside the fixed annulus. Through a complex connection method this planet rotation may be used as an output. This is the principle of operation of a ‘planocentric’ or ‘cycloidal’ gearbox [110, 111].

If the diameter of the planet is close to the diameter of the annulus, then the amount of rotation produced in the planet for one rotation of the carrier can be very small, hence a very high ratio can be produced. The ratio for a planet of diameter a, in an annulus of diameter c, is:

$$n = \frac{1}{\frac{c}{a} - 1} \tag{2.4}$$

This no longer has the balanced forces of a planetary system, and at high ratios there can be considerable sliding contact between gears; however high gear ratios are possible in a very compact space with this type of design.

Harmonic

A ‘harmonic drive’, or ‘strain wave’ gear, works in a similar way to a cycloidal drive; however the planetary gear is replaced by a flexible gear, or ‘flex-spline’, and the carrier is replaced by an elliptical disk called a ‘wave generator plug’ [112]. The flex-spline is deformed by the wave generator such that it makes contact with the annulus in two places. The wave generator is then rotated by the input and the points of contact between the flex spline and the annulus move. The output is connected to the flex-spline and rotated by a fraction of a turn for every full turn of the input.

The ratio for a harmonic drive also obeys Equation 2.4, where a can be considered to be the effective diameter of the flex-spline (if it were circular). As with all the drives considered up to this point, the diameters in the equations could be replaced by circumferences, or numbers of gear teeth, and still remain valid.

Harmonic drives are a proprietary technology produced by *Harmonic Drive LLC*. Similar to cycloidal drives they have very little backlash and can produce a very high gear ratio in a compact volume [113]. Due to making contact on both sides of the flex-spline they also place less force on the shaft bearings than cycloidal drives. Their weak point is likely to be the flex-spline, which can exhibit wind-up and fatigue over time.

Worm drive

A high ratio can be achieved from a single gear pair if one of them is a worm gear. Considered as a helical gear with a very large helix angle, the limit is a ‘single start’ worm with only one tooth threading along it. A single start worm in combination with a worm wheel will produce one tooth of rotation in the worm wheel for every full rotation of the worm shaft; similarly a two start worm will produce two teeth rotation in the worm wheel.

The helix (or ‘lead’) angle of the worm relates to its diameter, for example a very high helix angle, close to $90°$, will require a large diameter worm in the single start case. For perpendicular shafts the efficiency of the worm will be at a maximum for a $45°$ lead angle, reducing dramatically as it approaches $90°$ or $0°$ due to sliding friction. The inefficiency of a worm can be such that its thermal dissipation is more limiting than its mechanical stresses.

For any given helix angle ϕ, the tooth pitch may be related to the both the diameter of the worm input a, and the diameter of the worm drive output c. These may be combined to give the gear ratio n:

$$n = \frac{1}{2}\pi \tan\phi \frac{c}{a} \tag{2.5}$$

Assuming that a 45° lead angle is used, then a $57\,\%$ improvement in ratio over a pinion and gear ratio is produced, however in order to gain higher ratios some efficiency must be sacrificed. If the lead angle is increased to 70° then the efficiency would be expected to drop, however the improvement over a pinion and gear would increase to $334\,\%$.

2.5.3 Linear output gears

Gearing may be used to convert rotary motion into linear. For the turbocharger, the required output is a linear movement at the nozzle, so this type of gearing may be a viable choice; however integration into the turbocharger bearing housing would need to be considered in more detail than for the rotary gearboxes outlined above.

For comparison to rotary actuators, an angular input of θ_r in rad at the sector gear, will be considered commensurate with the linear motion of x required at the nozzle – effected through the yoke, wear-block and push-rod mechanism outlined in Section 2.2; therefore the distance moved by a linear gear option for a full motor rotation can be equated to a rotary gear ratio using the scaling factor:

$$\frac{\theta_r x}{2\pi} \tag{2.6}$$

Rack and pinion

The simplest option of a rack and pinion system would produce a linear movement of πa from a pinion wheel of diameter a. Therefore its equivalent gear ratio would be:

$$n = \frac{\theta_r x}{2\pi^2 a} \tag{2.7}$$

Worm screw

A worm drive may also be used to produce linear motion with the worm wheel being replaced by an equivalent rack. Similar comments to those made in Section 2.5.2 apply regarding the trade between efficiency and gear ratio; therefore the gear ratio could be between

$$n = \frac{\theta_r x}{4\pi a} \tag{2.8}$$

and

$$n = \frac{\theta_r x}{1.46\pi a} \tag{2.9}$$

for a 45° or a 70° worm helix angle respectively.

For the worm screw the meshing section of the two parts will be the full length of whichever is longer. The actual length of meshing thread is a compromise between friction and gear tooth stress.

Leadscrew/Ballscrew

Consider the worm screw discussed above, with the worm longer than the rack. The rack has no restriction to interface with the worm on only one side – in fact it may be extended all the way around the worm such that it is threaded onto it. This now resembles a nut and threaded rod, and is called a ‘leadscrew’. Either part can now be rotated to provide an input, with linear motion of the other component as the output.

Similar comments to the worm drive and worm screw apply; it is capable of producing a large gear ratio, however high levels of friction can reduce its efficiency. The choice of thread used has an impact on this, with a square section thread producing the least friction, but also being expensive to manufacture.

A development of the leadscrew is to run ball bearings between the screw thread and the nut, this considerably reduces friction and is referred to as a ‘ballscrew’. Due to the need for a ball recirculating path, and the precision required in manufacture, ballscrews are considerably more expensive and bulky than an equivalent leadscrew; however their precision and efficiency still make them a good choice for a number of applications. Recent investigation into optimal actuator designs using ballscrews is given in [114, 115].

Equations 2.8 and 2.9 for worm screws are also applicable to leadscrews and ballscrews; although the efficiency drop at high helix angles will be less pronounced for a ballscrew, which may still be able to achieve around $90\,\%$ efficiency.

Inverted roller screws

An inverted roller screw uses the rotation of a centre gear to drive rollers orbiting it in a planetary motion. These rollers drive an internally threaded shaft to move linearly, axial to the rotating gears. The structure of these components is similar to a planetary gear, as the output shaft, equivalent to the ring gear, is not allowed to rotate. The relationship between the sun and planets remains unchanged, whereas the relationship between carrier and the ring has changed and an extra degree of freedom has been introduced in the linear motion of the output shaft (or ring). The ratio of output motion to input rotation will depend upon the geometry of the gears and the threads, however the minimum ratio will be that of the leadscrew and wormscrew, with an increase on that depending on the number of rollers and the number of starts on the internal screw. [116] investigates standard roller screws (non-inverted) and suggests 9 to 13 rollers for 5 or 6 start screws. Similar work is done in [117]; this concludes that there exist some significant advantages in the roller screw over the ball screw in terms of slip.

2.5.4 Magnetic gears

Magnetic gearing may be used to increase reliability and reduce noise. This effectively replaces gear teeth with permanent magnets. At high load this type of gear may slip, which can prevent overload in some applications.

For positioning actuators, little benefit is expected to be gained from the use of magnetic gearing alone, however there are several designs that effectively integrate magnetic gearing within the motor. These are capable of producing high torque output in a relatively small package size, and therefore warrant consideration. The various concepts are presented as analogous to several of the gear designs discussed previously, as summarised in Table 2.3.

Table 2.3: Magnetic gear/motor to standard gear analogies

Gear type	Magnetic gear/motor type
Planetary	Pseudo Direct Drive
Cycloidal	Steromotor/Rolling Rotor machine
Harmonic	Harmonic Drive motor

Planetary/Pseudo Direct Drive motor

Brushless machines are often used to drive the sun gear of a planetary system. The direct integration of brushless permanent magnet motors with mechanical planetary gears has been recently reviewed in [118]. If magnetic gears are used then the permanent magnet rotor may also act as the sun gear, reducing the number of parts and the overall size of the system.

A direct analogue of a mechanical planetary gear is developed in [119], using several permanent magnet rotors as the sun, planets and ring gears. A similar gear is developed in [120, 121] as part of a brushless machine. This is designed for application to hybrid electric vehicle powertrains as a Continuously Variable Transmission (CVT).

A novel alternative to permanent magnet planets is to use stationary steel segments to couple the magnetic path between the sun and ring gears. This was first described in [122], and demonstrated in [123, 124], as achieving a very high torque transmission capability. This has been developed and patented to embed the magnetic gear within a brushless electric machine [125], referred to as a ‘pseudo’ direct-drive machine. This provides very high torque output from a small package. Modelling and control of such a machine is further considered in [126], finding that lack of mechanical damping in the system can lead to oscillation if sophisticated control methods are not employed. A CVT has also been developed using similar principles [127].

The use of magnetic gears for servo applications is addressed in [128], which proposes models, highlights issues with ‘pole-slipping’ at high torques, and proposes some solutions. Further investigation into mechanical resonance suppression and the detection of pole-slipping is given in [129].

Steromotor/Rolling-Rotor machine

Hypocycloidal, or rolling-rotor, machines operate on a similar principle to cycloidal gear systems. An eccentrically placed rotor is driven around a stator, generally by a reluctance minimisation. The rotor interfaces with the stator either through gear teeth or friction, such that it rolls as the magnetic field commutates. The eccentric motion of the rotor provides a high torque, low speed output. When used with permanent magnet biasing this design is referred to as a ‘Steromotor’. A coupling must be used to convert the eccentric motion of the rotor into useful output movement.

A thorough review of the operation of this type of motor is given in [130]. Drive electronics and control aspects of it are discussed in [131–133] and modelling for such a motor is discussed in [134–136]. A recent study finding benefit in adding permanent magnets to the stator has been performed in [137].

Harmonic Drive motor

The use of magnetic interaction, rather than mechanical teeth within a harmonic gear is investigated in [138–140]. This exhibits high torque density with no transmitted torque ripple. A two stage harmonic gear with a gear ratio that is greater than the product of its individual stages is also described. This type of design would be susceptible to resonances and pole-slipping similar to the magnetic planetary designs

A motor design using the flex-spline concept from a harmonic drive has been patented [141]. It replaces the wave generator plug with a switched reluctance type stator. This reduces the moving parts and should be capable of generating large torques. The gear also completely disengages when power is removed, which may be advantageous for some applications. Although still at the prototype stage, the designers claim very high torque output from a small package size [142, 143].

2.5.5 Discussion

This section has reviewed a variety of different gearing options for achieving an increase in torque and a reduction in speed between a driving motor and actuator output movement. The summary of different gearbox options presented in Table 2.2 draws attention to the considerable reductions in volume possible through the use of more complex gear designs, however manufacturing cost and robustness are particularly important in the automotive domain and likely to increase with the complexity of the design.

The limiting factor in the sizing of individual gearboxes is often the stress produced in the gear teeth. For most gear designs this is the Hertzian stress exerted on the tooth flanks rather than the bending stress at the tooth roots.

Cycloidal and harmonic drives appear to give further improvement over planetary gears, however calculations on tooth stress or similar for sizing have not been carried out. There are also disadvantages in terms of efficiency and potentially fatigue life with this type of design [98].

The use of a leadscrew or one of its derivatives would provide a large gear ratio and also give direct linear motion at the actuator, however it would require a redesign of the nozzle actuation linkage mechanism. A leadscrew actuation design has previously been tested within *Cummins* [144] and remains a potential candidate design for use in the future.

The selection of an optimal drivetrain is highly dependent upon the actuator requirements, particularly cost and packaging constraints. For typical current turbocharger actuator specifications the low cost and robust nature of spur or planetary transmissions make them the favoured choice. Using current technologies, a move toward more compact options such as cycloidal or harmonic drives is likely to incur significant financial or longevity costs. The decreased efficiency of these designs is also of concern, particularly for use at high temperatures. Detailed modelling and design studies would be recommended prior to committing to such a technology.

Developments in magnetic motor-gearboxes should be monitored, with the most promising currently being the pseudo direct-drive machines produced by *Magnomatics*. However this technology has yet to be demonstrated in an actuator type application, and will require significant further development before being mature enough for mass production items.

Within the remainder of this thesis, transmission components are modelled in general terms, such that the methods will remain applicable to most of the options presented in this section. The sizing equations, efficiencies and backlash detailed above provide an initial starting point for comparison between different options, which should be pursued further when a specific design requirement is presented. The overall focus of this work is on modelling and design methods,

2.6 Modelling

The trend across much of industry is towards simulation and model-based design practices, in order to bring products to market faster and more cost effectively [1]. Model-based design offers the potential to rapidly generate and assess a wide range of different motor designs, prior to committing to the time-consuming and costly process of producing a prototype. Performance within larger system simulations may also be investigated [145].

Generally, the individual components of the actuator may be modelled as subsystems and combined to assess their performance as a full system. This approach has been followed here and allows standard modelling practices to be followed, as well as the separate validation of component models. The actuator is separated into an electrical model, a thermal model and a mechanical model.

In the development of a new model the designer must balance model complexity, and therefore development and simulation time, against the accuracy of output that a higher fidelity model should produce. Models may be built using general purpose tools, such as textual or graphical programming languages – a popular choice for modelling being *Matlab Simulink* [146], or they can be constructed using a purpose-built package. An emerging trend in general modelling is towards the use of 'acausal' modelling languages, such as *Simscape* (for *Simulink*) and *Modelica*, as they offer the designer a level of abstraction from the mathematics of the low level components whilst also providing a high level of accuracy [147]. These acausal component libraries can come at a financial price, but there is also often an associated overhead in terms of execution time.

In this section model construction using general purpose packages will be reviewed and specific packages for modelling will be noted.

2.6.1 Electromagnetic motor modelling

Computer modelling and simulation of electric motors is now a standard step in many product designs. For detailed motor or product design, FE type models are commonly used to model the electromagnetics [148–150]. Several products exist to simplify and streamline the FE modelling process for machine design, such as those from *Motor Design Ltd*, *Infolytica*, *Ansys*, and *Comsol*. These typically produce highly accurate results but require detailed specification of the motor structural design and materials [151]; they are also slow to simulate due to their relatively large computational burden [152]. This type of modelling is therefore less appropriate for higher level actuator design, where the motor is likely to be a catalogue component choice rather than of bespoke design. At this level, lumped-parameter models are often used to simulate the electrical, magnetic, mechanical and thermal performance of a candidate motor [153]. An intermediate option is the implementation of a lumped-parameter model, with variable parameters populated based on FE analysis results [154]. The modelling performed in this work is aimed at actuator specification, and therefore detailed FE type design is not considered.

The primary function of an electromagnetic motor model within a larger actuator model is to predict current and torque production for a given input voltage. Several key electromagnetic parameters may be used to produce a mechanistic model of performance based on the physics of motor operation. The mathematics of this type of model is well documented in both textbooks [34, 155] and research literature [156–162], and there are a wide variety of simulation tools that can be used to implement the circuit equations – with *Matlab* and *Simulink* being popular in engineering and research.

For brushless motor modelling, a time-stepping simulation is generally used, due to the nonlinearity introduced by the electrical commutation [163]. For brushed motor models this commutation is handled mechanically, usually at higher frequency, meaning that nonlinearities introduced through torque ripple are often neglected – allowing simple linear motor equations to be used [27]. The ability to linearise the system and ignore commutation within the model enables simplified and faster-running simulations. This type of linear assumption is not reasonable for brushless machines with unmatched back-EMF and drive current profiles, as they will produce a torque ripple [34] that must be accounted for. Ignoring the commutation period can also introduce errors in the current that will affect losses, particularly where the electrical time constant of the system is not small [164].

Previous work in this area has developed a method of obtaining the steady-state behaviour of brushless machines [165], and average value equations have been produced by ignoring the commutation period [166]. More recent work has investigated including the commutation period for both sinusoidal [167, 168] and non-sinusoidal [169, 170] back-EMF machines. This work averages voltages in the rotor reference frame to calculate current and torque. It also precomputes the commutation interval for a given speed and torque using a full winding model. The need for precomputing is removed in [171] by finding the point at which current is equal in two phases. This result is used within [172] to compute speed-torque curves for the machine.

Chapter 3 uses standard textbook motor physics to develop mechanistic motor models. Also developed is an averaged voltage motor model that implicitly includes commutation effects, allowing it to operate using far larger time-steps than the explicit three-phase model. This simplification significantly reduces the simulation time required for long duration experiments. The effects of winding resistance and inductance are included within the model such that it produces similar results to a fully commutated 3-phase model. It differs from previous work in this area as it produces full equations for current and torque, and also includes a process for determining the commutation angle. This faster-running model, along with a thermal motor model, allows long duration motor thermal transient performance to be investigated. The steady-state equations also enable the generation of thermally adjusted speed-torque curves that are used in overall actuator assessment techniques in Chapter 6.

Models are developed to allow operation with a range of different parameters, and these must be populated with the correct values to produce an accurate representation of the motor. These motor parameters may be provided by the manufacturer, or they can be found by experimentally testing a sample motor [173]. A selection of simple motor parameterisation experiments are noted in [174] and a set of official standards for motor testing is specified by the National Electrical Manufacturers Association (NEMA) [175]. Similar tests are developed in this work, with an emphasis on simplicity and straightforward implementation. Care has been taken to produce tests that do not require dismantling the motor, or a knowledge of its internal structure. The tests presented in Chapter 4 allow a sample motor to be fully parameterised for simulation.

2.6.2 Thermal motor modelling

In most situations thermal performance is an important aspect of the design, due to high ambient operating temperatures, or the self heating effects of power losses in the machine. For automotive actuators both of these are significant; it is therefore important to ensure that thermal aspects are taken into account during actuator design, so that the specified component performance and lifespan are achieved. As discussed in Section 2.3.5, the continuous operating envelope of the machine is defined in terms of its thermal limit. Although the thermal limit is fixed, and generally provided by the manufacturer for a given machine at a certain temperature, the operating envelope will change with ambient operating temperature. Thermal modelling should therefore be undertaken during any design assessment process.

Power losses within the machine due to resistive Joule losses, iron losses and frictional losses will contribute to its heating [34]. This means that close coupling is required between thermal and electrical/mechanical machine models to produce accurate performance simulations. Recently a number of motor design packages have started to provide linked thermal, electrical and mechanical modelling packages, often referred to as ‘co-simulation’ [45].

FE and Computational Fluid Dynamics (CFD) type models may be used for thermal assessment during product design [34]. These require a detailed knowledge of the motor structural and material design; they are also slow to simulate, making this type of modelling less appropriate for actuator component selection, particularly where design techniques that seek to optimise performance requirements through iterative simulation are used. At this level ‘lumped-parameter’ physical motor models are commonly used to simulate motor thermal performance [45, 153, 176–178]. These separate the motor into ‘lumps’ of approximately uniform thermal behaviour – usually the physically distinct elements within the machine. Detailed lumped-parameter modelling of machine structure has been shown to produce results comparable to FE modelling [179]. These models typically have 10 to 80 separate lumps, each requiring two parameters – a thermal resistance and a thermal capacitance [180]. A detailed knowledge of the motor internal design is therefore still required to design and parameterise these models [181]. Packages such as *Motor-CAD* and *Infolytica* allow straightforward implementation of this type of model, and co-simulation with other packages to facilitate complete motor modelling [181–186].

At the other end of the scale, very simple models may be used to approximate the complete motor thermal behaviour. These are useful where the full design of a motor is unknown and it can be difficult to construct a detailed thermal model. Typically a manufacturer will supply a thermal capacitance and a thermal resistance to ambient, to characterise motor thermal performance [48] – this limits the simulation to a first-order system; such a model is referred to as a 'two-parameter' model. Some manufacturers provide one or two extra parameters, perhaps separating out the windings or rotor as separate components, however access to these parameters is highly manufacturer-specific. There is a gap in the literature between the crude two-parameter models, which can be parameterised through a simple test of a sample motor, and the higher-order models, with 10 or more parameters, that require a detailed knowledge of the motor internal design to parameterise them. Some previous work has been published noting that two-parameter models can potentially miss critical temperature fluctuations with in the machine, and hinting at the use of four-parameter models [187], but does not provide full details. Other work has reduced more complex lumped-parameter models down to around 20 parameters, whilst still requiring a knowledge of the motor internals for parameterisation [188–191]. Techniques for parametrising a simple two-parameter thermal model based on experimental step response results are presented in [192]

Chapter 3 develops a lumped four-parameter model which provides a middle ground between crude two-parameter models and more complex lumped parameter models. It requires only minimal parameterisation but still allows critical motor component temperatures to be monitored. The extraction of the required parameters for this model is addressed in Chapter 4.

2.6.3 Drive electronics modelling

A common technique for current regulation within brushless motor drives is to switch the voltage at high frequency. The rapid transition between zero and the supply voltage generates a changing current in the motor windings that is smoothed by their inductance. If the switching is at a high frequency with respect to the winding electrical time-constant, the current generated is equivalent to that which would be produced by the average of the switched voltage. This rapid switching may be effected by a Pulse Width Modulation scheme [34, 70]. The switching of solid state MOSFET or Insulated-Gate Bipolar Transistor (IGBT) devices and diodes in the driving half-bridge circuit may be modelled by discrete switch logic in models.

Simulations that include this switching are inherently nonlinear, and require time-steps at a frequency considerably greater than the switching frequency. However, the effects of switching are generally well approximated by averaging the voltage over the switching period [193]. As long as the control bandwidth is considerably less than the PWM switching frequency the motor response will not be sensitive to switching effects. Transition periods and losses in electronic components are not expected to be significant, and are therefore not mathematically modelled in this work; they are, however, included within the acausal model developed in Appendix D and validated alongside the other models in Chapter 5.

2.6.4 Mechanical modelling

Similar to the different techniques available for motor modelling, mechanical modelling of gears and linkages may also be performed at a variety of fidelities. FE modelling is used in the design of components to predict internal stress and strain [194]. This may be used to predict fatigue issues and identify weak points in a design, however it is too computationally intensive for general actuator performance modelling.

The multiple gear stages in an actuator design may be modelled separately and then combined to produce an overall actuator model. As discussed in Section 2.5, within each gear-stage there are a number of effects that should be included: gear ratio, backlash, friction and the inertia of the gear all affect the relationship between the torque-speed at the input and the torque-speed at the output. Gear ratio is a straightforward multiplier on torque and speed, and inertia is included in the calculation of speed from torque. A backlash model for use in simulations is developed in [195] and laid out further in [196]. Finally there is some mechanical power loss due to friction in the meshing of the teeth and in the shaft bearings. This will be a combination of different friction effects.

The sliding friction effects in gear-trains are both complex and nonlinear; they are therefore difficult to characterise and model. More detailed models for sliding friction have also been proposed by Dahl, Dankowicz, LuGre and Canudas De Wit [197,198]. Coulomb friction models may be extended into a 'Stribeck' friction model by increasing the constant friction force around zero speed [198].

There can be difficulty in determining the parameters of gear pair frictional components in order to populate models. Frictional effects are often considered in terms of gear efficiency. Various methods have been proposed for predicting the meshing efficiency of a gear pair based on its geometry and materials – a comprehensive assessment of the performance of five such methods is given in [101]. Some of the prediction methods predict efficiency independent of load torque, whilst others allow efficiency to vary with load. These later methods allow for no-load losses to be present in the system and may provide improved accuracy, although they are also likely to increase simulation complexity. A clear consensus on the best method of gear friction modelling does not seem to be formed.

In order to utilise the mathematical approximations of these effects in a model of a specific actuator they must be parameterised. Data on many of these effects may be available from the manufacturer, based on their material properties, or calculated by simple tests of a sample gear; gear efficiency parameterisation is however more involved.

Experiment designs for assessing gear efficiency can be split into two categories, either power input-output tests or power recirculating tests. The first technique requires a very precise measurement of both input and output power in order to calculate losses, and therefore the second technique tends to be favoured. A good review of gear testing methods is given in [199], along with arguments in favour of a mechanical power recirculating test – sometimes referred to as a 'Four-square' test setup. This places two identical gearboxes side-by-side, drives the same end of both them at a certain speed and then imposes a load torque between the outputs at the other end. The authors also propose a mechanism for imposing this load that can be varied during the test. A similar setup is used in [200] and results from their testing are presented.

2.7 Actuator specification

Motor and gear selection has been addressed in isolation above, and, whilst almost all of the motor and gear options mentioned could be combined in a design, an optimal arrangement will seldom be achieved if they are selected sequentially [201,202]. Typically, a specification will determine a move and a load requirement and a factor, or number of factors, that must be optimised within the design; for example, a specified period within which a distance must be moved against a set load torque, and a requirement that the volume of the actuator must be minimised. Once a motor and gearbox technology have been determined, manufacturers' catalogues may be consulted in order to determine plausible combinations.

This section reviews the key equations that may be used to assess whether motors are able to meet a set requirement, and with what gearbox ratio. Initially the movement of the actuator is considered, and the concept of movement conforming to a specified profile is introduced. The key parameters from this move profile, along with requirements for the load to be moved, are then used to derive equations that relate to motor and transmission capabilities.

2.7.1 Move profile

A 'Move profile', also referred to as a 'velocity profile' or 'motion profile', may be used to define the movement of a servo system between two points. This may be enforced within the position control loop by a 'trajectory generator'. This may offer advantages over directly feeding the desired position into a closed position-control loop, as it allows finer control over the speed-torque relationship of the actuator, and therefore also its efficiency and power loss [203].

A variety of different move profiles have been proposed and are used in practice. The most basic is a triangular velocity profile, in which acceleration is constant for a period and then deceleration is constant, until the output is halted at the desired location. In practice this is rarely used as either the peak speed of the hardware, or a control limit is reached. One of the most popular move profiles is therefore a trapezoid, with three periods, consisting of a constant acceleration, a constant speed and then a constant deceleration. The proportion of the move period that each of these periods occupy may be adjusted to optimise characteristics of the profile. It can be shown [204] that load Root Mean Square (RMS) acceleration, and therefore motor RMS torque, is minimised through the use of a $1/3$, $1/3$, $1/3$ split between periods. Consequently this is a common choice of move profile, as a trapezoidal trajectory is straightforward to generate in a microprocessor control system.

For certain motion control systems the sharp changes in acceleration generated by a trapezoidal move profile may be an issue. In these cases an ‘S-curve’ or ‘variable rate’ profile can be used. This ramps acceleration up and down at the start and end of the first and last periods of a trapezoidal move, thus minimising the jerk. Recent work has gone further and proposed trigonometric models for planning S-curve trajectories that minimise the derivative of the jerk – or ‘snap’ [205].

The overall move profile may also be optimised to minimise the overall energy dissipation in the machine. It has been shown that a parabolic profile is optimal for minimising winding joule losses in a machine with a purely inertial load [206, 207]. This can be modified to include a maximum speed limit and is shown to outperform a conventional variable rate profile with respect to energy efficiency [207]. This analysis has been extended to the more realistic case of the motor displaying a viscous type friction in [208]. The profile deviates from the parabolic profile as the effect of viscous friction is increased, reducing in peak speed but demanding harsher acceleration and deceleration. This profile can also be modified to include a maximum speed limit.

All the above profiles are symmetric, with similar acceleration and deceleration periods. This may cause issues for finding the correct steady-state position, and has been addressed by introducing asymmetric S-curve profiles with a smoother deceleration period [209].

Whilst the use of move profiles is standard in servo positioning applications such as robotics, it finds less use in actuator systems. Current *Cummins* actuators do not incorporate any trajectory planning, with the position control input driven directly from the closed loop positioning error. Considering the velocity profile achieved by an actuator driven in this way, for small moves under light load the move profile might be expected to be smooth and relatively efficient. It is for large moves under substantial load that inefficiencies in move profile might be significant. In these cases the motor acceleration is likely to be constrained by the current limit and maximum speed will also be reached. This will lead to the start of the profile resembling a trapezoidal move. The final portion of the move will be governed by the position control tuning – for a critically damped response this is expected to be roughly exponential. This final portion is less important from a turbocharger perspective, as the actuator output is approaching the correct position. Even with a trajectory generator in the loop there could be fluctuations during this period due to changing load disturbances.

Assuming that the motor speed limit will be reached during most moves, the maximum move acceleration is of interest. Acceleration is directly linked to motor torque through the rotor and referred load inertias. Torque is then linked to winding current, which is limited to prevent excessive power losses in the machine.

[207] suggests that the decrease in input energy required for a move using a modified parabolic trajectory over a trapezoidal trajectory is around $11\,\%$, discounting the energy required to overcome the load. This is achieved through a $33\,\%$ increase in initial acceleration. When holding torque is required against a continuous load, as in the turbocharger actuator case, then the efficiency saving generated through detailed move planning is expected to be significantly less. However, the concept of a pre-specified move profile is of considerable use in estimating overall actuator requirements. Even where a specific profile is not enforced within the application, an assumed profile can provide a valuable starting point for generating peak speed and torque requirements.

2.7.2 Motor and transmission specification

Based on a set of requirements for an actuator, a method of appraising candidate motors and transmissions is required. [34] introduces fundamental equations for determining the optimal gearbox ratio n to connect a motor to a load. In the most basic case for a constant speed load, assuming a perfect gearbox of $100\,\%$ efficiency, the motor torque T and load torque T_l can be matched, as:

$$n = \frac{T_l}{T} \tag{2.10}$$

For a positioning actuator the speed is dynamic – this is addressed by introducing a load acceleration α and related motor J_m and load J_l inertias [34, 210]

$$\widehat{T} = \alpha \left(J_m n + \frac{J_l}{n} \right) \tag{2.11}$$

noting in this case that it is the peak motor torque $\widehat{T}$ that is of interest.

Differentiating this function with respect to n to find a minimum gives the well-known ratio for optimal acceleration:

$$n = \sqrt{\frac{J_l}{J_m}} \tag{2.12}$$

Whilst this may be a reasonable initial estimate for many systems, it also has several shortcomings, the most important being that it assumes that the motor has already been selected. It also does not take into account any load torque applied to the system, it does not include any speed or efficiency related constraints, and it is based only on the peak torques, rather than their average values.

[211] starts to address these limitations through the introduction of a set of inequalities that must be fulfilled in a gear-motor pair

$$\begin{gathered} \widehat{\omega}_l n \leq \widehat{\omega}_m \\ \left\| \alpha J_m n + \frac{T_l'}{n} \right\|_p \leq \|T\|_p \end{gathered} \tag{2.13}$$

where $\|.\|_p$ indicates a particular norm relating to the torques; this might be peak or the RMS torque – relating to the important current considerations for the electronic drive and motor thermal requirements respectively. In practice both of these are usually important for brushless motor systems. The load torque T_l' now includes the torque required to accelerate the load. [211, 212] normalise this inequality using $\sqrt{J_m}$ and go on to find a range of transmission ratios that fulfil the requirements and derive an optimal ratio for the gear.

This technique may be developed further, either referring to the load as purely inertial [204], or extending to include both load torques and the effects of transmission inertia [213, 214]. Explicitly stating Equation 2.13 as RMS torque T_{RMS} and peak torque $\widehat{T}$ values gives

$$\begin{gathered} \widehat{\omega}_l n \leq \widehat{\omega}_m \\ \sqrt{\frac{1}{\tau} \int_0^\tau \left[\alpha J_m n + \frac{T_l'}{n} \right]^2 \mathrm{d}t} \leq T_{RMS} \\ \max \left| \alpha J_m n + \frac{T_l'}{n} \right| \leq \widehat{T} \end{gathered} \tag{2.14}$$

again these are normalised by multiplying the first by $\sqrt{J_m}$ and dividing the others by $\sqrt{J_m}$. Each member of these equations may be squared to give them physical meaning:

$$\begin{gathered} \frac{1}{2} J_m \widehat{\omega}_l^2 n^2 \leq \frac{1}{2} J_m \widehat{\omega}_m^2 \\ \frac{1}{\tau} \int_0^\tau \left[\alpha \sqrt{J_m} n + \frac{T_l'}{\sqrt{J_m} n} \right]^2 \mathrm{d}t \leq \frac{T_{RMS}^2}{J_m} \\ \left[\max \left| \alpha \sqrt{J_m} n + \frac{T_l'}{\sqrt{J_m} n} \right| \right]^2 \leq \frac{\widehat{T}^2}{J_m} \end{gathered} \tag{2.15}$$

The dependence on transmission ratio is removed by considering the motor inertia referred through the transmission

$$J'_m = J_m n^2 \tag{2.16}$$

this allows the previous inequalities to be rewritten as:

$$\begin{gathered} \frac{1}{2} J'_m \widehat{\omega}_l^2 \leq \frac{1}{2} J_m \widehat{\omega}_m^2 \\ \frac{1}{\tau} \int_0^\tau \left[\alpha \sqrt{J'_m} + \frac{T'_l}{\sqrt{J'_m}} \right]^2 \mathrm{d}t \leq \frac{T_{RMS}^2}{J_m} \\ \left[\max \left| \alpha \sqrt{J'_m} + \frac{T'_l}{\sqrt{J'_m}} \right| \right]^2 \leq \frac{\widehat{T}^2}{J_m} \end{gathered} \tag{2.17}$$

The right-hand side of first inequality can now be referred to as the maximum kinetic energy achievable by the motor, whilst the left-hand side is the maximum required to drive the load through the transmission. Similarly the two right-hand side torques are the motor's continuous duty power rate and dynamic power rate respectively, and the left-hand side inequalities are the maximums required to drive the load.

Once a move profile has been chosen, and requirements for the move period and load torque have been specified, the quantities ω, α, τ and T'_l will be known. Kinetic energy against power rate, or 'K-P diagrams', can then be plotted, one for continuous duty and one for dynamic use. Lines based on the left-hand side of Equations 2.17 may be plotted that are functions of motor inertia; these depend only on the load, not the transmission or motor. Candidate motors may be plotted as points, the data required to determine the points under ambient conditions being generally available from motor catalogue specifications. A motor is capable of driving the specified load if the quadrant between its point and zero contains a similar portion of the load curve in both the continuous and dynamic power plots; this portion of the load curve is referred to as the 'feasibility arc'. From the intersection of the continuous and dynamic feasibility arcs a range of possible referred inertias are found, and from these a range of feasible transmission ratios can be calculated. [214] suggests that an optimised motor and transmission will be limited more by the motor's continuous duty range, i.e. the motor's thermal limits, than its dynamic range.

Further work by the same author goes on to investigate the dynamic range limited case in more detail [215] and to include the transmission inefficiency for power flow in both directions [216].

Equations similar to 2.14 are developed in [105], however transmission inertia and efficiency are also included. In this case the authors are concerned with optimising the combined motor and gearhead with respect to specific criteria such as: motor torque, peak power, or efficiency. Gearboxes and motor are eliminated from a specified set that cannot drive the load, and the remainder are evaluated by plotting the optimisation criteria against gear ratio.

[217, 218] recently also included the effects of transmission efficiency η_g in the selection process. Assuming that power is being transferred from the motor to the load, Equation 2.14 is altered to:

$$\begin{gathered}
\widehat{\omega}_l n \leq \widehat{\omega}_m \\
\sqrt{\frac{1}{\tau}\int_0^\tau \left[\alpha J_m n + \frac{T_l'}{n\eta_g}\right]^2 \mathrm{d}t} \leq T_{RMS} \\
\max\left|\alpha J_m n + \frac{T_l'}{n\eta_g}\right| \leq \widehat{T}
\end{gathered} \tag{2.18}$$

The integration in the middle inequality can be manipulated to give

$$J_m^2 n^2 k_1 + \frac{1}{n^2\eta_g^2}k_2 + 2\frac{J_m}{\eta_g}k_3 \leq T_{RMS}^2 \tag{2.19}$$

where:

$$\begin{aligned}
k_1 &= \frac{1}{\tau}\int_0^\tau \alpha^2 \,\mathrm{d}t \\
k_2 &= \frac{1}{\tau}\int_0^\tau T_l'^2 \,\mathrm{d}t \\
k_3 &= \frac{1}{\tau}\int_0^\tau \alpha T_l' \,\mathrm{d}t
\end{aligned} \tag{2.20}$$

These integrals depend entirely on the load and move profiles in use.

Transmission inertia J_g may be included with the load torque, such that its full definition is:

$$T_l' = T_l + (J_l + J_g)\alpha \tag{2.21}$$

[217–219] refer to the continuous power duty rate of the motor as its ‘accelerating factor’ k_α

$$k_\alpha = \frac{T_{RMS}^2}{J_m} \tag{2.22}$$

and split Equation 2.19 to find a load factor k_β

$$k_\beta = \frac{2(\sqrt{k_1}\sqrt{k_2} + k_3)}{\eta_g} \tag{2.23}$$

such that it becomes:

$$k_\beta + \left[\frac{\sqrt{k_2}}{n\eta_g\sqrt{J_m}} - \sqrt{k_1}n\sqrt{J_m}\right]^2 \leq k_\alpha \tag{2.24}$$

Since the squared term in Equation 2.24 has a minimum of zero, k_β immediately suggests an initial criterion for sizing a motor. In other words the accelerating factor, which may be calculated from motor datasheet values, must be sufficiently larger than the load factor. The load factor is a numeric definition of the minimum of the load curve in the continuous power K-P diagram. The extra terms in Equation 2.24 may be referred to as the ‘extra-power factor’ and represent the additional power required to accelerate the motor or load when an optimal transmission ratio is not selected.

From the accelerating factor and the load factor it is possible the determine the range of transmission ratios that satisfy the criterion; however it is still necessary to check that both the maximum speed and dynamic torque criteria are fulfilled by the selected motor and transmission. The possible transmission ratios are given by

$$n_{min}, n_{max} = \frac{1}{\eta_g \sqrt{J_m}} \frac{2\sqrt{k_2}}{\sqrt{k_\alpha - k_\beta + \frac{4\sqrt{k_1}\sqrt{k_2}}{\eta_g}} \pm \sqrt{k_\alpha - k_\beta}} \tag{2.25}$$

although the maximum value does not take into account any upper speed limit. An optimal transmission ratio is also defined as

$$n_{opt} = \sqrt{\frac{\sqrt{k_2}}{\eta_g J_m \sqrt{k_1}}} \tag{2.26}$$

this is the ratio that corresponds to the load factor, or the ratio at the minimum of the load curve in the continuous power K-P diagram when a specific motor inertia is specified.

It is suggested that Equations 2.22, 2.23 and 2.25 could be used to determine possible transmission ratios for a motor and load combination initially assuming no transmission inefficiency. These results may then be used to produce a curve of transmission ratio against efficiency against which candidate transmissions may be assessed [217, 218]. A similar process can be performed to investigate the effects of transmission inertia.

[220] provides an assessment of accelerating factors for a range of commercial motors and investigates how the parameter changes with other motor parameters.

Whilst these equations are well developed, they may only be applied to a design process when the specific motor parameters are available. Previous work has assumed that accurate parameters are available from manufacturers to feed into this process; however this may not always be the case, particularly if operation away from ambient thermal conditions is expected. This thesis develops parameterised motor models to supply the motor parameters required to plot their points on K-P diagrams, allowing assessment of motor performance when used within an actuator at elevated temperatures.

2.8 Summary

This chapter has given a wide-ranging review of actuator concepts and previous work in the area. An exhaustive review of all possible technologies and options is beyond the scope of this work; however attention has been drawn to those designs and techniques which seem most appropriate to the actuator under consideration. An outline of the variable geometry turbocharger actuation system was provided, describing the actuator components within the turbo bearing housing and outlining the need for an external actuator to drive the sector gear on the cross-shaft.

From the review of motor technologies undertaken, brushed or brushless permanent magnet or switched reluctance motors could be used; however for reliability and robustness to vibration, brushless permanent magnet machines are the favoured choice. This may change if the cost of rare earth permanent magnet materials continues to increase, making ferrite magnet or switched reluctance machines potential candidates. The remainder of this work concentrates on a three-phase brushless permanent magnet motor design, utilising surface mounted NdFeB rotor magnets. Hall sensors are considered to be the cheapest and most robust option for position sensing.

A standard half-bridge is assumed throughout this work, and further investigation into the benefits of various switching schemes is undertaken in Appendix G. Current shape options, in conjunction with the back-EMF shape, are assessed in Chapter 3. The position control loop is also revisited in this chapter.

A full review of gearing technologies and gear combinations has been given, including several relatively high precision, sophisticated designs. Whilst many of these offer a very compact size for the gear ratio provided, they are likely to be less cost effective to produce and potentially less reliable due to fatigue issues. The remainder of this work uses a train of straight-cut spur gears, however the mechanical modelling and design process work is independent of the specific gear and gearbox type, provided appropriate parameters are used. A decision on gearbox design should be based on a cost to volume trade-off in the actuator requirements. Significant volume reductions may be possible in the future if gearing were introduced within the turbo body itself, for example through the use of leadscrew type designs.

Interesting concepts combining motors with magnetic gearing were mentioned. These are not commonplace and therefore off-the-shelf components utilising these designs are unlikely to be available; they may however be of interest in the future, or to achieve very demanding design requirements, such as high torque-density.

Techniques for modelling the selected components have been introduced. General purpose modelling software has been selected for flexibility and to provide control of the underlying mathematics. This also allows the electromagnetic, mechanical, thermal and control domain models to be handled by the same software. Developing models at various fidelities will support a variety of different studies. Mechanistic model development allows models to be populated with meaningful physical parameters, such that models may be constructed using only datasheet values, in the absence of a sample product. Simple lumped-parameter thermal models will also support this approach.

A whole system design will need to take into account both the motor and gearbox, due to their relationship through the gear ratio. A developing area of research has been identified that provides tools, such a K-P diagrams and motor- and load-factors, to support this type of design.

The development of a combined electromagnetic, mechanical and thermal motor model that is easily parameterised, represents a key contribution of this thesis. This will enable the assessment of candidate actuator designs, operating at elevated temperatures, both through the production of key motor parameters for use in K-P diagrams, and also through full closed-loop simulation of performance.

Chapter 3

Actuator modelling

3.1 Introduction

This chapter develops the mathematical actuator models that form the basis for analysis carried out later in the thesis. Details of how they are implemented in *Matlab Simulink* are given in Appendix C. The models are based on the underlying physics to form a complete description of actuator operation.

This work aims to make performance predictions for new actuator designs, to provide a tool to investigate the sensitivity of actuator designs to parameter changes, and to inform optimal design choices in a range of areas. These aims are addressed in Chapter 6, often by assessing the performance of actuator models. The outcome of this work, summarised in Chapter 7, relies on good quality, high fidelity actuator models that are well validated. This chapter details the mathematical basis for the models and Chapter 5 describes the model validation process and results.

Having detailed actuator models also allows integration with larger system models – such as whole turbocharger models. In order to allow flexibility in model application, and to investigate the impact of changing model fidelity, models at varying levels of complexity have been built.

Mathematical models can only ever provide an approximation of the true system, therefore an appropriate level of fidelity must be chosen, such that the model output is accurate enough for the task, but the model still remains useful. The underspecification of a model may reduce its accuracy such that results are not reliable enough for assessing performance. Over-specifying a model may introduce problems in parameter collection and simulation run-time, along with the unnecessary effort required to initially create the model.

More detailed modelling approaches, such as FE analysis, are available and frequently used in applications such as motor and actuator design. These have not been pursued in this work as they are computationally intensive, time-consuming to set up, and require design knowledge that would need to be provided by a manufacturer or be acquired through detailed measurement of sample components. Although vital for the design of new components, it is suggested that this level of modelling is not required for the assembly of systems from off-the-shelf components.

A recent trend in modelling is towards the use of ‘acausal’ approaches [147]. These offer high fidelity modelling capability whilst allowing the user to construct the model in terms of system components. The mathematics of the interfaces are handled internally by the modelling package. A model using this approach has been constructed and is outlined in Appendix D for comparison against the the models documented in this chapter.

Chapter 2 showed that the current design of actuator, a brushless motor connected through a set of spur gears to a rotary output gear, provides a robust and cost-effective system for automotive actuation. The designs developed are therefore based on these components; however, many of the modelling techniques used in this chapter would be equally applicable to alternative motor and gearbox types.

Much of the work in this chapter summarises explanations provided in undergraduate level textbooks [34, 221, 222], but these explanations are furthered by the development of: models of six-step switching to commutate the motor; a set of equations for efficient calculation of the average current and torque; and a low-order lumped-parameter thermal model for evaluation of motor component temperatures. Overall the key contribution of this chapter is the combination of models in different physical domains (electromagnetic, mechanical and thermal) into models at varying fidelities and tailored to the specific application being considered. It provides an example of an actuator modelling process and also multi-domain mechatronic model construction in general.

3.2 Motor electromagnetic model

This section initially details equations for calculating the current and torque produced by each motor phase, based on the voltage across it; the overall electrical torque is then the sum of the phase torques (assuming a balanced machine). The theoretical implications of different back-EMF and current shape combinations on torque and current is then considered, with six-step commutation and a sinusoidal back-EMF found to be the most likely candidate. This combination is used throughout the remainder of the work.

Once the theoretically ‘ideal’ electrical torque has been determined, account is taken of some electrical and magnetic loss mechanisms within the motor. These are included as loss torques opposing the ideal electrical torque. The modelling in this work has been limited to three phase motors, however the principles outlined could be extended to higher phase numbers.

3.2.1 Motor windings model

A standard three phase, Y-connected brushless motor is considered, having the electrical equivalent circuit shown in Figure 3.1 [34]. Connections 1, 2 and 3 on the left of the diagram are the connections to the driver circuit and the point on the right is the star-point. The L on each winding represents the winding's self-inductance, whilst the two right-most voltage sources represent the winding's mutual-inductance - its magnetic interaction with the other windings M. No saliency in the rotor or nonlinear magnetic circuit effects are considered, therefore inductance is assumed constant with rotor position. Also represented are the winding resistance R, the back-EMF generated in it by the rotor e, and the current i. Subscripts indicate the phase number.

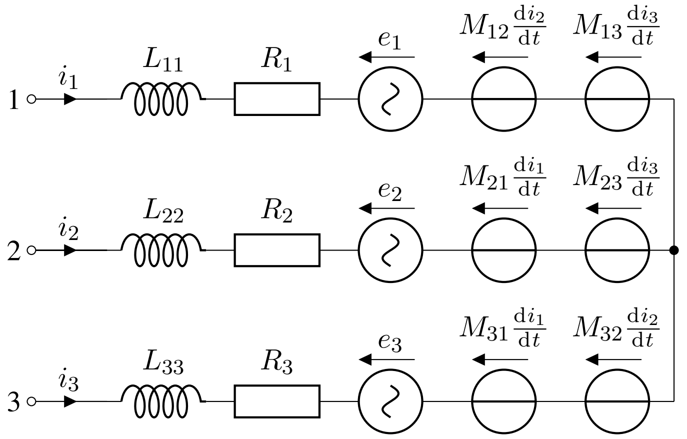

Figure 3.1: Motor winding equivalent circuit

The voltage across each winding v_1,v_2,v_3 can be represented in matrix form as:

$$\begin{bmatrix} v_1 \\ v_2 \\ v_3 \end{bmatrix} = \begin{bmatrix} R_1 i_1 \\ R_2 i_2 \\ R_3 i_3 \end{bmatrix} + \begin{bmatrix} L_{11} & M_{12} & M_{13} \\ M_{21} & L_{22} & M_{23} \\ M_{31} & M_{32} & L_{33} \end{bmatrix} \frac{\mathrm{d}}{\mathrm{d}t} \begin{bmatrix} i_1 \\ i_2 \\ i_3 \end{bmatrix} + \begin{bmatrix} e_1 \\ e_2 \\ e_3 \end{bmatrix} \tag{3.1}$$

Assuming a balanced motor (i.e. similarity between the windings), and an isolated star-point, this may be simplified using vector notation to give [34]

$$\boldsymbol{i} = \int \frac{\boldsymbol{v} - \boldsymbol{R}\boldsymbol{i} - \boldsymbol{e}}{L - M} \, \mathrm{d}t \tag{3.2}$$

where:

$$\begin{aligned} L &= L_{11} = L_{22} = L_{33} \\ M &= M_{12} = M_{13} = M_{21} = M_{23} = M_{31} = M_{32} \\ \boldsymbol{R} &= \begin{bmatrix} R_1 & 0 & 0 \\ 0 & R_2 & 0 \\ 0 & 0 & R_3 \end{bmatrix} \end{aligned} \tag{3.3}$$

The back-EMF voltages are dependent upon the electrical speed of the shaft ω_e and a term $\boldsymbol{K}_o$ which is a vector incorporating the peak back-EMF constant K_E and the shape of the back-EMF f_K; this is a function of the electrical position of the shaft θ_e and assumes that the windings are equally distributed around the stator:

$$\boldsymbol{K}_o = K_E f_K \left(\theta_e - \begin{bmatrix} 0 \\ {}^{2\pi}\!/_{3} \\ {}^{4\pi}\!/_{3} \end{bmatrix} \right) \tag{3.4}$$

If electrical losses are neglected, then all electromagnetic power developed by the windings is transferred to the rotor shaft. As the electrical and mechanical speeds are related through the number of magnet pole-pairs on the rotor n_{pp}, the torque produced at the rotor T_e may be found by [34]:

$$T_e = n_{pp} \boldsymbol{K}_o^{\top} \cdot \int \frac{\boldsymbol{v} - \boldsymbol{R}\boldsymbol{i} - \omega_e \boldsymbol{K}_o}{L - M} \, \mathrm{d}t \tag{3.5}$$

An isolated star-point voltage is floating. The remainder of this section therefore looks at modelling terminal voltages to ensure there is no neutral current and that current cannot flow in windings whilst they are disconnected. Currents in all windings must sum to zero, leading to a varying voltage across the winding during the commutation period, which depends upon current and the back-EMF in the winding. In order to force the sum of the current in the three phases to zero, and assuming that the back-EMFs also sum to zero, then it follows that:

$$\sum \boldsymbol{v} = R \sum \boldsymbol{i} + (L - M) \frac{\mathrm{d} \sum \boldsymbol{i}}{\mathrm{d}t} \tag{3.6}$$

If $\sum \boldsymbol{v} = 0$ then Laplace transforms give

$$\sum \boldsymbol{i} = i_{sum0} e^{\frac{-tR}{(L-M)}} \tag{3.7}$$

where i_{sum0} is the sum of the initial currents. This shows that by forcing the sum of the winding input voltages to be zero, the sum of currents will decay to zero at a rate governed by the winding resistance and inductance values, typically a negligible period over a complete simulation. In other words, ensuring that the voltages in the windings sum to zero will ensure that the currents sum to zero. This may be achieved by modifying the set of terminal phase input voltages $\boldsymbol{v}_n$ by subtracting their average from each one:

$$\boldsymbol{v} = \boldsymbol{v}_n - \frac{\sum \boldsymbol{v}_n}{3} \tag{3.8}$$

This means that during commutation each phase voltage is dependent upon the current in the other windings.

With certain current shapes, such as voltage control and a 120° conduction period, and driven by a standard half-bridge circuit, there will be periods of zero current flow in the off phase. During the zero current period the back-EMF of this phase is not able to force current through the drive circuit. A voltage equal to the back-EMF should therefore be present at the motor terminals to ensure that this does not occur. In order to completely cancel the back-EMF Equation 3.8 must be taken into account. The scaled back-EMF e_n that achieves this for the first winding is given by:

$$e_{1n} = \frac{3}{2}e_1 + \frac{(v_2 + v_3)}{2} \tag{3.9}$$

When this is included in the balancing of the other phases in Equation 3.8, the voltages of the on phases will cancel in the sum, leaving half the back-EMF of the off phase as a correction.

3.2.2 Back-EMF and current shape

The back-EMF is a function of the rotor magnetisation and stator winding layout within the motor. If either the winding distribution or the magnetisation is sinusoidal then the back-EMF is guaranteed to be sinusoidal [34]; for small machines, magnet field fringing effects make a sinusoidal back-EMF is easier to design than trapezoidal. All sample machines investigated in this work showed a Total Harmonic Distortion (THD) below $20\,\%$.

It is natural to couple a six-step drive system to a trapezoidal back-EMF motor, and a sinusoidal drive to a sinusoidal back-EMF, as these topologies produce constant torque; however for smaller low-cost systems six-step drive electronics controlling sinusoidal Electro-Motive Force (EMF) motors are often found. With this in mind, the theoretical performance of a generic sinusoidal switching scheme output may be compared against a six-step control scheme. Chapter 8 of [34] provides a detailed comparison of the four possible combinations of switching scheme, based on the assumption of a motor with the same RMS back-EMF, producing the same RMS torque, and neglecting any voltage drops due to winding resistance or switching devices. A summary of key comparisons between combinations is given in Table 3.1.

This comparison considers an ideal, mechanically-commutated (brushed) DC motor as a baseline. In comparison to this a six-step commutated brushless machine, with trapezoidal back-EMF of the same peak amplitude, will have the same peak line current, but this current will be shared between the three windings during commutation, such that only two are conducting at any time, leading to the $\sqrt{2/3}$ scaling for RMS line current. The phase currents, back-EMFs and continuous torque produced by this combination is shown in Figure 3.2.

If machines with conceptually the same structure (volume, magnetic material, etc) are compared then it is assumed that the average rectified line-line back-EMF should remain the same; therefore a machine designed with sinusoidal back-EMF will give a slight increase in peak line-line. This increase is a factor of $\pi/3$, based on the mean of the three phase rectified wave.

Table 3.1: Commutation schemes and back-EMF shape performance, normalised on RMS torque [34]

Commutation/ back-EMF	RMS torque	Peak line-line back-EMF	Peak line current	RMS line current
DC motor	1	1	1	1
Six-step/Trapezoid	1	1	1	$\sqrt{2/3} = 0.817$
Sine/Sine	1	$\pi/3 = 1.047$	$2\sqrt{3}/\pi = 1.103$	$\sqrt{6}/\pi = 0.780$
Six-step/Sine	1	$\pi/3 = 1.047$	1	$\sqrt{2/3} = 0.817$
Sine/Trapezoid	1	1	$\pi^2/9 = 1.097$	$\pi^2/9\sqrt{2} = 0.775$

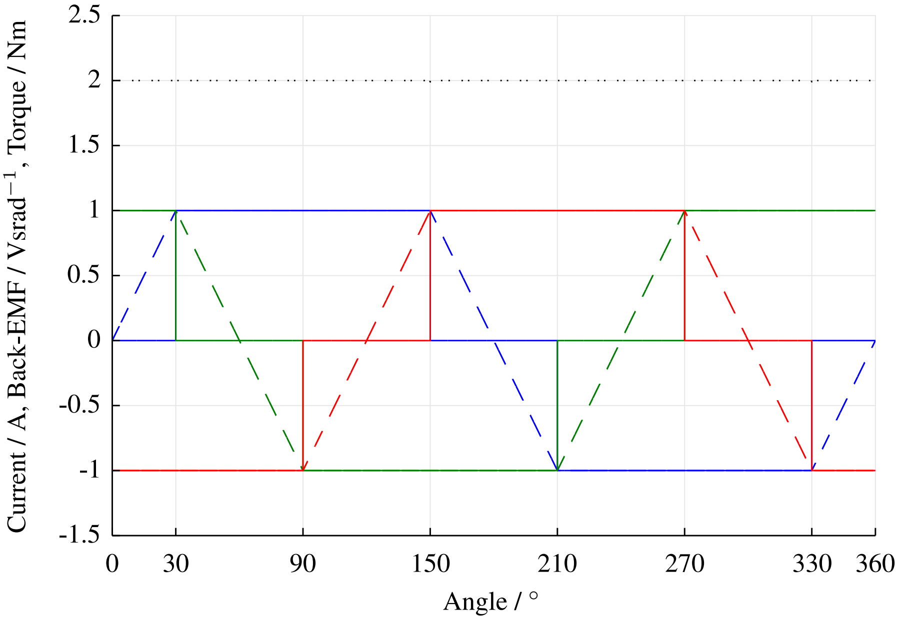

Figure 3.2: Current (solid) and back-EMF (dashed) waveforms for a six-step commutated trapezoidal machine with continuous torque of 2 Nm (dotted)

If a purely sinusoidal back-EMF machine is driven by a set of purely sinusoidal currents it will produce zero torque ripple – similar to the ideal six-step trapezoidal and DC machines already described. In this case the power will be given by $\widehat{e}_{ll}\widehat{i}_l\sqrt{3}/2$, where $\widehat{e}_{ll}$ is the peak line-line EMF discussed above. In order to produce equivalent torque and speed (and therefore power) to the other machines, the peak line current $\widehat{i}_l$ is therefore given by $2\sqrt{3}/\pi$. From this the RMS line current of $\sqrt{6}/\pi$ is found. The phase currents and back-EMFs to achieve the same continuous torque as the previous case are shown in Figure 3.3.

If the sinusoidal back-EMF machine is driven by a six-step commutation drive then a ripple is introduced into the torque. This is equivalent to the ripple in the peak

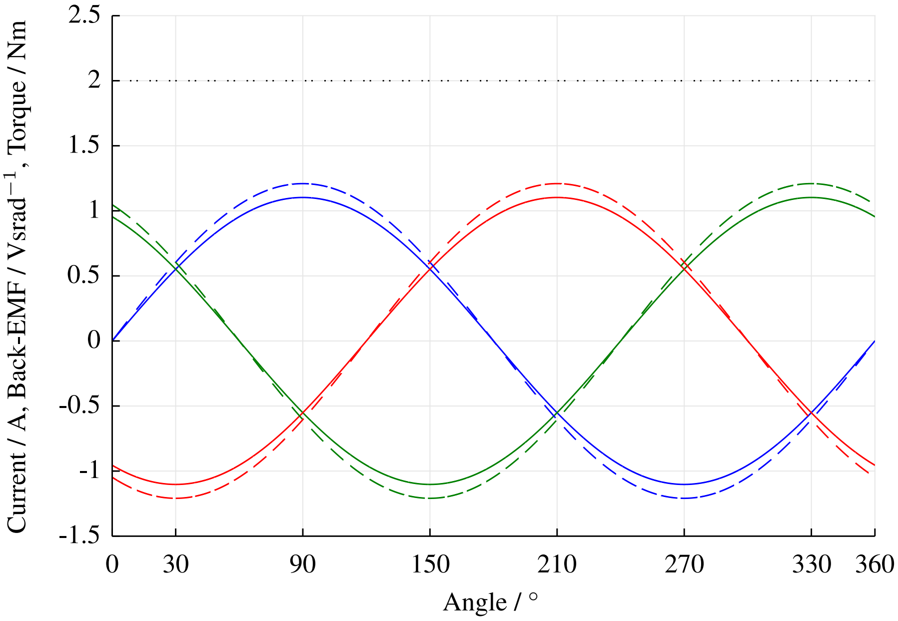

Figure 3.3: Current (solid) and back-EMF (dashed) waveforms for a sinusoidal current, sinusoidal back-EMF machine with continuous torque of 2 Nm (dotted)

line-line EMF already noted. There is also an increase in RMS line current required to produce an equivalent RMS torque (of $\pi/3$). Phase currents, back-EMFs and the torque ripple are shown in Figure 3.4.

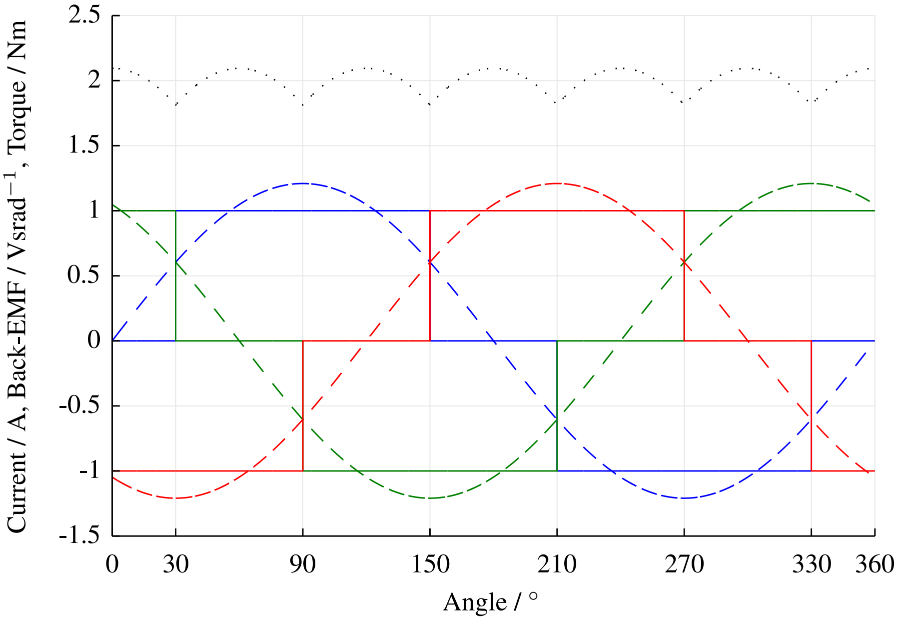

Figure 3.4: Current (solid) and back-EMF (dashed) waveforms for a six-step commutated sinusoidal machine with mean torque of 2 Nm (dotted)

Finally in the opposite case of a trapezoidal back-EMF machine driven by a sinusoidal current, Fourier analysis shows that the equivalent RMS line current is $^{\pi^2}/_{9\sqrt{2}}$ and the peak line current is $^{\pi^2}/_{9}$ [34]. In these last two hybrid cases there are losses due to the harmonics in the square waves of the commutation/back-EMF; however there is also a contribution to overall torque. Phase currents, back-EMFs and torque ripple for this case are shown in Figure 3.5.

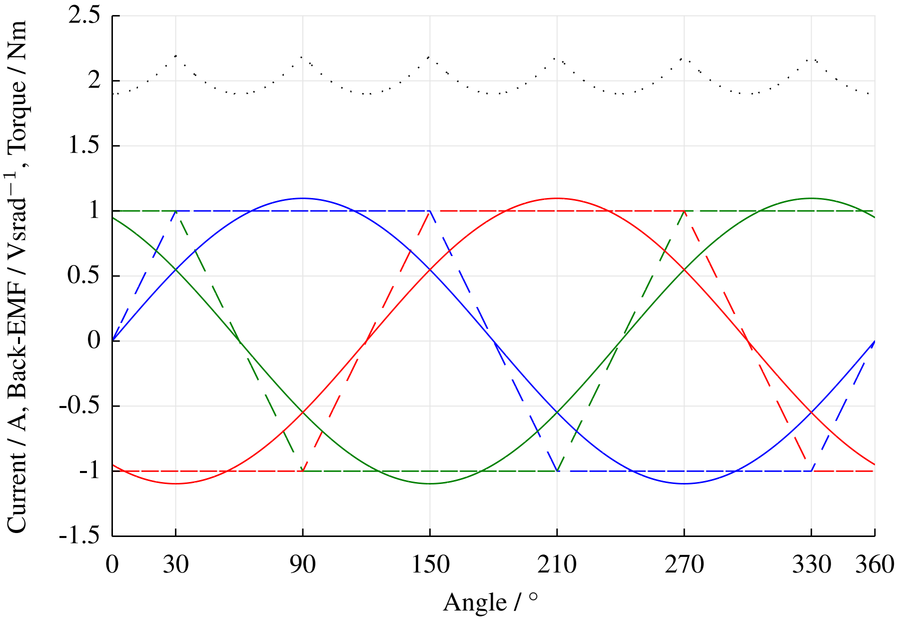

Figure 3.5: Current (solid) and back-EMF (dashed) waveforms for a sinusoidal current trapezoidal machine with mean torque of $2\,\mathrm{Nm}$ (dotted)

The RMS line current is important for efficiency in the drive and the thermal rating of the machine. This leads to the surprising conclusion that a trapezoidal back-EMF with a sinusoidal drive is the best option for minimal RMS current. In practice this is rarely seen due to the minimal $0.6\,\%$ improvement and the extra torque ripple introduced.

RMS current is next lowest for a sinusoidally commutated sinusoidal back-EMF machine. This provides a $4.7\,\%$ decrease in RMS current over the six-step commutation used in the existing products; however there is also a $10.3\,\%$ increase in peak line current. For a positioning application holding against a load force, such as an actuator, this peak current may be an issue (depending on the thermal specification method and any temperature regulation techniques used).

The results in Table 3.1 can be rescaled to compare the torque outputs if the currents are similar. This is shown in Tables 3.2 and 3.3 for peak and RMS current respectively.

For a positioning actuator motor, where the actuator spends sustained periods statically holding against a load torque, the peak current is of importance, as this must

Table 3.2: Commutation schemes and back-EMF shape performance, normalised on peak line current

Commutation/ back-EMF	Peak line current	Peak line-line back-EMF	RMS line current	RMS torque
DC motor	1	1	1	1
Six-step/Trapezoid	1	1	$\sqrt{2/3} = 0.817$	1
Sine/Sine	1	$\pi/3 = 1.047$	$\sqrt{2}/2 = 0.707$	$\pi/2\sqrt{3} = 0.907$
Six-step/Sine	1	$\pi/3 = 1.047$	$\sqrt{2/3} = 0.817$	1
Sine/Trapezoid	1	1	$1/\sqrt{2} = 0.707$	$9/\pi^2 = 0.912$

Table 3.3: Commutation schemes and back-EMF shape performance, normalised on RMS line current

Commutation/ back-EMF	RMS line current	Peak line-line back-EMF	Peak line current	RMS torque
DC motor	1	1	1	1
Six-step/Trapezoid	1	1	$\sqrt{3/2} = 1.225$	$\sqrt{3/2} = 1.225$
Sine/Sine	1	$\pi/3 = 1.047$	$2/\sqrt{2} = 1.414$	$\pi/\sqrt{6} = 1.283$
Six-step/Sine	1	$\pi/3 = 1.047$	$\sqrt{3/2} = 1.225$	$\sqrt{3/2} = 1.225$
Sine/Trapezoid	1	1	$\sqrt{2} = 1.414$	$9\sqrt{2}/\pi^2 = 1.290$

be limited to ensure the actuator remains within its thermal specification. Therefore Table 3.2 suggests that a six-step scheme will provide greater RMS torque (around 10 %) than sinusoidal commutation, for the same peak current.

For a continuous rotation application, or if the level of jitter or rate of demand change ensures that the period spent stationary is significantly less than the thermal time constant, the RMS current is more important. In this case Table 3.3 shows that sinusoidal excitation will supply the greatest RMS torque (around 5 % more than six-step).

Perhaps more of an issue for the sinusoidal systems is the need for accurate rotor position information (whereas three cheap and robust hall effect sensors are sufficient for six-step commutation). This information is usually provided by a quadrature encoder type sensor mounted on the motor shaft. This is likely to add sufficient expense and bulk to the system that will outweigh any benefits gained from applying sinusoidal currents. However if an encoder is specified in order to provide high resolution position information for other parts of the system then it makes sense to also use it to provide sinusoidal currents.

Alternatively the rotor position information could be provided through another mechanism. For example the actuator may have a position sensor on its output mechanism for use in the control loop. This may be sufficiently high resolution to control the sinusoidal currents in the motor phases, however any significant backlash and stiffness in the gear train may introduce errors into this measurement process. Another possibility may be to estimate the rotor position using hall sensors and a software estimation process. Again this is likely to be prone to measurement errors, especially at low speeds or highly variable load torques.

The impact of measurement errors on the different schemes is shown in Figure 3.6. This shows that the torque drops off for all schemes as the error increases. The six-step/trapezoidal scheme performs very slightly better than the others, but there is no difference between the three schemes with sinusoidal components; however the position measurement error is potentially much larger for sinusoidal current schemes in which there is no encoder. The 60° shown in Figure 3.6 is a full commutation step, within which there may be a few degrees of error due to hall sensing that affect a six-step scheme. Whereas for a sinusoidal scheme with position measurements made through several stages of gear backlash the error could be over 20° when gear ratios, typical backlash and pole-pair number are taken into account – see Section 4.5. For a position estimation scheme this could be higher, potentially up to 60° out, particularly at low speeds. It is important to note that this is 'electrical position', equal to the mechanical rotor position scaled by the number of rotor magnet pole-pairs; therefore high pole-pair number machines are expected to suffer more from these errors.

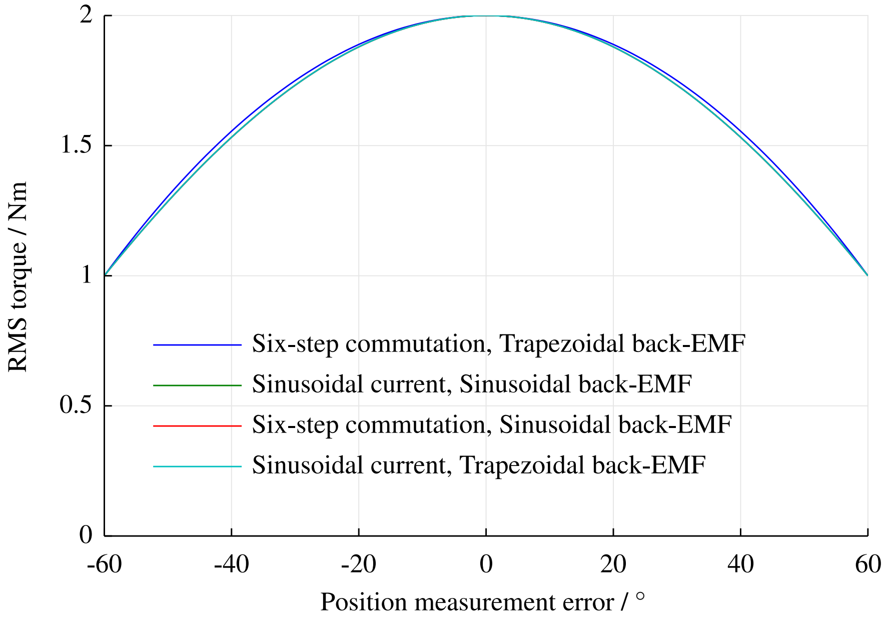

Figure 3.6: RMS torque change due to position measurement error for different drive schemes

Detailed investigation of the current generation *Cummins* actuator motor has been performed as part of an MSc dissertation project [33]. This report suggested that minor improvements in the torque density of this design may be possible, at the expense of an increase in torque ripple, through subtle changes to the design, particularly changing the magnet pole arc, reducing the number of magnet poles and altering the coil winding and stator geometry.

Overall, making a decision between a trapezoidal and sinusoidal back-EMF machine, based on Tables 3.1 to 3.3 the trapezoidal machine would be preferred for use in this application – if the designs were otherwise similar – as they show similar results with six-step commutation, but the trapezoidal back-EMF has less torque ripple. However, based on the sample motors used in this work it seems that sinusoidal rotor machines are more common at this size.

3.2.3 Iron losses

Power losses will occur in several parts of the motor. The equations above include the effects of resistive losses in the windings. There will also be iron loss in the motor stator. This is attributed to two separate phenomena, hysteresis loss and eddy current loss [223, 224].

Power loss due to magnetic hysteresis loops in the stator iron W_h (in $\mathrm{W\,kg^{-1}}$) may be calculated based on the frequency of electrical commutation f and the peak stator flux $\widehat{\mathcal{B}}$ using a standard Steinmetz equation [34, 225]

$$W_h = c_h f \widehat{\mathcal{B}}^{n_s} \tag{3.10}$$

where c_h and n_s are constants depending on the motor construction. It should be noted that the original equation proposed by Steinmetz in 1892 did not include the frequency term and had a fixed n_s of 1.6. Both parameters have since been found to depend on operating frequency and flux density, with fixed parameters only being accurate for small ranges of each. Nevertheless Equation 3.10 is a common approximation and is used in this work for actuator system modelling.

This hysteresis power loss may be converted into a loss torque by multiplying by the mass of the stator m_s and dividing by the speed of the rotor. As the frequency of commutation is dependent upon the rotor speed these two factors cancel, leaving a constant that is included in $c_{h'}$. If n_s is assumed constant, then total loss torque due to hysteresis is also a constant B_h:

$$B_h = m_s c_{h'} \widehat{\mathcal{B}}^{n_s} \tag{3.11}$$

This constant torque will only be applied whilst the motor is in motion (mechanical speed $\omega_m \neq 0$) and when the electrical torque exceeds it, (i.e. the loss torque is not capable of driving the motor, it is only capable of opposing motion) producing a dead-band in the torque around zero:

$$T_h = \begin{cases} T_e, & \text{if } B_h > T_e > -B_h \text{ and } \omega_m = 0, \\ B_h \operatorname{sgn}(\omega_m), & \text{otherwise.} \end{cases} \tag{3.12}$$

Although this is a physically reasonable approximation, it can cause issues during simulation due to the severe nonlinearity in the sign function. This can be a particular issue for variable time-step simulations where a solver attempts to find each signal 'zero-crossing' point. A common approximation that can assist in efficient simulation is to describe the torque as a hyperbolic-tangent function

$$T_h = \begin{cases} T_e, & \text{if } B_h > T_e > -B_h \text{ and } \omega_m = 0, \\ B_h \tanh\left(n_{\tanh} \omega_m\right), & \text{otherwise.} \end{cases} \tag{3.13}$$

where $n_{\tanh}$ is a constant that can be adjusted to set how closely Equation 3.13 approximates Equation 3.12 [198].

Power loss through eddy currents W_e (in $\mathrm{W\,kg^{-1}}$) is assumed to vary with the squares of both the peak flux-density and frequency [34] as

$$W_e = c_e f^2 \widehat{\mathcal{B}}^2 \tag{3.14}$$

where c_e is a constant depending on motor construction. Multiplying through by stator mass, converting frequency to rotor speed and dividing through by rotor speed to convert to torque gives

$$T_{ed} = B_e \omega_m \tag{3.15}$$

where B_e is the speed dependent eddy current losses constant:

$$B_e = m_s c_{e'} \widehat{\mathcal{B}}^2 \tag{3.16}$$

In Chapter 4 the loss terms B_h and B_e are derived from experimental testing of the motors, and therefore their definition based on motor design physical parameters (using Equations 3.11 and 3.16) is not used further in this work, but the form is retained.

3.2.4 Combined motor electrical torque

The torque exerted by the motor on the rotor shaft T is given by the combination of the torques outlined in the preceding sections:

$$T = T_e - T_h - T_{ed} \tag{3.17}$$

3.2.5 Temperature effects

The calculations presented above are valid for a fixed operating temperature, however motor behaviour will vary with temperature [51, 54]. The resistance of the windings will increase with operating temperature $\boldsymbol{\mathcal{T}}_w$, according to

$$\boldsymbol{R} = R_{\text{ref}}\left(1 + \psi(\boldsymbol{\mathcal{T}}_w - \mathcal{T}_{\text{ref}})\right) \tag{3.18}$$

where ψ is the temperature coefficient of resistivity. For annealed copper wire ψ is $0.003\,93\,\Omega\,{}^{\circ}\mathrm{C}^{-1}$ [37]. The reference temperature $\mathcal{T}_{\text{ref}}$ at which the resistance R_{ref} is defined is usually $25\,{}^{\circ}\mathrm{C}$. As windings heat and cool individually it should be noted that they can be at different temperatures (indeed this is likely to be the case, especially if the actuator is holding a static position against a load torque for any period of time). This explains why the matrix form of $\boldsymbol{R}$ has been used in Equations 3.2 and 3.18. Separate winding resistances were omitted in prior equations for simplicity.

Reversible demagnetization of the permanent magnets will also occur as rotor temperature $\mathcal{T}_r$ increases, leading to a reduction in back-EMF/torque constant, according to

$$K_E = K_{E\,\text{ref}}\left(1 - \gamma(\mathcal{T}_r - \mathcal{T}_{\text{ref}})\right) \tag{3.19}$$

where γ is the coefficient for demagnetisation, this is $0.001\,\mathrm{N\,m\,A^{-1}\,{}^{\circ}C^{-1}}$ for NdFeB magnets [34].

Thermal models are required in order to calculate the winding and rotor temperatures – see Section 3.3. In order to support these models, any heat generated within the motor must be calculated. The heat is generated through power loss, this occurs due to the resistance of the windings, sometimes referred to as 'Joule' losses, and also through iron losses in the rotor. The power dissipated in each winding P_w is given by:

$$\begin{aligned} P_{w_1} &= i_1^2 R_1 \\ P_{w_2} &= i_2^2 R_2 \\ P_{w_3} &= i_3^2 R_3 \end{aligned} \tag{3.20}$$

The power lost in the stator P_s through iron losses may be calculated based on the loss torques and the current rotor speed as:

$$P_s = \omega_m\left(T_h + T_{ed}\right) \tag{3.21}$$

3.2.6 Hall sensors

Most brushless motors used for positioning applications will have a method of absolute position measurement built in, either an encoder or hall sensors. For automotive applications designed to be operated with a six-step commutation scheme this is usually hall sensors. In order to operate motor models with the same software as used in the real hardware, the models must have a representation of the hall sensor outputs. A functional model of the hall sensors is included to output high or low signals based on the position of the rotor magnets relative to the sensor locations. The set of hall sensor outputs H_1, H_2, H_3 based on the rotor electrical position is given in Table 3.4.

Table 3.4: Hall sensor output H_1, H_2, H_3, based on rotor electrical position θ_e

θ_e	H_1	H_2	H_3
$0 \leq \theta_e < \frac{\pi}{6}$	0	0	1
$\frac{\pi}{6} \leq \theta_e < \frac{\pi}{2}$	1	0	1
$\frac{\pi}{2} \leq \theta_e < \frac{5\pi}{6}$	1	0	0
$\frac{5\pi}{6} \leq \theta_e < \frac{7\pi}{6}$	1	1	0
$\frac{7\pi}{6} \leq \theta_e < \frac{3\pi}{2}$	0	1	0
$\frac{3\pi}{2} \leq \theta_e < \frac{11\pi}{6}$	0	1	1
$\frac{11\pi}{6} \leq \theta_e < 2\pi$	0	0	1

3.3 Motor thermal model

As discussed in Section 2.6, a variety of different thermal modelling techniques are available. In this work a low-order lumped-parameter thermal model is developed, such that a detailed knowledge of the motor internal design is not required to parameterise it. The intention is to include temperature effects within the modelling, but without incurring a significant cost in terms of parameterisation or simulation performance.

A model with four separate parameters has been developed, as shown in Figure 3.7. It separates the motor into three motor windings and the combined stator, rotor and housing; these elements can all heat and cool independently. Self-heating within the stator and windings is also modelled. These have been hinted at in the literature [187], but have not previously been specified. The intention in proposing this model is to provide a higher level of thermal modelling accuracy than can be achieved using simple two-parameter models, but to also retain enough simplicity that the model may be parameterised using a few simple tests performed on a sample motor. These tests are developed in Chapter 4. Seven- and eight-parameter models that explicitly separated the rotor temperature were also considered, however these were found either to be difficult to parameterise, or to provide a poor estimate of rotor temperature. Additional details of models investigated but not taken forward are given in Appendix E.

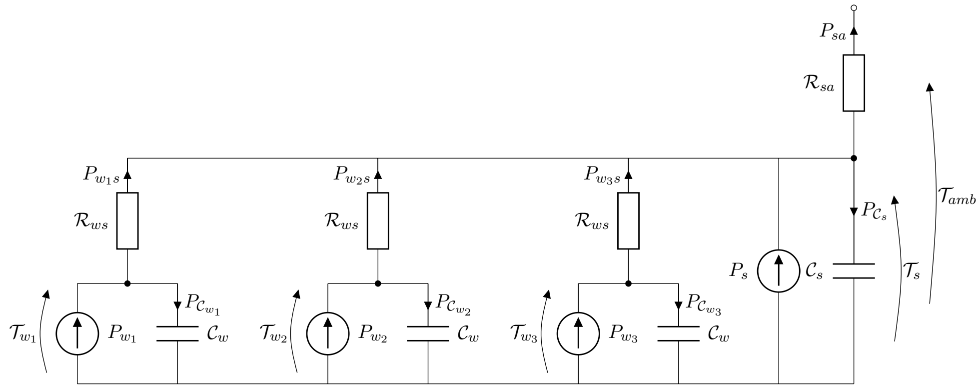

Figure 3.7: Lumped-parameter motor thermal network model

The power transferred into the motor as heat through Joule loss in the windings is shown by P_{w_1}, P_{w_2} and P_{w_3}. The separate windings each have the same thermal capacitance $\mathcal{C}_w$, and a thermally resistive connection to the stator $\mathcal{R}_{ws}$. The stator has a thermal capacitance $\mathcal{C}_s$ and also power transferred into it through iron losses P_s. The rotor thermal mass is assumed to be captured within the stator mass. The stator can transfer heat to ambient, via thermal resistance $\mathcal{R}_{sa}$.

The temperature of each winding $\mathcal{T}_{w_1}$, $\mathcal{T}_{w_2}$, $\mathcal{T}_{w_3}$ may be calculated from

$$\boldsymbol{\mathcal{T}_w} = \frac{\mathcal{R}_{ws}\boldsymbol{P_w} + \mathcal{T}_s}{\mathcal{R}_{ws}\mathcal{C}_w s + 1} \tag{3.22}$$

where $\mathcal{T}_s$ is the temperature of the stator, given by:

$$\mathcal{T}_s = \frac{\mathcal{R}_{ws}\mathcal{R}_{sa}P_s + \mathcal{R}_{sa}(\mathcal{T}_{w1} + \mathcal{T}_{w2} + \mathcal{T}_{w3}) + \mathcal{R}_{ws}\mathcal{T}_{amb}}{\mathcal{R}_{ws}\mathcal{R}_{sa}\mathcal{C}_s s + 3\mathcal{R}_{sa} + \mathcal{R}_{ws}} \tag{3.23}$$

These temperatures represent a rise with respect to the reference temperature $\mathcal{T}_{amb}$. In this work $\mathcal{T}_{amb}$ is defined as the fixed temperature surrounding the stator. During most testing this is a large volume of ambient air, however it could also be coolant, or an actuator casing, in a production actuator. It is assumed that the rotor mass is lumped with the stator, and therefore:

$$\mathcal{T}_r = \mathcal{T}_s \tag{3.24}$$

As the motor electromagnetic model relies on the winding and rotor temperatures, and supplies the power losses in the windings and stator (Section 3.2.5) to this thermal model, these two models can be run together to give a full thermal and electromagnetic model of the motor. Coupling these two models includes the important positive feedback effect of increased winding temperature leading to increased resistance and therefore power loss. By including individual windings the model allows peak winding temperatures to be investigated; this is often a limiting case for brushless motor use, particularly in high temperature applications. This type of assessment would be impossible with a two-parameter model.

3.4 Motor drive power electronics model

To be able to fully validate the models and assess the effect of different switching schemes, a model of the drive electronics is required. As detailed in Section 2.4 a standard drive topology is a three-phase half-bridge type circuit driven by a voltage source. The switches can be controlled to provide a range of different switching and commutation schemes.

3.4.1 Ideal switch responses

Each phase of the bridge is modelled separately, and switch requests passed from the software (S_1, S_2, S_3) are encoded as three states 1, -1 or 0, corresponding to the high switch, the low switch or neither switch, being activated. Although it would be physically possible to have the case where both high and low switches were activated, this would cause a short circuit and should therefore never happen.

It is also assumed that the switching responses are 'ideal', i.e. switching occurs instantaneously and with no losses. This is an approximation as real switches have current/voltage rise times and losses associated with them. They may also have snubber capacitors or other supporting electronics to aid switching.

As detailed in the motor electromagnetic model (Section 3.2) the input to the motor is a set of voltages with respect to a virtual neutral point. In order to simulate this the DC supply voltage V_s is halved before being passed to the drive electronics model.

In order to correctly deal with the case where both high and low switches of a phase are open, the drive electronics model must also model the freewheel diodes, based on the current flowing in the phase. The nominal drive model outputs are summarised in Table 3.5, however these are further transformed in the motor model to account for there being no zero connection to ground according to Equation 3.25.

Table 3.5: Drive electronics model output for a single phase

Switch state	Phase current	Voltage output	Physical state
$+1$		$+{}^{V_s}\!/_2$	Phase switched high
-1		$-{}^{V_s}\!/_2$	Phase switched low
0	> 0	$-{}^{V_s}\!/_2$	Lower diode conducting
0	< 0	$+{}^{V_s}\!/_2$	Upper diode conducting
0	≈ 0	0	No conduction

In the case where current is still flowing in motor coils (due to their inductance), but both switches of the bridge are open, the current must flow through one of the diodes. These connect the supply voltage in opposition to the current, quickly forcing the current to zero. Within modelling software that uses variable time-step simulations, a margin of $\pm 0.1\,\mathrm{mA}$ around zero current was used to avoid excessive computation time – otherwise introduced in the process of solving to find 'zero-crossings'.

3.4.2 PWM modelling

Depending on the drive scheme selected, the voltage may be regulated using PWM. Section 2.4.3 gives a range of different switching schemes that may be employed for six-step commutation. The model outlined above represents PWM switching introduced by changing the switch states. PWM switching within the model sets up a sawtooth wave at the duty cycle period and uses a threshold on the waveform output to drive the switches. Depending on what switches are controlled, schemes A, B, C or D from Table 2.1 are implemented [34, 69, 70]. Dead-time is not included in any models. Schemes E or F (centre-aligned switching) are implemented using a triangular waveform.

A simplification may be introduced to the model by approximating the PWM switching with the average voltage over the switching period. This can considerably increase the simulation time-step, allowing the model to run much faster. The trade-off between fidelity and speed using this simplification is investigated in Chapter 5.

Detail on the implementation of PWM switching within the models in *Matlab Simulink* is given in Appendix C. Models incorporating losses in the switching power electronics have not been developed, however switching losses are included in the pre-built acausal libraries in the *SimScape* model – see Appendix D. This difference is also taken into account in assessment of the model results in Chapter 5.

3.5 Computationally efficient motor model

In order to speed up simulation, a more computationally efficient motor model has been developed. This approximates the three motor phases by a single set of equations, including the effects of commutation analytically, such that it does not need to be explicitly accounted for in the model, allowing the simulation time-step to be significantly increased. Due to their size, the equations produced for this model are presented in Appendix A.

A naïve approach would be to use a standard brushed DC motor model, typically a single winding resistance and back-EMF constant, populated with the brushless motor's parameters. Although this will produce results of the right order-of-magnitude, it will not be accurate due to not properly taking into account the effects of inductance during commutation, or the impact of operating a sinusoidal back-EMF machine with a nominally square current waveform. Whilst it is possible to improve the accuracy of a DC motor model applied to a brushless motor through appropriate parameter scaling, particularly at very low or high speeds, the results will still show errors around the centre of the speed-torque curve. The error will be most significant where the commutation scheme switching frequency and winding time constant are similar, such that commutation is a major portion of the switching period [167, 170]. The work in this section retains the effect of commutation and inductance on the results.

The new model derived in this work follows from the same equations as presented for the individual coils in Section 3.2.1. Assuming the torque ripple produced by commutation is not of interest, the above model may be reduced by finding a direct expression for the average torque over a commutation period. The following analysis assumes a sinusoidal back-EMF – although the general methodology is also applicable for other shapes – and a six-step commutation strategy. The behaviour of current over half an electrical cycle is defined by three switching intervals (I, II, III) and the subset of these in which commutation is occurring (Iθ_{ec}, IIθ_{ec}, IIIθ_{ec}). Assuming the current in phase 1 to be zero at the start of the first switching interval, the sequence of current flow is:

Iθ_{ec} Current rising in phase 1 as it falls in phase 3 that has just turned off, back-EMFs in all phases are active.

I Current flowing in phases 1 and 2, the current in phase 3 is not active and the back-EMF should be cancelled.

IIθ_{ec} Current falling in phase 2 and rising in phase 3, back-EMFs in all phases are active.

II Current flowing in phases 1 and 3, the current in phase 2 is not active and the back-EMF should be cancelled.

IIIθ_{ec} Current falling in phase 1 after it has turned off and phase 2 has turned on, back-EMFs in all phases are active.

III Current is zero in phase 1, and its back-EMF should be cancelled.

The durations of these phases are dependent upon the operating conditions and electrical time constants of the system. Using Equations 3.1 and 3.8 the exact phase voltages in these periods may be calculated in terms of the supply voltage V_s, including any scaling to represent a change in duty ratio:

$$v_1 = \begin{cases} \frac{V_s}{2} + \frac{V_s}{6}, & \text{if } \frac{\pi}{6} \le \theta_e < \frac{\pi}{2} \text{ and } i_3 > 0, \\ \frac{V_s}{2} - \frac{1}{2}\omega_e K_E f_K(\theta_e - \frac{2\pi}{3}), & \text{if } \frac{\pi}{6} \le \theta_e < \frac{\pi}{2} \text{ and } i_3 = 0, \\ \frac{V_s}{2} - \frac{V_s}{6}, & \text{if } \frac{\pi}{2} \le \theta_e < \frac{5\pi}{6} \text{ and } i_2 > 0, \\ \frac{V_s}{2} - \frac{1}{2}\omega_e K_E f_K(\theta_e - \frac{4\pi}{3}), & \text{if } \frac{\pi}{2} \le \theta_e < \frac{5\pi}{6} \text{ and } i_2 = 0, \\ -\frac{V_s}{2} + \frac{V_s}{6}, & \text{if } \frac{5\pi}{6} \le \theta_e < \frac{7\pi}{6} \text{ and } i_1 > 0, \\ \omega_e K_E f_K(\theta_e), & \text{if } \frac{5\pi}{6} \le \theta_e < \frac{7\pi}{6} \text{ and } i_1 = 0. \end{cases} \tag{3.25}$$

An example voltage waveform resulting from Equation 3.25 is shown in Figure 3.8. This voltage function is represented as a superposition of step and back-EMF functions and then integrated using Equation 3.2 to find the average current. A similar process is performed using Equation 3.5 to find the average torque. However, these integrations require a knowledge of the period, or equivalent electrical angle, during which current is reducing in the 'off' winding. This electrical angle where current reaches zero, referred to as θ_{ef}, will be equal for all windings and will remain constant for fixed speed and torque conditions. Initially assuming that this is known, it is treated as a constant and the integration of the voltage step functions performed.

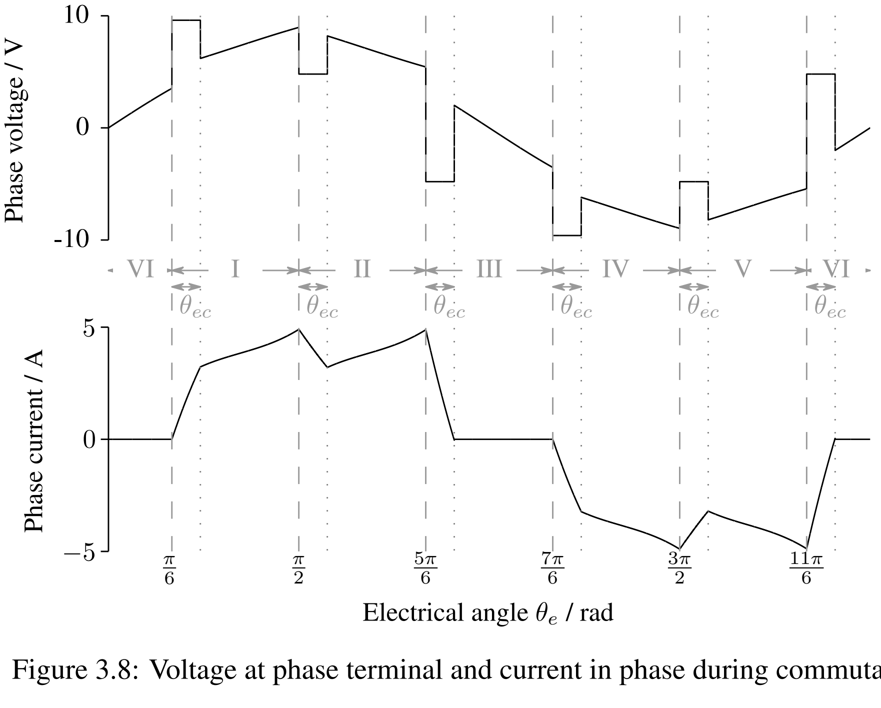

Figure 3.8: Voltage at phase terminal and current in phase during commutation

Integration of the current and torque was performed using the *MuPad* symbolic toolbox. The expression for the average current over a commutation interval $\overline{I}$ is shown in Equation A.1. A similar expression for average torque $\overline{T}$ is given in Equation A.2. These were exported from *Mupad* in *Matlab* format and used directly in simulations without requiring any manual manipulation.

If the correct commutation angle is used, then the full current waveform may also be produced analytically as shown in Figure 3.8. An incorrect commutation angle leads to a mismatch in the amplitude of the current at the end of the first and second switching periods; too large a commutation angle will create a higher peak in the first period, whereas too small a commutation angle will create a higher peak in the second. Steady-state conditions in balanced windings should produce equal current peaks – the difference in current peaks may therefore be used to indicate any error in the commutation angle.

Similar to the average current and torque, expressions for the current at the end of switching intervals I and II may be found by analytically substituting their angles into the equations using *MuPad*. The expression for the first current peak $\widehat{I_1}$ is given by Equation A.3 and second current peak $\widehat{I_2}$ is given by Equation A.4. The difference in the two current peak values may be used to drive a gradient descent process. As commutation angle changes smoothly with speed and torque, it is reasonable to estimate it during simulation.

Implementing Equations A.1, A.2, A.3 and A.4 as a *Matlab* function block within *Simulink* is straightforward. A simple integrated difference loop between the two current peaks can be then fed back to estimate the commutation angle. The average current and electrical torque produced are then available to the simulation. An example implementation is shown in Figure 3.9. The gain of the feedback loop is set large enough provide fast tracking of the commutation angle, without producing instability. The setting of this value will depend upon the simulation time-step used.

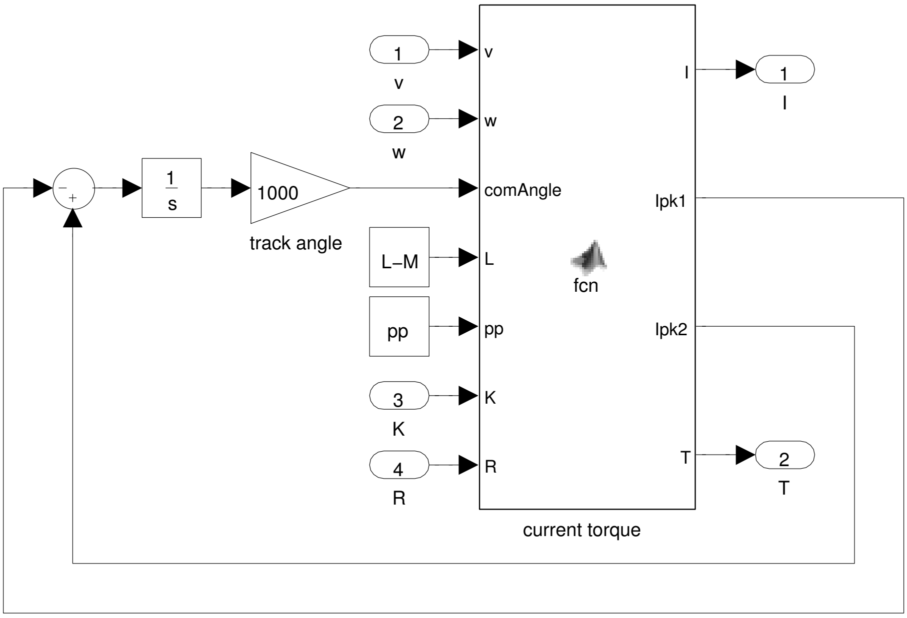

Figure 3.9: *Simulink* implementation of the current and torque equations

The stator thermal model calculations remain unchanged for the efficient model, however not having separate phases means the coil thermal model is an approximation, especially at stationary and low speeds, where there can be a large difference between winding temperatures. The thermal aspects of this model can therefore only be considered valid during continuous rotation, where the separate windings are expected to be at similar temperatures.

Although it is possible to analytically compute the average of the square current, in a similar manner to Equation A.1, the resulting equation is unwieldy for practical use. Therefore an approximation is developed by scaling the square of the average current.

If commutation were to occur instantaneously, and the current were an ideal rectangular shape, then its average $\overline{I}$ would be two thirds of its peak value $\widehat{I}$, or:

$$\overline{I} = \frac{2}{3}\widehat{I} \tag{3.26}$$

The average of this ideal current squared, that would be used to find its average resistive losses, would likewise be two thirds of the square of its peak:

$$\overline{I^2} = \frac{2}{3}\widehat{I^2} \tag{3.27}$$

Therefore the average-square current may be calculated as

$$\overline{I^2} = \frac{3}{2}\overline{I}^2 \tag{3.28}$$

or, the average-square current is one-and-a-half times the square of the average current. This leads to

$$\overline{P_w} = \frac{3}{2}\overline{I}^2 R \tag{3.29}$$

where using average winding power loss $\overline{P_w}$, in place of the vector of power loss in the windings $\boldsymbol{P_w}$, within Equation 3.22, will provide an estimate of the average winding temperature. All previous calculations for resistance and back-EMF adjustments based on temperature from Section 3.2.5 are still applicable.

This equation is an approximation due to the current not conforming to an ideal rectangular shape. The extent of the error introduced is investigated in Appendix B, with the conclusion that this model produces a slight underestimate of power loss compared to a fully commutated model. An alternative piecewise linear approximation of the current waveform is also considered. This provides a slight improvement in model estimate for most of the operational envelope, however can produce an unacceptably large level of error for certain motor designs at low speed.

3.6 Control loop model

Control loop design options have been discussed in Section 2.4, for current, position and velocity control and over-temperature protection. In use as a positioning actuator a closed position loop is used to achieve and maintain a changing position demand, against a variable load force. However, control loops within models have been reconfigured to match the test conditions.

For the testing performed in Chapters 4 and 5 open-loop control is used. This uses hall sensor outputs for commutation, but not for position measurement. PWM duty ratio, or average supply voltage, is used for motor control. The use of open-loop control enables the motor models to be validated independently of any control scheme, or model thereof.

For assessing the positioning performance of a full actuator, a closed-loop control scheme is required. A general positioning control scheme is outlined in this section that may be tuned to operate in a variety of modes. A PID structure incorporating set-point weighting of the proportional and derivative terms, and back-calculation anti-windup for the integral term, is shown in Figure 3.10. The opportunity for feed-forward control based on load torque estimation is included, however the specifics of what could be provided would depend upon the signals available from the ECU, their update rate, and having a good quality model of their relationship to load torque.

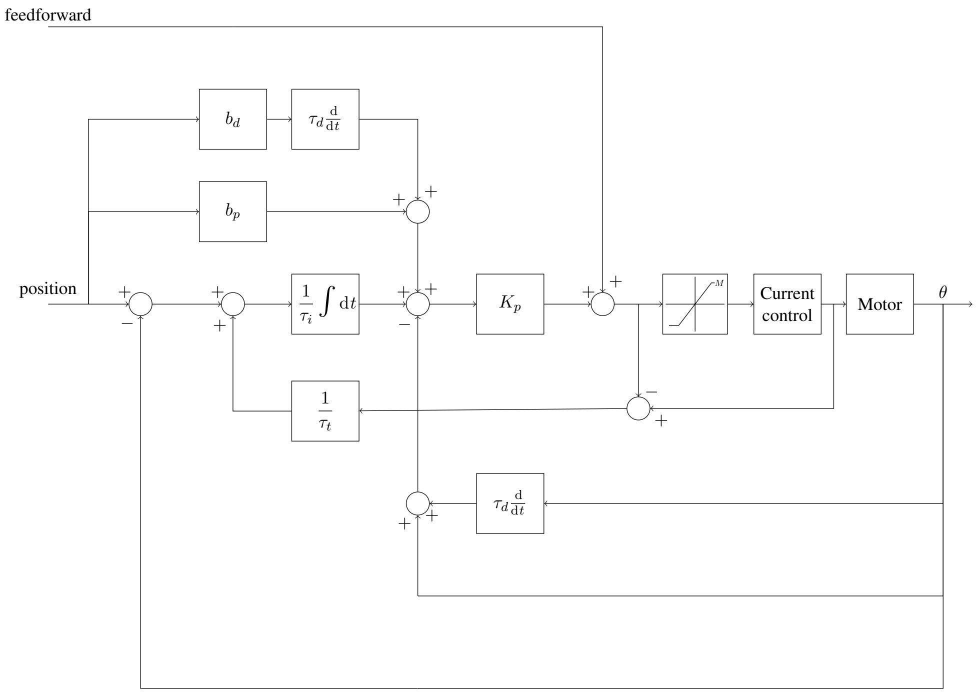

Figure 3.10: Proposed position control loop

The proposed scheme requires six tuning parameters. If the set-point weights b_p and b_d are set to unity then the loop will behave as a standard PID controller;

reducing them to zero will base the terms entirely on feedback, decreasing overshoot but also reducing sensitivity to set-point changes. The time constant for integral back-calculation τ_t is suggested to be between τ_i and τ_d; $\sqrt{\tau_i \tau_d}$ is sometimes proposed [74]. Standard PID tuning methods can be used for the K_p, τ_i and τ_d parameters [74, 94].

Current control options will depend upon the hardware being used for implementation. As discussed in Section 2.4, a straightforward method is to set the PWM output to zero when a specified current limit is exceeded, providing overcurrent protection, but not closed-loop control.

Experience during this work has shown that control loop models should incorporate the processing delays and update rates present in the hardware. These can have a significant impact on model performance and the accuracy of model results.

The implementation of this control loop within *Matlab Simulink*, for simulation and for autogeneration of microcontroller code, is shown in Appendix C.

3.7 General gear pair mechanical model

The existing *Cummins* Variable Geometry Turbocharger actuators all use a brushless motor connected through a set of spur gears. This is expected to remain as a favourable option, since the gears allow a high speed, low torque motor to drive the high torque, low speed load. Spur gears provide a robust and low-cost gearing option that produces a reasonably power-dense actuator. The following model is designed to capture the behaviour of the train of gears, to investigate their impact on overall actuator performance. It combines equations documented in previous work in the literature described in Section 2.6 to provide a generic mechanical model.

In order to build a causal model of the gear train, speed has been selected as the primary input ω_{in} on the motor side and output ω_{out} on the turbocharger side. Load torque acting on the motor side T_{in} is calculated by the model, based on the load torque presented at the turbo side T_{out}. The position of the input and output shafts, θ_{in} and θ_{out}, may be found as the integral of their speeds with respect to time.

An outline of the system model is shown in Figure 3.11. This includes all the physical effects usually associated with a mechanical gear pair, modelled using standard equations. It can be considered as an ideal input gear pair of ratio n, with no friction or mass, connected through a backlash mechanism with movement $2\widehat{\theta}_b$, stiffness K_t and damping B_t, to an output gear with rotational inertia J, viscous friction B_v, Coulomb friction B_c and efficiency B_g. An explanation of the mathematics is given in the sections below, and an implementation of this model is shown in Section C.4.

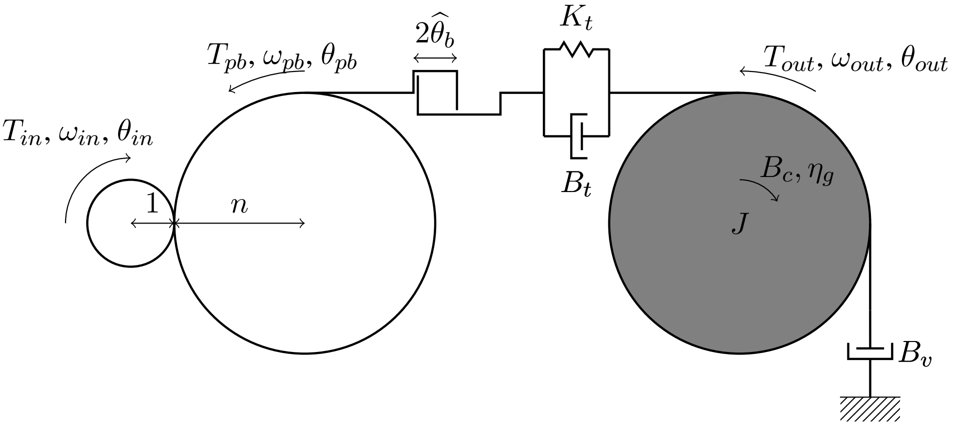

Figure 3.11: General mechanical gear pair model

3.7.1 Ratio

The gear ratio is modelled at the input and is defined as:

$$n = \frac{-\omega_{in}}{\omega_{pb}} = \frac{-T_{pb}}{T_{in}} \tag{3.30}$$

3.7.2 Backlash

The backlash model is based on that developed in [195] and laid out in [196]. If the input to this process is a 'pre-backlash speed' ω_{pb}, then the torque applied through the backlash system T_{pb}, is given by

$$T_{pb} = K_t(\theta_{pb} - \theta_{out} - \theta_b) + B_t(\omega_{pb} - \omega_{out} - \omega_b) \tag{3.31}$$

where θ_b is the backlash angle, limited to be within $\pm\widehat{\theta}_b$

$$\theta_b = \max(\widehat{\theta}_b, \min(-\widehat{\theta}_b, \int \omega_b \, \mathrm{d}t)) \tag{3.32}$$

and ω_b is its rate of change, limited thus:

$$\omega_b = \begin{cases} \max(0, \omega_{pb} - \omega_{out} + \frac{K_t}{B_t}(\theta_{pb} - \theta_{out} - \theta_b)), & \text{for } \theta_b = -\widehat{\theta}_b, \\ \omega_{pb} - \omega_{out} + \frac{K_t}{B_t}(\theta_{pb} - \theta_{out} - \theta_b), & \text{for } |\theta_b| < \widehat{\theta}_b, \\ \min(0, \omega_{pb} - \omega_{out} + \frac{K_t}{B_t}(\theta_{pb} - \theta_{out} - \theta_b)), & \text{for } \theta_b = \widehat{\theta}_b. \end{cases} \tag{3.33}$$

3.7.3 Friction

Viscous friction, occurring in the bearings of the gear, is included in the model as a speed dependent friction:

$$T_v = B_v \omega_{out} \tag{3.34}$$

Coulomb friction in the bearings, B_c, is a constant friction force opposing motion with a special case at stationary that prevents motion until the constant friction limit is reached (although this is sometimes omitted). This could be extended into a Stribeck friction model if the constant friction force is increased in the vicinity of zero speed [198]; however this will increase the nonlinearity of the model and has therefore not been pursued in this work. Coulomb friction can be included in a similar manner to the hysteresis torque in Section 3.2.3:

$$T_c = \begin{cases} T_{out}, & \text{if } B_c > T_{out} > -B_c \text{ and } \omega_{out} = 0, \\ B_c \operatorname{sgn}(\omega_{out}), & \text{otherwise.} \end{cases} \tag{3.35}$$

Similar to the hysteresis torque, the nonlinear behaviour around zero speed can be represented by a hyperbolic-tangent function, so that the scaling factor $n_{\tanh}$ may be used to trade-off the representation of the nonlinearity against simulation performance:

$$T_c = \begin{cases} T_{out}, & \text{if } B_c > T_{out} > -B_c \text{ and } \omega_{out} = 0, \\ B_c \tanh\left(n_{\tanh}\, \omega_{out}\right), & \text{otherwise.} \end{cases} \tag{3.36}$$

A clear consensus on the best method of gear mesh modelling has not been found in the literature, and detailed investigation of different methods is beyond the scope of this work; therefore a simple constant efficiency for meshing power loss has been assumed. In order to create a constant efficiency, the frictional torque must vary with the load torque. Gear mesh frictional losses are therefore defined by a gear efficiency η_g, assumed to exist in the tooth mesh and expressed as a proportion of the overall torque transferred:

$$T_g = \operatorname{sgn}(\omega_{out})|T_{pb}|(1 - \eta_g) \tag{3.37}$$

The total torque transferred to the inertia is then the sum of the torque transferred through the backlash, the torque supplied on the load side of the gear, and the torque supplied by the two frictional sources. This total torque acting upon the gear inertia J gives the acceleration of the output gear $\frac{\mathrm{d}\omega_{out}}{\mathrm{d}t}$ as:

$$\frac{\mathrm{d}\omega_{out}}{\mathrm{d}t} = \frac{T_{pb} - T_{out} - T_c - T_v - T_g}{J} \tag{3.38}$$

3.7.4 Use in models

The general model developed above may be used to transform an input speed and an output load, into an output load and an input speed, for any gear pair. With appropriate substitution of parameters (e.g. mass for inertia) the model also holds for most mechanical linkages. Gear or linkage trains may be built up through the series connection of several such models. This forms the basis of a full mechanical model of the variable geometry turbocharger actuator.

Within the motor, torque is generated electromagnetically and there is therefore no ratio, other than the scaling due to the rotor pole-pair number, or backlash present at its output. Shaft stiffness is present, however this is usually large enough that it can be neglected. The inertia and viscous and Coulomb friction effects are still present however, so Equation 3.38 is still applicable, but with T_{pb} replaced by the electrical torque produced by the motor, as given in Equation 3.17.

It is convenient to combine the frictional torques described in Equations 3.34 and 3.36, with the iron loss torques described in Equations 3.15 and 3.13, as they have an identical structure. Care should be taken with the calculation of power loss however, as this will cause heating in different areas of the machine. This is discussed further during motor parameterisation in Chapter 4.

3.8 Motor parameter sensitivity

A large number of physical motor parameters have been introduced in this chapter, all of which impact upon actuator performance. These parameters will vary considerably between designs, there may be variation between models in the same range, and there will also be variation within the same product due to manufacturing tolerances and material wear. It is important to understand the effect of these variations on the overall actuator performance, such that an optimal and robust product design is produced.

Without a specific design for investigation, it is not possible to quantitatively discuss parameter sensitivity. Different designs may exhibit markedly different sensitivities to different parameters. The models outlined in this chapter are suggested as a starting point for carrying out such an analysis once a design is proposed. Table 3.6 provides the expected impact on motor performance, in terms of the speed-torque curve, of an increase in individual parameters. Decrease in parameters will produce the opposite effect. This information has been gathered through observation of the changes in the speed-torque envelope generated by the models introduced in this chapter. It is applicable to motors with parameters similar to those of the sample motors introduced in Appendix H. More detailed discussion of the process for producing speed-torque curves, along with specific examples for the sample motors parameterised in Chapter 4, is given in Section 5.2.

Table 3.6 assumes that all other parameters remain constant. Due to the interdependency of certain parameters in motor design these suggestions should not be considered as a technique for improving motor performance, however familiarity will aid a designer in understanding the implications of small parameter changes.

If the candidate designs are all three-phase brushless motors connected through the same number of gear stages, then a model may be constructed that requires only numerical parameter changes to cover a range of different actuator designs. The con-

Table 3.6: Motor parameter effects on speed-torque curve

Parameter	Effect of increase
Resistance R	Slightly reduced no-load speed, reduced stall torque
Inductance L	Slightly reduced no-load speed, reduced performance in high-speed, high-torque region
back-EMF constant K_E	Reduced no-load speed, increased stall torque
Number of pole-pairs n_{pp}	Reduced performance in high-speed, high-torque region
Eddy current iron loss B_e	Reduction in no-load speed, reduction in continuous acceptable RMS current
Hysteresis iron loss B_h	Reduction of whole speed torque curve, reduction in continuous acceptable RMS current
Motor inertia J	No effect on speed-torque curve, but slower transient mechanical response
Viscous friction B_v	Reduction in no-load speed
Coulomb friction B_c	Reduction of whole speed-torque curve
Winding-to-stator thermal resistance $\mathcal{R}_{ws}$	Reduction in continuous torque limit
Stator-to-ambient thermal resistance $\mathcal{R}_{sa}$	Reduction in continuous torque limit
Ambient temperature $\mathcal{T}_{amb}$	Reduction in continuous torque limit, slight increase in no-load speed and decrease in stall torque
Winding temperature limit	Increase in continuous torque limit
Nominal voltage V_s	Increase of whole speed-torque curve

trol scheme tuning will need to be specific to the application or test being performed, but the general structure may be standard across different design candidates.

3.9 Summary

Initially this chapter introduced the mathematics of the motor winding model. There was then a short analytical investigation of the theoretical performance of different combinations of back-EMF shape and current waveform. A summary of the conclusions from this work is presented in Table 3.7. The six-step commutated sinusoidal back-EMF machine is likely to be most appropriate for the turbocharger actuator application due to its availability at low cost – this combination is used in the remainder of the work.

Table 3.7: Back-EMF shape and commutation summary

	Advantages	Disadvantages
Six-step commutation + Trapezoid back-EMF	Low position sensing resolution required	Small machine trapezoidal back-EMF availability/design
Sine commutation + Sine back-EMF	Low RMS line current	Increased peak line current, accurate position sensing required
Six-step commutation + Sine back-EMF	Low position sensing resolution required	Torque ripple
Sine commutation + Trapezoid back-EMF	Minimal RMS line current	Torque ripple, accurate position sensing required, small machine trapezoidal back-EMF availability/design

Further detail of mathematical models that may be used to represent actuator components has been given. In some cases alternative representations are given with different levels of complexity and fidelity. An overview of how the actuator model is constructed, and its defining equations, is given in Figure 3.12. Independent electrical, thermal and mechanical models have been developed and presented. The interaction between the thermal and electrical aspects have been outlined and the conversion of electrical to mechanical torque has been shown. This group of equations forms the complete motor model. A model of the drive electronics, a control scheme and a general mechanical model have also been presented. All of these components may be combined to produce a full time-stepping actuator model that can be used to predict the response of a design to a set of inputs, and then to assess its performance.

The mathematical models outlined in this chapter have been implemented in *Matlab Simulink*, and further details are provided in Appendix C. The purpose of developing the models is to provide tools to enable the assessment of different actuator designs. In order to use the models laid out in this chapter, a set of model parameters is required; a process for the extraction of these parameters from a set of sample motors is given in Chapter 4.

The models presented neglect magnetic saturation of the motor iron paths, losses within connectors, drive switching losses, rotor saliency effects and any windage or churning losses in the moving components. The validity of these assumptions is demonstrated in Chapter 5. Care should however be exercised in applying these models in other applications, particularly for larger or higher-speed machines. Within the validation process the difference in fidelity between models is also assessed, along with the differences in time taken for simulation.

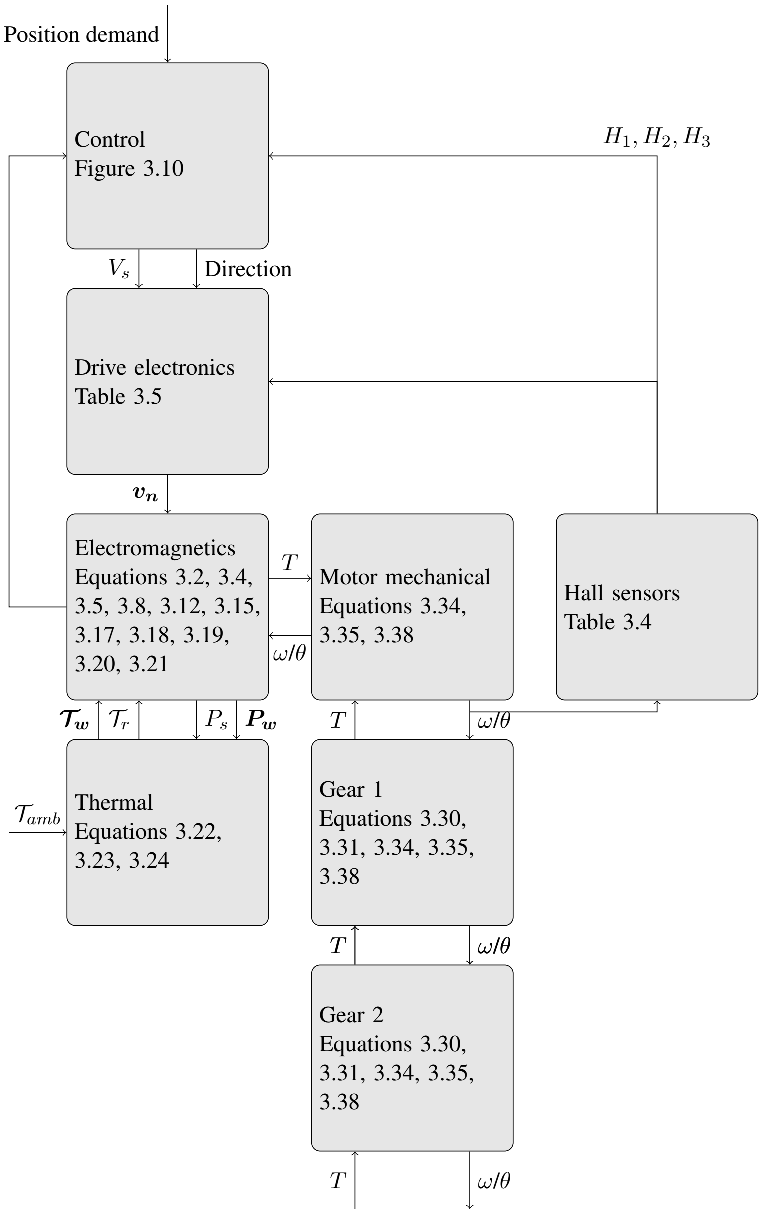

Figure 3.12: Complete actuator model construction from equations in this chapter

Chapter 4

Parameter determination

4.1 Introduction

The models developed in Chapter 3 are based on a physical representation of the system. It should therefore be possible to populate the model based on information supplied by the component manufacturers; for standard components this is usually available in datasheets or similar. In practice, datasheet information is often highly variable between suppliers, both in terms of the quantity of data supplied, and the accuracy of the figures. For certain motor parameters, such as the torque constant, there can also be variation in how the value is specified.

In order to cope with a lack of data for certain parameters, and to provide a check on the accuracy of manufacturer supplied data, this chapter provides a series of simple tests that may be performed on a sample motor in order to parameterise it.

A test facility has been constructed to test motors of the size expected to be suitable for the application, shown in Figure 4.1 and henceforth referred to as the 'testrig'. This can dynamically load the motor and allows for a range of measurements to be made. The motor under test is driven by a reprogrammable driver circuit, which allows different control and switching schemes to be tested. The design of the testrig and its measurement facilities is outlined in Appendix F.

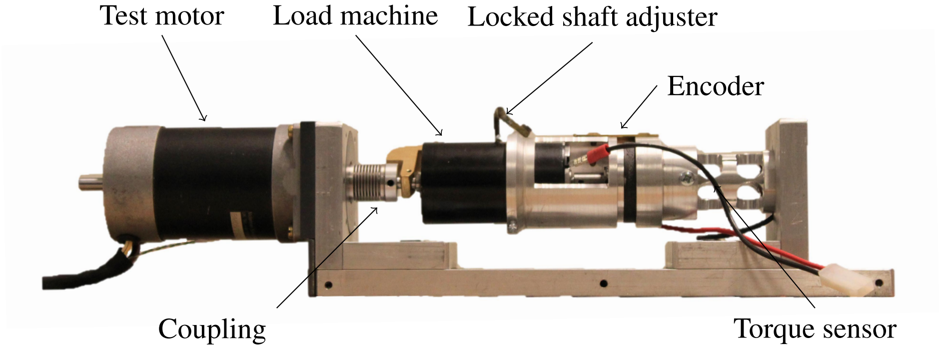

Figure 4.1: Motor testrig

A set of five different motors was used for testing. They are similar in output to those in the current generation *Cummins* actuators, but have a range of different design features. A summary of the motors used for testing is given in Appendix H. These motors are coupled to the testrig for parameter extraction and validation testing.

The set of simple tests and calculations to extract parameters are detailed in the following sections. These are split into measurement of the testrig parameters (Section 4.2), measurement of the motor parameters (Section 4.3), and estimation of gear parameters (Section 4.5). Within each section several separate tests are described to extract one or more parameters. The order of testing is unimportant as long as the ambient temperature and motor starting temperature are known in each case.

No direct testing of the drive electronics or geartrain has been performed in this work, as the focus has been on the motor and its integration with these components. However, the choice of gear parameters used in subsequent modelling is justified in Section 4.5.

The overall results of performing these tests on the sample motors are given in brackets in the tables in Appendix H, along with the datasheet parameters. Comparison between the parameters extracted from the sample motors and their datasheet values gives a idea of the level of accuracy that can be expected from motor manufacturers.

4.2 Testrig parameters

To use the testrig described in Appendix F to measure motor parameters, the basic parameters of the rig must first be measured, in order that they may be subtracted from the motor measurements. The following tests are performed without a test motor attached. Specific results for the testrig are summarised in Section F.11

4.2.1 Spin-down

The friction of the load machine may be measured by observing its deceleration with its winding open circuit, if the inertia is known. The inertia will be a combination of the load machine and any additional couplings or moving parts. A plot of the speed of the testrig decelerating against time is shown in Figure 4.2 (solid line).

The friction is assumed to consist of Coulomb and viscous components, applying a decelerating torque such that

$$J\frac{\mathrm{d}\omega_{out}}{\mathrm{d}t} = -T_c - T_v \tag{4.1}$$

where the friction torques are given by Equations 3.34 and 3.35. By fitting an exponential curve to a deceleration plot using least squares regression (shown by a dashed

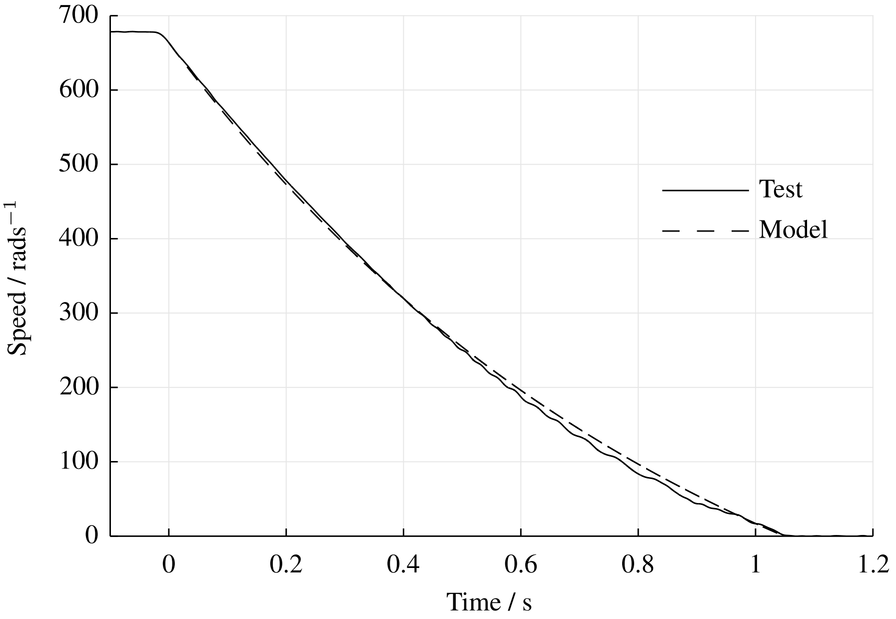

Figure 4.2: Spin-down tests on the testrig with no test motor attached

black line in Figure 4.2) parameters for the Coulomb and viscous friction constants can be found. The load machine friction is slightly greater than that seen in the test motors due to the brushes.

Equation 4.1 neglects any windage; the accuracy of the fit in Figure 4.2 shows that this assumption is valid, but it might need to be included for higher speed testing.

No explicit test is performed to separate iron loss and friction parameters for the testrig load machine. This is not an issue as iron losses are not used separately from the friction loss in any of the subsequent analysis.

4.2.2 Back-EMF measurement

By driving the load machine at a set speed (measured from the encoder) with the armature open-circuit, using one of the sample motors, the back-EMF of the load machine can be measured.

4.2.3 Starting torque

By measuring the torque required to initially start the load machine in motion, a value for the Coulomb friction in the load machine can be found. The torque constant of the load machine is known from its datasheet, and has been measured in the back-EMF test above. Therefore, by observing the current in the load machine windings when the shaft starts to rotate, the Coulomb friction may be found. This will vary with shaft position, due to brush and commutator friction. Due to this variation, the potential for observational errors in discerning the movement point, and more complex unmodelled friction effects around zero speed, the spin down method for determining Coulomb friction is considered to produce more accurate results; however similarity between results promotes confidence.

4.3 Motor electrical parameters

The following tests are used to extract electromagnetic parameters from the set of sample motors. The results of testing are shown in Tables H.4 and H.2.

4.3.1 Winding resistance and inductance

Measurement of the sample motor winding resistance and inductance were made using a standard Inductance Capacitance Resistance (LCR) meter. Connection was made across each combination of phase pairs in turn, and measurement of series resistance and inductance taken over a range of excitation frequencies. Averaging over the frequencies and combinations gives a single value that can be used for modelling. Within the motor models in Chapter 3 the self- and mutual-inductances of the motor winding always appear together as an $L - M$ term, neglecting saliency in the rotor. There is therefore no benefit in performing tests to separate them out. Winding inductance measurements suggest that saliency is low for the surface mounted magnets of all the sample motors, with variation below $10\,\%$.

4.3.2 Spin-down

As described in Section 4.2, spin-down tests may also be performed with a test motor attached. The load machine was run at a fixed speed, and then connections to both machines were open-circuited to allow them to decelerate under friction. The results of these tests for all sample motors is given in Figure 4.3 (solid lines). Fitting a curve to this using least-squares regression (dashed lines) and taking into account the motor inertia (specified in the motor datasheet), along with the testrig inertias discussed previously, gives values for Coulomb and viscous friction. Regression fit errors are typically below $1\,\%$ for the spin-down test results, however repeatability between results was found to be more significant, as indicated alongside the results in Table H.4.

The resulting friction values include testrig friction, which is subtracted as found in previous tests. They will also include contributions due to hysteresis iron loss and eddy current iron loss – in the Coulomb and viscous frictions respectively. These values are also subtracted once they have been calculated using the tests described below.

The differences between motors in Figure 4.3 highlight the different designs of the sample motors. Both *Maxon* motors have low friction bearings and the EC-Flat motor has the greatest inertia. There is a slight difference in the starting speed for the

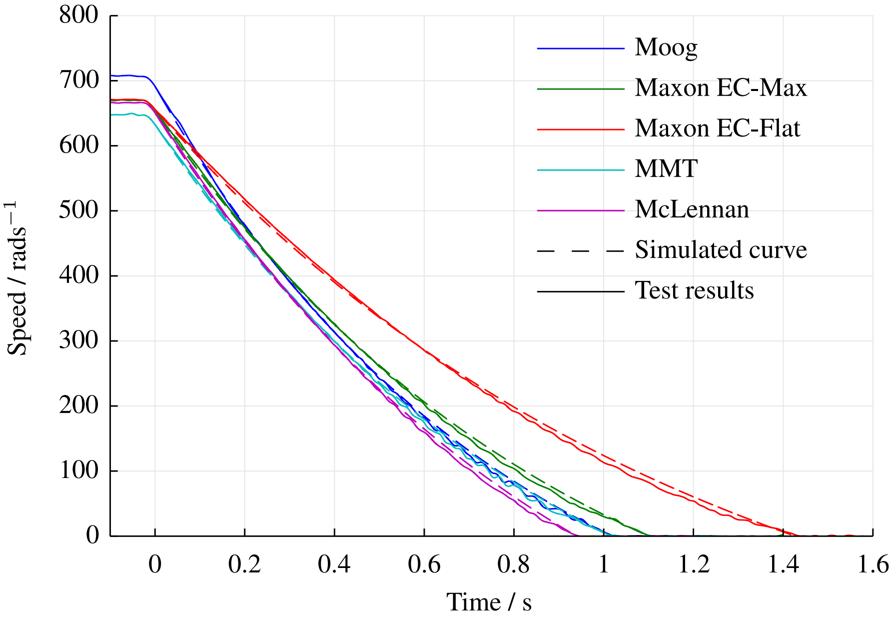

Figure 4.3: Spin-down tests for the sample motors on the testrig

tests due to a fixed voltage being used. This does not matter to the regression process used to calculate the results.

Although the test relies upon the datasheet value for motor inertia, this is easy to measure during manufacture and is unlikely to vary substantially from part-to-part.

4.3.3 Back-EMF measurement

Driving the test motor at a set speed (measured from the encoder), using the load machine, the back-EMF of the test motor (with the stator open-circuit) can be measured on an oscilloscope. This shows the shape of the back-EMF and also enables calculation of the back-EMF constant. A back-EMF waveform is shown in Figure 4.4 for a single phase of each sample motor at $420\,\mathrm{rad\,s^{-1}}$. The differences in magnitude and frequency reflect the motor back-EMF constants and number of pole-pairs.

All sample motor back-EMFs are well approximated by a sinusoid, as shown in Figure 4.5, with THD below $20\,\%$. This shows the waveforms normalised using the number of pole-pairs and the back-EMF constant. There is very little difference between them, with only slight differences in the width of the wave peak and the gradient at which it passes through zero.

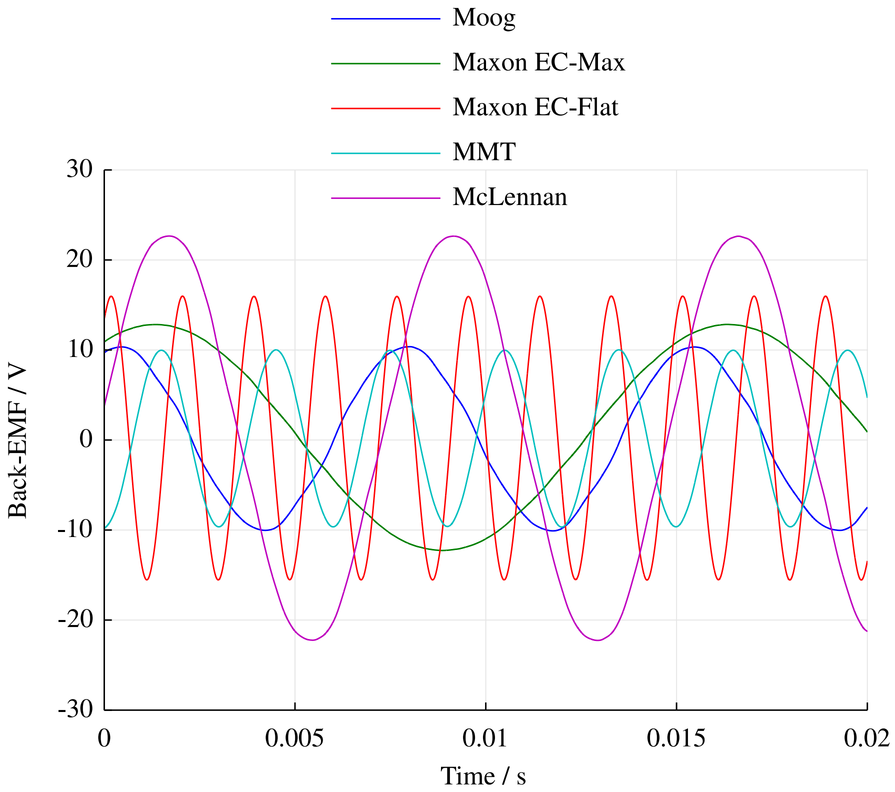

Figure 4.4: Single phase back-EMF waveforms for all sample motors at $420\,\mathrm{rad\,s^{-1}}$

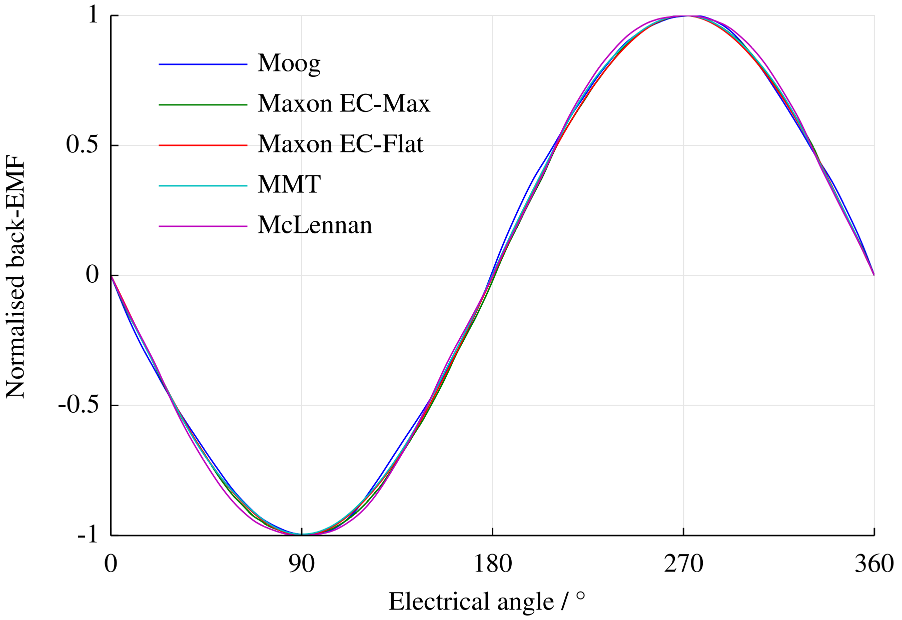

Figure 4.5: Normalised back-EMF waveform shapes for all sample motors

4.4 Motor thermal parameters

Subsequent tests propose methods for extracting thermal parameters from the sample motors, this is necessary when the full machine internal design is not available. They have been used to determine thermal parameters for the set of sample motors.

4.4.1 Stator to ambient thermal resistance calculation

An estimate of the thermal resistance between the motor casing and ambient may be gained based only on the motor external measurements and its material. This parameter will change depending on the environment and mounting arrangement. Calculating this thermal resistance provides a check on the value measured in tests below.

Heat is transferred from the stator/casing of the test motor through two different mechanisms. Firstly heat is transferred to the surrounding air through convection based on the size and shape of the motor. This assumes an ambient temperature in the surrounding air and no other air currents around the machine. Secondly the stator radiates some heat based on its colour and size. It is assumed that there is no significant conduction of heat through the end mounting, due to it being mounted through a high thermal resistance plastic adapter. If this were not the case then the thermal characterisation of the stator and casing may include the mounting within its thermal mass. Its geometry should then be taken into account in the following calculations.

Thermal conductance due to convection $\mathcal{U}_{con}$ may be calculated as [226]

$$\mathcal{U}_{con} = \frac{AN_u k}{D} \tag{4.2}$$

where A is the surface area of the stator, D is the diameter of the stator, k the fluid thermal conductivity ($0.0257\,\mathrm{W\,m^{-1}\,K^{-1}}$ for dry air at $20\,°\mathrm{C}$) and N_u is Nusselt number given by

$$N_u = 5.25(G_r P_r)^{0.25} \tag{4.3}$$

for laminar (non-turbulent) flow around a horizontal cylinder, where G_r and P_r are the Grashof and Prandtl numbers, given by

$$G_r = \frac{\beta g(\mathcal{T}_s - \mathcal{T}_{\mathrm{amb}})\rho^2 D^3}{\mu^2} \tag{4.4}$$

$$P_r = \frac{c_p \mu}{k} \tag{4.5}$$

where β is the coefficient of cubical expansion ($\frac{1}{293}$ for air at $20\,°\mathrm{C}$), g is acceleration due to gravity, ρ is the fluid density of air ($1.205\,\mathrm{kg\,m^3}$ at $20\,°\mathrm{C}$), μ is the dynamic viscosity of air ($1.85 \times 10^{-5}\,\mathrm{kg\,m^{-1}\,s^{-1}}$ at $20\,°\mathrm{C}$), and c_p is the specific heat capacity of dry air ($1005\,\mathrm{J\,kg^{-1}\,K^{-1}}$ at $20\,°\mathrm{C}$).

Thermal conductance due to radiation $\mathcal{U}_{rad}$ is given by [179]

$$\mathcal{U}_{rad} = A\sigma\varepsilon\frac{\mathcal{T}_s^4 - \mathcal{T}_{\mathrm{amb}}^4}{\mathcal{T}_s - \mathcal{T}_{\mathrm{amb}}} \tag{4.6}$$

for total radiation to general ambient, where ε is the emissivity of the stator surface (range 0 to 1) and σ is the Stefan-Boltzmann constant ($5.6704 \times 10^{-8}\,\mathrm{W\,m^{-2}\,K^{-4}}$). Note that the temperatures $\mathcal{T}_s$ and $\mathcal{T}_{\mathrm{amb}}$ should be in Kelvin.

The conductance due to convection and radiation may be combined to give the thermal resistance as:

$$\mathcal{R}_{sa} = \frac{1}{\mathcal{U}_{con} + \mathcal{U}_{rad}} \tag{4.7}$$

These equations show that the thermal resistance varies with motor temperature. This could be incorporated into the motor models by using a interpolated lookup table rather than an absolute resistance value; however, taking the average value around the expected operating temperature of the actuator is sufficient for the simple thermal model used in this work. The split between convective and radiative heat transfer depends heavily on the value of emissivity for each motor. The sample motors are predominantly either painted matt black (*Moving Magnet Technologies* (*MMT*) and *McLennan* motors) or polished stainless steel (both *Maxon* motors and the *Moog* motor), these have been given the emissivity values of 0.9 and 0.1 respectively [227].

An example of the split between the two calculated thermal conduction mechanisms is given in Figures 4.6 and 4.7 for the *MMT* and *Moog* motors at a range of motor temperatures and an ambient temperature of 20 °C. These show the significant difference the body material makes to the radiative resistance and how this influences the total thermal resistance.

A comparison of total thermal resistances to ambient for all sample motors is shown in Figure 4.8. Note that due to the *Maxon* EC-Flat motor having an external rotor and an internal stator, with the stator mounting face being against the high thermal resistance plastic, the above analysis applies to the rotor-to-ambient thermal resistance rather than the stator-to-ambient resistance; however the lumped thermal parameter proposed in Section 3.3 assumes these to be the same.

4.4.2 Static torque and thermal parameters

With the motor initially at room ambient temperature (around 20 °C), and with the rotor locked at a position of peak torque (found during the previous back-EMF tests), a fixed DC current is injected through two windings from a controlled current source – producing a torque against the torque sensor. The current and the initial measured torque are used to calculate the torque constant. The result of this test is shown in the measured torque constant values of Table H.4. These are lower than the measured back-EMF value for all the motors, due to higher-order effects in the motor, such as the current altering the net magnetic field or local saturation around the stator tooth

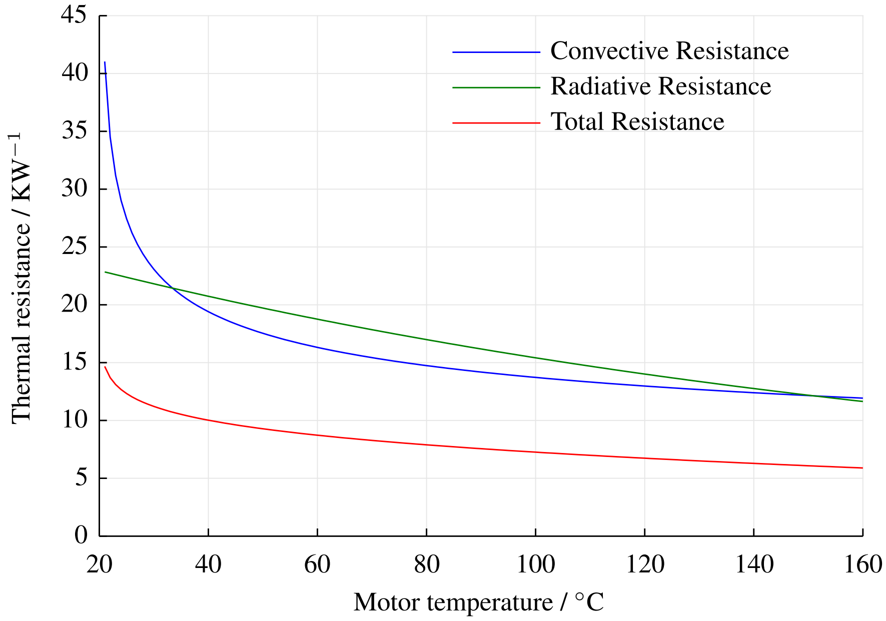

Figure 4.6: Thermal resistance stator to ambient due to different mechanisms in the *MMT* test motor, black $\varepsilon = 0.9$

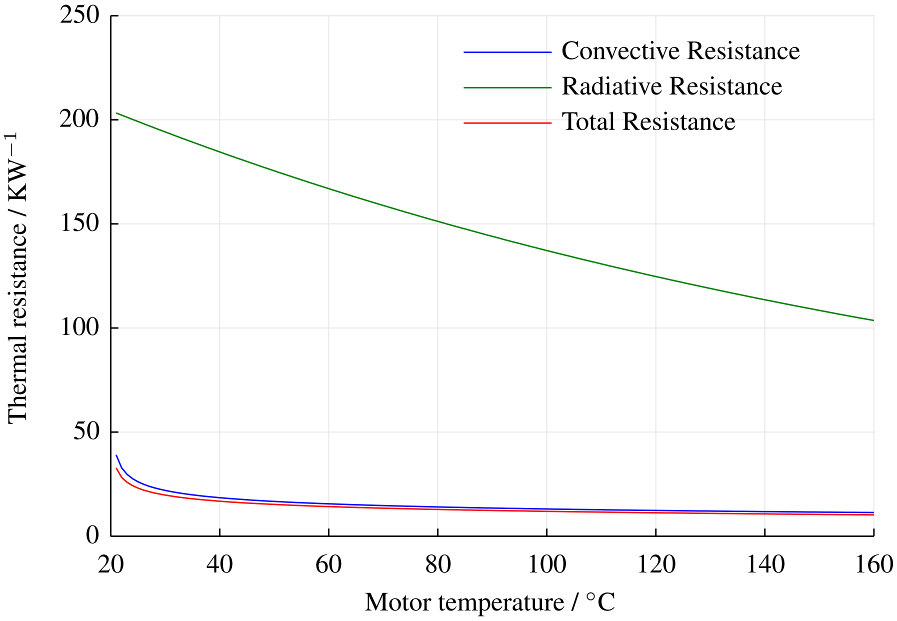

Figure 4.7: Thermal resistance stator to ambient due to different mechanisms in the *Moog* test motor, polished steel $\varepsilon = 0.1$

affecting the torque. Minor detent torque effects are also not taken into account. Torque sensor measurements are generally more susceptible to noise and drift than oscilloscope voltage measurements, and therefore the back-EMF value has been used within the models.

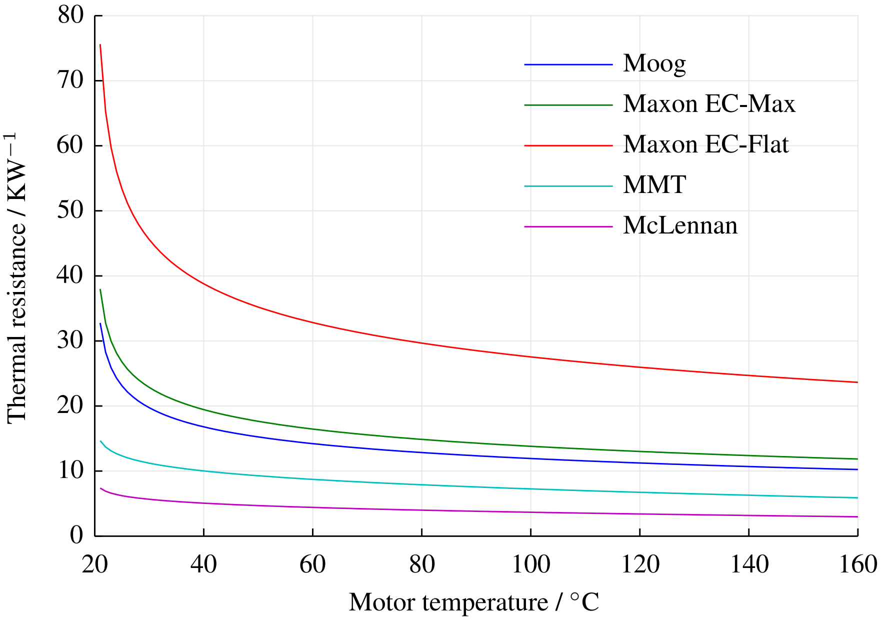

Figure 4.8: Total thermal resistance to ambient for all sample motors

The testrig is left in this configuration for an extended period (several hours) to observe the effects of heating caused by Joule losses in the windings. Regular measurements from a thermocouple mounted on the motor stator show the change in stator temperature over time. The voltage at the motor terminals, maintaining the fixed current in the windings, may be used to calculate the resistance of the two energised windings. The change in this resistance over time shows how the windings heat up through the test, according to Equation 3.18.

The measured torque is expected to decrease during the test, as although the current in the winding remains fixed, the rotor undergoes reversible thermal demagnetisation as it heats up. The measured torque may be used with Equation 3.19, and a knowledge of the rotor magnet material, to estimate the rotor temperature. All motors were assumed to use NdFeB magnet material with a temperature coefficient of $0.001\,\mathrm{N\,m\,A^{-1}\,°C^{-1}}$, however some variation in this value might be expected with material grade [228] – which was not known.

The temperature changes for the *MMT* motor during this test are shown in Figure 4.9, based on logged values from the stator thermocouple, winding voltage and torque sensor. The steady increase in the temperature of all three components to a new equilibrium is evident. This is typical of the sample motor results. The rotor temperature is generally cooler than the stator temperature for this test, between $5\,°\mathrm{C}$ to $10\,°\mathrm{C}$ for four of the motors. The only exception being the external rotor machine, in which the rotor was $4\,°\mathrm{C}$ hotter than the stator.

The *MMT* motor also has temperature sensors within two of its windings. The measurements from these, included in Figure 4.9, show good agreement with the

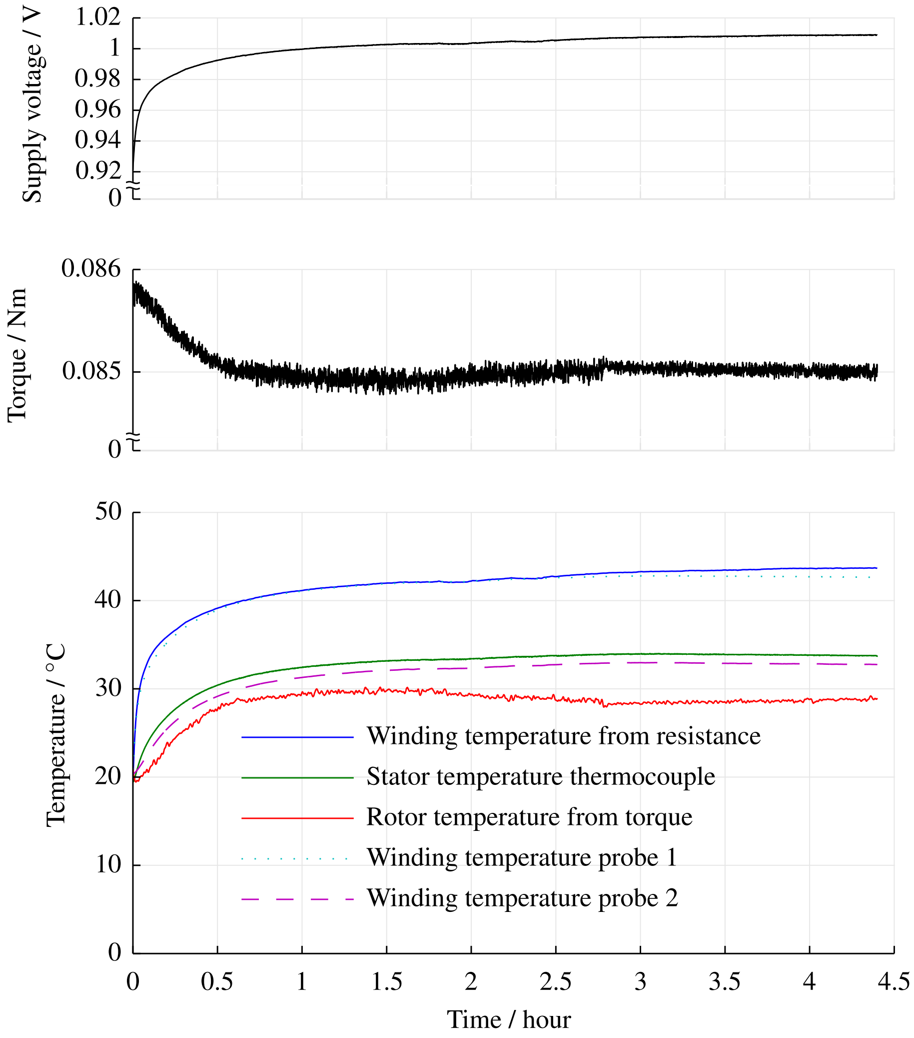

Figure 4.9: Conditions during static torque tests of the *MMT* test motor

resistance-based temperature measurements. Slight differences are expected due to the fact that the probes are separated from the windings by the potting compound, and because the resistance measurement provides an average temperature over both windings, whereas they would be expected to have a slightly varying temperature distribution across them, with some hotter and cooler areas. It can be seen that one winding probe is within 1 °C below the calculated temperature and the other shows a temperature 2 °C below the stator measured temperature – as this is the non-energised winding.

The power loss causing the winding heating is calculated from the fixed current and the measured supply voltage (using Equation 3.20), and increases as resistance rises throughout the test.

Values for the thermal parameters may be calculated from the results of this test. The thermal resistances between components may be found from the steady-state temperatures that each component reaches after the test has settled to a new equilibrium point. This may be performed analytically by substituting parameters into the equations given in Section 3.3, under steady-state conditions.

The values of thermal capacitance may also be estimated analytically, by assuming the power loss is constant and treating the temperature rises as a first-order system. An alternative approach is to start with initial estimates and simulate the response of the thermal system using the measured power loss as an input. The error between the simulation output and the real test results may then be used to drive a gradient descent process to estimate the values of thermal capacitance. The outputs of the thermal model from Section 3.3 using these parameters is compared against the test results in Figure 4.10. As the model parameters have been fitted to these results, the steady-state temperatures match to within the measurement noise; the errors during the rise period demonstrate the lack of flexibility in the low parameter modelling approach used. Full validation of the thermal models and parameters is given in Chapter 5.

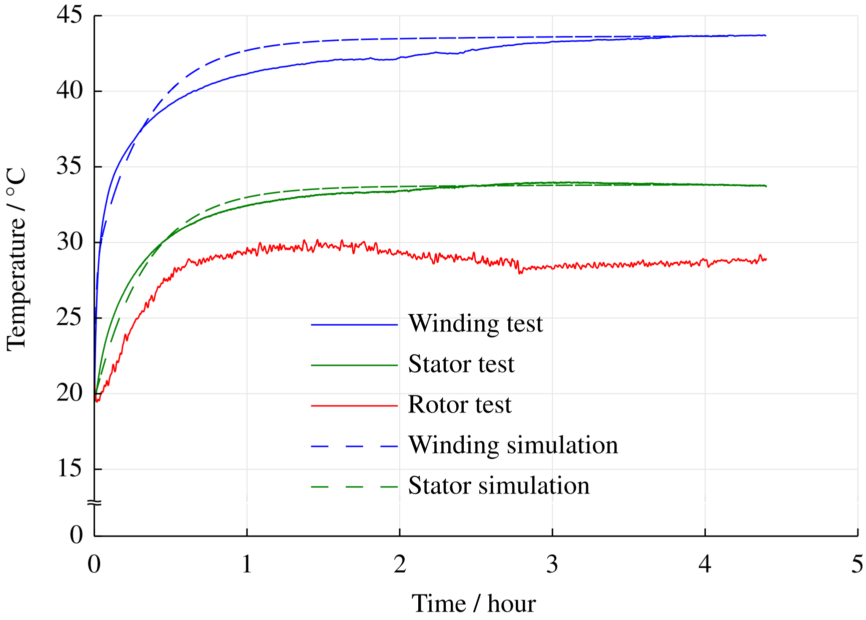

Figure 4.10: Simulated and measured static torque test temperatures for the *MMT* test motor

4.4.3 Stator loss

In the previous static tests the power losses were introduced into a stationary machine through Joule losses in the windings – this has provided all the parameters required to populate the thermal models. However there is another mechanism for introducing heat into the motor, as shown in Figure 3.7; this is through iron losses generated in the stator. These losses are proportional to speed and therefore only occur in dynamic tests. The thermal model outlined in Chapter 3 assumes that iron loss contributes to motor heating, but that the frictional losses do not, with heat being lost down the motor shaft, or directly to ambient. Therefore a test is required to separate the iron loss parameters from the frictions extracted in the spin down tests described above. This assumption is unlikely to be true, however by extracting parameters in a manner that matches the model, the proportion of frictional losses that do contribute to heating are included with the iron loss parameters and therefore modelled correctly. Consequently the split between iron loss and friction may differ from values found using theoretical techniques or independent testing and they should not be compared in this way.

By driving the test motor at a fixed speed using the load machine, with the test motor windings open circuit, the only losses occurring in the motor should be due to iron loss; therefore by logging the temperature sensor outputs (stator thermocouple and winding probes where available) over an extended period (several hours) the heating caused by this power loss can be measured. An example of the motor temperatures logged over a period of driving the motor at $658\,\mathrm{rad\,s^{-1}}$ is shown in Figure 4.11.

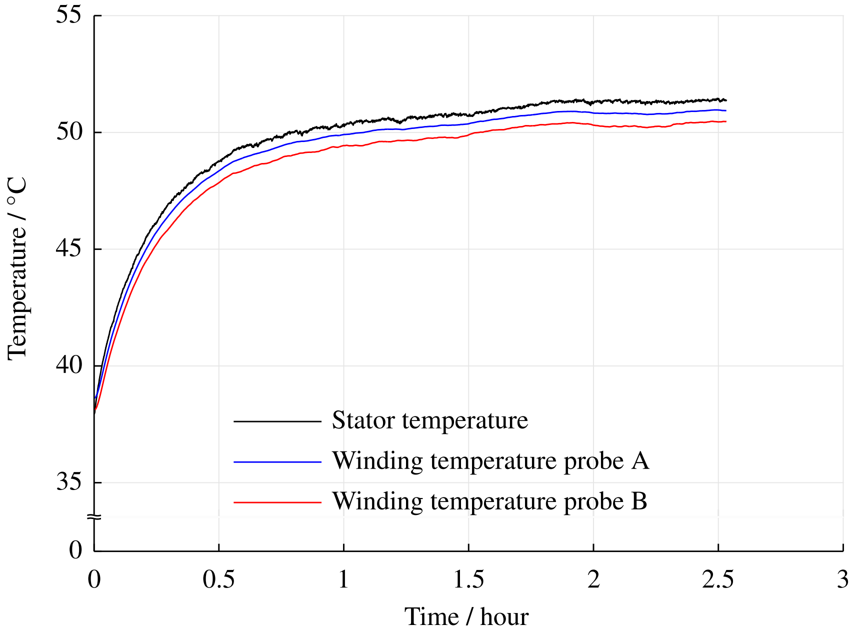

Figure 4.11: Stator loss test temperatures for the *MMT* test motor

A clear temperature rise to a new steady-state is shown. This new steady-state temperature difference (from ambient) can be used, along with the thermal resistance parameters found previously, to calculate the amount of power loss occurring in the stator. Repeating this experiment at a range of different speeds shows a relationship between speed and power loss that characterises the iron losses. This relationship is shown in Figure 4.12, where the dashed line shows a regression fit to find the hysteresis and eddy current components using Equations 3.12, 3.15 and 3.21.

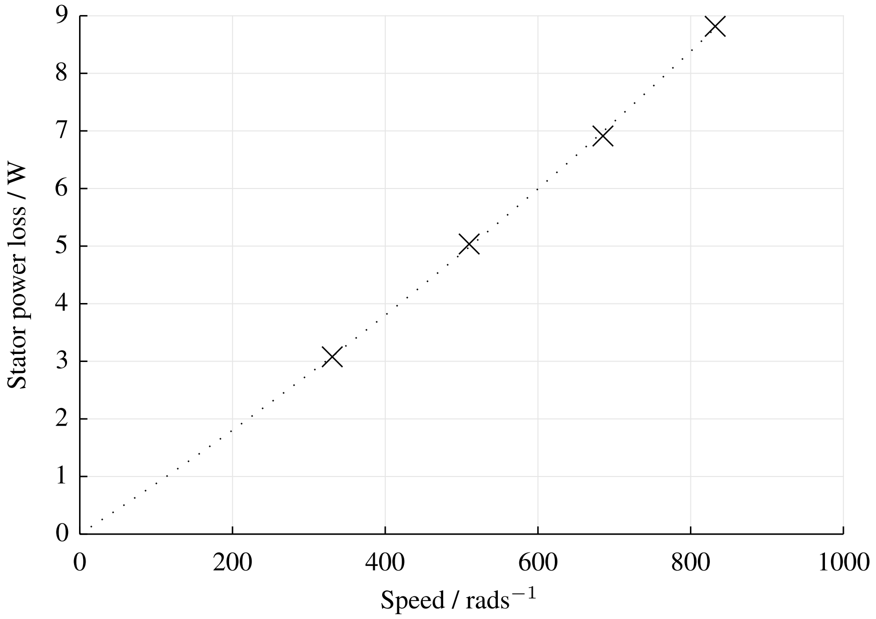

Figure 4.12: Stator loss power to speed relationship for the *MMT* test motor

Due to the duration of the experiment required for each point in this curve, it is not practical to generate a large number of points; the error in the regression fit is therefore typically quite large, particularly for the eddy current losses.

The rise time for each of these tests is also used to recalculate the thermal capacitance of the stator. This allows revision of the estimate made during the static torque test above. The results presented in Table H.2 for thermal capacitance are an average of both techniques, which typically give similar results – as indicated by their measurement error.

The results of performing this test on the sample motors is shown in Table H.4. In all cases the hysteresis loss constant came out as larger than the total Coulomb friction (when the friction in the testrig had been subtracted). As the spin-down test is expected to be more accurate, it is assumed that all of these losses contribute to heating the stator. The viscous friction parameter is generally 5 to 20 times larger than the eddy current parameter. For the *Maxon* EC-Max motor the eddy current losses were found to be negligible.

4.5 Gear parameters

The mechanical model proposed in Section 3.7 requires a set of parameters for simulation, these have been specified based on details provided by *Cummins* and the suppliers of their current actuator products. A full parameterisation of the gear train in the model is beyond the scope of this work.

Table 4.1 provides typical values for use in spur gear simulations for the turbocharger actuator. These are all specified at the output of a single stage, as shown in Figure 3.11. This should be considered when comparing against datasheet or other values, as it is common to ‘refer’ parameters through a multi-stage system to the overall input or output point. Parameters such as backlash will also appear much larger if considered at the input of a speed reducing gear.

Table 4.1: Suggested gear train parameters for turbocharger actuator simulation

	Typical value	Comments
Gear ratio n	1 to 5	Higher ratios decrease efficiency
Bearing viscous friction B_v	5 to 15 $\mathrm{\mu N\,m\,s\,rad^{-1}}$	Similar to motor roller bearing values
Bearing Coulomb friction B_c	1 to 10 $\mathrm{mN\,m}$	Similar to motor roller bearing values
Gear mesh efficiency η_g	95 to 99 $\%$	Typical values for spur gears
Gear backlash 2α	0.4 $^\circ$	Testing performed at *Cummins*
Gear tooth stiffness K_t	1000 $\mathrm{kN\,m\,rad^{-1}}$	Estimate to allow efficient simulation
Gear tooth damping B_t	10 $\mathrm{mN\,m\,s\,rad^{-1}}$	Estimate to allow efficient simulation
Gear inertia J	$0.02\,\mathrm{g\,m^{-2}}$	Average existing product

4.6 Summary

This chapter has proposed a set of tests for parametrising motor models using the test hardware detailed in Appendix F. Results are presented for five sample motors in Appendix H. The identified parameters are generally similar to those provided in the manufacturer datasheets, although some differences are discussed below.

A complete datasheet was not available for the *McLennan* motor. The significant difference in torque constant and winding resistance found when measuring this motor indicates that the test motor is a different specification from the datasheet.

Very few datasheet parameters were supplied relating to motor friction parameters. It is assumed that the Coulomb friction parameter provided for the *MMT* motor includes a contribution due to hysteresis iron loss, in which case the value obtained from the spin-down test is very similar.

Back-EMF measurement is suggested as a more accurate method of obtaining the torque constant than static torque testing – which produced universally lower figures. In all cases, except for the *McLennan* motor discussed above, the back-EMF constant was found to be slightly above the manufacturer specified value. This may be due to conservative estimates being used by the manufacturers, or differences in the method by which the constant is specified. For example, the *MMT* constant is specified as the minimum torque generated in the ripple waveform produced by six-step commutation.

Winding resistances and inductances were largely similar, for all except the flat motor inductance; the reason for the difference in this value is unknown.

Thermal parameters are generally difficult to measure, however a simple test for assessing thermal resistances and capacitances has been proposed. The equations for calculation of stator-to-ambient thermal resistance have also been presented. It is clear from comparison of the thermal resistances presented in Figure 4.8 and the second column of Table H.2 that the calculations suggest a higher resistance. This is expected, since they do not take into account heat loss from the end of the machine (to ambient), the mounting face of the machine (to the plastic mount) or down the rotor shaft (to ambient and the motor coupling). These would all contribute to lowering the calculated values, however they would also increase the complexity of the calculation. In general the calculated values overestimate the measured values by around three or four times, and the ordering of the motors is similar. Calculation is therefore suggested as an good technique to provide an initial estimate of thermal resistance, prior to testing or where a sample motor is unavailable.

Measurement of thermal resistance is straightforward through investigation of steady-state temperature differences when power loss is known. Improved estimates might be achieved through repetition of this test for different levels of power loss.

Thermal resistance may be specified in the motor datasheet, either for the whole motor or, in some cases, for the winding and body separately. Measured values were of a similar order-of-magnitude, but varied significantly from the datasheet values. This may be due to differences in the way they are specified or the point at which they are measured on the machine.

Thermal capacitances may be estimated if the datasheet provides both a thermal resistance and a thermal time constant. In most cases these were similar to those derived from testing. This is to be expected, since the thermal capacitance depends upon the volume of material, which is well-defined.

Based on these findings, sample motor testing is advised as the ideal method of parameterising models, however if a sample motor or test facility is unavailable then they may be requested from the supplier; however it is important to also agree how they are defined.

Similar processes might be developed to parameterise and validate the mechanical gear models proposed in Section 3.7, but would require a specialised testrig to support this. Parameters for use in mechanical models, in lieu of complete testing, have been obtained from *Cummins*.

Chapter 5 uses the parameters extracted from the sample motors, along with further motor tests, to validate the overall motor models.

Chapter 5

Model validation

5.1 Introduction

In Chapter 3 a full mathematical actuator model is developed and some options for varying model fidelity are given; a specific implementation of these models is shown in Appendix C, and an acausal model with similar functionality is described in Appendix D. A series of tests is outlined in Chapter 4 to parameterise the models using measurements from a sample motor. In order to gain confidence that both the models and the parameters extracted provide a good representation of the real system, this chapter undertakes a validation process, using the sample motors listed in Appendix H as test subjects. The validation indicates how representative of the final system the models are, in terms of the level of error expected in their results.

Due to the differences in time constant between the electromechanical and thermal domains, the validation has been divided into three sets of tests. In Section 5.2 the steady-state performance of the mechanical and thermal aspects of the models is addressed through comparison of speed-torque curve data. This compares the speed and winding temperature achieved in simulation against both test results and datasheet parameters. This does not include any model differences due to mechanical inertia or thermal capacitance, however electrical inductance effects are included due to the commutation required to maintain rotation.

Mechanical inertia and nonlinear effects are then considered by investigating the mechanical frequency response of the system in Section 5.3. These tests do not include thermal variation due to the significant time period that would be needed to excite the thermal system at a fixed frequency. Transient thermal model validation is carried out in Section 5.4, by varying the load and duty profiles over an extended period. For all tests the testrig outlined in Appendix F is used.

Not included in this work is a thorough validation of the transmission aspects of the models. This has not been performed for the following reasons: spur gear trains are well understood and there is little variation between designs; the spur gear train, although a significant part of the actuator construction, is not expected to be the defining aspect; gear train testing is non-trivial, requiring specialist test equipment. Future work could include the construction of a test facility to assess this. Suggestions for tests that might aid in the validation of a full actuator transmission were provided in Section 2.6.

5.2 Speed-torque validation

The concept of speed-torque curves was introduced in Section 2.3.5. These may be provided as a plot in a motor datasheet, or several key points on the curve may be provided. It is important to note that no speed-torque performance parameters are used to parameterise the models in Chapter 3, and therefore their use within a validation process for those models is reasonable.

Speed-torque curves may be generated for a machine under either fixed thermal conditions, in which the temperature of all machine components remains at ambient, or at thermal steady-state, where the components have heated to an equilibrium. The first case is normal for motor datasheet specfications, however it is difficult to achieve in testing. Measurements may be taken as soon as the motor has reached a steady-state speed – which, for low load tests, is typically before significant self-heating has occurred. At higher loads there will be a larger current, and Joule losses will cause much more rapid heating. The second case may be more instructive for the actuator designer concerned with high temperature operation, as the steady-state winding temperature, along with the winding temperature limit, is generally what sets the continuous working point of the machine. For both types of speed-torque curve the ambient temperature is important, as it will have an impact on the curve produced. Although all testing has taken place in $20\,^{\circ}\mathrm{C}$ to $25\,^{\circ}\mathrm{C}$ ambient conditions, and these are also the typical conditions used in motor datasheets, simulated results are also presented for $155\,^{\circ}\mathrm{C}$ conditions, as these are at the limit of most motors' winding specifications.

Figure 5.1 shows a comparison of datasheet and model performance for fixed thermal conditions for the *MMT* sample motor; also included are results from testing the sample motor at thermal steady-state. The blue and green curves are from the computationally efficient model and show the effect of temperature, with the decreased back-EMF constant and increased winding resistance at $155\,^{\circ}\mathrm{C}$ producing a slightly faster no-load speed but a considerable reduction in stall torque. The full model results would be exactly the same as the efficient model, however a delay of $0.11\,\mathrm{ms}$ has been introduced into the hall sensor feedback to replicate processor delays measured in the real system. This reduces the peak speed capability of the system, although it is similar at lower speeds. In all speed-torque curves presented in this work the current axis is generated from the model results. Measurements from the real system show similar currents, although they are not directly comparable as an average measurement was not available due to the high sample rate and memory required to log time-varying currents with sufficient resolution.

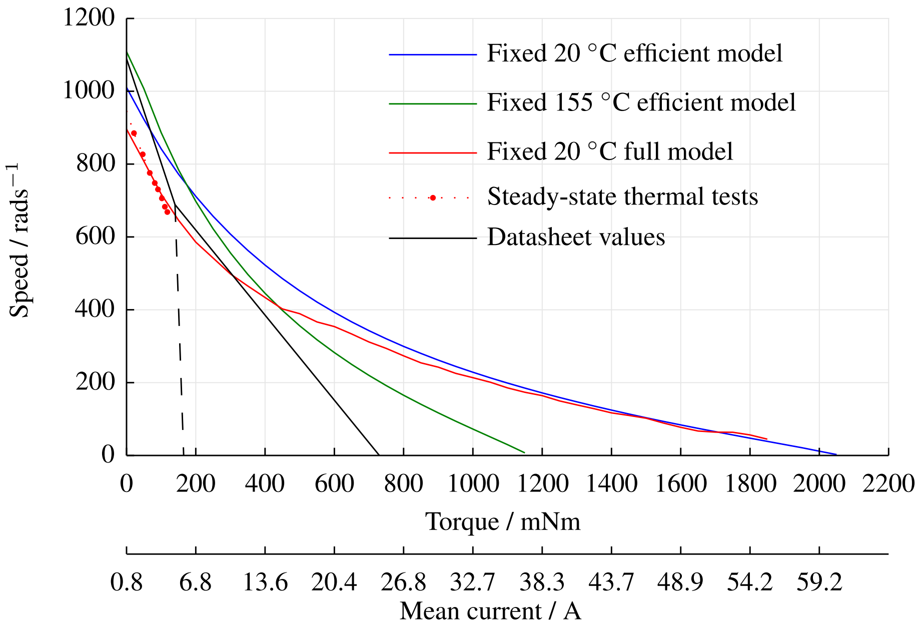

Figure 5.1: Speed-torque curve for fixed temperature simulations, datasheet and steady-state test values for the *MMT* motor at 24 V

The datasheet values appear conservative for the continuous load/speed case, based on the suggested performance from the models, however drive circuits with a reduced processing delay were not available to investigate whether these performance improvements could be realised.

A similar situation occurs for the *Maxon* EC-Flat motor in Figure 5.2. In this case the datasheet continuous duty area is very well matched by the model for 20 °C conditions. The intermittent duty area above peak continuous torque will vary depending on the manufacturer's assumptions about usage. It is reasonable for the manufacturers to have assumed some heating of the machine when operating in this region, therefore the datasheet stall torque is below that theoretically achieved by the models at 20 °C for all machines.

As both the *MMT* and *Maxon* EC-Flat machine have a relatively high number of magnet pole-pairs, they exhibit the greatest curvature in their speed-torque curves. They are also the most affected by the delays in hall sensor processing, lowering their peak speed. They may be compared against the *Maxon* EC-Max motor in Figure 5.3, where all curves at the same temperature are very close. Results for simulation of the *McLennan* and *Moog* machines are very similar, however complete data for the datasheet and from testing was not available for them respectively.

The test measurements for all the above cases are similar to those from the fixed temperature full model at low load, but trend away slightly as load increases. This is

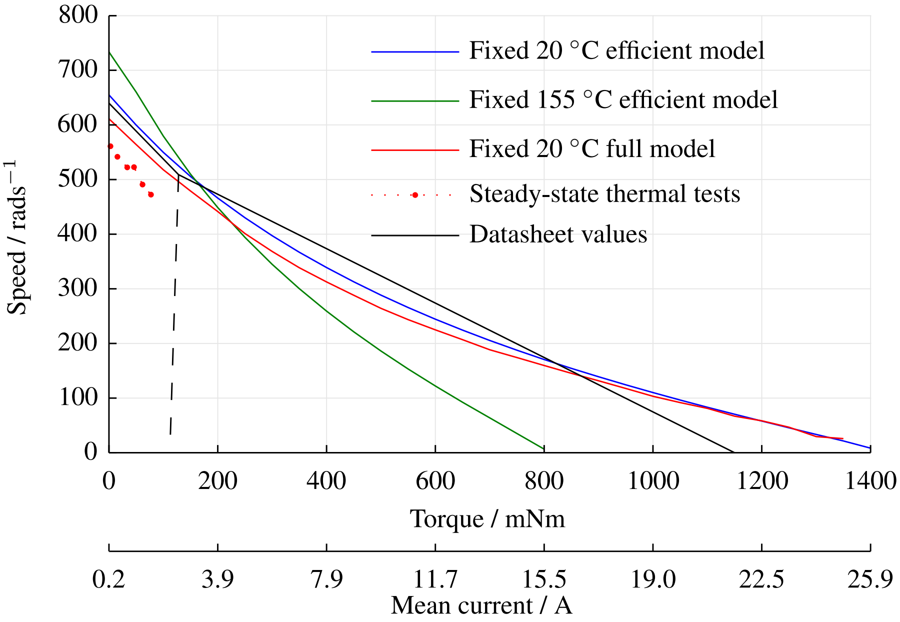

Figure 5.2: Speed-torque curve for fixed temperature simulations, datasheet and steady-state test values for the *Maxon* EC-Flat motor at 24 V

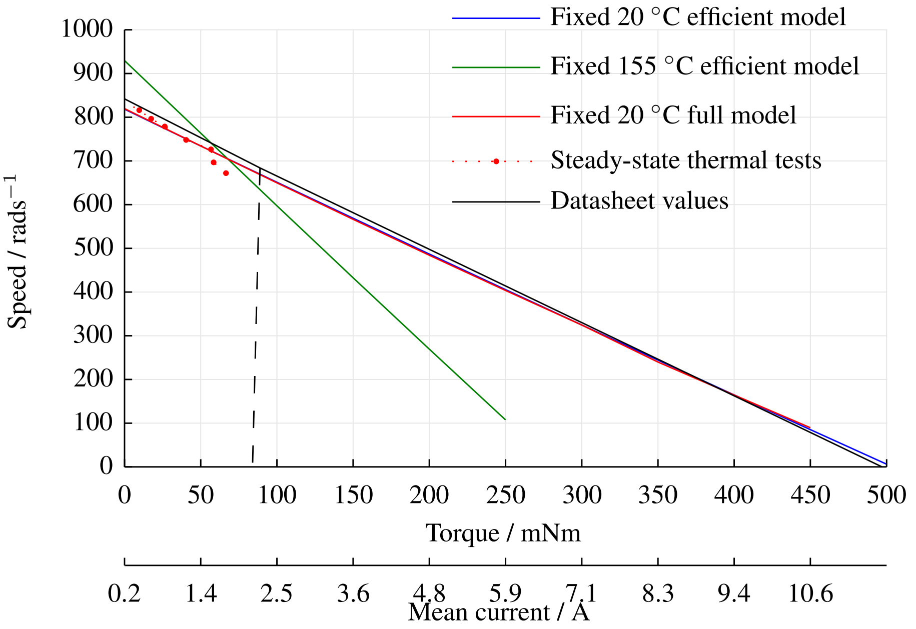

Figure 5.3: Speed-torque curve for fixed temperature simulations, datasheet and steady-state test values for the *Maxon* EC-Max motor at 24 V

due to the operating temperature of the machine increasing, and the curve steepening – similar to the change seen in the efficient model results. This is investigated further in Figure 5.4 for the *MMT* motor, where the efficient model has been run until thermal steady-state conditions are reached for each point.

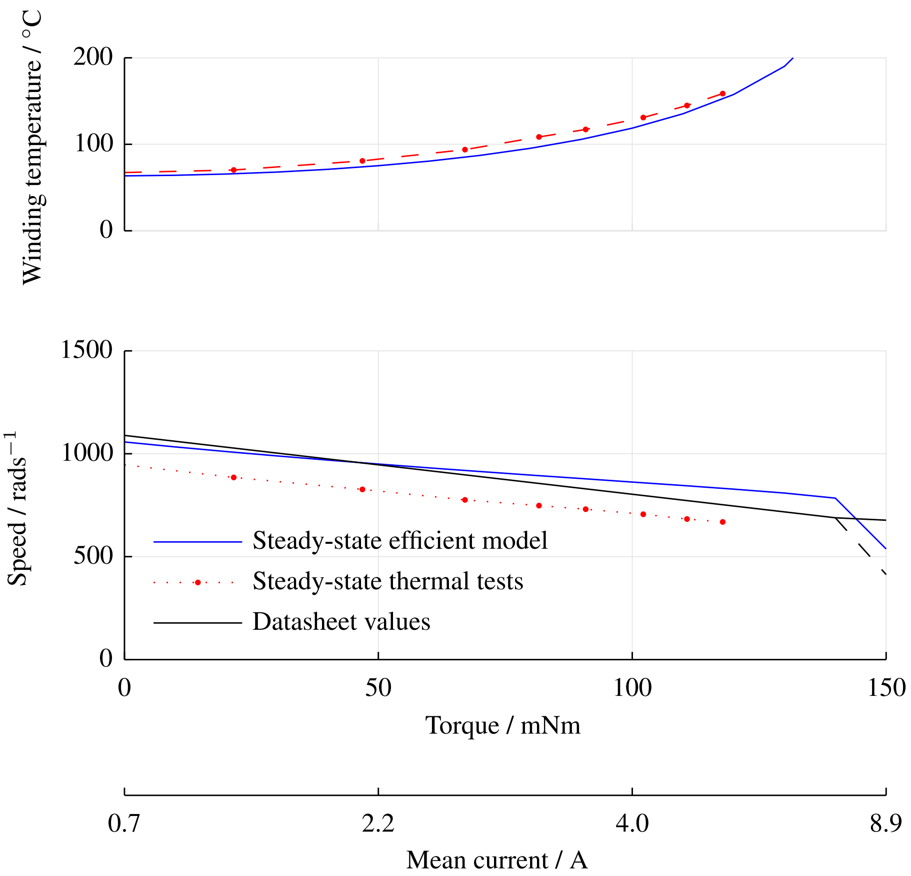

Figure 5.4: Speed-torque curve for steady-state temperature simulations, datasheet and test values for the *MMT* motor at 24 V

The simulated winding temperature shows a good match to measurements from the winding temperature sensors, although as previously, the speed is an over-estimate due to hall sensor delays not being included in the efficient model. The full model could not be run to steady-state thermal conditions as the required simulation duration was prohibitive. It is expected that results would show a similar trend, but with a closer fit in speed. For this motor the winding temperature limit is 150 °C, after which point further load increases were not made. These results show that operation at the datasheet continuous load point, under recommended ambient conditions, results in the winding temperatures exceeding their specified limit; this was the case for all the motors tested.

The *Maxon* EC-Flat results are shown in Figure 5.5. The winding temperature readings for this machine were calculated based on measurement of the winding resistance during brief disconnection from the supply. This model also shows a close thermal match and an overestimate of speed due to not including the hall sensor delay. Unfortunately a test point near the winding temperature 125 °C was not obtained as the next step up in torque caused irreparable damage to the windings.

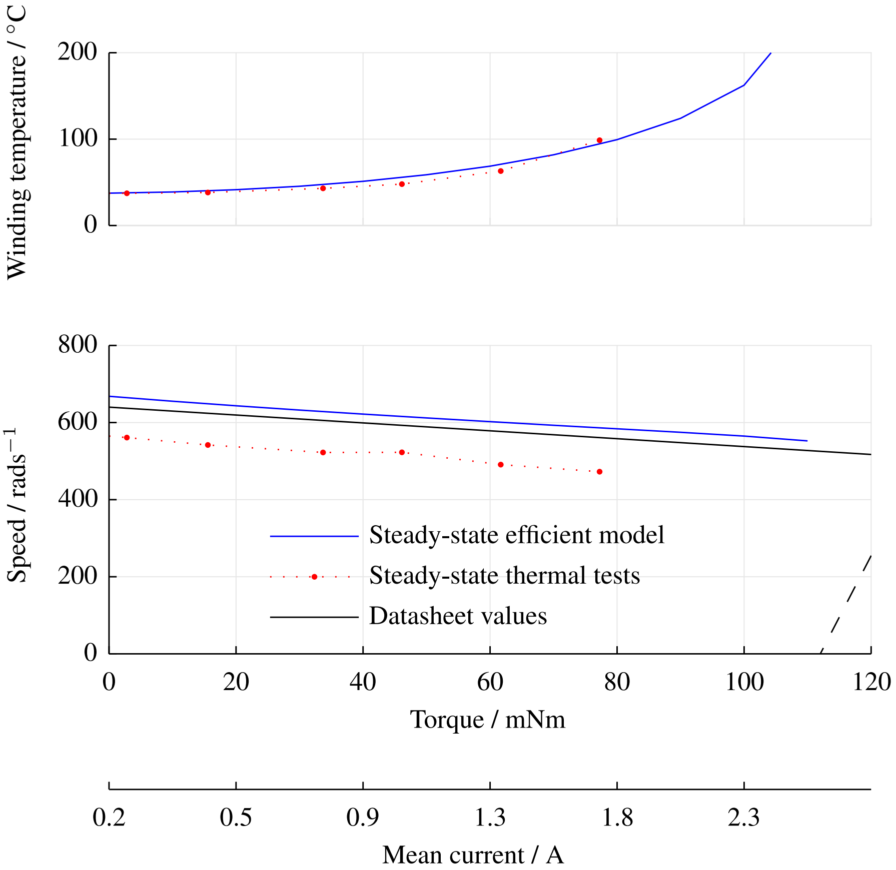

Figure 5.5: Speed-torque curve for steady-state temperature simulations, datasheet and test values for the *Maxon* EC-Flat motor at 24 V

Closer speed matches are seen in the other motors; an example for the *McLennan* motor is shown in Figure 5.6. Due to the larger size and torque capacity of this machine, it was not possible to test it up to its thermal limit with the equipment available.

As discussed in Section 2.3.5, it is common for datasheets to supply no-load, continuous and stall current details. These are often displayed as a current axis below the torque axis, and that convention has been followed within this thesis; however, it is important to note that the relationship between torque and current is not necessarily linear – although this is a reasonable first approximation. Nonlinearity is introduced through the mismatch in back-EMF and current waveforms, and therefore a curvature is introduced in the same manner as for the speed-torque relationship, dependent upon the commutation angle and the electrical time-constant of the windings. The nonlinearity is increased if thermal effects are also considered, as temperature increases – and therefore back-EMF constant decreases – with torque. Where a mean current axis has been presented it should be treated as indicative only, and is correct only for the first set of data presented on the speed-torque curve, as shown by the order of the legend entries.

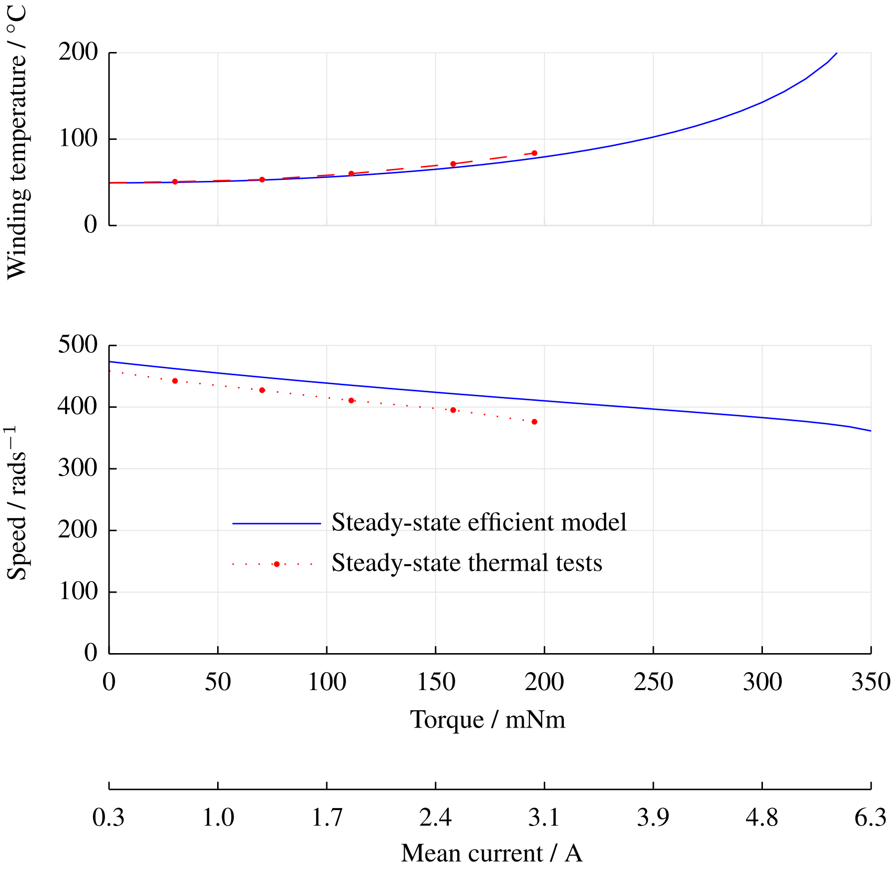

Figure 5.6: Speed-torque curve for steady-state temperature simulations and test values for the *McLennan* motor at 24 V

5.3 Electromagnetic/mechanical model validation

In order to assess model validity during mechanical transients, a frequency response has been generated both from the models and the sample motors. The motors on the testrig were stimulated with a low frequency sinusoidal variation in duty ratio and the speed response recorded by observing the open circuit voltage generated at the load motor terminals. No control feedback was used, except for the hall sensor feedback required to electronically commutate the machine. The voltage input to the sample motor was synthesised using a 24 V supply and a sinusoidally varying duty ratio from -0.5 to 0.5. This gives motor terminal voltage limits of ± 12 V, selected as a compromise between difficulty in measuring small signals and seeing large signal distortions in the results. Centring the sinusoid around zero and exerting no additional load ensures that the motor speed tends to stationary at high input frequencies. The load machine open-circuit voltage was recorded on an oscilloscope.

Sinusoidal variations in duty cycle at a range of input frequencies (to cover the full response of the motor) were applied, although speed output signals were found to have a low signal-to-noise ratio at high frequencies. Observation of the output speed signal – compared to the sinusoidal duty ratio input – for each sample, allows calculation of the gain and phase shift at that frequency. Combining the series of measurements gives a frequency response plot for the motor under the test operating conditions. This is the equivalent of a 'Bode' plot for a linear system. In the experiments no attempt was made to control temperatures, however monitoring suggests that motor temperatures were in the range 20 °C to 70 °C for all motor measurements, with the higher temperatures only being reached during the high frequency tests. This may have a slight impact on results, but is not expected to be significant.

A comparison of the frequency responses measured from the five sample motors is given in Figure 5.7. Mechanical inertia is the main factor that affects the roll-off frequency and a combination of back-EMF and mechanical friction affects maximum speed. The motor is coupled to the testrig for these results and therefore additional inertias and frictions are involved; these have also been included in the model results.

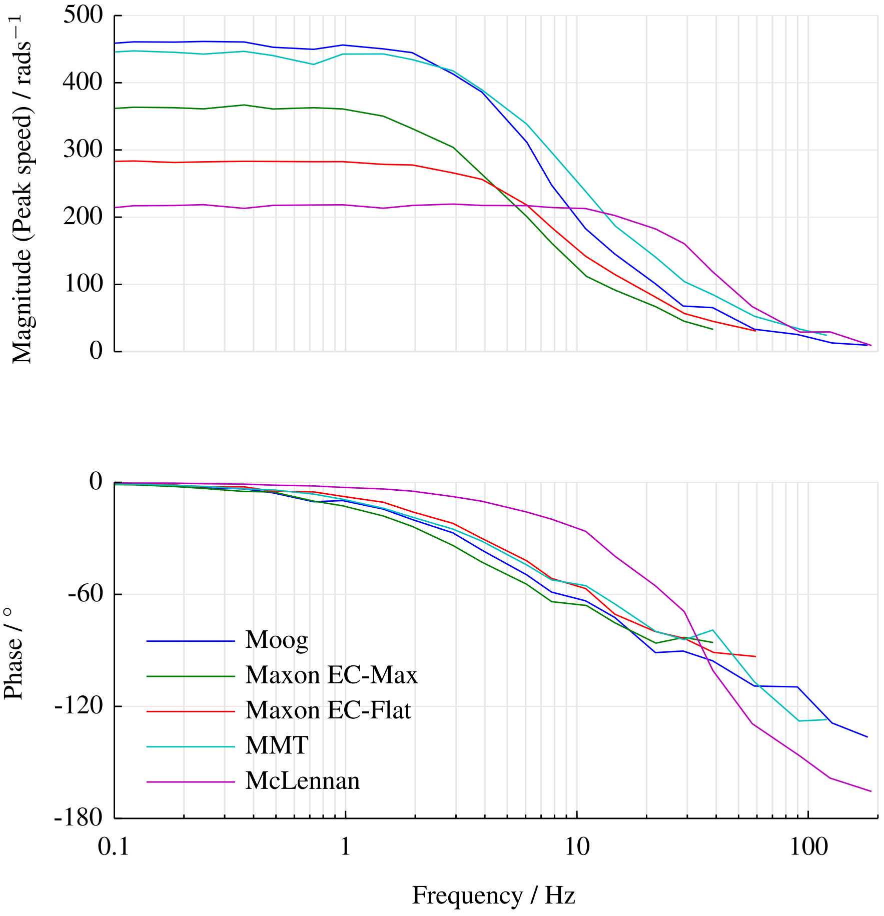

Figure 5.7: Frequency responses of the sample motors on the testrig

There is a clear difference in maxium speed, as would be expected from the difference in motor back-EMF constants (see Table H.4). As with the speed-torque curves, the delay in hall sensor processing also affects peak speed, particularly for the high pole-pair *MMT* and *Maxon* EC-Flat machines. There are also slight differences in roll-off frequency, roll-off slope and high frequency phase shift. At high frequencies all tests have some noise on their measurements; this is due to the increased signal-to-noise ratio for low-gain signals.

A similar process is followed to generate a frequency response from the motor models, by supplying input sinusoids and observing the output over the same set of frequency points. Four models have been tested for each motor: the efficient model outlined in Section 3.5 that does not explicitly include commutation; two full motor models following the equations in Chapter 3, one with an averaged voltage input and one with a full PWM input; and an acausal *SimScape* based motor model as detailed in Appendix D, also with a full PWM input. A comparison of the measured motor frequency response and the model frequency responses for the *MMT* motor is shown in Figure 5.8. Simulation settings for each model were selected to deliver accurate results, and the *Simulink* 'accelerator' was used for all except the efficient model – in this case the model runs so quickly that the additional compilation time of the accelerated model actually increases simulation time. For all simulations in this section the motor temperature has been fixed at 20 °C.

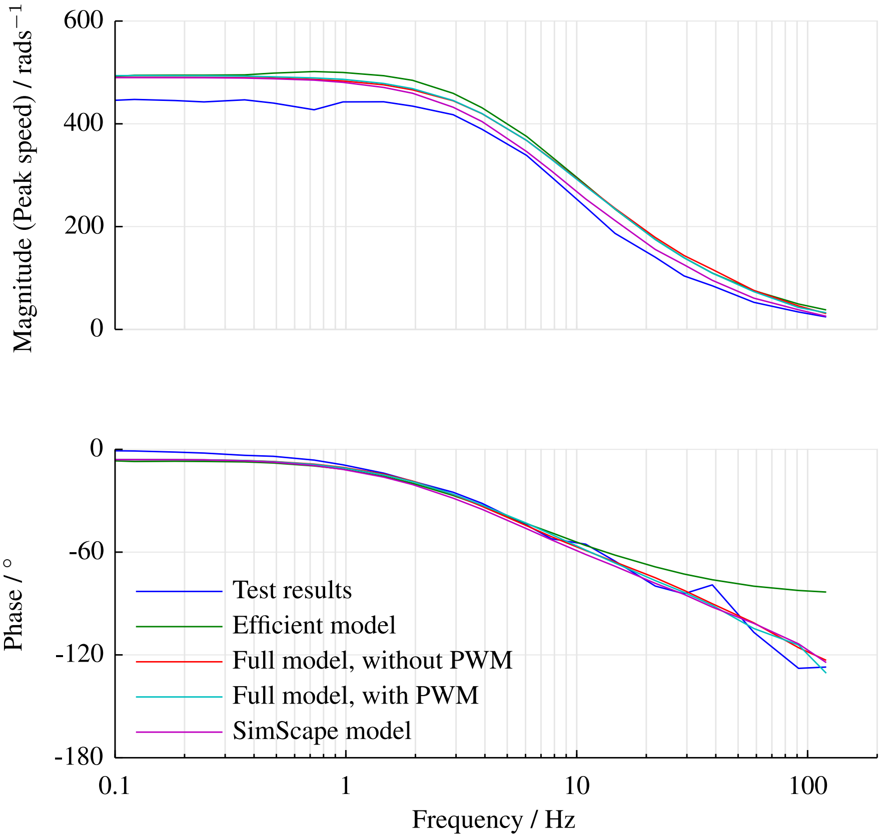

Figure 5.8: Simulated and measured frequency response for the *MMT* test motor

The model responses are all close to the measured response, with slight differences in maximum speed, corner and roll-off frequencies. The errors at high frequency in both the gain and phase are due to the decreasing signal-to-noise ratio. The *MMT* and *Maxon* EC-Flat models tend to overestimate speed, even for the models where hall sensor delays are included. More detailed investigation and modelling of processing delays and switching losses may be required to account for this. These are more apparent in the frequency response tests, as PWM switching occurs, reducing the effective voltage at the winding. Previous speed-torque tests were at full voltage, and therefore no switching was taking place in the drive other than for commutation. These tests show open-loop results, whereas a practical implementation with a closed control loop would minimise this type of error.

As might be expected, the higher fidelity models generally provide a better fit, however this difference is not particularly pronounced, and comes at a considerable cost in simulation time. Including commutation or PWM switching in the model requires a shorter model time-step, increasing simulation times significantly. Indication of the simulation time required to generate the results in Figure 5.8 is given in Table 5.1.

Table 5.1: Simulation times for different models

Model	Simulation time
Computationally efficient model	$2\,\mathrm{min}$
Full model without PWM	$27\,\mathrm{min}$
Full model with PWM	$9.7\,\mathrm{h}$
SimScape model with PWM	$33.8\,\mathrm{h}$

Further examples of frequency response tests are given in Figure 5.9 and 5.10. These show a similar pattern between models, with the PWM models generally providing a closer match to the real system. There is little to choose between the acausal *SimScape* model and the full mathematical model developed in this work. The full model is more flexible for an expert developer, but perhaps less intuitive for a basic user. Very little performance is sacrificed if an average voltage is used, rather than explicitly including PWM switching in the model. Whilst not investigated in this work, it is also possible to operate the *SimScape* model with an average voltage. This is expected to give similar results to the full model.

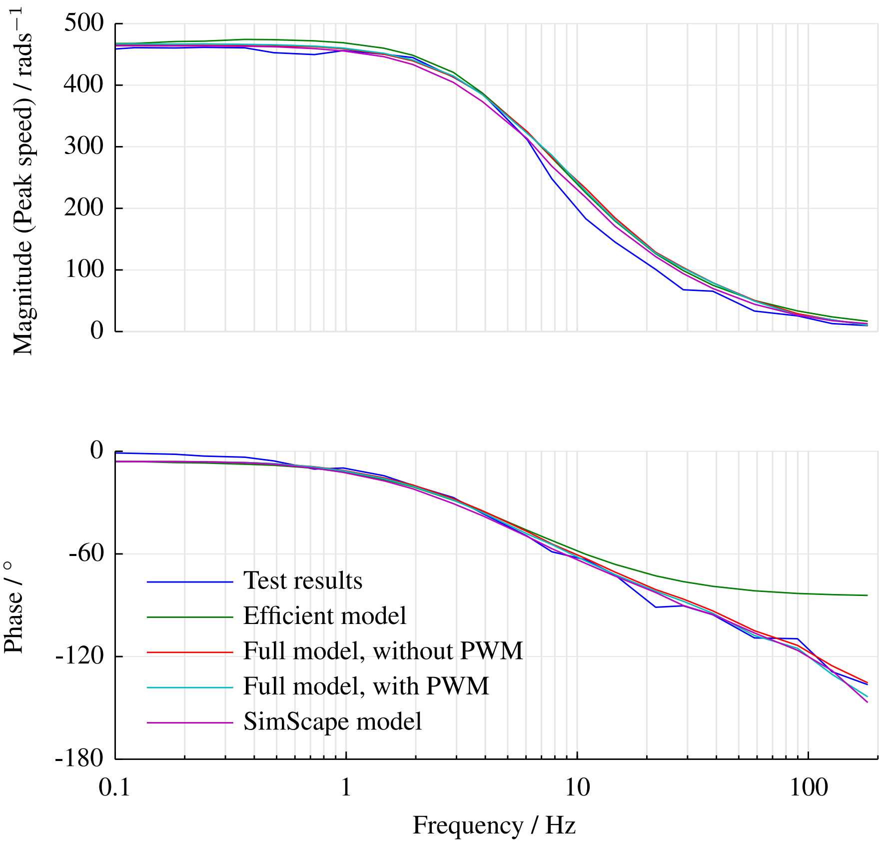

Figure 5.9: Simulated and measured frequency response for the *Moog* test motor

The efficient model gives a similar response to the full model, with slight differences in the gain around the corner frequency and the phase at high frequencies. Performance of the efficient model decreases as frequency increases, as the method of finding the commutation angle described in Chapter 3 can produce tracking errors if the speed changes significantly between commutation intervals.

The similarities between models shown in these tests, particularly at low frequencies, demonstrate that it is reasonable to use the faster-running models for thermal analysis and draw conclusions for all models.

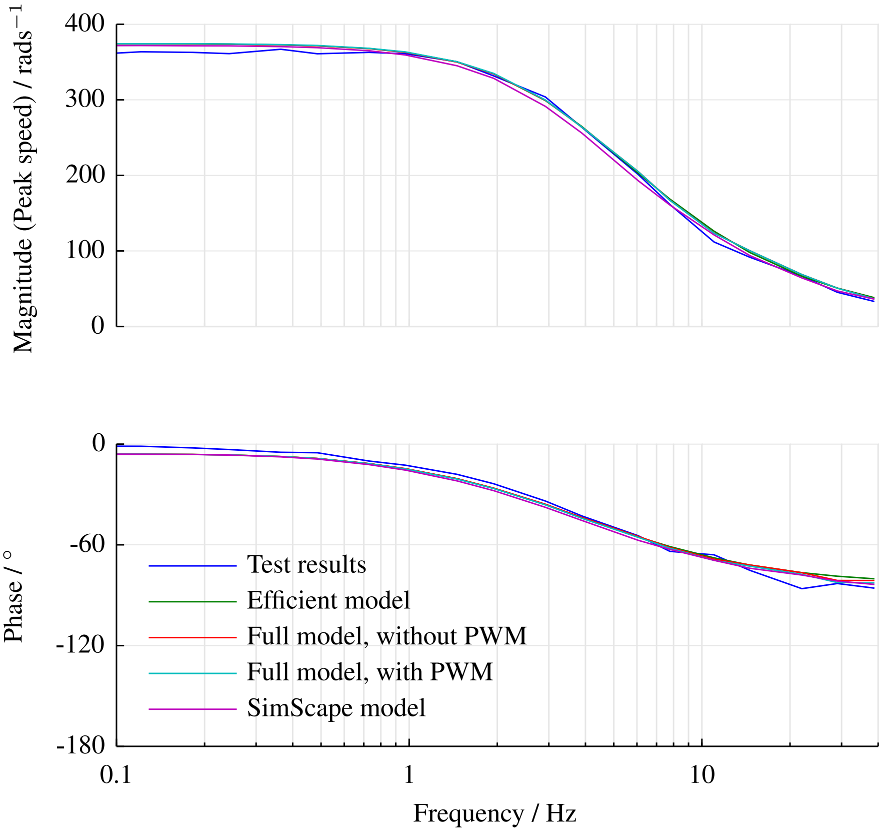

Figure 5.10: Simulated and measured frequency response for the *Maxon* EC-Max test motor

5.4 Thermal model validation

The preceding validation work has addressed both electrical and mechanical aspects of the system, both of which operate with relatively short time constants. Whilst the steady-state thermal behaviour has been considered in the speed-torque curves, the transient thermal aspects of the system have not been addressed.

A frequency sweeping approach similar to that outlined above could be taken to validate the thermal transient aspects of the models, however this would require very long duration tests on the testrig and also extremely lengthy simulations. Instead a less comprehensive approach has been taken, that compares temperatures for a varying input demand. Over a sustained period of several hours the test motor was driven from a controlled voltage against a load machine, providing a fixed load torque. During this period the duty ratio and the load torque are both altered in a number of step changes. Each step produces a change in motor thermal conditions, and the period between steps is long enough that a reasonable thermal change occurs – although not necessarily long enough to reach thermal steady-state conditions.

Where sample motors did not have winding temperature sensors, temperature was measured through temporary disconnection from the supply and winding resistance measurement. Rotor temperatures could not be effectively measured in this type of test without significant modification of the machines, which was beyond the scope of this work. Results are compared against the efficient model and the full model without PWM switching; models including PWM switching are not suitable for use in thermal analysis, due to their long simulation time.

The results of this test on the *MMT* sample motor, along with model results for the same sequence of duty ratio and load torque inputs, are shown in Figure 5.11. As previously, the efficient model overestimates speed due to neglecting the effects of processing delays on the commutation. Thermal results are reasonably accurate, with both the stator and winding simulated temperatures remaining within $4\,^{\circ}\mathrm{C}$ of their measured values, including during thermal transients.

Further examples are given for the *Moog* motor in Figure 5.12, and the *McLennan* in Figure 5.13. These show good results for the *McLennan*, but a significant underestimate of winding temperatures for the *Moog*. This is due to the low thermal resistance parameter between the winding and the stator estimated during static torque testing. The thermal results would be improved considerably if this resistance were increased from $1.09\,\mathrm{K\,W^{-1}}$ to around $4\,\mathrm{K\,W^{-1}}$, with little impact on the speed estimate. This would require the the stator temperature measurement to have been around $20\,^{\circ}\mathrm{C}$ too high during parameterisation; therefore this parameter may have been underestimated due to the placement of the stator thermocouple on this machine, in relation to the pair of windings that were energised in the torque test. It is also possible that the winding thermocouples measured particular hot-spots on this motor, and the average winding temperature during the validation test was actually lower.

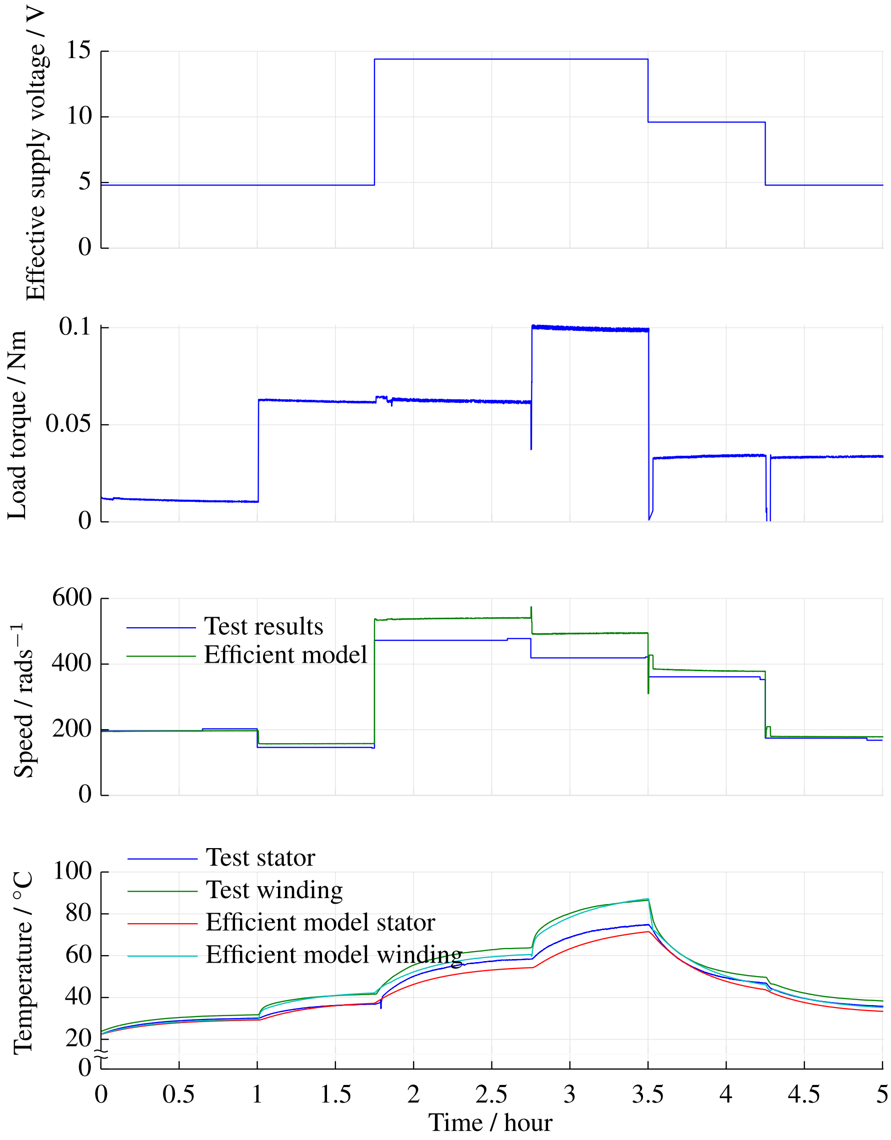

Figure 5.11: Simulated and measured thermal response for the *MMT* test motor

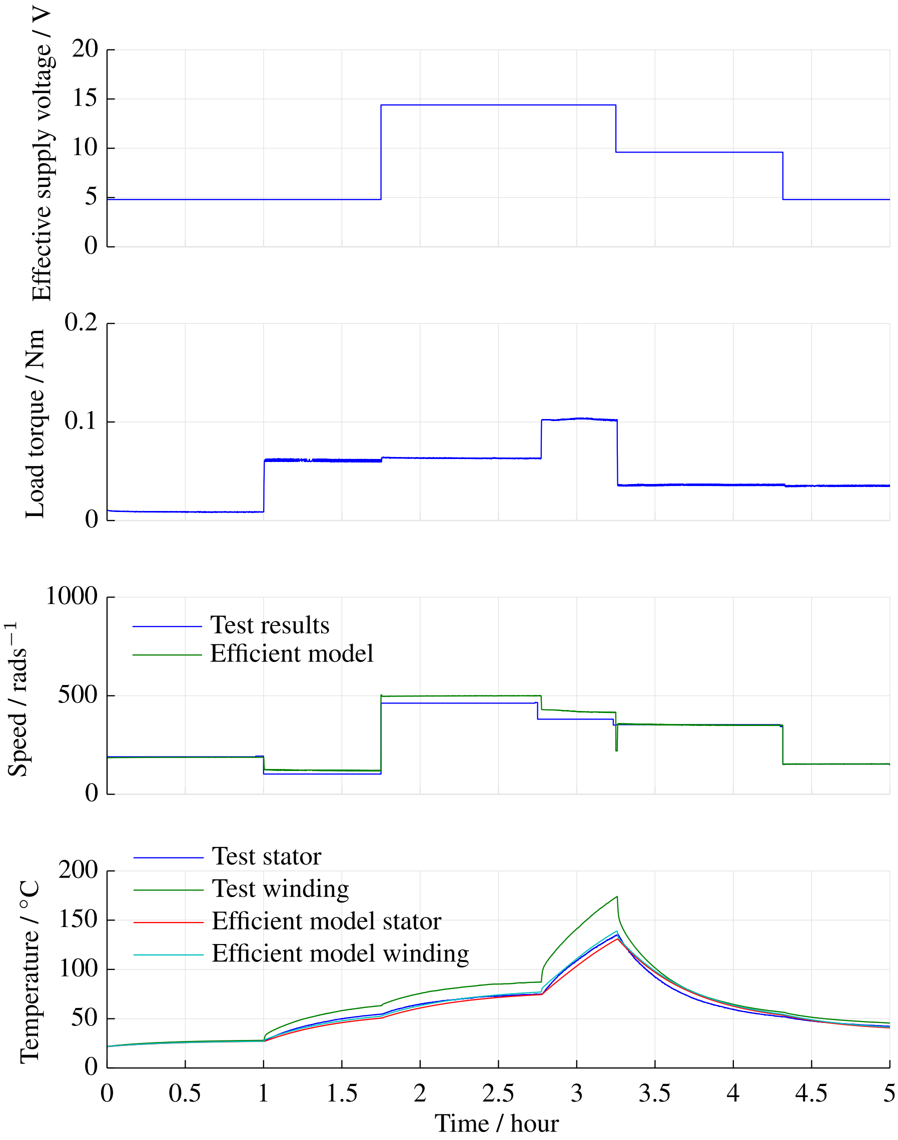

Figure 5.12: Simulated and measured thermal response for the *Moog* test motor

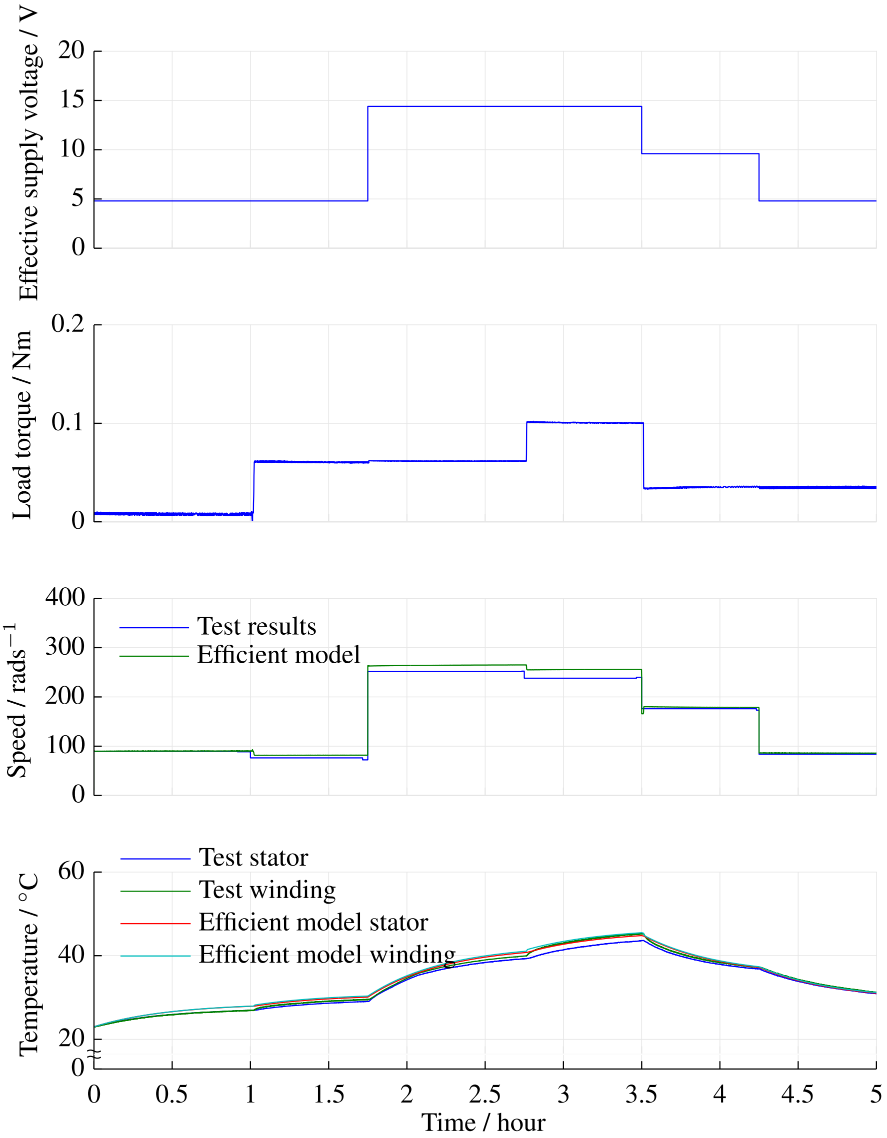

Figure 5.13: Simulated and measured thermal response for the *McLennan* test motor

5.5 Summary

A set of tests has been presented for validating motor simulations. The results of these tests have been shown for the set of sample motors and different fidelities of model. Not all models were suitable for use in all tests, particularly the higher fidelity models in the longer duration thermal tests. Some test results are omitted, either for brevity or as they were not possible due to testing limitations, such as a lack of temperature sensors, or damage to sample machines prior to testing.

The results have shown that the models can provide a good fit to the sample motor measurements in the electromagnetic, mechanical and thermal domains. Although the higher fidelity models do provide some increase in accuracy, the improvement is not significant, and must be offset against the considerable increase in simulation time required. There is very little difference between the *SimScape* model and the most complex mathematical model and therefore users are free to select the most appropriate model for their purpose; this will most likely be a trade-off between ease of modelling and the reduced financial cost and increased flexibility in constructing a model from first principles.

Using an average effective voltage within the models is shown to be almost as accurate as the inclusion of full PWM switching, however the models can be run considerably faster. An acausal model with an averaged voltage input is expected to provide similar levels of accuracy.

The computationally efficient model, although the least accurate of those tested, still provides a high level of accuracy that is expected to be appropriate for many tasks, including actuator design and modelling. It is also far faster than other models to simulate. Its inaccuracy at higher frequencies is not expected to be an issue, as these are beyond the bandwidth required for the position control application. Slight variation is seen in its speed prediction around the corner frequency, however the corner frequency itself is still well predicted; this is expected to be the important aspect for positioning applications. For thermal modelling in stall conditions it may not be appropriate, due to not separating out individual winding temperatures. This has not been investigated in any detail during this validation and could be considered in more detail if the model were to be used for this purpose.

Speed estimation has been shown to be in error for some models of certain machines. This is always an over-estimate, with the reduction in tests being attributed to switching delays introduced in processing hall signals. This cannot be included in the efficient model as presented, however re-deriving the equations with delay included is identified as scope for future work. It has been shown that including the delay in the full model does reduce the speed-torque curve, and improve the estimate. A more detailed investigation of the causes of this delay and inclusion in the model may improve the estimates. It is shown to be most significant in machines that require higher switching speeds, due to their combination of pole-pair number and rotation speed.

A poor match was found for the *Moog* winding temperature prediction under high load, which may be due to errors in the winding-to-stator thermal resistance parameter. Care in placement of temperature sensors is suggested during parameterisation to mitigate this in future.

Although areas of improvement have been identified, overall the models provided a good estimate of motor performance, based on the simple parameterisation tests used to populate them. Whilst improved accuracy would be expected from more detailed modelling or more involved parameterisation, this would involve a substantial increase in motor internal design knowledge, or additional instrumentation of the motor. The achieved performance is sufficient for actuator performance modelling and assessment.

Chapter 6 uses the validated models within a specific actuator assessment process. An example actuator is parameterised and assessed. The performance of the example actuator is demonstrated within a full turbocharger actuation system, however the validation techniques shown in this chapter could also have been used to validate the motor model independently.

Chapter 6

Design process

6.1 Introduction

Detailed actuator models have been introduced in Chapter 3, parameterised in Chapter 4, and validated in Chapter 5. These models, in conjunction with the theory reviewed in Chapter 2, are used in this chapter to develop and demonstrate a process for specifying or assessing an actuator design. An overview of this process is given in Figure 6.1.

Throughout the chapter reference is made to an example design, demonstrating the process applied to a production actuator. This uses an internal rotor brushless DC motor, coupled through two stages of spur gears to a third (sector) gear stage attached to the cross-shaft of the variable geometry actuation mechanism outlined in Section 2.2. It is driven from the same electronics as the sample motors, as outlined in Appendix F. This is a standard three-phase half-bridge configuration, with sense resistors for current limiting. Hall sensors are mounted in the motor stator for position feedback, but no absolute position sensor is used.

Initially a general set of actuator requirements is drawn up in Section 6.2. These attempt to succinctly capture the important criteria for assessing an actuator design. A move profile and a load profile, based on these requirements, are calculated in Sections 6.3 and 6.4. The example actuator motor is then parameterised in Section 6.5, using the techniques described in Chapter 4. It is shown in Section 6.6 how these parameters may be used to generate speed-torque curves, from which motor working points may be obtained. These points for the motor may be used in K-P diagrams with the load profile to assess performance; this is shown in Section 6.7.

A model of the full actuator and variable geometry linkage mechanism is then constructed using the techniques from Chapter 3 in Section 6.8. Simulations using this model confirm that it is suitable to meet the requirements; they are presented alongside test results from the actuator on a pneumatic test facility in Section 6.9, demonstrating a good match.

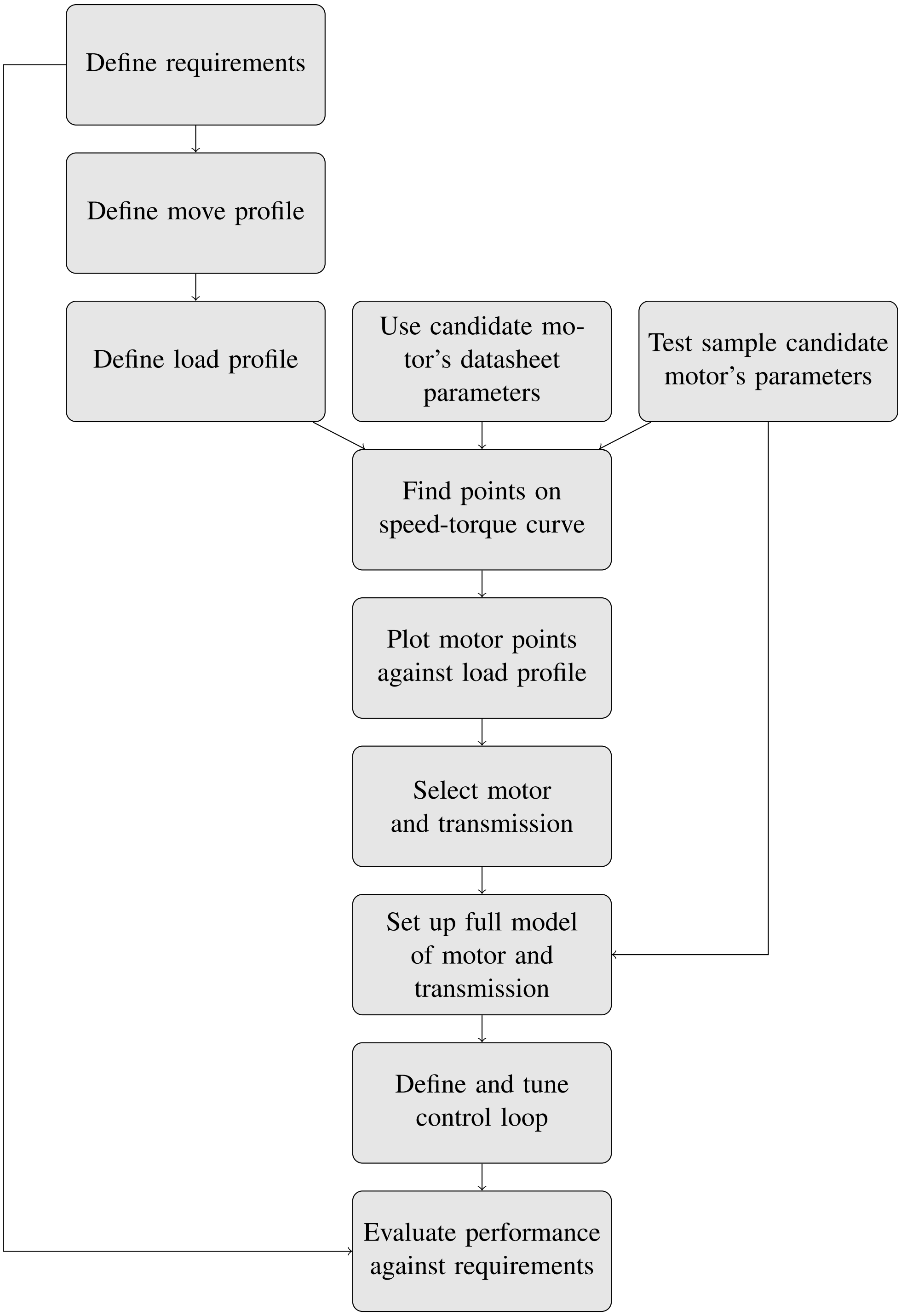

Figure 6.1: Overview of the design process, additional loops for iterating may also be incorporated

6.2 Actuator requirements

The overall need for an actuator in the variable geometry turbocharging application has been outlined in Chapter 1, and in Chapter 2 some of the compelling reasons for choosing electrical actuation were given. In this section the key parameters that should be given in an electrical actuator requirements specification are discussed. In most cases general requirements are given; however an example turbocharger actuator specification is also provided.

The aim of this section is to provide a compact set of requirements that may be used to drive the design process. Requirements have been divided into 'limiting' parameters that have a specified value that needs to be met, and 'optimising' parameters that need to be minimised or maximised. The split of requirements between these two categories will depend upon the specific application and will affect the design processes used. The split given here is representative of the *Cummins* actuator specification process.

6.2.1 Limiting parameters

Movement

The turbocharger actuator connects through a series of linkages to a nozzle in the turbine housing. The stroke of this nozzle depends upon the design and the turbo size. There is a fixed ratio of linkages between the nozzle and the actuating cross-shaft.

To ensure the performance of the higher level engine control systems, a maximum time is specified for the actuator to move the nozzle through its full stroke. Additional requirements may be set to achieve a portion of the full stroke; these may be more demanding in terms of average movement speed than the full stroke requirement. Requirements may also be specified on the positioning overshoot and settling error.

Load

Within the turbocharger there is a variable force on the nozzle, and hence the actuator, due to exhaust gas pressure. This force exhibits low frequency variation during operation, both dependent upon nozzle position, and due to engine and drive cycle dynamics. It also has high frequency pulsations due to engine cylinders firing – these vary with engine speed, load, and actuator position. This high frequency ripple is typically between $40\,\mathrm{Hz}$ and $150\,\mathrm{Hz}$.

In some cases the gas flow in the turbine can be such that the force on the nozzle reverses and it 'sucks shut' rather than 'blowing open' – this is especially likely at high engine speed. It is possible to use a spring in actuator designs to shift the load profile and ensure that the load is unidirectional, however this can introduce other complications in design and control tuning.

Nozzle mass

The mass of the actuated components, predominantly the nozzle – but also the push-rods, yoke and cross-shaft – add an inertia to the system that must be accelerated and decelerated during a positioning move.

Power input

A vehicle electrical network typically runs from either a nominal $12\,\mathrm{V}$ or $24\,\mathrm{V}$ battery supply. The battery is drained and recharged during operation, therefore some fluctuation from these nominal voltages is to be expected.

Temperature

The temperature inside the bearing housing of the turbocharger, where the nozzle push-rods are located, can reach temperatures of $110\,^{\circ}\mathrm{C}$, however the average will be around $95\,^{\circ}\mathrm{C}$.

During storage the turbocharger could experience a temperature range between $-55\,^{\circ}\mathrm{C}$ and $155\,^{\circ}\mathrm{C}$. In operation this will be limited to between $-40\,^{\circ}\mathrm{C}$ and $110\,^{\circ}\mathrm{C}$. Current generation actuators are cooled by the engine cooling system to sustain these temperatures.

Drive cycle

Detailed analysis of typical turbocharger actuator drive cycles has not been performed within *Cummins*. This is partly due to the actuator position demands originating from the ECU, and therefore being outside of *Cummins* control. They are known to differ substantially between engine manufacturers, models and driving modes.

6.2.2 Optimisation parameters

Space claim

The volume the actuator occupies or its 'space claim' is a key variable that may be optimised using the techniques outlined in this thesis. A reduction in actuator space claim is desirable. The main constraint in the turbocharging application is the mounting design on the turbo body, although the mounting of the turbo within the engine compartment is also of concern.

Current *Cummins* actuator motor and transmissions have external dimensions of around $85\,\mathrm{mm} \times 60\,\mathrm{mm} \times 100\,\mathrm{mm}$, ignoring cooling and casing volume.

Environmental

Cummins aim to minimise the impact of their designs in terms of use of raw materials, avoidance of hazardous substances, generation of waste and overall energy use – both in production and through the products' life.

Of concern in this area is the quantity of rare-earth magnetic material required for the permanent magnet motor. This is expensive to obtain both financially and environmentally, therefore minimising its use is desirable. This is not currently a significant issue, however design processes that allow consideration of this variable are advantageous.

Reliability

Reliability is a key requirement in the automotive industry, typically also with large service intervals. *Cummins* target failure rates for the actuator are:

- Less than $0.05\,\%$ at $5000\,\mathrm{h}$ or $250\,000\,\mathrm{miles}$
- Less than $2\,\%$ at $20\,000\,\mathrm{h}$ or $1\,000\,000\,\mathrm{miles}$

Whilst it is difficult to apply these figures to an overall design, they suggest that actuator subcomponent failure rates should be substantially less than this. In the harsh automotive powertrain environment this reinforces the focus of this work on brushless motors for their increased reliability.

Positioning resolution

Whilst it is generally acknowledged that increased actuator positioning resolution is beneficial, no specific studies have been done within *Cummins* to determine the effect of low resolution positioning on turbocharger performance. Typically current actuators provide a resolution of better than $1\,\%$ of the full stroke – not accounting for mechanical effects such as friction and backlash. For higher level control purposes the achieved position is fed back to the ECU.

Cost

Component cost is a significant factor in any automotive design and should therefore be considered throughout the process. Whilst an upper limit on actuator cost may be set for a specific product, minimising cost during the design will almost always be preferred. Cost considerations may initially preclude some designs, and subsystem component selection should take item cost into account during any optimisation.

6.2.3 Example requirements

The specific requirements below are generally representative of a typical set of actuator requirements. Environmental considerations and reliability have been omitted, as they are not relevant to the proposed design process, and can usually be met without significant changes to the motor and transmission specifics.

Movement

1. The full actuator output stroke will be $21°$, converting through a $42.5\,\mathrm{mm}$ lever arm in the turbo body to give a nozzle movement of $16\,\mathrm{mm}$.
2. The actuator must be able to achieve $90\,\%$ of a full stroke step change in position within $300\,\mathrm{ms}$.
3. It must have settled to within $1°$, or $0.76\,\mathrm{mm}$, of the steady-state position in $450\,\mathrm{ms}$.
4. Overshoot of the demanded position must be below $0.4°$, or $0.30\,\mathrm{mm}$.
5. It must be possible to maintain repeated full stroke movements with a ‘dwell period’ of $12\,\mathrm{s}$ whilst remaining within specification.

Load

6. Maximum average force on the nozzle will be $\pm 170\,\mathrm{N}$, producing a torque of $7.2\,\mathrm{N\,m}$ on the actuator. This is generated by a pulsating load between $40\,\mathrm{Hz}$ and $150\,\mathrm{Hz}$ with a peak of up to $15\,\mathrm{N\,m}$ at the actuator output, however it is expected that the inertia of the system will attenuate the effect of fluctuations in position on the load such that only the average need be considered for actuator design.
7. Load force is bi-directional and may change direction during movement.

Inertia

8. The mass of the moving and rotational components within the turbo body is $865\,\mathrm{g}$, producing a load inertia of approximately $1.6\,\mathrm{g\,m^2}$ at the actuator.

Power input

9. The actuator will be powered from a nominal $24\,\mathrm{V}$ vehicle battery, meaning it must be able to achieve all requirements between 18 V and 34 V.
10. Current draw from the battery must be kept below a peak of 4 A and an average of 1.75 A.

Temperature

11. The actuator must be able to achieve all requirements between $-40\,°\mathrm{C}$ and $110\,°\mathrm{C}$, whilst maintaining the motor within its specified thermal limits. This will be regulated by coolant flowing through the actuator with an average temperature of 95 $°\mathrm{C}$ under most operating conditions.

Optimisation

12. Whilst achieving the requirements specified above it is also desirable to reduce the size and cost of the actuator.
13. The positioning resolution of the actuator should be maximised as far as practical.

6.3 Move profile

Move profiles are discussed in detail in Section 2.7.1 and several that are commonly used in servo positioning applications are outlined. The benefits of specifying a profile on the overall control loop have not been investigated in detail; however, they are particularly useful in order to provide a starting point for an actuator design process. This allows an initial move requirement, specified as a move distance and maximum time limit, to be translated into a set of more useful actuator parameters. A trapezoidal move with a $1/3, 1/3, 1/3$ split is suggested as a reasonable starting point.

If an actuator design is able to achieve the distance and time requirements using a trapezoidal profile then it should be capable of achieving it using closed-loop position control. There is a danger that moving from a trapezoidal profile to a closed loop response may push the specified motor beyond its thermal limits, however the introduction of current or speed limits within the control loop should force a more trapezoidal response and bring the performance back within limits.

The most demanding move requirement from the specification should be used to determine the move profile. For the purpose of actuator sizing it may be assumed that this move is made repeatedly with no stationary period; alternatively a stationary 'dwell' period may be included in the requirements. The assumption of constant movement will produce a more demanding profile than the actual positioning signal, therefore producing a slightly conservative actuator design. These issues can be investigated during the more detailed modelling phase of the design, if necessary returning to this point and adjusting the move profile to relax or tighten the requirements.

A trapezoidal profile that moves an output through a rotation of θ_r within a period τ_r with a rise ratio of n_{rise} and a fall ratio of n_{fall} will have time periods of

$$\begin{aligned} \tau_{rise} &= \tau_r n_{rise} \\ \tau_{fall} &= \tau_r n_{fall} \\ \tau_{const} &= \tau_r - \tau_{rise} - \tau_{fall} \end{aligned} \tag{6.1}$$

this will produce a maximum speed requirement $\widehat{\omega}_r$ of

$$\widehat{\omega}_r = \frac{\theta_r}{\tau_{rise}/2 + \tau_{const} + \tau_{fall}/2} \tag{6.2}$$

and rise α_{rise} and fall α_{fall} accelerations of:

$$\begin{aligned}\alpha_{rise} &= \frac{\widehat{\omega}_r}{\tau_{rise}} \\ \alpha_{fall} &= \frac{\widehat{\omega}_r}{\tau_{fall}}\end{aligned} \tag{6.3}$$

From these the maximum $\widehat{\alpha}_r$ and RMS $\alpha_{r_{RMS}}$ accelerations can be calculated as:

$$\begin{aligned}\widehat{\alpha}_r &= \max\left(|\alpha_{rise}|, |\alpha_{fall}|\right) \\ \alpha_{r_{RMS}} &= \sqrt{\frac{\alpha_{rise}^2 \tau_{rise} + \alpha_{fall}^2 \tau_{fall}}{\tau_r}}\end{aligned} \tag{6.4}$$

If a dwell period is present between moves, then the τ_r term may be replaced by the full move plus dwell time.

The actuator torque can then be calculated based on the average load torque T_l, the load inertia J_l and an estimate of the transmission inertia J_g by modifying Equation 2.21 to:

$$\begin{aligned}\widehat{T}_l' &= T_l + (J_l + J_g)\widehat{\alpha}_r \\ T_{l_{RMS}}' &= \sqrt{T_l^2 + (J_l + J_g)^2 \alpha_{r_{RMS}}^2}\end{aligned} \tag{6.5}$$

The effects of Coulomb friction in the load and the transmission may be subsumed into the load torque, however viscous friction within the load is not included in this model.

For simplicity, regeneration or reverse power flow is not considered within the models. Modifications to the overall process would be possible in order to take this into account; a starting point for analysis of reverse power flow scenarios is given in [216]. This assumption means that the estimates produced will be representative of a worst-case loading situation – this will be a pessimistic estimate in most cases.

These equations provide all the information required to calculate a load profile for the actuator that a motor and transmission combination must be able to achieve.

6.3.1 Example move profile

Based on Requirements 1 and 2, the actuator output must move through $19°$, or $0.33\,\mathrm{rad}$, in $300\,\mathrm{ms}$. This requires an acceleration and deceleration of $16.6\,\mathrm{rad\,s^{-2}}$ and a maximum speed of $1.66\,\mathrm{rad\,s^{-1}}$ (Equations 6.2 and 6.4). Over the whole move period, including the $12\,\mathrm{s}$ dwell time, the RMS acceleration is $2.14\,\mathrm{rad\,s^{-2}}$ (Equation 6.4).

In order to accelerate the inertia in Requirement 8 and overcome the mean load in Requirement 6, assuming the worst case scenario where the load torque is always in opposition to the acceleration, as is possible from Requirement 7, the maximum torque required from the actuator is $7.25\,\mathrm{N\,m}$ and the RMS torque is $7.23\,\mathrm{N\,m}$ (Equation 6.5). At this point no allowance has been made for any transmission inertia or friction.

6.4 Load profile

The motor and transmission must be able to achieve the maximum speed of the move profile, as well as the peak load and RMS load requirements as defined above. A first step in eliminating motors that will be unable to drive the specified load is to calculate the 'load factor' of the actuator requirements k_β, from Equation 2.23 this can be simplified to:

$$k_\beta = \frac{4\alpha_{r_{RMS}} T'_{l_{RMS}}}{\eta_g} \tag{6.6}$$

This must be lower than the 'accelerating factor' of the motor k_α, given by:

$$k_\alpha = \frac{T_{RMS}^2}{J_m} \tag{6.7}$$

The RMS torque T_{RMS} is effectively the maximum continuous torque that a motor can sustain within its winding temperature limits.

Similar calculations can be carried out for maximum, or 'dynamic', accelerating $\widehat{k}_\alpha$ and load $\widehat{k}_\beta$ factors:

$$\widehat{k}_\alpha = \frac{\widehat{T}^2}{J_m} \tag{6.8}$$

$$\widehat{k}_\beta = \frac{4\widehat{\alpha}_r \widehat{T}'_l}{\eta_g} \tag{6.9}$$

The motor dynamic torque limit $\widehat{T}$ may be set by the current limit of the motor drive electronics, or the stall torque of the motor, depending on the specific design. The move period during which the motor is in dynamic operation – at torques greater than the continuous torque limit – must be small compared to the thermal time constant of the motor windings. These inequalities are later visualised using K-P diagrams as discussed in Section 2.7.

Initial numbers to determine the motor accelerating factors and speed limit are usually available from the manufacturer's datasheet. These are generally specified at a reference temperature and voltage that may not always be appropriate for the application. For example, in the turbocharger application, the standard motor reference temperature of 25 °C is unrealistically low. Increased temperatures will increase winding resistance and therefore power losses. They will also decrease back-EMF constants reducing torque and increasing speed. Therefore at increased temperatures the set of motors and transmissions capable of driving the load may be significantly reduced. Derivation of the correct parameters through efficient motor simulation is addressed in Section 6.6.

6.4.1 Example load profile

The example load profile can be used to calculate an initial load factor for the example requirements using Equations 2.20 and 2.23. Initially assuming $100\,\%$ transmission efficiency the load factor is $61.9\,\mathrm{W\,s^{-1}}$. This is the minimum point on the curve of continuous power rate against kinetic energy, and could be used to immediately exclude motors that have accelerating factors below this. Once transmission efficiency and inertia are included, this will increase and therefore motors with an accelerating factor only slightly in excess of the load factor should also be excluded. For some sets of requirements the minimum point of the power rate curve occurs at a very high kinetic energy and is therefore not a practically useful measure. This highlights the importance of plotting out the power rate plots as well as simply considering the load factor.

The load curves may be plotted out for a range of possible motor inertias using Equation 2.17. These are shown by the dashed line in Figure 6.2, where the solid line also shows a more realistic estimate – including the efficiency and transmission with the inertias found in Section 6.5. The curve in the upper plot shows the left-hand side of the final inequality of Equation 2.17, whilst the lower plot shows the left-hand side of the middle inequality. The left side of the first inequality is shown on the common horizontal axis.

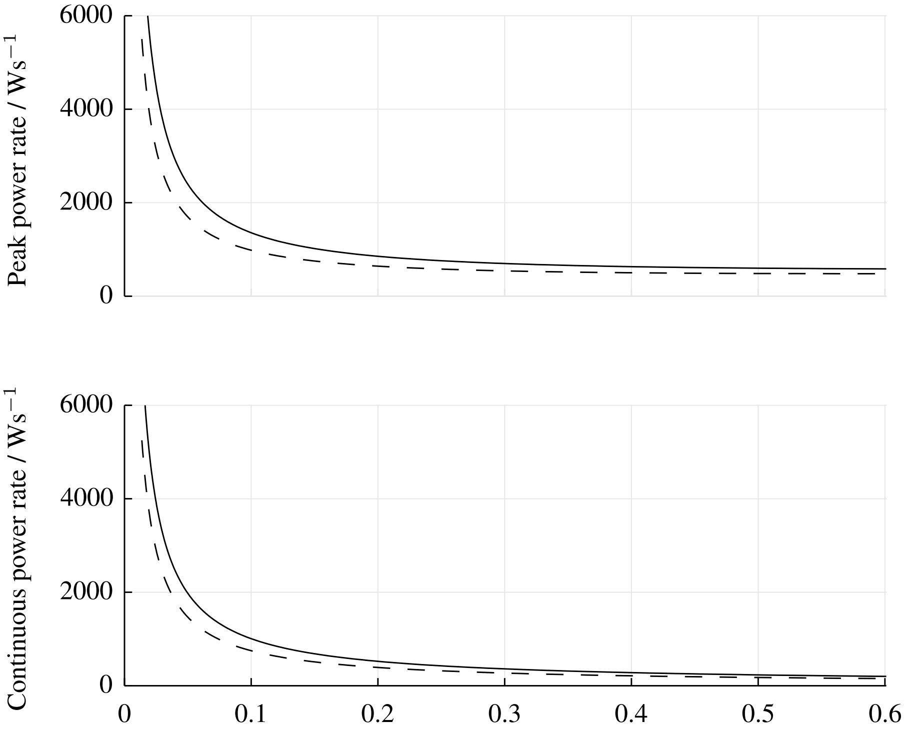

Figure 6.2: Power rate plots showing load curves based on the actuator requirements

6.5 Actuator parameterisation

In order to accurately model the example actuator it has been parameterised according to the tests set out in Chapter 4. The motor was separated from the transmission and coupled to the testrig described in Appendix F using an adapter plate, with connection to the load machine made from the end of the pinion gear, as shown in Figure 6.3. A summary of the parameters extracted for the actuator motor is given in Table 6.1.

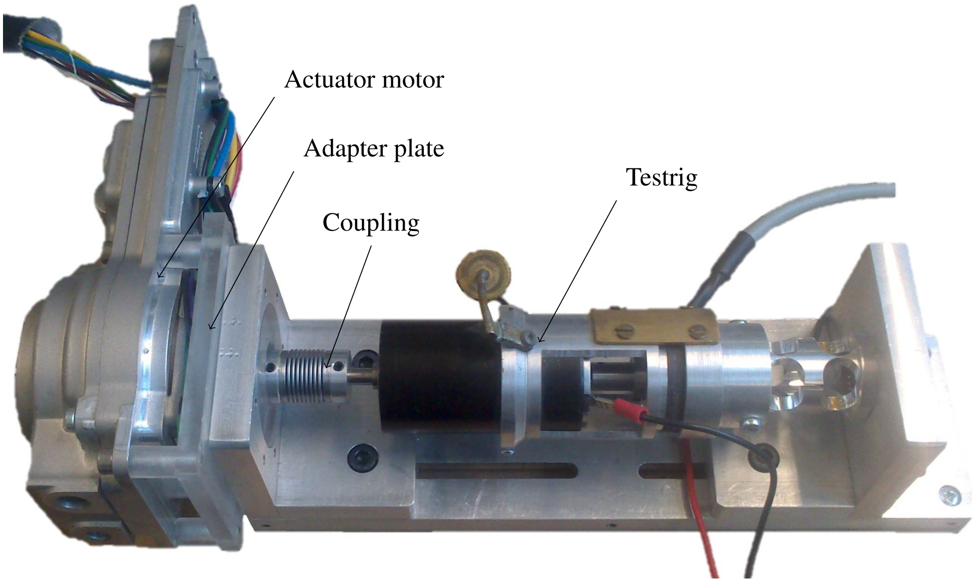

Figure 6.3: Actuator motor mounted on the motor testrig

The rotor and pinion inertia was provided by the manufacturer, and a spin-down test was used to determine the total friction parameters, as shown in Figure 6.4. This also shows an exponential form regression fit to the results, as used in Section 4.3.

Table 6.1: Actuator motor measured parameters (errors are similar to those indicated in Tables H.2 and H.4)

Back-EMF constant K_e	$37.5\ \mathrm{mV\,s\,rad^{-1}}$
Torque constant K_t	$33.9\ \mathrm{mN\,m\,A^{-1}}$
Winding resistance R	$2.35\,\Omega$
Winding inductance L	$1.5\ \mathrm{mH}$
Rotor inertia J	$11.56\,\mathrm{mg\,m^2}$
Pole-pairs n_{pp}	5
Coulomb friction B_c	$3.8\ \mathrm{mN\,m}$
Viscous friction B_v	$0\ \mathrm{\mu N\,m\,s\,rad^{-1}}$
Hysteresis constant B_h	$8.6\ \mathrm{mN\,m}$
Eddy current constant B_e	$6\ \mathrm{\mu N\,m\,s\,rad^{-1}}$
Thermal resistance winding-stator $\mathcal{R}_{ws}$	$5.15\,\mathrm{K\,W^{-1}}$
Thermal resistance stator-ambient $\mathcal{R}_{sa}$	$0.52\,\mathrm{K\,W^{-1}}$
Thermal capacitance winding $\mathcal{C}_w$	$11.7\ \mathrm{J\,K^{-1}}$
Thermal capacitance stator $\mathcal{C}_s$	$320\ \mathrm{J\,K^{-1}}$

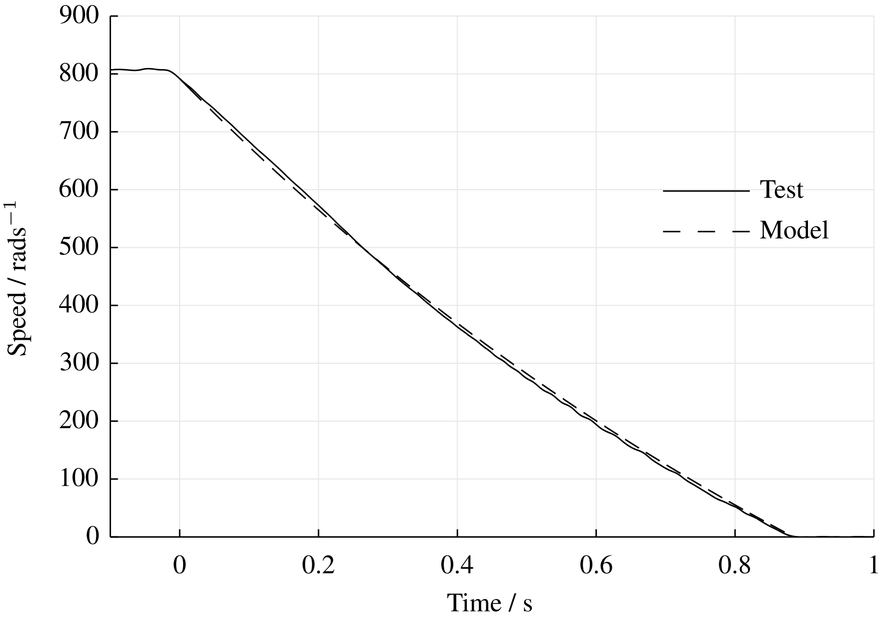

Figure 6.4: Spin-down test for the actuator motor on the testrig

By driving the motor at a range of speeds using the load machine, plots of the back-EMF were obtained. These were used to determine the number of magnet pole pairs on the rotor and the back-EMF constant. The shape of the back-EMF was found to be sinusoidal with a THD of around $6\,\%$.

Winding resistance and inductance were accurately measured using an LCR meter, as shown in Figure 6.5. Inductance variation with position was found to be below $20\,\%$, indicating little saliency in the rotor. Variation with frequency of excitation is shown, particularly in resistance, however this has not been included in any modelling, and therefore the value at $100\,\mathrm{Hz}$ has been used in all subsequent analysis. This was selected as a compromise between stationary power loss and the fundamental electrical frequency at maximum speed of $370\,\mathrm{rad\,s^{-1}}$, or around $300\,\mathrm{Hz}$; the error will therefore be below $5\,\%$ at maximum speed. This is not an issue as winding resistance has more impact on motor high torque performance than on high speed performance, as explained in Table 3.6. The slight inductance overestimate of around $1\,\%$ at high speed is not expected to have a significant impact.

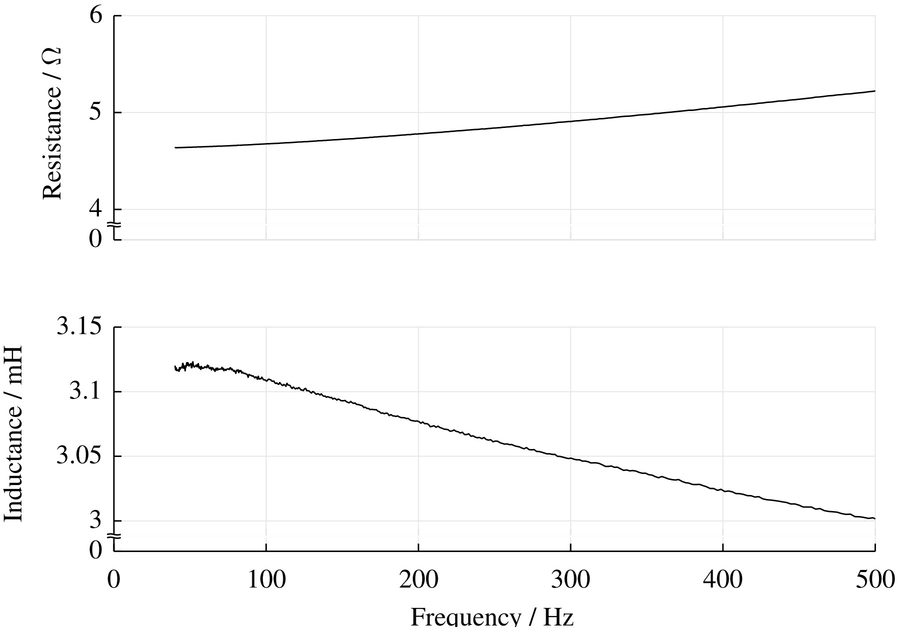

Figure 6.5: Phase-to-phase winding resistance and inductance for the actuator motor

Due to the motor casing being an irregular shape, the simple calculations shown in Section 4.4 could not be used to estimate its thermal resistance to ambient. The motor assembly was instrumented with three thermocouples as shown in Figure 6.6: on the outside of the stator material, the outside of the motor casing, and on the plate that would be in contact with coolant fluid in the application. Due to being unable to test the motor in isolation from the casing, and this providing a significant extra thermal mass, ambient was taken as the actuator housing temperature. Stator to ambient resistance in the thermal model therefore corresponded to stator to housing thermal resistance.

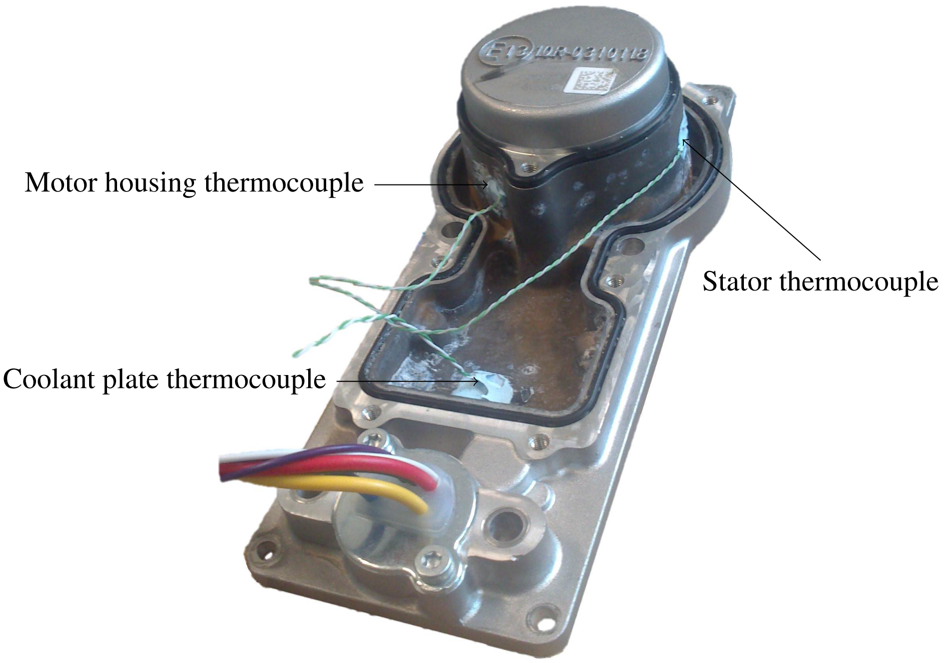

Figure 6.6: Thermocouple mountings on the actuator motor, with the coolant cover removed

A static torque test with the rotor locked at a position of maximum back-EMF and with two phases of the winding excited from a current controlled source, allowed measurement of the stator and casing thermocouple temperature rises, and calculation of the winding and rotor temperatures, as shown in Figure 6.7. The final temperatures achieved in this test allowed the thermal resistance between the windings and stator to be calculated. The measured temperature of the casing was used to calculate the stator to ambient (casing) thermal resistance. Thermal model fitting to the transients in the test then allowed estimates of the thermal capacitances to be calculated.

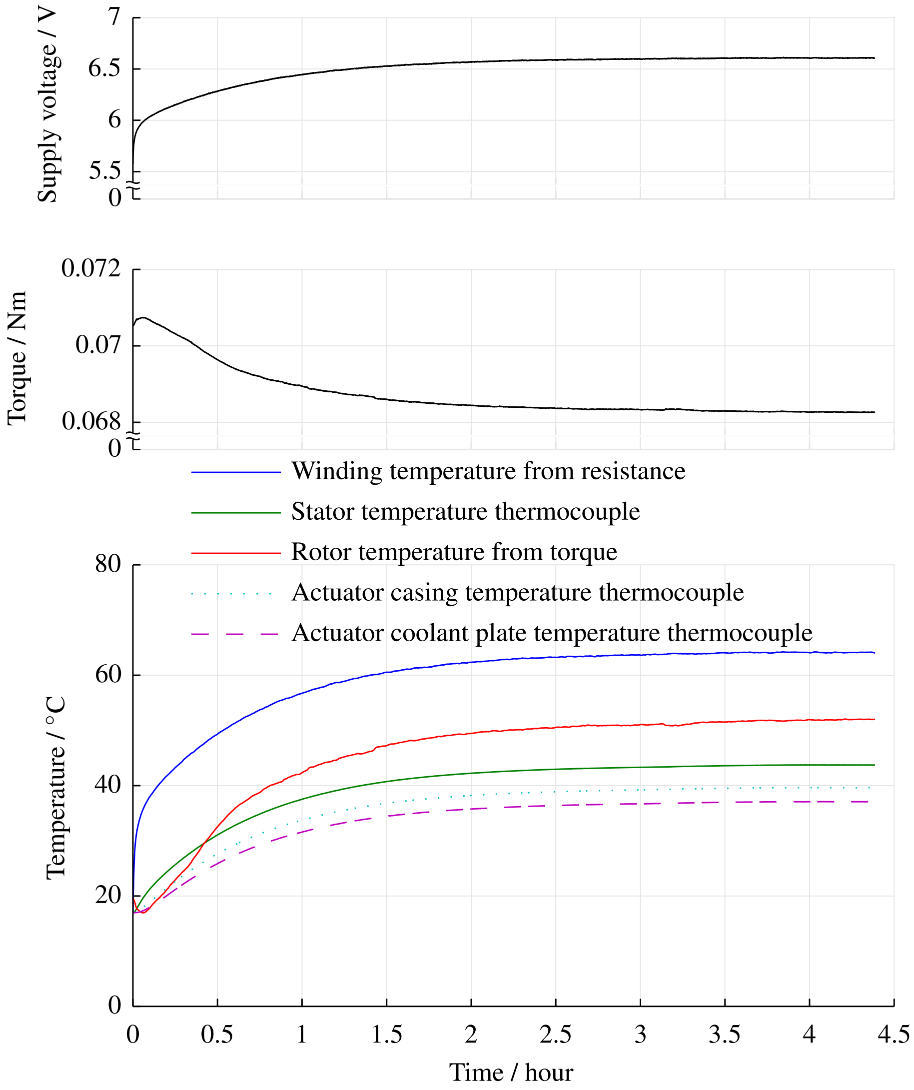

Figure 6.7: Conditions during static torque test of the actuator motor

Finally stator loss tests were performed by driving the motor from the load machine with its windings open-circuit and allowing the assembly to heat up. The final temperatures achieved, along with the stator to ambient thermal resistance calculated previously, allowed total power loss to be calculated, as shown in Figure 6.8. Fitting a curve to these points allowed constant and speed-dependent stator losses to be calculated. These were deducted from the spin-down test results to separate the losses causing stator heating from those lost directly to the casing or down the motor shaft.

Explicit testing to parameterise the actuator gears was not undertaken. Instead, parameters were taken from manufacturer specifications, previous tests performed at *Cummins*, or estimated based on numbers cited in the literature. In order to reduce the order of the model, the three stages of the gear train were lumped together. This is an approximation due to the nonlinearity introduced by the backlash, however it is

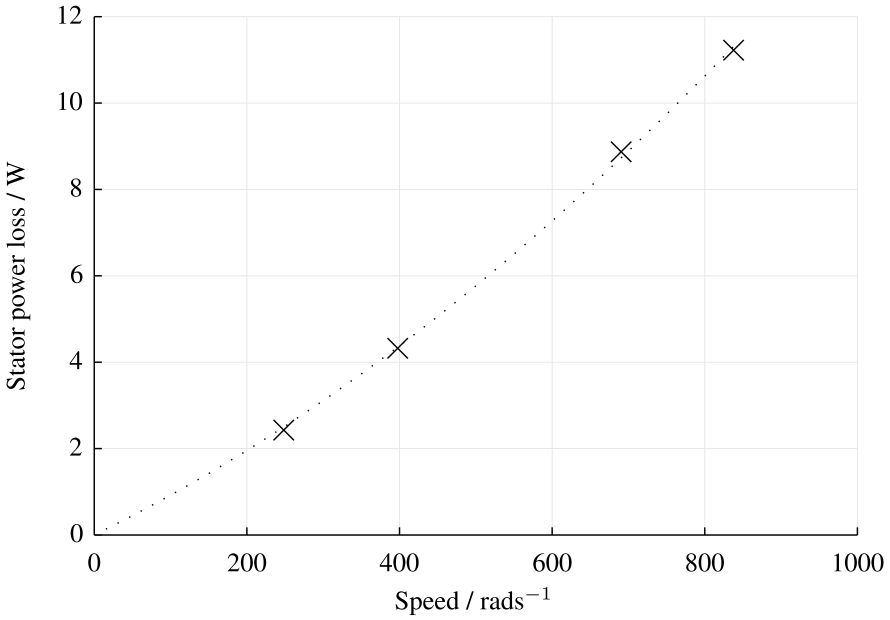

Figure 6.8: Stator loss power to speed relationship for the actuator motor, measured points and fitted curve

expected to be reasonable for initial modelling purposes. Referred backlash for each stage has been summed to provide a worst-case performance estimate.

Backlash parameters were based on measurements performed at *Cummins* by locking output gears and mounting a visual indicator on the input. Stiffness and damping for the backlash were adjusted to provide an acceptable simulation period. These parameters are not expected to have a significant impact on performance, but are required in order to provide a stable numerical solution for backlash within the models.

Efficiency of each gear mesh was assumed to be $95\,\%$, as this was a suggested value from the *Cummins* data. This is slightly lower than that suggested in the literature and shown in Table 2.2. These were combined to give an overall gear train efficiency. The inertia of each gear stage was provided by the supplier. Gear bearings were assumed similar to the motor bearings, allowing values for Coulomb and viscous friction to be estimated. All gear parameters were referred to the output before combining values. The gear parameter values for each component and their combined values are given in Table 6.2.

Independent testing was not performed on the variable geometry linkage mechanism within the turbo bearing housing. Parameters were taken from *Cummins* product testing and manufacturing tolerances. Previous work by *Cummins* has shown that friction losses are dominated by significant Coulomb friction in the push-rod seals. The gear ratio was unity for all components except the wear-blocks that transform the rotary motion of the yoke into linear motion. The ratio for these was based on the

Table 6.2: Actuator gear train parameters, referred to the output

	Gear 1	Gear 2	Sector/yoke/ cross-shaft	Combined
Gear ratio n	$\frac{65}{13}$	$\frac{64}{16}$	$\frac{84}{17}$	98.82
Bearing viscous friction B_v / $\mu\mathrm{N\,m\,s\,rad^{-1}}$	10	10	10	4200
Bearing Coulomb friction B_c / $\mathrm{mN\,m}$	2	2	2	51.4
Gear mesh efficiency η_g / $\%$	95	95	95	86
Gear backlash 2α / °	0.4	0.4	0.4	0.506
Gear tooth stiffness K_t / $\mathrm{kN\,m\,rad^{-1}}$	1000	1000	1000	1000
Gear tooth damping B_t / $\mathrm{kN\,m\,s\,rad^{-1}}$	10	10	10	10
Gear inertia J / $\mathrm{g\,m^2}$	0.0312	0.130	0.154	15.5

equivalent movement per rotation of the cross-shaft. The values for separate components and a combined value for all components is given in Table 6.3. Again this is a worst-case value due to the addition of backlash nonlinearities; this is reasonable for component selection as it is better to over-specify than under-specify.

Table 6.3: Variable geometry linkage mechanism parameters

	Wear blocks	Push-rods	Nozzle	Combined
Ratio n	$\frac{1}{0.0425}$	1	1	23.53
Viscous friction B_v / $\mathrm{N\,s\,m^{-1}}$	0	0	0	0
Coulomb friction B_c / N	0	32.2	0	32.2
Efficiency η_g / %	100	100	100	100
Backlash 2α / mm	0.121	0.1	0.175	0.396
Contact stiffness K_t / $\mathrm{kN\,m^{-1}}$	1000	1000	1000	1000
Contact damping B_t / kN	10	10	10	10
Mass J / g	15.6	290	560	865.6

6.6 Speed-Torque curves

It is possible to utilise the models developed in this work to determine speed-torque curves for a parameterised motor design. These curves may be adjusted for the operating temperature and used to determine continuous and dynamic torque limits of the motor. These motor limits can then be used in power rate diagrams to determine whether it is suitable for driving the load. Using the computationally efficient model outlined in Section 3.5 full speed-torque curves may be generated in fractions of a second.

For operation at a fixed voltage, a curve is generated by performing repeated simulations, increasing the steady-state motor speed from zero and using the model to calculate the current and torque produced. The thermal model is be used to calculate the steady-state winding and stator temperatures at each point on the curve. These temperatures are used to adjust the resistance and back-EMF constant during calculation as described in Section 3.2.5. By specifying a maximum winding temperature limit the maximum continuous torque T_{RMS} is found. Beyond the maximum continuous torque limit temperatures can become excessive very quickly, due to positive feedback effects within the system. Operation at temperatures above the winding temperature limit would not be permitted, and therefore the resistance and back-EMF values are not varied within the dynamic torque region. The dynamic torque limit $\widehat{T}$ of the motor may also be found by specifying a maximum drive current, or by the stall torque – whichever is lower. It is the maximum continuous torque and the dynamic torque limit that are of interest in assessing motor performance in K-P diagram analysis. Depending upon the step size chosen for computing the speed-torque curve, some interpolation or iteration may be required to find these points within an acceptable level of precision. For the machines considered in this work the torque interval used was $10\,\mathrm{mN\,m}$, giving a thermal interval of around $20\,°\mathrm{C}$ at the winding temperature limit.

Viewing motor performance as a speed-torque curve highlights the fact that speed can vary considerably with load torque. This is not generally accounted for in K-P diagram analysis, where a single motor speed measure is compared against the load movement requirement – the ‘nominal speed’ at the continuous torque limit is generally used for this. If the move profile demands maximum speed during a period where torque exceeds the continuous limit this may be optimistic, nevertheless it is expected to be reasonable for most designs.

The generation of a speed-torque curve based on simulation, using physical motor parameters, also allows investigation of parameter variations. Of particular interest for actuator specification are the effect of changes in supply voltage and an increase in ambient temperature. For the latter it is important to consider the motor cooling, which will depend upon the overall actuator housing design. The thermal model of the motor should take this into account during performance analysis.

6.6.1 Example speed-torque curve

Plotting the speed-torque curve using the computationally efficient model, parameterised using Table 6.1, allows the continuous current, torque and speed that will generate the limiting $155\,°\mathrm{C}$ in the winding to be calculated. This is shown in Figure 6.9, for a fixed $95\,°\mathrm{C}$ in all components (blue), and using the thermal model with a casing temperature of $95\,°\mathrm{C}$ (green). $95\,\mathrm{mN\,m}$ at $150\,\mathrm{rad\,s^{-1}}$ can be sustained at this limit.

This plot also shows that the current demanded by the motor is always less than the peak $4\,\mathrm{A}$, and the average current at the continuous point is below the $1.75\,\mathrm{A}$ set in requirement 10. The stall torque available from this motor at $95\,°\mathrm{C}$ is predicted to be in the range $140\,\mathrm{mN\,m}$ to $210\,\mathrm{mN\,m}$, depending on the component temperatures at that point.

6.7 Motor comparison against load profile

A set of motors that can potentially drive the actuator may be initially defined using a load factor and motor accelerating factors. These can then be checked in more detail by adding their point to full power rate plots using Equation 2.17. This will provide a further confirmation that they are capable of fulfilling the requirements. The gear ratios required to achieve this are given by Equation 2.25.

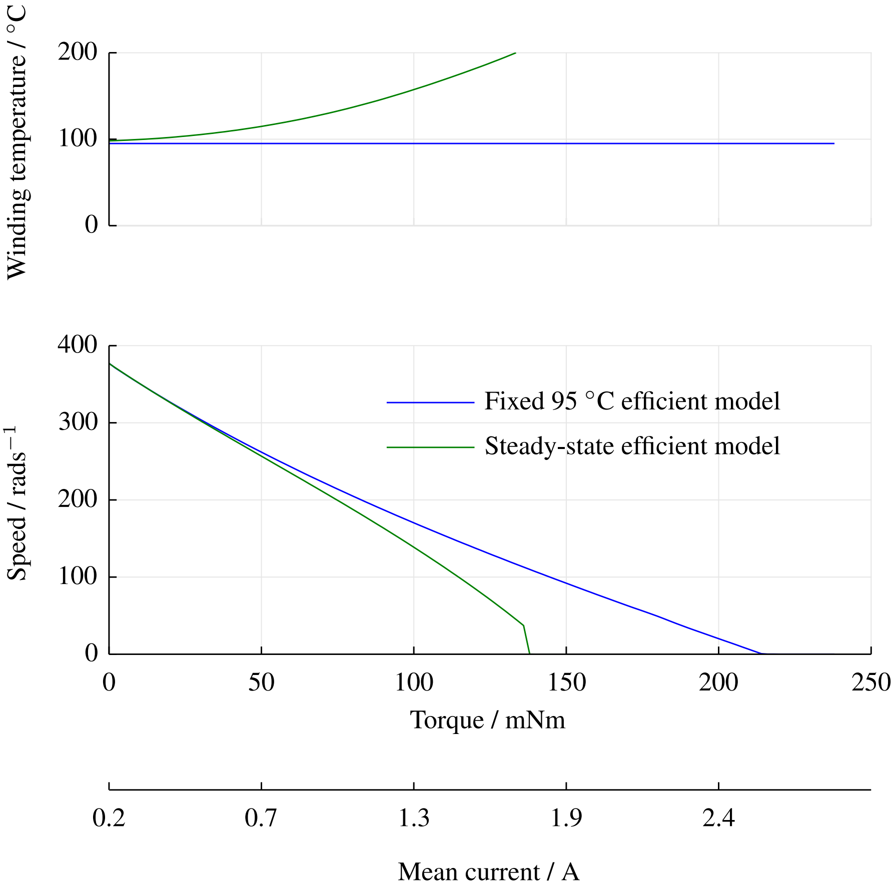

Figure 6.9: Speed-torque curves for the parameterised actuator motor, at a fixed 95 °C and at thermal steady-state in ambient 95 °C conditions at 24 V

Selection from a set of possible motors may be made based on a range of criteria; these could include size, cost, available transmission ratios, supplier limitations and other design factors. Due to physical constraints on motor design it is expected that optimal motors will often lie close to the load curve limits.

Alongside the motor, a suitable transmission may be selected using the K-P diagrams. In the process of selection, its inertia J_g and efficiency η_g should be taken into account by modifying the load curve and rechecking the motor's suitability. It may be necessary to iterate the process if previously acceptable motors are pushed into the unacceptable region by inefficient or unacceptable gear ratios.

If accurate figures are used for the motor torques and accelerations, and the selected move profile is a reasonable representation of the most demanding closed-loop profile, then the selected motor and transmission should be capable of achieving the actuator requirements. It is recommended that this be confirmed through more detailed simulations using a full closed-loop control system as described in the next section.

6.7.1 Example comparison

The motor continuous and dynamic torque ratings found from Figure 6.9 may be combined with the motor inertia using Equation 2.17 to give: a maximum motor kinetic energy of $0.13\,\mathrm{J}$; a continuous duty power rate, or 'accelerating factor', of $780\,\mathrm{W\,s^{-1}}$; and dynamic power rate of $2214\,\mathrm{W\,s^{-1}}$. This accelerating factor is considerably in excess of the load factor of $62\,\mathrm{W\,s^{-1}}$; however this does not take into account the peak speed of the machine and the variation of the load requirement with speed, or transmission. This is visible when the motor points are plotted on Figure 6.2, as shown in Figure 6.10. The cross marking the motor point being above the load curve shows that performance is acceptable in the peak power-rate plot. It should be noted however that continuous speed has been used to plot this point and the speed-torque curve suggests that continuous speed would not be available at this torque, and therefore the point would move to the left depending upon the torque demanded. The motor point lying on the load curve in the continuous power-rate plot shows that performance is marginal – particularly when transmission inefficiency and inertia are taken into account.

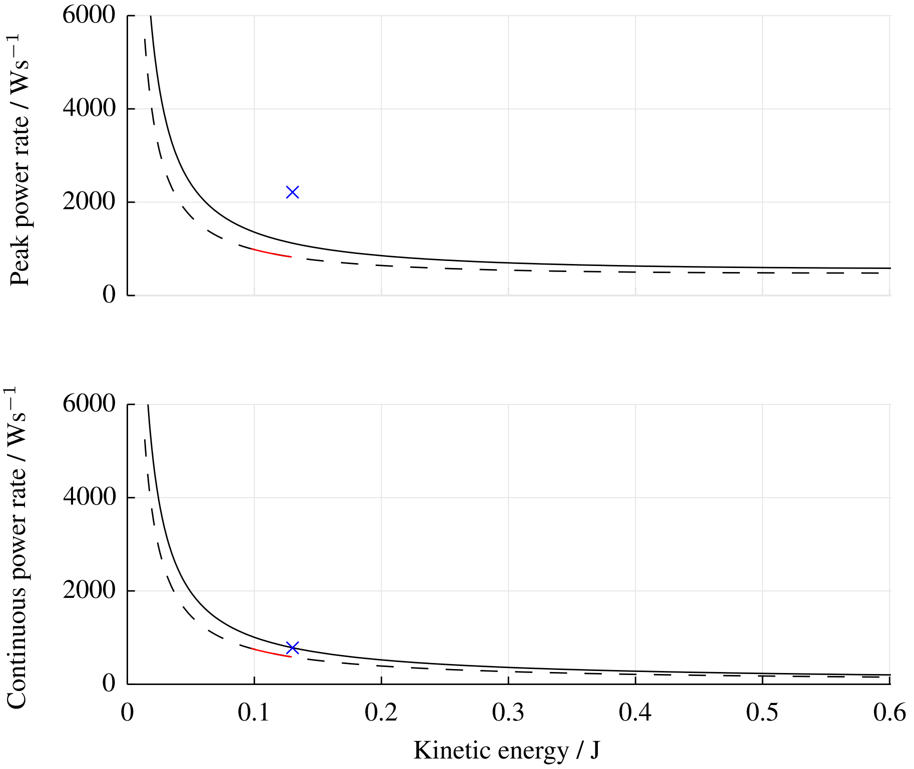

Figure 6.10: Power rate plots showing load curves, the point associated with the parameterised actuator motor, and the feasibility arc (red)

The fact that the peak torque is limited by the motor stall torque, not the current limit, suggests that a trapezoidal move profile would not be the best choice for the actuator, as high speed is not available at peak torque. An s-curve or parabolic move profile would allow a more gradual move from high torque into high speed, in keeping with the speed-torque envelope available. The trade between maximum speed and acceleration for a different move profile would change the load profile. These alternative types of move profile have not been investigated in detail, but are expected to work well with this type of speed-torque curve, and are recommended for future investigation.

Equation 2.25 suggests a minimum transmission ratio of 1:78 for this motor in the application, which is similar to – but below – the 1:98.82 used in the design. The maximum gear ratio is set by the ratio of maximum load speed to maximum continuous motor speed, giving 1:90; however, this is again an artefact of the trapezoidal move profile being used, and would increase to include the designed ratio if a different move profile were chosen.

Shown in red in Figure 6.10 is the feasibility arc associated with the range of possible transmission ratios; this is only shown for the load curve that does not take into account transmission inertia or inefficiency, as it is too short to be visible on the solid curve. Note that it is the accelerating factor of the motor that is limiting the range of ratios in the continuous power rate curve, and this is carried through into the arc on the peak curve. The minimum point of the load curve is not of interest in this case as the transmission ratio is constrained by the peak speed of the motor.

The design methodology shows that the motor is marginally capable of fulfilling the load requirements, and therefore a lower specification motor would not be suitable. More detailed closed-loop modelling of this motor within an actuator should be used to confirm performance.

6.8 Full actuator modelling

Investigations using the techniques described above have confirmed a candidate motor and transmission for the actuator. The models described in Chapter 3 are then used to produce a simulation of the actuator for testing, particularly to investigate transient performance. They are also useful for initial control loop tuning.

Depending on the requirements specification, a model of the linkage between the actuator output and load can be included in the simulation. The generic mechanical model, with appropriate conversions included for rotational to linear transformations, is used for this type of linkage modelling.

Where candidate or example drive cycles are available they may be run in simulation. This is particularly useful to investigate actuator thermal performance. These tests will ensure that the thermal steady-state actuator performance, under representative ambient temperature or coolant conditions, conforms to the specification.

Once performance of the design has been shown to be satisfactory in simulation, a full prototype may be manufactured. Prototype performance may then be used to further validate the model. Control loop parameter tuning initially performed using the model may be transferred to the prototype, however fine tuning and code optimisation for the target microcontroller may be beneficial to improve performance.

6.8.1 Example full actuator model

As described in Section 2.2 *Cummins* variable geometry turbochargers vary exhaust gas flow over the turbine using a sliding nozzle arrangement; the actuator drives this through a pair of push-rods, a rotating yoke mechanism and two wear-blocks. Within each stage of this series of linkages there will be a small amount of friction, elasticity, backlash and inertia introduced, along with ratio changes in force, movement and direction. If backlash were neglected it would be possible to linearly combine these effects into a single lumped load, however if backlash is expected to be significant then each stage would require individual modelling.

The general mechanical model developed in Section 3.7 may be used to represent either an individual or combined series of links and connected to the motor model to produce a full model of the actuation system. The *Cummins* nozzle actuation mechanism has been modelled as two general model components: the rotary portion of the mechanism, including the gearbox transmission, sector gear, cross-shaft and yoke mechanism, as parameterised in Table 6.2; and the linear portion of the mechanism, including the nozzle, push-rods and wear-blocks, as listed in Table 6.3. This full actuator and mechanism model is implemented in *Simulink*, along with the general position control scheme outlined in Section 3.6.

The computationally efficient motor model described in Section 3.5 has been used to provide a speed input to the gear model, populated with the parameters in Table 6.1. It is assumed that PWM voltage control will be at high enough frequency that average value modelling is acceptable; this requires the electrical time constant of the windings, $0.64\,\mathrm{ms}$, to be larger than the PWM interval, $0.12\,\mathrm{ms}$ for the drive system used in testing.

Current control is handled in the drive electronics by a comparator acting on the voltage generated in the common sense resistor. A binary signal from the comparator disables the PWM output when a hardware set current limit of $4\,\mathrm{A}$ is exceeded. This ensures that the battery peak current draw aspect of Requirement 10 is met. A similar binary signal is generated in the model and used to disable the output voltage when the current limit is exceeded.

The control loop shown in Figure 3.10 has been implemented within the model, and also in the test system. In this work the aims are to show that the actuator is capable of meeting the requirements and that the model provides a reasonable representation of the final actuator. Extensive control tuning has therefore not been performed and some simplifications have been introduced. Derivative control is not used, as its benefit is expected to be marginal in a speed-limited system. Set-point weighting for the proportional term is also set to unity, meaning that the system will behave as a standard PI controller with back-calculation anti-windup. Tuning is performed by setting the gain K_p and the integrator constants τ_i and τ_t; the same parameters are used in modelling as in the test system. Considerable further control investigation and tuning would be recommended for a production item, but is beyond the scope of this work.

Performance of the design is assessed through step responses at various operating temperatures and load conditions, and longer duration thermal runs. The simulation results are provided, and compared against real actuator test data, in the next section.

6.9 Performance evaluation

In order to exercise the actuator against a simulated load force a test facility has been constructed. This couples the actuator through a standard *Cummins* turbocharger bearing housing to drive a nozzle. Load is applied to the nozzle via a pneumatic diaphragm valve and measured by a load cell. The position of the nozzle is sensed using a Linear Variable Differential Transformer (LVDT). The whole assembly can be operated within a thermal chamber for testing at elevated temperatures. An image of the test facility is given in Figure 6.11.

Figure 6.11: Full actuator pneumatic test facility

The pneumatic valve is fed from an industrial compressed air supply through a regulator. A $1\,\mathrm{l}$ air reservoir is also attached to the line in close proximity to the valve in order to maintain a constant pressure during rapid position changes. This was confirmed by monitoring the load cell output during step changes. The maximum stroke of the test nozzle and pneumatic valve is $20\,\mathrm{mm}$. Measurement of the load force for a constant valve air pressure demonstrated a relatively constant relationship for the initial $16\,\mathrm{mm}$ of the stroke, followed by a steady increase in load over the final $4\,\mathrm{mm}$, as shown in Figure 6.12. This is due to the internal geometry of the diaphragm valve and is not representative of a typical turbocharger load profile. Consequently only the initial $16\,\mathrm{mm}$ of the stroke was used for testing. This figure also shows some hysteresis variability in the load cell measurements, as position was cycled through the full range several times to generate the plot.

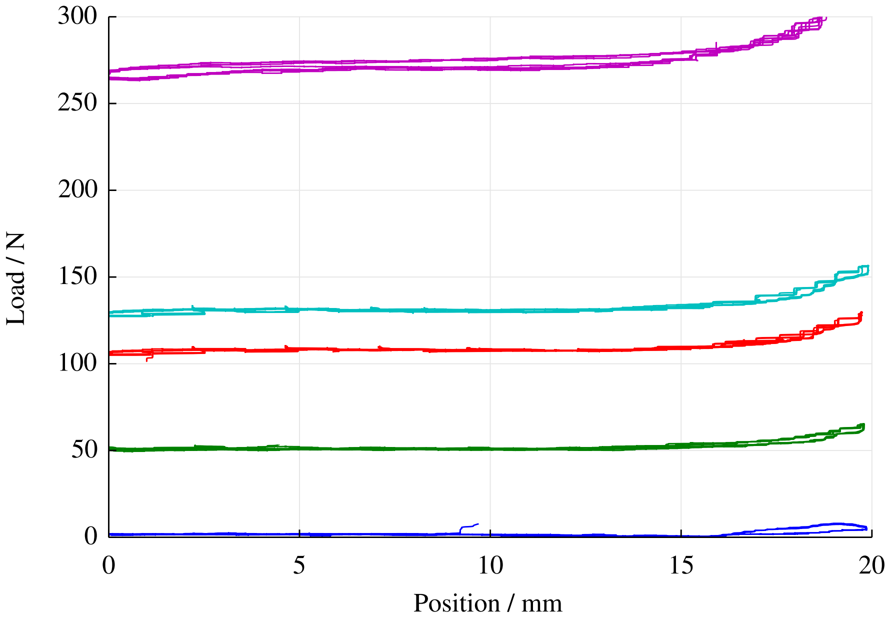

Figure 6.12: Effective nozzle load force with position, for several fixed pneumatic pressures

Motion of the nozzle is mechanically limited at each end of its stroke. This is visible during transition to the fully open $0\,\mathrm{mm}$, or $0\,\%$, position in some of the test results, where an elastic collision can cause bouncing. This has not been included in the modelling and is also not present at the fully closed $16\,\mathrm{mm}$, or $100\,\%$, position.

Manual tuning was carried out on the control gain and time constants in order to give a reasonable response across a range of position demands and load forces, balancing speed of response against minimal positional overshoot – resulting in the parameters shown in Table 6.4. The same control parameters were implemented in the model. A control signal delay of $10\,\mathrm{ms}$ was also included in the model feedback loop (as shown in Appendix C), representative of the processing delay present in the test hardware.

Table 6.4: Actuator control loop tuning parameters used in testing and simulation

PID position gain K_p	200
PID integral time constant τ_i	$\frac{1}{3000}$
PID derivative time constant τ_d	0
PID integral balance compensation time constant τ_t	$\frac{1}{40}$

Rising and falling step responses of $0\,\%$ to $100\,\%$, $5\,\%$ to $95\,\%$ and $45\,\%$ to $55\,\%$ were investigated, at nozzle loads of around $0\,\mathrm{N}$, $100\,\mathrm{N}$ and $170\,\mathrm{N}$, and at temperatures of around $20\,°\mathrm{C}$, $95\,°\mathrm{C}$ and $110\,°\mathrm{C}$. Exact setting of temperature and nozzle load was not possible due to experimental complexity. Prior to elevated temperature testing the actuator was allowed to heat up to reach a thermal equilibrium; however motor internal temperatures may not have returned to their initial value between tests. This is most likely to be significant in the high temperature, high load tests, where heating is fastest and has the largest impact on performance.

Comparison of $5\,\%$ to $95\,\%$ positioning moves for varying load force at $95\,°\mathrm{C}$ is shown in Figure 6.13, along with model performance for the same tests. Whilst there is overshoot in the no load case, for all other results the response is close to critically damped, or exhibits some undershoot before settling. The winding resistance, supply voltage and back-EMF limit the maximum current that can be achieved in the winding to approximately $3.5\,\mathrm{A}$. This limits the maximum speed and rise time of the response. Increasing load further increases the rise time.

Performance at different temperatures for the same $5\,\%$ to $95\,\%$ step response, under three different loads are compared in Figures 6.14 to 6.16, along with model performance. There is an interesting difference in performance with temperature in these results; with no load the rise time decreases as temperature increases, leading to overshoot in the higher temperature cases, however this effect is reversed at higher loads, with increased temperatures giving a slower response. This is explained by the decrease in back-EMF constant and increase in winding resistance at higher temperature. Without load a reduced back-EMF constant allows a higher maximum speed to be reached, i.e. the actuator is speed-limited. When operating against a load, a decreased back-EMF constant produces less torque, and an increased resistance reduces the available voltage, therefore the actuator becomes torque-limited.

Control tuning was a compromise between rise and fall performance at various loads. This is evident in the undershoot seen in Figure 6.17. Some variation is noticeable between successive step responses, particularly for small steps and very low or high load cases. At low load there can be an element of randomness in the nozzle position at stationary, within the backlash limits of the actuator. For small steps

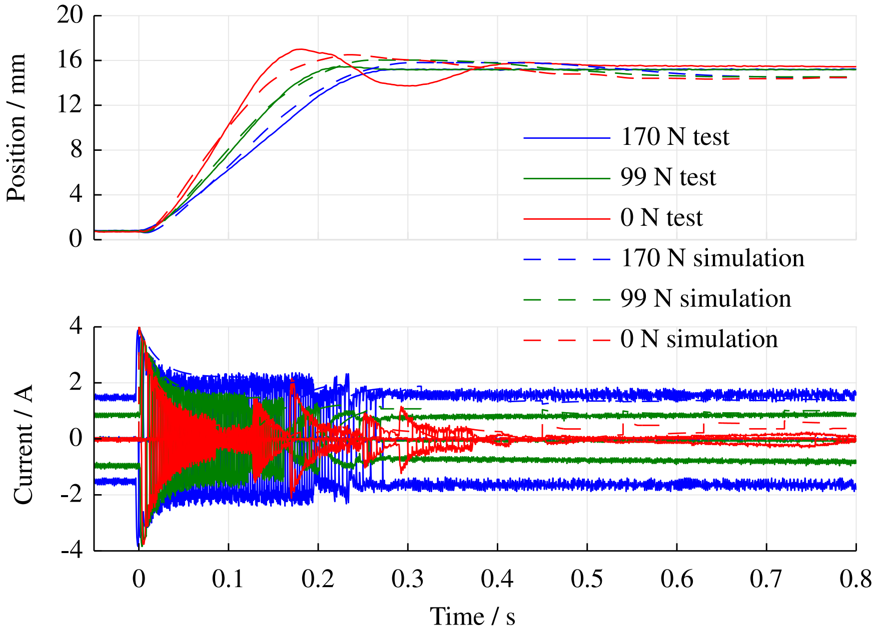

Figure 6.13: 5 % to 95 % position step response tests at 95 °C, for the actuator on the pneumatic test facility and the computationally efficient model

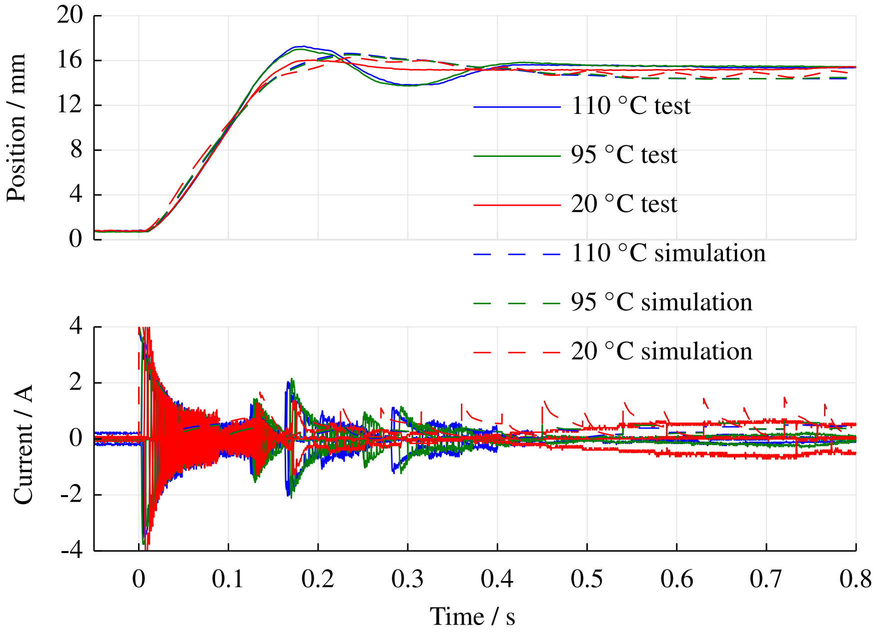

Figure 6.14: 5 % to 95 % position step response tests with no load force, for the actuator on the pneumatic test facility and the computationally efficient model

in position demand the acceleration and deceleration periods constitute a significant portion of the move, and this is therefore more noticeable. The anti-windup suppresses the integral gain initially; during moves under high load this can lead to an undershoot, before the integral term pulls the output to its final value.

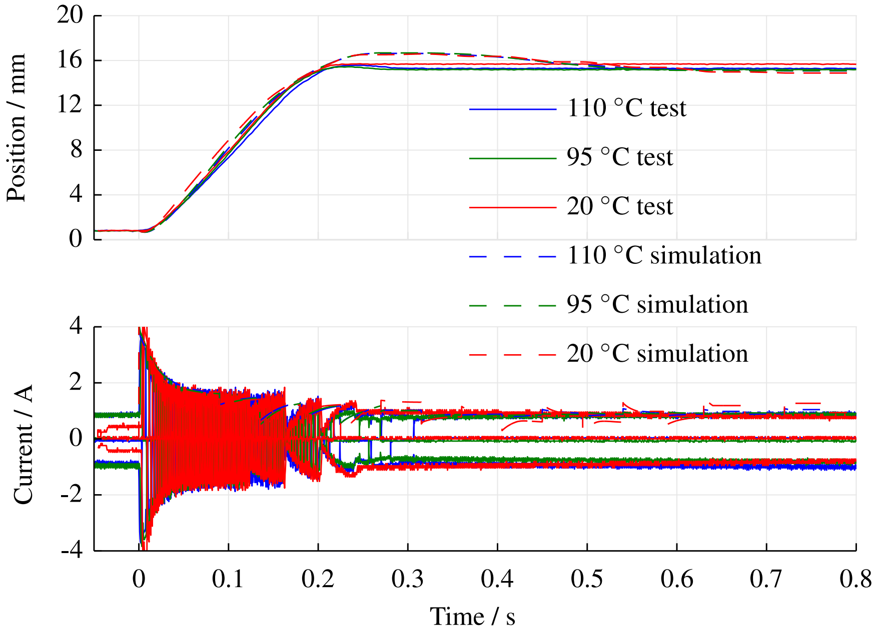

Figure 6.15: 5 % to 95 % position step response tests with 100 N load force, for the actuator on the pneumatic test facility and the computationally efficient model

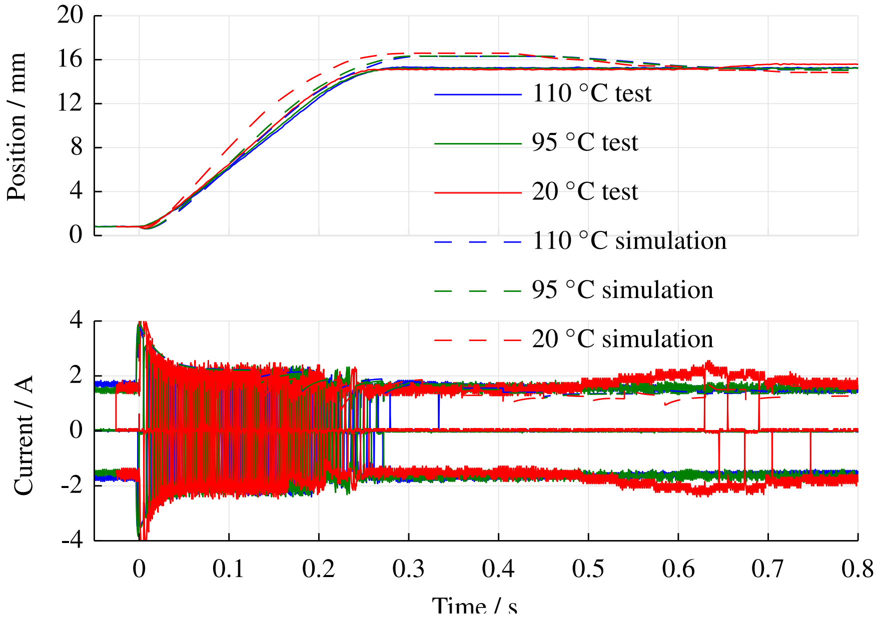

Figure 6.16: 5 % to 95 % position step response tests with full 170 N load force, for the actuator on the pneumatic test facility and the computationally efficient model

In all cases Requirements 2 and 3 (travel time and settling time respectively) are comfortably met, however Requirement 4 (overshoot) is violated in some cases – particularly when the move is in the same direction as the load force. It is expected that more careful tuning of the PID gains could significantly reduce this overshoot,

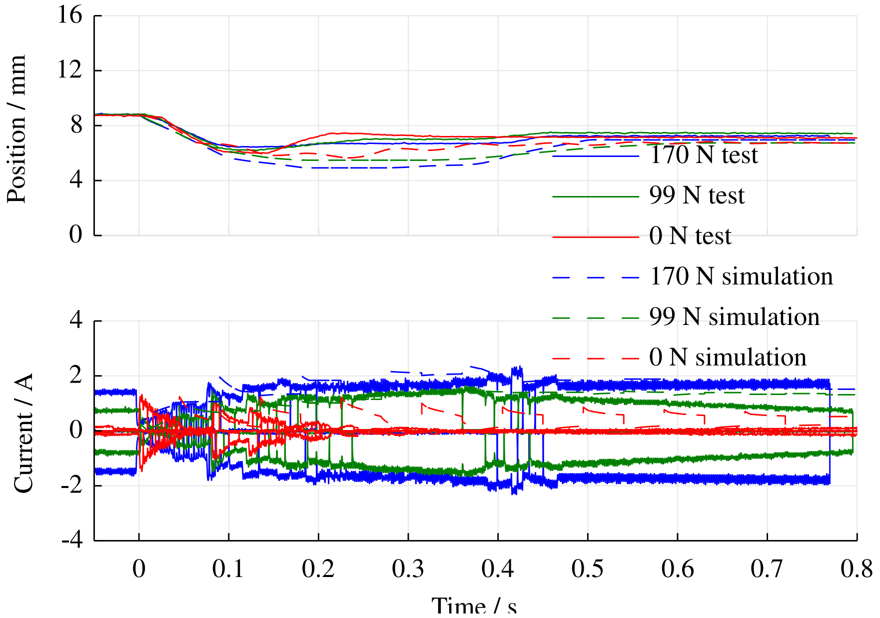

Figure 6.17: 55 % to 45 % position step response tests at 95 °C, for the actuator on the pneumatic test facility and the computationally efficient model

perhaps at the expense of response time. Unfortunately it was not possible to test with varying load as in Requirement 6, as equipment to generate such a load was not available.

All testing was performed at the nominal 24 V. Performance is expected to improve at increased voltages and therefore meet Requirement 11 up to 34 V. Down to 18 V performance may be marginal and Requirement 2 may be violated if this is combined with high temperatures and high loads. This may still be acceptable for the application, depending upon expected operating conditions.

A long duration thermal test was performed during which a 5 % to 95 % square wave position was demanded with a period of 12.036 s and a constant load of 170 N applied, corresponding to Requirement 5. Ambient temperature was maintained at 110 °C, producing 95 °C in the unpowered actuator at thermal equilibrium. The rise in actuator temperatures during this test is shown in Figure 6.18. Winding temperatures were measured based on change of resistance. This required temporary disconnection from the motor drive. This was performed only briefly for measurement purposes, and is not expected to have significantly impacted upon the overall thermal status of the actuator, however the winding temperatures themselves did drop considerably during measurement. Coolant flow was not available for the test and would be expected to give reduced temperatures at the new equilibrium. Winding temperature at the new thermal equilibrium was around 140 °C, below the 155 °C limit for the winding insulation used. For the final 1.5 h of the test the actuator was commanded to hold at the 50 % position, and Figure 6.18 shows the components cooling to a new equilibrium point, with the windings at around 125 °C.

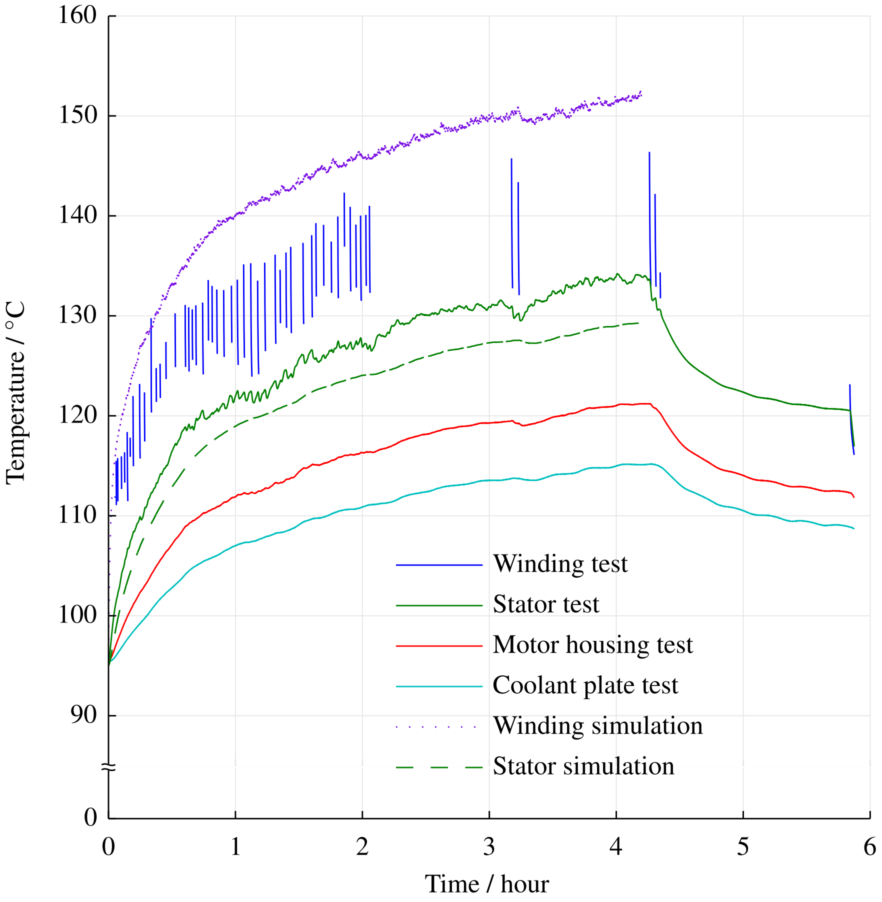

Figure 6.18: Actuator temperature rise during repeated square wave 5 % to 95 % moves in 110 °C ambient conditions without coolant flow, under a constant load of 170 N, for the actuator on the pneumatic test facility and the motor model

Performance was monitored during this test and a steady reduction in maximum speed, and therefore increase in rise time, was seen. The calculated maximum speed during rising steps is shown in Figure 6.19.

Current required to hold position during this test was different between the 5 % and 95 % positions, due to the variation in load force detailed in Figure 6.12. The change in current draw throughout the test is shown in Figure 6.20. This shows significant variation due to the settling process and minor motor stepping around the steady-state value. Current draw in the range of 1.4 A to 2.1 A suggests that the actuator design should meet Requirement 10, however performance is marginal in high-load, repeated-move conditions.

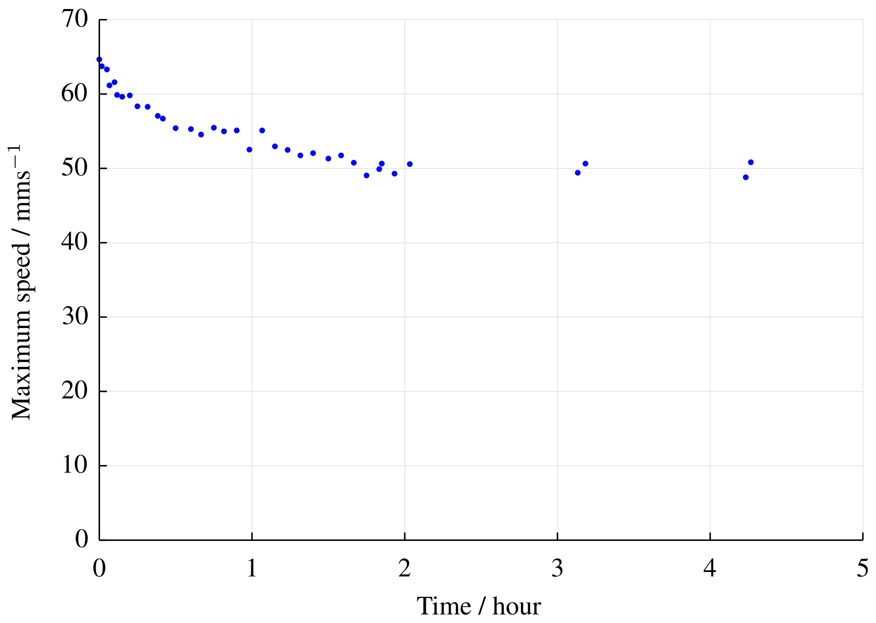

Figure 6.19: Maximum actuator speed during rising steps of a repeated square wave 5 % to 95 % in 110 °C ambient conditions without coolant flow, for the actuator on the pneumatic test facility

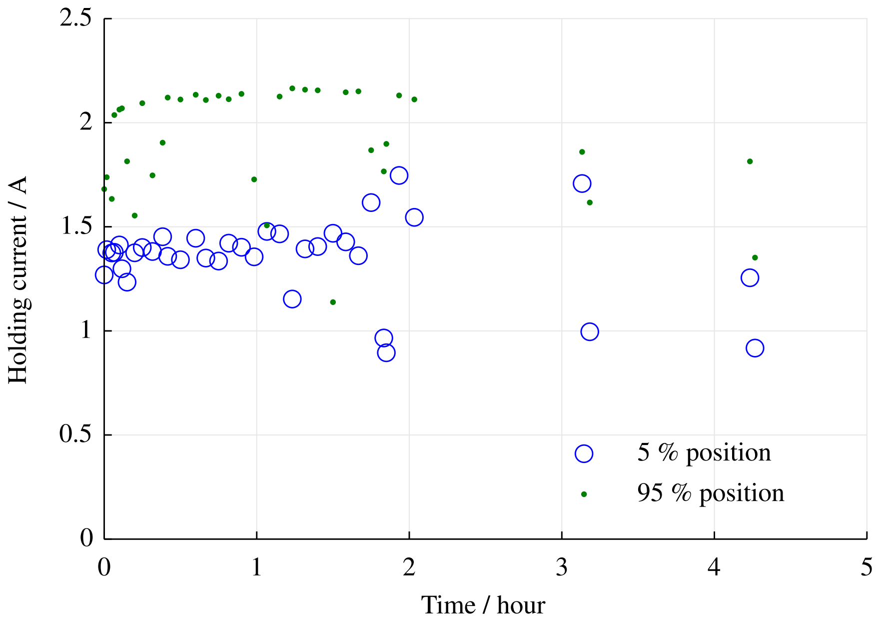

Figure 6.20: Current at holding positions during a repeated square wave 5 % to 95 % in 110 °C ambient conditions without coolant flow, for the actuator on the pneumatic test facility

Through Figures 6.13 to 6.20 model results for the same input parameters are also shown. This demonstrates a reasonable match between the model and the full actuator performance, in both rise time and overshoot. Although an exact match has not been achieved, trends are similar between model and test results, particularly to variation in load and temperature. Settle time and steady-state error do not show a close match, as these are both influenced by nonlinearities in the system, however the match is good enough for both assessment of requirement fulfilment and initial tuning

It should be emphasised that the same tuning parameters were used in both the model and test control loops, and no attempt was made to 'fit' the model results to the test results. Several parameters for the actuator linkage system were estimated, and these are a likely source of error. There is also no account taken of mechanical friction variation with temperature; this may be significant where component expansion affects tolerances in sliding parts.

Thermal model performance, shown for the repeated move portion of Figure 6.18, is reasonable, slightly overestimating winding temperature and underestimating stator temperature. Transient performance is well captured. Although there is around 9 °C error in the peak winding temperature, this is sufficient to establish whether the design is likely to meet its requirement.

6.10 Summary

This chapter has used the mathematical models developed in Chapter 3 and parameterised and validated in Chapters 4 and 5, to investigate the process of designing an actuator. An overall design methodology has been proposed, as shown in Figure 6.1, to work from specifying a set of actuator requirements, through the selection and modelling of subcomponents to achieve them.

Throughout the chapter an example actuator system has been used to demonstrate the process, including: requirements specification; motor parameterisation; the development of move and load profiles; calculation of speed-torque curves; assessment of capability to fulfil the requirements using K-P diagrams; full actuator modelling; and comparison of test actuator performance against model results. This example has demonstrated the process and shown that the models provide a reasonable prediction of actuator performance. This makes them a good candidate for predicting actuator behaviour prior to construction, for control loop testing, and for use within larger system simulations. Likewise the power rate curves used to predict performance offer a fast and easy assessment of actuator system performance against requirements.

A pneumatic test facility has been constructed in order to exercise the actuator under load and at elevated temperatures. This is suitable for further *Cummins* actuator testing as the load is applied against a standard *Cummins* nozzle and bearing housing, making it largely independent of the actuator design itself.

Splitting actuator requirements into those with specific limits, and those that require some form of optimisation, is a useful step in starting a design process. Based on these requirements a series of decisions can be made about the specifics of the design. Tables G.1, 3.6 and 3.7 provide a summary of the effects of different design changes. Once general sub-component types are selected, specific sizes and models must be chosen. A process for comparing the performance of different designs has been specified. This allows components that cannot meet the limiting requirements to be eliminated, whilst allowing an optimal selection to be made from the remaining candidates. Finally a general control loop is proposed for position control; this must be tuned for the specific design and requirements under consideration.

Modelling of the components has been shown to be important in accounting for thermal effects on speed and torque capability. Model simulation allows the designer to evaluate performance at varying fidelities as the design progresses. Full modelling of the final design is recommended to ensure that the requirements will be met and to assist in tuning the control loop.

Further improvement in model accuracy might be expected if a more thorough parameterisation of the transmission and mechanical linkage system were undertaken – particularly if mechanical thermal effects could be parameterised and included within the models.

The work in this chapter demonstrates the modelling and actuator design process outlined in this thesis. It shows that the process may be used to assess actuator performance and to confirm that a particular design will fulfil requirements prior to manufacture. It also gives an example of the level of error that might be expected in typical actuator simulation results.

Chapter 7

Conclusions

7.1 Summary

This work has outlined the research challenges in turbocharger actuator specification. The primary knowledge gap, particularly for a company such as *Cummins*, is the integration of tools and techniques to enable design performance prediction and to support decision making, optimisation and selection. It has then gone on to develop, parameterise and validate models of actuators, and shown how to use appropriate fidelity models to assess candidate actuator design performance. A motor testrig has been assembled and five different sample motors have been parameterised and used for model validation. A pneumatic test facility for complete actuators has also been constructed and used to measure actuator performance. Code has been written to drive the half-bridge circuit and control the motors and the actuator during testing.

Test results have been compared against model simulations to demonstrate that correctly parameterised models can provide a close approximation to motor and full actuator performance. Suggestions have been made to aid a designer in specifying an actuator for the application. Where the decision depends upon the specific application requirements, mathematical tools have been provided to assist in making an optimal selection. A summary of key challenges and achievements in the work are detailed below.

A review of actuator construction and operation has identified that:

- Brushless permanent magnet motors currently provide the best solution for compact, robust, high torque actuator performance (Section 2.3). However, switched reluctance motors may be considered if the cost or availability of rare-earth permanent magnet materials becomes an issue.
- Direct drive linear and rotary actuators are not appropriate for the requirements, therefore a transmission is required to generate sufficient torque at the output (Section 2.5). A simple spur gear transmission will be the most cost-effective, however planetary gearboxes might be considered if reduction in overall space-claim were a high priority.

- Six-step commutation, based on hall sensor feedback, is the best option for electrically commutating the machine for position control applications, even with a sinusoidal back-EMF machine (Section 3.2.2).

Model development and validation has shown that:

- A four-parameter thermal model can be parameterised using sample motor tests (Chapter 4) and provides a reasonable prediction of winding temperatures (Chapter 5) to ensure that important limits are not exceeded during operation. Higher-order models are difficult to parameterise and lower-order models do not provide sufficient accuracy. Alternative low-parameter thermal models were also considered (Appendix E) and rejected due to difficulties in parameterisation or poor performance.

- Models may be produced at varying fidelities, allowing results of the required accuracy to be produced with minimal computational burden. For example, computationally efficient averaged-value electrical motor models can provide fast simulation of long duration thermal tests (Section 3.5 and Chapter 5). Acausal modelling provides accurate results and straightforward construction, without requiring detailed mathematical descriptions of the system (Appendix D), but at a financial and simulation-duration cost.

- A general mechanical model may be parameterised to express various stages in an actuator transmission or linkage mechanism (Sections 4.5 and 6.5). Although constructed from well known physical relationships, a complete mechanical model at this level could not previously be found in the literature.

- Datasheet parameters are suitable for parametrising motor models only where there is a good understanding of the manufacturer's parameter definitions (Chapter 5 and Appendix H). A complete list of parameters required for the modelling process has been identified. Parameters can be determined through testing sample motors, without requiring a knowledge of internal design (Chapter 4). These tests might also be used by a component integrator such as *Cummins* to request the correct data from prospective suppliers.

- PWM switching using scheme C or F$'$ from Table 2.1 is a good choice for positioning applications, based on good control of the phase currents during braking, and a linear duty-ratio to average-voltage relationship (Appendix G). This information is not readily available in the literature and is important for achieving design performance.

The design methodology developed includes the following effects within the modelling process:

- Accounting for the variation in speed-torque curves due to machine operating temperature has been shown to be critical to the actuator assessment process (Sections 5.2 and 6.7).
- Continuous and peak power-rate curves are useful for initial appraisal of motors against actuator requirements and for selection of suitable gear ratios (Section 6.7). Elevated thermal conditions and move profile design should be part of the power-rate curve decision process. This is an extension of the current literature on using power-rate curves for mechatronic design.
- PID type control schemes are suitable for actuator positioning applications, and more work is recommended to investigate suitable tuning methods (Section 2.4). Processing delays should be included within the modelling process, as significantly more accurate results will be produced (Chapter 5).

The remainder of this chapter provides more detail on specific novel areas in which this thesis has contributed to the research literature. Several opportunities to extend the work are discussed, and a summary of papers published from the work is given.

7.2 Contribution to knowledge

This research makes a significant contribution by extending previous work in a number of distinct areas to develop an overall actuator design methodology. This allows a user to work from a specific set of actuator requirements through to an evaluated design. The areas of significant novel contribution are noted below.

7.2.1 Thermal modelling

To model a machine thermally, without access to its material characteristics and internal structure, a low-order lumped thermal model has been developed (Section 3.3), implemented and validated (Section 5.4). Although this does not provide the same detail as a high-order lumped or FE model, it provides the ability to characterise the thermal behaviour of performance-limiting components (windings and magnets) with a low number of parameters, in a computationally efficient model, without requiring expert knowledge of the motor construction. Specific motor component temperatures cannot be tracked with a very basic two-parameter motor thermal model.

The inclusion of thermal behaviour within actuator models is essential for the *Cummins* application, as it has been shown that actuator operating temperatures can come close to component temperature limits during operation. Datasheet motor performance parameters are not suitable for use in this case, as continuous operation at temperatures considerably in excess of those used in manufacturer specifications is the norm.

7.2.2 Computationally efficient commutation modelling

A modification of the standard three-phase commutating brushless motor model is presented (Section 3.5). This analytically includes the effects of commutation without the need to time-step a simulation at a rate above the commutation frequency. Although there is a small sacrifice in accuracy, there is a significant decrease in simulation time. The high simulation speed allows long duration thermal simulations and evaluation of steady-state conditions approximately ten-times faster than a fully commutated model, making the models a useful tool for assessing the impact of parameter changes. This will enable *Cummins* to perform large-scale parameter sensitivity studies and thermal performance investigations in a considerably shorter timeframe and with lower computational overheads.

7.2.3 Combined motor-transmission specification

Published academic work has provided a set of equations and plotting techniques for evaluating the ability of motor-transmission pair to achieve a specified set of actuator requirements. These may be used to select a set of candidates for optimisation according to application specific criteria. In order to assess motors within this process a set of motor performance parameters is required. Although these are often available from manufacturer datasheets, there has previously been no mechanism for investigating the impact of changes in fundamental motor parameters on the overall suitability of the motor. This led to difficulty in considering motor suitability for increased temperatures without physical testing.

The new thermal and computationally efficient models are combined to calculate the required parameters for motor-transmission assessment (Section 3.3). This allows investigation of the effects of parameter changes on overall actuator performance, particularly at high temperatures. The combined motor-transmission specification will allow *Cummins* to efficiently determine subcomponents that meet the actuator requirements, aiding the overall design process.

7.2.4 Sample motor parameter extraction

In order to support motor electromagnetic and thermal modelling, a set of motor tests has been evaluated which allow extraction of the necessary model parameters from a sample motor (Chapter 4). These have been designed such that they do not require any machine disassembly and can be performed using simple test facilities. Even where detailed parameters are available from a supplier, these tests confirm that the parameters are specified correctly for the model, and that the supplier's figures are correctly applied. For example the meaning of the motor 'torque constant' differs between manufacturers, depending on the current waveform shape, motor speed and ambient temperature for which it is defined.

7.3 Further work

Several possibilities for extending this work have been identified – these are briefly discussed below.

7.3.1 Transmission parameterisation

Although a comprehensive process for parametrising and validating the motor models has been presented in this work, transmission parameters have been estimated based on manufacturer-supplied data and information from *Cummins*. These parameters are expected to have significant uncertainty bounds, and would benefit from more accurate parameterisation and model validation. Of particular interest is the variation in mechanical parameters due to temperature variation, possibly including any self-heating within them. This is expected to be significant where grease or similar lubricants are used, or where thermal expansion is likely to change tolerances.

Techniques for transmission testing were briefly discussed in Section 2.6. These ideas could be used to construct a power recirculating test setup to allow parameterisation testing to be performed. Testing at a range of temperatures could be carried out through the use of a thermal chamber or similar. Many of the tests and validation procedures described in this thesis for the motor could have direct analogues developed for the transmission.

7.3.2 Alternative transmission designs

Spur gear trains were primarily considered within the modelling undertaken in this work, although a review of several different transmission options was presented in Section 2.5. The general mechanical model could be applied to many of the other gear options discussed; however careful consideration of the parameters and the combination of stages would be required. For example, a model of a planetary gearbox could be constructed from combinations of the general model; however the parallel nature of the planet gears would need to be included when calculating friction and inertia.

Leadscrew, or similar rotary-to-linear gear designs, could be used to reduce the volume of the transmission, provided they could be effectively integrated into the turbocharger bearing housing.

7.3.3 Control tuning

A general positioning control loop has been proposed in Section 3.6. This has a compact set of parameters to enable straightforward tuning; however techniques for setting those parameters have not been considered. It is expected that significantly improved control performance could be achieved if the load force on the nozzle could be estimated or measured during operation; this would allow the feedforward path to be used to directly compensate for this.

Whilst a reasonable response may be obtained through experimental testing, aided by the simulation of control performance in the models, formal techniques for setting these could be considered. Such techniques should take account of uncertainty in the system itself, including component tolerances, part-to-part variation and through-life wear, to ensure that positioning performance was maintained. The impact of sampling delays and finite measurement resolution could also be assessed. 'Robust control' methods allow this type of system uncertainty to be factored into the tuning process. If robustness is found to be a significant issue then specific control designs such as 'H-inifinity loop shaping', or 'Sliding Mode Control' could be considered [11, 229].

7.3.4 Greater than three-phase motor design

As discussed in Section 2.3.3, Alternating Current (AC) motors typically use three-phase power and there is no benefit in moving to a four-phase supply. Academic research into five and higher phases is ongoing and has found potential improvements in torque. Whilst there would be issues of electronic component cost and non-standard design to contend with, benefits in fault tolerance and torque density may merit further investigation of this as an actuator option.

7.3.5 Terminal voltage

As noted in Chapter 2, automotive power supplies are conventionally either 12 V or 24 V. With the trend towards increased electrification, leading towards fully electric vehicles, the standard voltages may increase to 48 V or higher. Actuators may be constructed to operate from a fixed voltage, or they might include built-in converters to step-up or step-down the voltage. This latter approach leads to reduced part proliferation, however it also increases the individual component cost. It is feasible that the performance improvements gained through motor operation at an increased terminal voltage may outweigh the additional costs of including a voltage converter. This would also allow for compensation of fluctuations in battery voltage, due to changes in vehicle operating conditions. Investigation of the possibilities for including a DC/DC voltage converter within the actuator system is recommended. It may also be possible to bring aspects of the voltage conversion within the motor drive circuit itself, thereby reducing the number of components.

7.3.6 Number of rotor magnet pole-pairs

The models developed in this work allow for investigation of the impact of changing the magnet pole-pair number on the motor performance; it was seen in Chapter 5 that higher pole-pair numbers led to a suppression in the mid-point of the speed-torque curve. Given otherwise equivalent motor parameters this would suggest that torque performance would be better for a lower pole-pair count; however the positioning resolution of the actuator is also directly influenced by this. Therefore a trade-off study could be carried out to investigate the impact of magnet count on overall actuator design.

7.3.7 External rotor design

Within the set of sample motors tested there is one external rotor machine, the *Maxon* EC-Flat motor. It is noticeable from the specifications in Table H.1 that this provides a very compact package for a similar power output. These numbers for motor size cannot be directly compared, as the *Maxon* motor does not have any housing around its external rotor, and therefore would need an additional housing for use in an automotive environment. Nevertheless the use of external rotor machines warrants consideration, as the low space claim, high static torque and large pole-pair numbers might provide significant advantages.

An investigation of external rotor machine packaging for use in an actuator would need to take into account cooling of the windings, as they are less accessible in this type of machine design. A classic argument against their use in positioning applications is the large increase in inertia that the external rotor topology introduces, however this may be less of an issue with modern machines. A recent review of the performance differences between interior and exterior rotor machines for robotics applications found that equivalent exterior rotor machines offered significant improvements in motor constants and stall torque density [36].

7.3.8 Active thermal regulation

Section 2.4.6 discussed techniques for actively monitoring winding temperatures within the machine. This should allow operation closer to the actuator's thermal limits, potentially allowing reductions in other aspects of the design. The models developed in Chapter 3 would be well suited to use in online thermal estimation and therefore this could form a natural extension of this work. As motor temperatures depend heavily on the demanded position and the load torque it is subjected to, an understanding of the intended drive cycle would be required to assess the potential for performance improvement in this area. The models could be simulated with a variety of drive cycles to investigate motor thermal conditions and consider whether the likely gains would merit the extra complexity of active temperature regulation.

7.4 Publications

During the course of this PhD work two publications have been submitted, reviewed, accepted and presented into the research literature. Details of the conferences and the paper abstracts are given here.

1. J. Welford, J. Apsley, A. Forsyth, and A. Sophian. Fidelity requirements in brushless permanent magnet motor modelling. In *Power Electronics, Machines and Drives (PEMD), 6th International Conference on*, pages 1-6, 2012.

   The paper discusses the development and validation of motor simulation models to aid in the design of actuators for use with automotive variable geometry turbochargers. The specific focus is on the benefit of increasing the fidelity of the motor model, against the tradeoff of increased complexity. Several separate models of the same brushless permanent magnet motor are developed and validated against measurements made from a sample motor. These results, along with the simulation time required for different types of model, are presented and used to draw conclusions on the appropriate fidelity of model for different types of analysis.

2. J. Welford, J. Apsley, A. Forsyth, and A. Sophian. Computationally efficient brushless permanent magnet motor modelling. In *Power Electronics, Machines and Drives (PEMD), 7th International Conference on*, 2014.

   Physically derived mathematical models of motors are frequently used to simulate system performance. These can be constructed at various levels of fidelity depending on the application requirements. To accurately capture the dynamics of brushless permanent magnet motors, the effects of electrical commutation should be included. Short time-step simulations are required to include electrical effects explicitly. If the experimental time durations are large, for example during thermal analysis, this type of model can take unacceptably long to run.

   This work develops a new motor model that includes commutation effects implicitly, and is therefore capable of operating using increased time-steps, significantly reducing simulation time. The effects of winding resistance and inductance within the model ensure that it produces similar results to a fully commutated 3-phase model.

   The new model is demonstrated through comparison against other models and real motor test results. This validation process is performed in the frequency domain.

A further publication to detail the complete design methodology, including the use of the computationally efficient model, thermal model and K-P diagrams, is being investigated. Work is currently being undertaken, using the test facilities developed in this thesis, to support this.

References

[1] P. F. Smith, S. M. Prabhu, and J. Friedman. Best practices for establishing a model-based design culture. *SAE Technical Paper*, 2007.

[2] Cummins Turbo Technologies. Cummins internal documents and correspondence. 2010.

[3] Cummins Turbo Technologies. Cummins Turbo Technologies Website. `http://www.holset.co.uk`, August 2011.

[4] F. Roos. *Towards a methodology for integrated design of mechatronic servo systems*. PhD thesis, KTH, Stockholm, Sweden, 2007.

[5] D. Iles-Klumpner, I. Serban, and M. Risticevic. Automotive electrical actuation technologies. In *Vehicle Power and Propulsion Conference, 2006. VPPC'06. IEEE*, pages 1 – 6. IEEE, 2006.

[6] M. Algrain and U. Hopmann. Diesel engine waste heat recovery utilizing electric turbocompound technology. In *DEER Conf., Newport, Rhode Island*, volume 29, pages 25 – 29, 2003.

[7] U. Hopman and R.W. Kruiswyk. Diesel engine waste heat recovery utilizing electric turbocompound technology. In *DEER Conf., Newport, Rhode Island*, 2005.

[8] J.R. Bumby, E.S. Spooner, J. Carter, H. Tennant, G.G. Mego, G. Dellora, W. Gstrein, H. Sutter, and J. Wagner. Electrical machines for use in electrically assisted turbochargers. In *Power Electronics, Machines and Drives (PEMD), 2nd International Conference on*, volume 1, pages 344 – 349, 2004.

[9] S. Kim and J.K. Seok. Comprehensive PM motor controller design for electrically assisted turbo-charger systems. In *Energy Conversion Congress and Exposition (ECCE), 2013 IEEE*, pages 860 – 866. IEEE, 2013.

[10] D. Angleviel, J. Alzingre, L. Billet, and D. Frachon. Development of a Contactless Brushless DC Actuator for Engine Management. *SAE Technical Paper*, 2006.

[11] F. S. Ahmed, S. Laghrouche, and M. El Bagdouri. Analysis, modeling, identification and control of pancake DC torque motors: Application to automobile air path actuators. *Mechatronics*, 22(2):195 – 212, 2012.

[12] K. Spanner. Survey of the various operating principles of ultrasonic piezomotors. In *Proceedings of the 10th International Conference on New Actuators*, 2006.

[13] T. Sashida and T. Kenjo. *An introduction to ultrasonic motors*, volume 28. Oxford Science Publications, 1993.

[14] S. Ueha and Y. Tomikawa. *Ultrasonic motors: Theory and applications*, volume 29. Oxford Science Publications, 1993.

[15] K. Uchino. Piezoelectric ultrasonic motors: Overview. *Smart Materials and Structures*, 7(3):273, 1998.

[16] *Ultrasonic motors catalogue*. PI, 2009.

[17] *Piezo Nano Positioning - Inspirations Catalogue*. Physik Instrumente (PI) GmbH & Co., 2009.

[18] K. Uchino, S. Cagatay, B. Koc, S. Dong, P. Bouchilloux, and M. Strauss. Micro piezoelectric ultrasonic motors. *Journal of electroceramics*, 13:393 – 401, 2004.

[19] J. H. Oh, H. E. Jung, J. Lee, K. J. Lim, H. H. Kim, B. H. Ryu, and D. H. Park. Design and performances of high torque ultrasonic motor for application of automobile. *Journal of electroceramics*, 22(1):150 – 155, 2009.

[20] *Ultrasonic motor general catalogue*. Shinsei, 2005.

[21] A. Basak and F. J. Anayi. A DC linear motor with a square armature. *Energy Conversion, IEEE Transactions on*, 10(3):462 – 469, 1995.

[22] A. Basak. *Permanent-magnet DC linear motors*, volume 40. Oxford Science Publications, 1996.

[23] R. C. Okonkwo. Design and performance of permanent-magnet DC linear motors. *Magnetics, IEEE Transactions on*, 42(9):2179 – 2183, 2006.

[24] J. Carter, R. E. Clark, and G. W. Jewell. Linear reluctance actuator for variable-geometry turbo-chargers. In *Proc. Fourth Int. Symp. Linear Drives for Industry Applications*, pages 564 – 567, 2003.

[25] J. Carter. Variable geometry turbine patent, 2003. Patent No.: US 7,140,849 B2.

[26] S. Gibson, G. W. Jewell, and R. E. Clark. Variable-airgap, cylindrical, linear variable reluctance actuators for high-force, medium-stroke applications. *Electric Power Applications, IET*, 3(4):352 – 362, 2009.

[27] N. Mohan, T. M. Undeland, and W. P. Robbins. *Power electronics: Converters, applications, and design*. Wiley, 2003.

[28] D. A. Marckx, G. J. Hjelmeland, A. K. Wallace, A. R. von Jouanne, J. Han, and X. Zhou. Linear Actuator Using the Switched Reluctance Motor. Technical report, Office of Naval Research, 2004.

[29] D. Murphy. Rare Earth Sourcing Challenges for Permanent Magnets, from the Perspective of the Miner and Processor. In *Making rare earth magnets rarer, UK Magnetic's Society and IET Seminar on*. Less Common Metals, November 2011.

[30] C. Pollock and H. Pollock. Flux Switching and Synchronous Reluctance Motors and Generators. In *Making rare earth magnets rarer, UK Magnetic's Society and IET Seminar on*. Less Common Metals, November 2011.

[31] S. Randall. SR Machines – Nothing Rare About Reluctance. In *Making rare earth magnets rarer, UK Magnetic's Society and IET Seminar on*. Nidec Drives, November 2011.

[32] B. Mecrow. Switched Reluctance Concepts for Electric Vehicle Applications. In *Making rare earth magnets rarer, UK Magnetic's Society and IET Seminar on*, November 2011.

[33] S.A. Krishnan. Motor design for a linear position actuator. Master's thesis, University of Manchester, 2011.

[34] J.R. Hendershot and T.J.E. Miller. *Design of Brushless Permanent-Magnet Machines*. Motor Design Books, 2010.

[35] P. Yedamale. *Brushless DC (BLDC) motor fundamentals, Application note 885*. Microchip.

[36] J. W. Sensinger, S. D. Clark, and J. F. Schorsch. Exterior vs. Interior Rotors in Robotic Brushless Motors. *IEEE International Conference on Robotics and Automation*, 13:9 – 13, 2011.

[37] W. D. Callister. *Materials science and engineering: An introduction*. John Wiley & Sons New York, 4 edition, 1997.

[38] J. Malaizé and J. Lévine. An Observer-based design for cogging forces cancellation in permanent magnet linear motors. In *Decision and Control, 2009 held jointly with the 2009 28th Chinese Control Conference. CDC/CCC 2009. Proceedings of the 48th IEEE Conference on*, pages 6811 – 6816.

[39] Z. Q. Zhu and D. Howe. Influence of design parameters on cogging torque in permanent magnet machines. *Energy Conversion, IEEE Transactions on*, 15(4):407 – 412, 2000.

[40] J. F. Gieras. Analytical approach to cogging torque calculation of PM brushless motors. *Industry Applications, IEEE Transactions on*, 40(5):1310 – 1316, 2004.

[41] M. S. Islam, S. Mir, and T. Sebastian. Issues in reducing the cogging torque of mass-produced permanent-magnet brushless DC motor. *Industry Applications, IEEE Transactions on*, 40(3):813 – 820, 2004.

[42] P. Lefley, L. Petkovska, and G. Cvetkovski. Optimisation of the design parameters of an asymmetric brushless DC motor for cogging torque minimisation. In *Power Electronics and Applications (EPE 2011), Proceedings of the 2011-14th European Conference on*, pages 1 – 8. IEEE, 2011.

[43] S. J. Sung, S. J. Park, and G. H. Jang. Cogging Torque of Brushless DC Motors Due to the Interaction Between the Uneven Magnetization of a Permanent Magnet and Teeth Curvature. *Magnetics, IEEE Transactions on*, 47(7):1923 – 1928, 2011.

[44] Y. Duan and D. M. Ionel. A review of recent developments in electrical machine design optimization methods with a permanent magnet synchronous motor benchmark study. In *Energy Conversion Congress and Exposition (ECCE), 2011 IEEE*, pages 3694 – 3701. IEEE, 2011.

[45] T. Hamiti, C. Gerada, and M. Rottach. Weight optimisation of a surface mount permanent magnet synchronous motor using genetic algorithms and a combined electromagnetic-thermal co-simulation environment. In *Energy Conversion Congress and Exposition (ECCE), 2011 IEEE*, pages 1536 – 1540, Sept. 2011.

[46] A. Sarikhani and O. A. Mohammed. Multiobjective Design Optimization of Coupled PM Synchronous Motor-Drive Using Physics-Based Modeling Approach. *Magnetics, IEEE Transactions on*, 47(5):1266 – 1269, 2011.

[47] E. Fitan, F. Messine, and B. Nogarede. The electromagnetic actuator design problem: A general and rational approach. *Magnetics, IEEE Transactions on*, 40(3):1579 – 1590, 2004.

[48] *High Precision Drives and Systems - Program 2013/14.* Maxon Motor, 2013.

[49] Z. Q. Zhu, S. Bentouati, and D. Howe. Control of single-phase permanent magnet brushless DC drives for high-speed applications. In *Power Electronics and Variable Speed Drives, 2000. Eighth International Conference on (IEE Conf. Publ. No. 475)*, pages 327 – 332. IET, 2000.

[50] E. Levi. Multiphase electric machines for variable-speed applications. *Industrial Electronics, IEEE Transactions on*, 55(5):1893 – 1909, 2008.

[51] T. Sebastian. Temperature effects on torque production and efficiency of PM motors using NdFeB magnets. *Industry Applications, IEEE Transactions on*, 31(2):353 – 357, 1995.

[52] N. Bianchi, S. Bolognani, and F. Luise. Potentials and limits of high-speed PM motors. *Industry Applications, IEEE Transactions on*, 40(6):1570 – 1578, 2004.

[53] H. Mitsui, K. Yoshida, Y. Inoue, and S. Kenjo. Thermal cyclic degradation of coil insulation for rotating machines. *Power Apparatus and Systems, IEEE Transactions on*, (1):67 – 73, 1983.

[54] R. H. Welch Jr and G. W. Younkin. How temperature affects a servomotor's electrical and mechanical time constants. In *Industry Applications Conference, 2002. 37Th IAS Annual Meeting. Conference Record of the*, volume 2, pages 1041 – 1046. IEEE, 2002.

[55] J. Lepkowski. *Motor Control Sensor Feedback Circuits, Application note 894.* Microchip, 2003.

[56] H. C. Lin and C. L. Chen. Torque ripples due to positioning errors of Hall sensors and armature windings for PWM permanent magnent brushless dc motors. In *Industrial Electronics and Applications (ICIEA), 2011 6th IEEE Conference on*, pages 698 – 702. IEEE, 2011.

[57] J. Shao, D. Nolan, and T. Hopkins. A novel direct back EMF detection for sensorless brushless DC (BLDC) motor drives. In *Applied Power Electronics Conference and Exposition, APEC*, volume 1, pages 33 – 37. IEEE, 2002.

[58] J. Shao. Direct back EMF detection method for sensorless brushless DC (BLDC) motor drives. Master's thesis, 2003.

[59] J. Shao and D. Nolan. Further improvement of direct back EMF detection for sensorless brushless DC (BLDC) motor drives. In *Applied Power Electronics Conference and Exposition, 2005. APEC 2005. Twentieth Annual IEEE*, volume 2, pages 933 – 937. IEEE, 2005.

[60] A. K. Bansal, R. A. Gupta, and R. Kumar. Fuzzy estimator for sensorless PMBLDC motor drive under speed reversal. In *Power Electronics (IICPE), 2010 India International Conference on*, pages 1 – 7. IEEE.

[61] J. Zambada. *Sensorless Field Oriented Control of PMSM Motors, Application note 1078*. Microchip.

[62] Q. Wu, G. Meng, H. Xiong, H. Li, and L. Zhou. A novel starting control for sensorless three-phase permanent-magnet brushless DC motor. In *Electric Information and Control Engineering (ICEICE), 2011 International Conference on*, pages 1081 – 1087. IEEE.

[63] M. Schroedl. Sensorless control of AC machines at low speed and standstill based on the INFORM method. In *Industry Applications Conference, Conference Record of the*, volume 1, pages 270 – 277. IEEE, 1996.

[64] J.H. Jang, S.K. Sul, J.I. Ha, K. Ide, and M. Sawamura. Sensorless drive of surface-mounted permanent-magnet motor by high-frequency signal injection based on magnetic saliency. *Industry Applications, IEEE Transactions on*, 39(4):1031 – 1039, 2003.

[65] J.H. Jang, J.I. Ha, M. Ohto, K. Ide, and S.K. Sul. Analysis of permanent-magnet machine for sensorless control based on high-frequency signal injection. *Industry Applications, IEEE Transactions on*, 40(6):1595 – 1604, 2004.

[66] Y. Hou, S. Sun, and E. Li. Detection for Rotor Position of Brushless DC Motor Based on Pulse Injection Method. *Applied Informatics and Communication*, pages 407 – 412, 2011.

[67] V. Krishnakumar and S. Jeevanandhan. Four switch three phase inverter control of BLDC motor. In *Electrical Energy Systems (ICEES), 2011 1st International Conference on*, pages 139 – 144. IEEE.

[68] S.P. Kanjhani, M.S. Gupta, and H. Singh. Review of different control topologies for the permanent magnet brushless dc motor drives. *International Journal of Advanced Engineering Research and Studies*, 2012.

[69] W. Brown. *Brushless DC Motor Control Made Easy, Application note 857*. Microchip, 2002.

[70] D. Y. Ohm and R. J. Oleksuk. Influence of PWM schemes and commutation methods for DC and brushless motors and drives. In *PE Technology Conference, Stephens Convention Center (Rosemont, IL, US)*, 2002.

[71] T. Åsberg. PI-control of an Electrically Actuated Throttle. Master's thesis, KTH, Stockholm, Sweden, April 2013.

[72] P. K. Nandam and P. C. Sen. Analog and digital speed control of DC drives using proportional-integral and integral-proportional control techniques. *Industrial Electronics, IEEE Transactions on*, (2):227 – 233, 1987.

[73] F.J. Lin. Real-time IP position controller design with torque feedforward control for PM synchronous motor. *Industrial Electronics, IEEE Transactions on*, 44(3):398 – 407, 1997.

[74] K. J. Åström and T. Hägglund. *PID Controller: Theory, Design and Tuning*. Instrument Society of America, 2nd edition, 1995.

[75] D.Y. Ohm. Analysis of PID and PDF compensators for motion control systems. In *Industry Applications Society Annual Meeting, Conference Record of the*, pages 1923–1929 vol.3, 1994.

[76] G. Ellis and R. D. Lorenz. Comparison of motion control loops for industrial applications. In *Industry Applications Conference*, volume 4, pages 2599 – 2605. IEEE, 1999.

[77] L. Harnefors, S. E. Saarakkala, and M. Hinkkanen. Speed control of electrical drives using classical control methods. In *Energy Conversion Congress and Exposition (ECCE)*, pages 1713 – 1720. IEEE, 2011.

[78] A. Visioli. Modified anti-windup scheme for PID controllers. *Control Theory and Applications, IEE Proceedings on*, 150(1):49 – 54, 2003.

[79] S. Tarbouriech and M. Turner. Anti-windup design: An overview of some recent advances and open problems. *Control Theory Applications, IET*, 3(1):1 – 19, 2009.

[80] M. Oszwaldowski and T. Berus. High temperature Hall sensors. *Sensors and Actuators A: Physical*, 136(1):234 – 237, 2007.

[81] A. H. Eltom and N. S. Moharari. Motor temperature estimation incorporating dynamic rotor impedance. *Energy Conversion, IEEE Transactions on*, 6(1):107 – 113, March 1991.

[82] P. P. Acarnley and J. K. Al-Tayie. Estimation of speed and armature temperature in a brushed DC drive using the extended Kalman filter. *Electric Power Applications, IEE Proceedings* -, 144(1):13 – 20, January 1997.

[83] S.B. Lee and T. G. Habetler. An online stator winding resistance estimation technique for temperature monitoring of line-connected induction machines. *Industry Applications, IEEE Transactions on*, 39(3):685 – 694, 2003.

[84] M. Stiebler and Y. Plotkin. Online winding temperature monitoring of PWM inverter-fed induction machines. In *Power Electronics and Applications, European Conference on*, 2005.

[85] Y. Wu and H. Gao. Induction motor stator and rotor winding temperature estimation using signal injection method. In *Electric Machines and Drives, 2005 IEEE International Conference on*, pages 615 – 621, May 2005.

[86] Z. Gao. *Sensorless stator winding temperature estimation for induction machines*. PhD thesis, Georgia Institute of Technology, 2006.

[87] H. Weili, H. Weijian, and L. Lin. Estimation of Stator Resistance and Temperature Measurement in Induction Motor Using Wavelet Network. In *Chinese Control Conference (CCC)*, pages 203 – 207, June 2007.

[88] Z. Gao, T.G. Habetler, R.G. Harley, and R.S. Colby. A Sensorless Adaptive Stator Winding Temperature Estimator for Mains-Fed Induction Machines With Continuous-Operation Periodic Duty Cycles. *Industry Applications, IEEE Transactions on*, 44(5):1533 –1542, sept.-oct. 2008.

[89] D. Yi, Z. Pinjia, G. Zhi, and T. G. Habetler. Assessment of available methods for estimating rotor temperatures of induction motor. In *International Electric Machines and Drives Conference (IEMDC)*, pages 1340 – 1345, May 2009.

[90] D. A. Paice. Motor Thermal Protection by Continuous Monitoring of Winding Resistance. *Industrial Electronics and Control Instrumentation, IEEE Transactions on*, 27(3):137 – 141, 1980.

[91] R. Beguenane and M. E. H. Benbouzid. Induction motors thermal monitoring by means of rotor resistance identification. *Energy Conversion, IEEE Transactions on*, 14(3):566 – 570, September 1999.

[92] S.B. Lee, T. G. Habetler, and D. J. Gritter. Device and method for estimating the resistance of a stator winding for an ac induction motor, 16 September 2003. US Patent 6,621,291.

[93] D. J. Leith and W. E. Leithead. Survey of gain-scheduling analysis and design. *International Journal of Control*, 73(11):1001 – 1025, 2000.

[94] K. J. Åström. Control system design lecture notes for me 155a. *Department of Mechanical and Environmental Engineering University of California Santa Barbara*, 2002.

[95] K. J. Åström and R. M. Murray. *Feedback systems: An introduction for scientists and engineers*. Princeton university press, 2008.

[96] Stock Drive Products/Sterling Instrument Website. `http://www.sdp-si.com`, August 2013.

[97] J. Landry. Backlash vs. Lost motion. *Design News*, 57(15):55 – 56, 2002.

[98] Bayside Precision Gearheads. Using gearheads in motion control - Precision Planetary vs. Harmonic/Cycloidal drives. `http://www.parkermotion.com/whitepages/white_pages.htm`, 1997.

[99] A. Lagerberg and B. Egardt. Backlash gap position estimation in automotive powertrains. In *European Control Conference*, volume 4, pages 1 – 4, 2003.

[100] J. Kuria and J. Kihiu. Prediction of Overall Efficiency in Multistage Gear Trains. *International Journal of Aerospace and Mechanical Engineering*, 2011.

[101] N. E. Anderson and S. H. Loewenthal. *Spur-gear-system efficiency at part and full load*, volume 79. National Aeronautics and Space Administration, Scientific and Technical Information Office, 1980.

[102] G. G. Antony. *Rating and sizing of precision low backlash planetary gearboxes for Automation Motion Control and Robotics applications*. Neugart, 2000.

[103] F. Roos and C. Spiegelberg. *Relations between size and gear ratio in spur and planetary gear trains*. KTH, Stockholm, Sweden, 2004.

[104] F. Roos. *On Design Methods for Mechatronics-Servo motor and Gearhead*. PhD thesis, KTH, Stockholm, Sweden, 2005.

[105] F. Roos, H. Johansson, and J. Wikander. Optimal selection of motor and gearhead in mechatronic applications. *Mechatronics*, 16(1):63 – 72, 2006.

[106] J. McGuinn. Talking Truth to Power: Plastic Gears Taking Back Seat to No One. `www.geartechnology.com`, March/April 2013.

[107] S. Burns. Hypoid vs Worm Gear Efficiencies. `www.sumitomodrive.com`, 2009.

[108] R. Beardmore. RoyMech. `http://www.roymech.co.uk`, January 2011.

[109] *Circulute 3000 catalogue*. Shimpo, 2007.

[110] A. Dăscălescu. The determination of the cycloid profile limits of the cycloid reducer satellite gear. *Fascicle of Management and Technological Engineering*, 2007.

[111] B. K. Chen, T. T. Fang, C. Y. Li, and S. Y. Wang. Gear geometry of cycloid drives. *Sci. China, Ser. E*, 51(5):598 – 610, 2008.

[112] T. D. Tuttle. Understanding and modeling the behavior of a harmonic drive gear transmission. Master's thesis, Massachusetts Institute of Technology, 1992.

[113] I. Schafer and R. Slatter. Precision Pointing and Actuation Systems for UAVs Using Harmonic Drive Gears. In *2nd AIAA "Unmanned Unlimited" Systems, Technologies, and Operations- Aerospace, Land, and Sea Conference, Workshop and Exhibition*, 2003.

[114] T. Izumi, L. Zuowei, Z. Hai, and M. Kanesaka. Minimization of energy dissipated in a ball screw-nut with all kinds of friction. In *Advanced Intelligent Mechatronics, 2008. AIM 2008. IEEE/ASME International Conference on*, pages 1302 – 1307, July 2008.

[115] Z. Li, T. Izumi, and H. Zhou. An optimal lead of a ball screw-nut for minimizing energy dissipated in a linear actuator. In *Mechatronics and Automation, 2008. ICMA 2008. IEEE International Conference on*, pages 1006 – 1011. IEEE, 2008.

[116] P. C. Lemor. The roller screw, an efficient and reliable mechanical component of electro-mechanical actuators. In *Energy Conversion Engineering Conference (IECEC), Proceedings of the 31st Intersociety*, volume 1, pages 215 – 220. IEEE, 1996.

[117] S. A. Velinsky, B. Chu, and T. A. Lasky. Kinematics and Efficiency Analysis of the Planetary Roller Screw Mechanism. *Journal of Mechanical Design*, 131, January 2009.

[118] Y. C. Wu. Conceptual Design of Integrated Brushless Permanent-Magnet Motors and Planetary Gear Trains. *Applied Mechanics and Materials*, 284:634 – 637, 2013.

[119] C. C. Huang, M. C. Tsai, D. G. Dorrell, and B. J. Lin. Development of a magnetic planetary gearbox. *Magnetics, IEEE Transactions on*, 44(3):403 – 412, 2008.

[120] X. Zhu, L. Kong, L. Chen, W. Zhao, L. Quan, and M. Cheng. Electromagnetic performances analysis of a new magnetic-planetary-geared permanent magnet brushless machine for hybrid electric vehicles. In *Industrial Electronics Society (IECON), 38th Annual Conference on*, pages 4110 – 4114, October 2012.

[121] X. Zhu, L. Chen, L. Quan, Y. Sun, W. Hua, and Z. Wang. A New Magnetic-Planetary-Geared Permanent Magnet Brushless Machine for Hybrid Electric Vehicle. *Magnetics, IEEE Transactions on*, 48(11):4642 – 4645, November 2012.

[122] K. Atallah and D. Howe. A novel high-performance magnetic gear. *Magnetics, IEEE Transactions on*, 37(4):2844 – 2846, 2001.

[123] K. Atallah, S. D. Calverley, and D. Howe. Design, analysis and realisation of a high-performance magnetic gear. In *Electric Power Applications, IEE Proceedings*, volume 151, pages 135 – 143. IET, 2004.

[124] K. Atallah, S. D. Calverley, and D. Howe. High-performance magnetic gears. *Journal of Magnetism and Magnetic Materials*, 272:E1727 – E1729, 2004.

[125] K. Atallah, J. Rens, S. Mezani, and D. Howe. A Novel Pseudo Direct-Drive Brushless Permanent Magnet Machine. *Magnetics, IEEE Transactions on*, 44(11):4349 – 4352, 2008.

[126] J. Wang and K. Atallah. Modeling and control of pseudo direct-drive brushless permanent magnet machines. In *International Electric Machines and Drives Conference (IEMDC)*, pages 870 – 875. IEEE, 2009.

[127] K. Atallah, J. Wang, S. D. Calverley, and S. Duggan. Design and operation of a magnetic continuously variable transmission. *Industry Applications, IEEE Transactions on*, 48(4):1288 – 1295, 2012.

[128] R. G. Montague, C. M. Bingham, and K. Atallah. Magnetic gear dynamics for servo control. In *15th Mediterranean Electrotechnical Conference (MELECON)*, pages 1192 – 1197. IEEE, 2010.

[129] R. Montague, C. Bingham, and K. Atallah. Servo control of magnetic gears. *Mechatronics, IEEE/ASME Transactions on*, 17(2):269 – 278, 2012.

[130] R. A. Ashen and H. R. Bolton. Aspects of the hypocycloidal reluctance motor. *Electric Power Applications, IEE Proceedings B*, 128(6):313 – 322, 1981.

[131] J. Reinert, E. D. Smith, and J. H. R. Enslin. Drive of a high torque, low speed switched reluctance machine. In *Power Electronics Specialists Conference (PESC), 22nd Annual*, pages 39 – 42. IEEE, 1991.

[132] J. Reinert, J. H. R. Enslin, and E. D. Smith. Digital control and optimization of a rolling rotor switched reluctance machine. In *Industry Applications Society Annual Meeting, Conference Record of the*, volume 1, pages 130 – 136, 1993.

[133] M. Franke, O. Punk, H. Mrech, and U. Schmucker. Electrical actuation of a Rolling Rotor Switched Reluctance Motor. In *Electronics Technology (ISSE), 2011 34th International Spring Seminar on*, pages 451 – 456. IEEE, 2011.

[134] M. Franke, M. Brutscheck, and U. Schmucker. Modeling and simulation of a rolling rotor switched reluctance motor. In *Electronics Technology (ISSE), 32nd International Spring Seminar on*, pages 1 – 6. IEEE, 2009.

[135] A. Arkkio, A. Biernat, B. Bucki, G. Kaminski, A. Niemenmaa, A. Smak, and P. Staszewski. Finite-Element Analysis for a Rolling-Rotor Electrical Machine. *Magnetics, IEEE Transactions on*, 46(8):2727 – 2730, 2010.

[136] M. Franke, O. Punk, M. Brutscheck, and U. Schmucker. Magnetic equivalent circuit modeling of rolling rotor switched reluctance motors. In *Electronics Technology (ISSE), 33rd International Spring Seminar on*, pages 320 – 325. IEEE, 2010.

[137] Å. K. Nilsen. Design of a Permanently Magnetized Hypocycloidal Reluctance Machine. Master's thesis, Norwegian University of Science and Technology, 2011.

[138] J. Rens, K. Atallah, S. D. Calverley, and D. Howe. A novel magnetic harmonic gear. In *International Electric Machines and Drives Conference (IEMDC)*, volume 1, pages 698 – 703, May 2007.

[139] J. Rens, R. Clark, S. Calverley, K. Atallah, and D. Howe. Design, analysis and realization of a novel magnetic harmonic gear. In *Electrical Machines (ICEM), 18th International Conference on*, pages 1 – 4. IEEE, 2008.

[140] K. Davey. A harmonic gear like motor. In *International Electric Machines and Drives Conference (IEMDC)*, pages 1795 – 1800, May 2009.

[141] E. Davison. Harmonic drive motor, 18 November 2008. US Patent 7,453,176.

[142] E. Davison. A New Approach To: High Torque, Variable, Low Speed Motor Generator Technology. In *Orlando eDrive Conference*. EDM Resources Inc., 2009.

[143] E. Davison. Recently Patented Innovative Motor Generator Technology. In *SMMA Technical Conference, Chicago*. EDM Resources Inc., November 2009.

[144] Cummins. Dynamic Modelling Deep Dive – Internal report. 2010.

[145] M. P. Ford. A simplified turbocharged diesel engine model. *Proceedings of the Institution of Mechanical Engineers, Part D: Transport Engineering 1984-1988 (vols 198-202)*, 201(44):229 – 234, 1987.

[146] J. Friedman. MATLAB/Simulink for automotive systems design. In *Design, automation and test in Europe, conference on*, pages 87 – 88. European Design and Automation Association, 2006.

[147] T. Egel. Real Time Simulation Using Non-causal Physical Models. *SAE Technical Paper*, page 1021, 2009.

[148] G. H. Jang, J. H. Chang, D. P. Hong, and K. S. Kim. Finite-element analysis of an electromechanical field of a BLDC motor considering speed control and mechanical flexibility. *Magnetics, IEEE Transactions on*, 38(2):945 – 948, 2002.

[149] M. A. Jabbar, H. N. Phyu, Z. Liu, and C. Bi. Modeling and numerical simulation of a brushless permanent-magnet DC motor in dynamic conditions by time-stepping technique. *Industry Applications, IEEE Transactions on*, 40(3):763 – 770, 2004.

[150] T. H. Akinaga, C. Pompermaier, F. J. H. Kalluf, and M. V. F. da Luz. Performance evaluation of brushless DC permanent magnet motor using Finite Element Method. In *International Electric Machines and Drives Conference (IEMDC)*, pages 1165 – 1170. IEEE, 2011.

[151] A. C. Smith. Integrating FE into induction motor design-a marriage of inconvenience? In *Current Trends in the Use of Finite Elements (FE) in Electromechanical Design and Analysis (Ref. No. 2000/013), IEE Seminar on*, pages 1 – 7, 2000.

[152] E. S. Hung and S. D. Senturia. Generating efficient dynamical models for microelectromechanical systems from a few finite-element simulation runs. *Microelectromechanical Systems, Journal of*, 8(3):280 – 289, 1999.

[153] N. Bracikowski, M. Hecquet, P. Brochet, and S. Shirinskii. Multi-physics modeling of a permanent magnet synchronous machine by using lumped models. *Industrial Electronics, IEEE Transactions on*, 59(6):2426–2437, 2012.

[154] O. A. Mohammed, S. Liu, and Z. Liu. A phase variable model of brushless dc motors based on finite element analysis and its coupling with external circuits. *Magnetics, IEEE Transactions on*, 41(5):1576 – 1579, 2005.

[155] D. C. Hanselman. *Brushless permanent magnet motor design*. McGraw-Hill New York, 1994.

[156] B. Tibor, V. Fedak, and F. Durovsky. Modeling and simulation of the BLDC motor in MATLAB GUI. In *Industrial Electronics (ISIE), International Symposium on*, pages 1403 – 1407. IEEE, 2011.

[157] C. Gencer and M. Gedikpinar. Modeling and Simulation of BLDCM Using Matlab/Simulink. *Journal of Applied Sciences*, 6:688 – 691, 2006.

[158] W. Hong, W. Lee, and B. K. Lee. Dynamic simulation of brushless DC motor drives considering phase commutation for automotive applications. In *International Electric Machines and Drives Conference (IEMDC)*, volume 2, pages 1377 – 1383. IEEE, 2007.

[159] V. Hubik and V. Singule. Sensor BLDC Motor Model in Simulink Environment. *Recent Advances in Mechatronics*, pages 275 – 280, 2010.

[160] M. S. Hussin, M. N. Azuwir, and Y. N. Zaiazmin. Modeling and validation of brushless DC motor. In *Modeling, Simulation and Applied Optimization (ICMSAO), 4th International Conference on*, pages 1 – 4. IEEE, 2011.

[161] M. F. Tsai, T. P. Quy, B. F. Wu, and C. S. Tseng. Model construction and verification of a BLDC motor using MATLAB/SIMULINK and FPGA control. In *Industrial Electronics and Applications (ICIEA), 6th Conference on*, pages 1797 – 1802. IEEE, 2011.

[162] A. Tashakori, M. Ektesabi, and N. Hosseinzadeh. Modeling of bldc motor with ideal back-emf for automotive applications. In *Proceedings of the World Congress on Engineering*, volume 2, pages 6 – 8, 2011.

[163] R. Carlson, M. Lajoie-Mazenc, and J. C. D. S. Fagundes. Analysis of torque ripple due to phase commutation in brushless DC machines. *Industry Applications, IEEE Transactions on*, 28(3):632 – 638, 1992.

[164] S. D. Sudhoff and P. C. Krause. Operating modes of the brushless DC motor with a 120° inverter. *Energy Conversion, IEEE Transactions on*, 5(3):558 – 564, 1990.

[165] R. R. Nucera, S. D. Sudhoff, and P. C. Krause. Computation of steady-state performance of an electronically commutated motor. *Industry Applications, IEEE Transactions on*, 25(6):1110 – 1117, 1989.

[166] S. D. Sudhoff and P. C. Krause. Average-value model of the brushless DC 120° inverter system. *Energy Conversion, IEEE Transactions on*, 5(3):553 – 557, 1990.

[167] Q. Han, N. Samoylenko, and J. Jatskevich. Average-Value Modeling of Brushless DC Motors With 120 Voltage Source Inverter. *Energy Conversion, IEEE Transactions on*, 23(2):423 – 432, 2008.

[168] Q. Han, N. Samoylenko, and J. Jatskevich. Comparison of Brushless DC Motor Drives with 180/120-degree Inverter Systems. In *Electrical and Computer Engineering (CCECE), Canadian Conference on*, pages 111 – 114. IEEE.

[169] K. Tabarraee. Dynamic average-value modeling of the 120 VSI-commutated brushless dc motors with non-sinusoidal back EMF. Master's thesis, University of British Columbia, 2011.

[170] K. Tabarraee, J. Iyer, H. Atighechi, and J. Jatskevich. Dynamic Average-Value Modeling of 120 VSI-Commutated Brushless DC Motors With Trapezoidal Back EMF. *Energy Conversion, IEEE Transactions on*, 27(2):296 – 307, 2012.

[171] M. Markovic, A. Hodder, and Y. Perriard. Analysis of the commutation currents for a sinusoidal BLDC motor. In *Electrical Machines and Systems, International Conference on*, pages 3016 – 3019. IEEE, 2008.

[172] M. Markovic, A. Hodder, and Y. Perriard. An analytical determination of the torque-speed and efficiency-speed characteristics of a BLDC motor. In *Energy Conversion Congress and Exposition (ECCE)*, pages 168 – 172. IEEE, 2009.

[173] A. Kapun, M. Curkovic, A. Hace, and K. Jezernik. Identifying dynamic model parameters of a BLDC motor. *Simulation Modelling Practice and Theory*, 16(9):1254 – 1265, 2008.

[174] B. Hieb and H. Hofmann. Characterizing and Validating a Permanent Magnet Synchronous Motor Model. In *MathWorks Automotive Conference*, May 2012.

[175] National Electrical Manufacturers Association. *NEMA Standards Publication MG 1-1998 (Revision 3, 2002) Interfiled Motors and Generators* , 2002.

[176] D. Borg-Bartolo, D. Gerada, C. Micallef, A. Mebarki, N. L. Brown, and C. Gerada. Thermal modelling and selection of a high speed permanent magnet surface mount electrical machine. In *Power Electronics, Machines and Drives (PEMD), 6th International Conference on*, pages 1 – 6, March 2012.

[177] T. Sawata, P. Sangha, M. Benarous, and C. Maxwell. Thermal Modeling of Brushless DC Motor and Brake Solenoid in Electro-Mechanical Actuators for the More Electric Aircraft Engine. In *Industrial Electronics (ISIE), International Symposium on*, pages 1236 – 1241, June 2007.

[178] G. Dajaku and D. Gerling. An improved lumped parameter thermal model for electrical machines. In *Electrical Machines (ICEM), 17th International Conference on*, 2006.

[179] A. Boglietti, A. Cavagnino, D. Staton, M. Shanel, M. Mueller, and C. Mejuto. Evolution and Modern Approaches for Thermal Analysis of Electrical Machines. *Industrial Electronics, IEEE Transactions on*, 56(3):871 – 882, March 2009.

[180] R. Wrobel, P. H. Mellor, M. Popescu, and D. Staton. Thermal Analysis of Electrical Machines - Tutorial session. *Power Electronics, Machines and Drives (PEMD), 5th International Conference on*, 2010.

[181] A. Boglietti, A. Cavagnino, and D. Staton. Determination of critical parameters in electrical machine thermal models. *Industry Applications, IEEE Transactions on*, 44(4):1150 – 1159, 2008.

[182] D. A. Staton and E. So. Determination of optimal thermal parameters for brushless permanent magnet motor design. In *Industry Applications Conference, 33rd IAS Annual Meeting*, pages 41 – 49.

[183] D. Staton, A. Boglietti, and A. Cavagnino. Solving the more difficult aspects of electric motor thermal analysis. In *International Electric Machines and Drives Conference (IEMDC)*, volume 2, pages 747 – 755. IEEE, 2003.

[184] A. Boglietti, A. Cavagnino, and D. A. Staton. TEFC induction motors thermal models: A parameter sensitivity analysis. *Industry Applications, IEEE Transactions On*, 41(3):756 – 763, 2005.

[185] D. G. Dorrell, D. A. Staton, J. Kahout, D. Hawkins, and M. I. McGilp. Linked Electromagnetic and Thermal Modelling of a Permanent Magnet Motor. In *Power Electronics, Machines and Drives (PEMD), 3rd International Conference on*, pages 536 – 540, March 2006.

[186] D. G. Dorrell, D. A. Staton, and M. I. McGilp. Design of Brushless Permanent Magnet Motors - A Combined Electromagnetic and Thermal Approach to High Performance Specification. In *Industrial Electronics (IECON), 32nd Annual Conference on*, pages 4853 – 4858, November 2006.

[187] R. Welch. Why All Exlar SLM Servomotors Have a 50°C Hot Spot Temperature Safety Margin. Technical report, Exlar.

[188] G. D. Demetriades, H. Z. de la Parra, E. Andersson, and H. Olsson. A Real-Time Thermal Model of a Permanent-Magnet Synchronous Motor. *Power Electronics, IEEE Transactions on*, 25(2):463 – 474, February 2010.

[189] J. Fan, C. Zhang, Z. Wang, Y. Dong, C. E. Nino, A. R. Tariq, and E. G. Strangas. Thermal analysis of permanent magnet motor for the electric vehicle application considering driving duty cycle. *Magnetics, IEEE Transactions on*, 46(6):2493 – 2496, 2010.

[190] J. Nerg, M. Rilla, and J. Pyrhonen. Thermal Analysis of Radial-Flux Electrical Machines With a High Power Density. *Industrial Electronics, IEEE Transactions on*, 55(10):3543 – 3554, October 2008.

[191] P. H. Mellor, D. Roberts, and D. R. Turner. Lumped parameter thermal model for electrical machines of TEFC design. *Electric Power Applications, IEE Proceedings B*, 138(5):205 – 218, 1991.

[192] G. Fraisse, B. Souyri, S. Pinard, and C. Ménézo. Identification of equivalent thermal rc network models based on step response and genetic algorithms. In *International Building Performance Simulation Association, 12th Conference of*, 2011.

[193] Y. Zhao and Y. Yang. Application of an average current control method in Double-loop control systems of brushless DC motor. In *Consumer Electronics, Communications and Networks (CECNet), International Conference on*, pages 102105 – 102105. IEEE, 2011.

[194] P. P. Benham, R. J. Crawford, and C. G. Armstrong. *Mechanics of engineering materials*. Second edition, 1998.

[195] M. Nordin, J. Galic, and P. O. Gutman. New models for backlash and gear play. *Adaptive control and signal processing, International journal of*, 11(1):49 – 63, 1997.

[196] K. C. Craig and R. C. Greenheck. Control-Oriented Modeling for Backlash. *Design News*, page 20, 2011.

[197] C. Makkar, W. E. Dixon, W. G. Sawyer, and G. Hu. A new continuously differentiable friction model for control systems design. In *Advanced Intelligent Mechatronics, International Conference on*, pages 600 – 605. IEEE/ASME, 2005.

[198] S. Andersson, A. Söderberg, and S. Björklund. Friction models for sliding dry, boundary and mixed lubricated contacts. *Tribology International*, 40(4):580 – 587, 2007.

[199] A. Mihailidis and I. Nerantzis. A New System for Testing Gears Under Variable Torque and Speed. *Recent patents on mechanical engineering*, 2:179 – 192, 2009.

[200] T. T. Petry-Johnson, A. Kahraman, N. E. Anderson, and D. R. Chase. An experimental investigation of spur gear efficiency. *Journal of Mechanical Design*, 130(6):62601, 2008.

[201] S. Cetinkunt. Optimal design issues in high-speed high-precision motion servo systems. *Mechatronics*, 1(2):187 – 201, 1991.

[202] M. Pettersson. *Design Optimization in Industrial Robotics: Methods and Algorithms for Drive Train Design*. PhD thesis, Linköping University, 2008.

[203] P. Karlsson. Survey of Methods of Combining Velocity Profiles with Position control. Technical report, Mälardalen University.

[204] G. Cusimano. A procedure for a suitable selection of laws of motion and electric drive systems under inertial loads. *Mechanism and machine theory*, 38(6):519 – 533, 2003.

[205] K. D. Nguyen, T.C. Ng, and I.M. Chen. On algorithms for planning S-curve motion profiles. *International Journal of Advanced Robotic Systems*, 5(1):99 – 106, 2008.

[206] J. Tal. The optimal design of incremental motion servo systems. In *Incremental motion control systems and devices campaign, 2nd annual symposium of*, 1973.

[207] J. S. Park. Motion profile planning of repetitive point-to-point control for maximum energy conversion efficiency under acceleration conditions. *Mechatronics*, 6(6):649 – 663, 1996.

[208] S. T. Kwok and C. K. Lee. Optimal velocity profile design in incremental servo motor systems based on a digital signal processor. In *Industrial Electronics Society (IECON), 16th Annual Conference of*, pages 262 – 266. IEEE, 1990.

[209] D.M. Tsay and C.F. Lin. Asymmetrical inputs for minimizing residual response. In *Mechatronics (ICM), International Conference on*, pages 235 – 240. IEEE, 2005.

[210] K. A. Pasch and W. P. Seering. On the drive systems for high-performance machines. *Journal of Mechanisms, Transmissions, and Automation in Design*, 1983.

[211] H. J. Van de Straete, P. Degezelle, J. De Schutter, and R. J. M. Belmans. Servo motor selection criterion for mechatronic applications. *Mechatronics, Transactions on*, 3(1):43 – 50, 1998.

[212] H. J. Van de Straete, J. De Schutter, and R. Belmans. An efficient procedure for checking performance limits in servo drive selection and optimization. *Mechatronics, Transactions on*, 4(4):378 – 386, 1999.

[213] G. Cusimano. Generalization of a method for the selection of drive systems and transmissions under dynamic loads. *Mechanism and machine theory*, 40(5):530 – 558, 2005.

[214] G. Cusimano. Optimization of the choice of the system electric drive-device–transmission for mechatronic applications. *Mechanism and machine theory*, 42(1):48 – 65, 2007.

[215] G. Cusimano. Choice of electrical motor and transmission in mechatronic applications: The torque peak. *Mechanism and Machine Theory*, 46(9):1207 – 1235, 2011.

[216] G. Cusimano. Influence of the reducer efficiencies on the choice of motor and transmission: Torque peak of the motor. *Mechanism and Machine Theory*, 67:122 – 151, 2013.

[217] H. Giberti, S. Cinquemani, and G. Legnani. Effects of transmission mechanical characteristics on the choice of a motor-reducer. *Mechatronics*, 20(5):604 – 610, 2010.

[218] H. Giberti, S. Cinquemani, and G. Legnani. Evaluation of motor-reducer coupling in high demanding industrial applications. In *Engineering and Technological Innovation (IMETI), 2nd International Multi-Conference on*, volume 9, 2010.

[219] H. Giberti, S. Cinquemani, and G. Legnani. A Practical Approach to the Selection of the Motor-Reducer Unit in Electric Drive Systems. *Mechanics Based Design of Structures and Machines*, 39(3):303 – 319, 2011.

[220] H. Giberti and S. Cinquemani. Servo Motors Classification Based on the Accelerating Factor. In *Engineering and Technological Innovation (IMETI), 3rd International Multi-Conference on*, 2010.

[221] R.E. Steven. *Electrical Machines and Power Electronics*. Van Nostrand Reinhold (UK) Company, 1983.

[222] A. Fitzgerald, C. Kingsley, and S. Umans. *Electric Machinery*. Series in Electrical and Computer Engineering. McGraw-Hill, 2002.

[223] Y. Chen and P. Pillay. An improved formula for lamination core loss calculations in machines operating with high frequency and high flux density excitation. In *Industry Applications Conference (IAS), 37th Annual*, volume 2, pages 759 – 766. IEEE, 2002.

[224] A. S. O. Al-Mashakbeh. Proportional Integral and Derivative Control of Brushless DC Motor. *European Journal of Scientific Research*, 35(2):198 – 203, 2009.

[225] C. P. Steinmetz. On the law of hysteresis. *Proceedings of the IEEE*, 72(2):197 – 221, 1984.

[226] D. A. Staton and A. Cavagnino. Convection Heat Transfer and Flow Calculations Suitable for Analytical Modelling of Electric Machines. In *Industrial Electronics (IECON), 32nd Annual Conference on*, pages 4841 – 4846, November 2006.

[227] M. Q. Brewster. *Thermal radiative transfer and properties*. John Wiley & Sons, 1992.

[228] S. Constantinides. Understanding and Using Reversible Temperature Coefficients. In *Magnetics*. Arnold Magnetic Technologies, 2010.

[229] D. Langarica-Córdoba, G. V. Guerrero-Ramirez, A. Claudio-Sánchez, M. A. Durán-Fonseca, M. Adam-Medina, and C. M. Astorga-Zaragoza. Robust Nonlinear Control of AC Brushless Motor for Electric Vehicles Application. *Journal of Power Electronics*, 11(4):430–438, 2011.

[230] *MMT – MM41 Family Datasheet*. MMT.

[231] *General purpose brushless motors BM05/SQ series*. McLennan.

[232] *Silencer Series Brushless DC Motors*. Moog Components Group.

Appendix A

Computationally efficient motor model equations

The large equations for the computationally efficient motor model outlined in Section 3.5 are presented here. These were derived using the *MuPad* symbolic toolbox.

The expression for the average current over a commutation period $\overline{I}$ is:

$$
\begin{aligned}
\overline{I} = \frac{1}{\pi}\Bigg(& \frac{2\,\theta_{ef}\,V}{3\,R} - \frac{2\,\pi\,V}{3\,R} + \frac{K_E\,R\,\omega_e\,\sin(\theta_{ef})}{2\,\left(L^2\,{n_{pp}}^2\,\omega_e^2 + R^2\right)} - \frac{2\,L\,n_{pp}\,V\,\omega_e}{3\,R^2} \\
& + \frac{\sqrt{3}\,K_E\,R\,\omega_e}{2\,\left(L^2\,{n_{pp}}^2\,\omega_e^2 + R^2\right)} - \frac{K_E\,L\,n_{pp}\,\omega_e^2\,\cos(\theta_{ef})}{2\,\left(L^2\,{n_{pp}}^2\,\omega_e^2 + R^2\right)} \\
& - \frac{K_E\,L\,n_{pp}\,\omega_e^2\,\mathrm{e}^{-\frac{\theta_{ef}\,R}{L\,n_{pp}\,\omega_e}}}{4\,\left(L^2\,{n_{pp}}^2\,\omega_e^2 + R^2\right)} + \frac{5\,L\,n_{pp}\,V\,\omega_e\,\mathrm{e}^{-\frac{\theta_{ef}\,R}{L\,n_{pp}\,\omega_e}}}{3\,R^2} - \frac{L\,n_{pp}\,V\,\omega_e\,\mathrm{e}^{-\frac{\pi\,R}{3\,L\,n_{pp}\,\omega_e}}}{3\,R^2} \\
& + \frac{L\,n_{pp}\,V\,\omega_e\,\mathrm{e}^{-\frac{2\,\pi\,R}{3\,L\,n_{pp}\,\omega_e}}}{3\,R^2} + \frac{\sqrt{3}\,K_E\,R\,\omega_e\,\cos(\theta_{ef})}{2\,\left(L^2\,{n_{pp}}^2\,\omega_e^2 + R^2\right)} + \frac{\sqrt{3}\,K_E\,L^2\,{n_{pp}}^2\,\omega_e^3}{2\,\left(L^2\,R\,{n_{pp}}^2\,\omega_e^2 + R^3\right)} \\
& + \frac{L\,n_{pp}\,V\,\omega_e\,\mathrm{e}^{-\frac{\theta_{ef}\,R}{L\,n_{pp}\,\omega_e}}\,\mathrm{e}^{-\frac{\pi\,R}{3\,L\,n_{pp}\,\omega_e}}}{3\,R^2} - \frac{4\,L\,n_{pp}\,V\,\omega_e\,\mathrm{e}^{-\frac{\theta_{ef}\,R}{L\,n_{pp}\,\omega_e}}\,\mathrm{e}^{-\frac{2\,\pi\,R}{3\,L\,n_{pp}\,\omega_e}}}{3\,R^2} \\
& + \frac{\sqrt{3}\,K_E\,L\,n_{pp}\,\omega_e^2\,\sin(\theta_{ef})}{2\,\left(L^2\,{n_{pp}}^2\,\omega_e^2 + R^2\right)} + \frac{\sqrt{3}\,K_E\,L^2\,{n_{pp}}^2\,\omega_e^3\,\mathrm{e}^{-\frac{\theta_{ef}\,R}{L\,n_{pp}\,\omega_e}}}{4\,\left(L^2\,R\,{n_{pp}}^2\,\omega_e^2 + R^3\right)} \\
& - \frac{K_E\,L\,n_{pp}\,\omega_e^2\,\mathrm{e}^{-\frac{\pi\,R}{3\,L\,n_{pp}\,\omega_e}}\,\cos(\theta_{ef})}{4\,\left(L^2\,{n_{pp}}^2\,\omega_e^2 + R^2\right)} + \frac{K_E\,L\,n_{pp}\,\omega_e^2\,\mathrm{e}^{-\frac{2\,\pi\,R}{3\,L\,n_{pp}\,\omega_e}}\,\cos(\theta_{ef})}{4\,\left(L^2\,{n_{pp}}^2\,\omega_e^2 + R^2\right)} \\
& + \frac{K_E\,L\,n_{pp}\,\omega_e^2\,\mathrm{e}^{-\frac{\theta_{ef}\,R}{L\,n_{pp}\,\omega_e}}\,\mathrm{e}^{-\frac{\pi\,R}{3\,L\,n_{pp}\,\omega_e}}}{4\,\left(L^2\,{n_{pp}}^2\,\omega_e^2 + R^2\right)} + \frac{K_E\,L\,n_{pp}\,\omega_e^2\,\mathrm{e}^{-\frac{\theta_{ef}\,R}{L\,n_{pp}\,\omega_e}}\,\mathrm{e}^{-\frac{2\,\pi\,R}{3\,L\,n_{pp}\,\omega_e}}}{2\,\left(L^2\,{n_{pp}}^2\,\omega_e^2 + R^2\right)} \\
& - \frac{K_E\,L^2\,{n_{pp}}^2\,\omega_e^3\,\mathrm{e}^{-\frac{\pi\,R}{3\,L\,n_{pp}\,\omega_e}}\,\sin(\theta_{ef})}{4\,\left(L^2\,R\,{n_{pp}}^2\,\omega_e^2 + R^3\right)} + \frac{K_E\,L^2\,{n_{pp}}^2\,\omega_e^3\,\mathrm{e}^{-\frac{2\,\pi\,R}{3\,L\,n_{pp}\,\omega_e}}\,\sin(\theta_{ef})}{4\,\left(L^2\,R\,{n_{pp}}^2\,\omega_e^2 + R^3\right)} \\
& + \frac{\sqrt{3}\,K_E\,L\,n_{pp}\,\omega_e^2\,\mathrm{e}^{-\frac{\pi\,R}{3\,L\,n_{pp}\,\omega_e}}\,\sin(\theta_{ef})}{4\,\left(L^2\,{n_{pp}}^2\,\omega_e^2 + R^2\right)} - \frac{\sqrt{3}\,K_E\,L\,n_{pp}\,\omega_e^2\,\mathrm{e}^{-\frac{2\,\pi\,R}{3\,L\,n_{pp}\,\omega_e}}\,\sin(\theta_{ef})}{4\,\left(L^2\,{n_{pp}}^2\,\omega_e^2 + R^2\right)} \\
& - \frac{\sqrt{3}\,K_E\,L^2\,{n_{pp}}^2\,\omega_e^3\,\mathrm{e}^{-\frac{\pi\,R}{3\,L\,n_{pp}\,\omega_e}}\,\cos(\theta_{ef})}{4\,\left(L^2\,R\,{n_{pp}}^2\,\omega_e^2 + R^3\right)} + \frac{\sqrt{3}\,K_E\,L^2\,{n_{pp}}^2\,\omega_e^3\,\mathrm{e}^{-\frac{2\,\pi\,R}{3\,L\,n_{pp}\,\omega_e}}\,\cos(\theta_{ef})}{4\,\left(L^2\,R\,{n_{pp}}^2\,\omega_e^2 + R^3\right)} \\
& - \frac{\sqrt{3}\,K_E\,L^2\,{n_{pp}}^2\,\omega_e^3\,\mathrm{e}^{-\frac{\theta_{ef}\,R}{L\,n_{pp}\,\omega_e}}\,\mathrm{e}^{-\frac{\pi\,R}{3\,L\,n_{pp}\,\omega_e}}}{4\,\left(L^2\,R\,{n_{pp}}^2\,\omega_e^2 + R^3\right)} - \frac{\sqrt{3}\,K_E\,L^2\,{n_{pp}}^2\,\omega_e^3\,\mathrm{e}^{-\frac{\theta_{ef}\,R}{L\,n_{pp}\,\omega_e}}\,\mathrm{e}^{-\frac{2\,\pi\,R}{3\,L\,n_{pp}\,\omega_e}}}{2\,\left(L^2\,R\,{n_{pp}}^2\,\omega_e^2 + R^3\right)}\Bigg)
\end{aligned}
\tag{A.1}
$$

The expression for the average torque over a commutation period $\overline{T}$ is:

$$
\begin{aligned}
\overline{T} = \frac{3}{2\,\pi} \Biggl(& \frac{2\,K_E\,V\,\sin\left(\theta_{ef}+\frac{\pi}{3}\right)}{3\,R} \\
& + \frac{8\,K_E\,V\,\left(\cos\left(\theta_{ef}+\frac{5\,\pi}{6}\right)-\frac{\sqrt{3}}{2}\right)}{3\,R} \\
& - \frac{10\,K_E\,V\,\left(\cos\left(\theta_{ef}+\frac{5\,\pi}{6}\right)+\frac{\sqrt{3}}{2}\right)}{3\,R} \\
& + \frac{2\,K_E\,V\,\left(\frac{\sin\left(\theta_{ef}\right)}{2}-\frac{\sqrt{3}\,\cos\left(\theta_{ef}\right)}{2}\right)}{3\,R} \\
& - \frac{2\,K_E\,V\,\left(\frac{\left(2\,L^2\,{n_{pp}}^2\,\omega_e^2\,\sin\left(\theta_{ef}\right)-2\,L\,R\,n_{pp}\,\omega_e\,\cos\left(\theta_{ef}\right)\right)}{\left(2\,L^2\,{n_{pp}}^2\,\omega_e^2+2\,R^2\right)}\right)}{3\,R} \\
& - \frac{2\,K_E\,V\,\left(-\frac{\left(L^2\,{n_{pp}}^2\,\omega_e^2\,\sin\left(\theta_{ef}\right)-L\,R\,n_{pp}\,\omega_e\,\cos\left(\theta_{ef}\right)+\sqrt{3}\,L^2\,{n_{pp}}^2\,\omega_e^2\,\cos\left(\theta_{ef}\right)+\sqrt{3}\,L\,R\,n_{pp}\,\omega_e\,\sin\left(\theta_{ef}\right)\right)}{\left(2\,R^2\,\mathrm{e}^{\frac{\pi\,R}{3\,L\,n_{pp}\,\omega_e}}+2\,L^2\,{n_{pp}}^2\,\omega_e^2\,\mathrm{e}^{\frac{\pi\,R}{3\,L\,n_{pp}\,\omega_e}}\right)}\right)}{3\,R} \\
& + \frac{K_E^2\,R\,\omega_e\,\left(\frac{\theta_{ef}}{2}+\frac{\pi}{6}-\frac{\sin\left(2\,\theta_{ef}+\frac{5\,\pi}{3}\right)}{4}\right)}{2\,\left(L^2\,{n_{pp}}^2\,\omega_e^2+R^2\right)} - \frac{K_E^2\,R\,\omega_e\,\left(-\frac{\sqrt{3}\,\sin\left(\theta_{ef}\right)^2}{4}+\frac{\theta_{ef}}{4}+\frac{\sin\left(2\,\theta_{ef}\right)}{8}\right)}{2\,\left(L^2\,{n_{pp}}^2\,\omega_e^2+R^2\right)} \\
& - \frac{2\,K_E\,V\,\left(R\,\left(L\,n_{pp}\,\omega_e\,\sin\left(\theta_{ef}+\frac{\pi}{6}\right)-L\,n_{pp}\,\omega_e\,\mathrm{e}^{-\frac{2\,\pi\,R}{3\,L\,n_{pp}\,\omega_e}}\,\sin\left(\theta_{ef}+\frac{5\,\pi}{6}\right)\right)\right)}{3\,R\,\left(L^2\,{n_{pp}}^2\,\omega_e^2+R^2\right)} \\
& - \frac{2\,K_E\,V\,\left(L^2\,{n_{pp}}^2\,\omega_e^2\,\cos\left(\theta_{ef}+\frac{\pi}{6}\right)-L^2\,{n_{pp}}^2\,\omega_e^2\,\mathrm{e}^{-\frac{2\,\pi\,R}{3\,L\,n_{pp}\,\omega_e}}\,\cos\left(\theta_{ef}+\frac{5\,\pi}{6}\right)\right)}{3\,R\,\left(L^2\,{n_{pp}}^2\,\omega_e^2+R^2\right)} \\
& + \frac{10\,K_E\,V\,\left(\sqrt{3}\,L^2\,{n_{pp}}^2\,\omega_e^2-R\,\left(L\,n_{pp}\,\omega_e-2\,L\,n_{pp}\,\omega_e\,\mathrm{e}^{-\frac{\theta_{ef}\,R}{L\,n_{pp}\,\omega_e}}\,\sin\left(\theta_{ef}+\frac{5\,\pi}{6}\right)\right)\right)}{3\,R\,\left(2\,L^2\,{n_{pp}}^2\,\omega_e^2+2\,R^2\right)} \\
& + \frac{10\,K_E\,V\,\left(2\,L^2\,{n_{pp}}^2\,\omega_e^2\,\mathrm{e}^{-\frac{\theta_{ef}\,R}{L\,n_{pp}\,\omega_e}}\,\cos\left(\theta_{ef}+\frac{5\,\pi}{6}\right)\right)}{3\,R\,\left(2\,L^2\,{n_{pp}}^2\,\omega_e^2+2\,R^2\right)} \\
& - \frac{2\,K_E\,V\,\left(R\,\left(L\,n_{pp}\,\omega_e-L\,n_{pp}\,\omega_e\,\mathrm{e}^{-\frac{\left(\pi\,R+3\,\theta_{ef}\,R\right)}{3\,L\,n_{pp}\,\omega_e}}\,\sin\left(\theta_{ef}+\frac{5\,\pi}{6}\right)\right)\right)}{3\,R\,\left(L^2\,{n_{pp}}^2\,\omega_e^2+R^2\right)} \\
& - \frac{2\,K_E\,V\,\left(-L^2\,{n_{pp}}^2\,\omega_e^2\,\mathrm{e}^{-\frac{\left(\pi\,R+3\,\theta_{ef}\,R\right)}{3\,L\,n_{pp}\,\omega_e}}\,\cos\left(\theta_{ef}+\frac{5\,\pi}{6}\right)\right)}{3\,R\,\left(L^2\,{n_{pp}}^2\,\omega_e^2+R^2\right)} \\
& - \frac{K_E^2\,R\,\omega_e\,\left(R\,\left(L\,n_{pp}\,\omega_e-L\,n_{pp}\,\omega_e\,\mathrm{e}^{-\frac{\left(\pi\,R+3\,\theta_{ef}\,R\right)}{3\,L\,n_{pp}\,\omega_e}}\,\sin\left(\theta_{ef}+\frac{5\,\pi}{6}\right)\right)\right)}{2\,\left(L^2\,{n_{pp}}^2\,\omega_e^2+R^2\right)^2} \\
& - \frac{K_E^2\,R\,\omega_e\,\left(-L^2\,{n_{pp}}^2\,\omega_e^2\,\mathrm{e}^{-\frac{\left(\pi\,R+3\,\theta_{ef}\,R\right)}{3\,L\,n_{pp}\,\omega_e}}\,\cos\left(\theta_{ef}+\frac{5\,\pi}{6}\right)\right)}{2\,\left(L^2\,{n_{pp}}^2\,\omega_e^2+R^2\right)^2} \\
& + \frac{8\,K_E\,V\,\left(\frac{L\,n_{pp}\,\omega_e\,\left(\sqrt{3}\,L\,n_{pp}\,\omega_e-2\,L\,n_{pp}\,\omega_e\,\mathrm{e}^{-\frac{\left(2\,\pi\,R+3\,\theta_{ef}\,R\right)}{3\,L\,n_{pp}\,\omega_e}}\,\cos\left(\theta_{ef}+\frac{5\,\pi}{6}\right)\right)}{2}\right)}{3\,R\,\left(L^2\,{n_{pp}}^2\,\omega_e^2+R^2\right)} \\
& + \frac{8\,K_E\,V\,\left(-\frac{L\,R\,n_{pp}\,\omega_e\,\left(2\,\mathrm{e}^{-\frac{\left(2\,\pi\,R+3\,\theta_{ef}\,R\right)}{3\,L\,n_{pp}\,\omega_e}}\,\sin\left(\theta_{ef}+\frac{5\,\pi}{6}\right)-1\right)}{2}\right)}{3\,R\,\left(L^2\,{n_{pp}}^2\,\omega_e^2+R^2\right)}\ \ldots
\end{aligned}
\tag{A.2}
$$

$$\begin{aligned}
\ldots &- \frac{K_E^2\,R\,\omega_e\,\left(\frac{L\,n_{pp}\,\omega_e\,\left(\sqrt{3}\,L\,n_{pp}\,\omega_e - 2\,L\,n_{pp}\,\omega_e\,\mathrm{e}^{-\frac{\left(2\,\pi\,R + 3\,\theta_{ef}\,R\right)}{3\,L\,n_{pp}\,\omega_e}}\,\cos\left(\theta_{ef} + \frac{5\,\pi}{6}\right)\right)}{2}\right)}{\left(L^2\,{n_{pp}}^2\,\omega_e^2 + R^2\right)^2} \\
&- \frac{K_E^2\,R\,\omega_e\,\left(\frac{L\,n_{pp}\,\omega_e\,\left(\sqrt{3}\,L\,n_{pp}\,\omega_e - 2\,L\,n_{pp}\,\omega_e\,\mathrm{e}^{-\frac{\left(2\,\pi\,R + 3\,\theta_{ef}\,R\right)}{3\,L\,n_{pp}\,\omega_e}}\,\cos\left(\theta_{ef} + \frac{5\,\pi}{6}\right)\right)}{2}\right)}{\left(L^2\,{n_{pp}}^2\,\omega_e^2 + R^2\right)^2} \\
&+ \frac{2\,\sqrt{3}\,K_E\,V\,\cos\left(\theta_{ef}\right)}{3\,R} \\
&+ \frac{K_E^2\,R\,\omega_e\,\left(\frac{\theta_{ef}}{4} + \frac{\pi}{6} - \frac{\sin\left(2\,\theta_{ef}\right)}{4} + \frac{\sqrt{3}}{8}\right)}{\left(L^2\,{n_{pp}}^2\,\omega_e^2 + R^2\right)} \\
&- \frac{K_E^2\,R\,\omega_e\,\sin\left(\theta_{ef} + \frac{5\,\pi}{6}\right)\,\left(R\,\left(L\,n_{pp}\,\omega_e\,\sin\left(\theta_{ef} + \frac{\pi}{6}\right) - L\,n_{pp}\,\omega_e\,\mathrm{e}^{-\frac{2\,\pi\,R}{3\,L\,n_{pp}\,\omega_e}}\,\sin\left(\theta_{ef} + \frac{5\,\pi}{6}\right)\right)\right)}{\left(L^2\,{n_{pp}}^2\,\omega_e^2 + R^2\right)^2} \\
&- \frac{K_E^2\,R\,\omega_e\,\sin\left(\theta_{ef} + \frac{5\,\pi}{6}\right)\,\left(L^2\,{n_{pp}}^2\,\omega_e^2\,\cos\left(\theta_{ef} + \frac{\pi}{6}\right) - L^2\,{n_{pp}}^2\,\omega_e^2\,\mathrm{e}^{-\frac{2\,\pi\,R}{3\,L\,n_{pp}\,\omega_e}}\,\cos\left(\theta_{ef} + \frac{5\,\pi}{6}\right)\right)}{\left(L^2\,{n_{pp}}^2\,\omega_e^2 + R^2\right)^2} \\
&+ \frac{\sqrt{3}\,K_E^2\,R\,\omega_e\,\left(\frac{\cos\left(\theta_{ef}\right)^2}{2} + \frac{\theta_{ef}\,\sqrt{3}}{4} + \frac{\pi\,\sqrt{3}}{6} - \frac{1}{8}\right)}{\left(L^2\,{n_{pp}}^2\,\omega_e^2 + R^2\right)} \\
&+ \frac{\sqrt{3}\,K_E^2\,R\,\omega_e\,\cos\left(\theta_{ef} + \frac{5\,\pi}{6}\right)^2}{4\,\left(L^2\,{n_{pp}}^2\,\omega_e^2 + R^2\right)} \\
&- \frac{K_E^2\,L\,n_{pp}\,\omega_e^2\,\left(\frac{\sin\left(\theta_{ef}\right)^2}{4} - \frac{\theta_{ef}\,\sqrt{3}}{4} + \frac{\sqrt{3}\,\sin\left(2\,\theta_{ef}\right)}{8}\right)}{2\,\left(L^2\,{n_{pp}}^2\,\omega_e^2 + R^2\right)} \\
&+ \frac{K_E^2\,L\,n_{pp}\,\omega_e^2\,\left(\frac{\cos\left(\theta_{ef}\right)^2}{2} + \frac{\theta_{ef}\,\sqrt{3}}{4} + \frac{\pi\,\sqrt{3}}{6} - \frac{1}{8}\right)}{\left(L^2\,{n_{pp}}^2\,\omega_e^2 + R^2\right)} \\
&- \frac{K_E^2\,R\,\omega_e\,\left(\sqrt{3}\,L^2\,{n_{pp}}^2\,\omega_e^2 - R\,\left(L\,n_{pp}\,\omega_e - 2\,L\,n_{pp}\,\omega_e\,\mathrm{e}^{-\frac{\theta_{ef}\,R}{L\,n_{pp}\,\omega_e}}\,\sin\left(\theta_{ef} + \frac{5\,\pi}{6}\right)\right)\right)}{2\,\left(2\,L^2\,{n_{pp}}^2\,\omega_e^2 + 2\,R^2\right)\,\left(L^2\,{n_{pp}}^2\,\omega_e^2 + R^2\right)} \\
&- \frac{K_E^2\,R\,\omega_e\,\left(2\,L^2\,{n_{pp}}^2\,\omega_e^2\,\mathrm{e}^{-\frac{\theta_{ef}\,R}{L\,n_{pp}\,\omega_e}}\,\cos\left(\theta_{ef} + \frac{5\,\pi}{6}\right)\right)}{2\,\left(2\,L^2\,{n_{pp}}^2\,\omega_e^2 + 2\,R^2\right)\,\left(L^2\,{n_{pp}}^2\,\omega_e^2 + R^2\right)} \\
&+ \frac{K_E^2\,R\,\omega_e\,\cos\left(\theta_{ef} + \frac{5\,\pi}{6}\right)\,\left(\frac{3\,\cos\left(\theta_{ef}\right)}{8} - \frac{\pi\,\sin\left(\theta_{ef}\right)}{6} + \frac{\sqrt{3}\,\sin\left(\theta_{ef}\right)}{8} + \frac{\pi\,\sqrt{3}\,\cos\left(\theta_{ef}\right)}{6}\right)}{\left(L^2\,{n_{pp}}^2\,\omega_e^2 + R^2\right)} \\
&+ \frac{K_E^2\,R\,\omega_e\,\sin\left(\theta_{ef} + \frac{11\,\pi}{6}\right)\,\left(\frac{\left(2\,L^2\,{n_{pp}}^2\,\omega_e^2\,\sin\left(\theta_{ef}\right) - 2\,L\,R\,n_{pp}\,\omega_e\,\cos\left(\theta_{ef}\right)\right)}{\left(2\,L^2\,{n_{pp}}^2\,\omega_e^2 + 2\,R^2\right)}\right)}{\left(L^2\,{n_{pp}}^2\,\omega_e^2 + R^2\right)} \\
&+ \frac{K_E^2\,R\,\omega_e\,\sin\left(\theta_{ef} + \frac{11\,\pi}{6}\right)\,\left(-\frac{\left(L^2\,{n_{pp}}^2\,\omega_e^2\,\sin\left(\theta_{ef}\right) - L\,R\,n_{pp}\,\omega_e\,\cos\left(\theta_{ef}\right) + \sqrt{3}\,L^2\,{n_{pp}}^2\,\omega_e^2\,\cos\left(\theta_{ef}\right) + \sqrt{3}\,L\,R\,n_{pp}\,\omega_e\,\sin\left(\theta_{ef}\right)\right)}{\left(2\,R^2\,\mathrm{e}^{\frac{\pi\,R}{3\,L\,n_{pp}\,\omega_e}} + 2\,L^2\,{n_{pp}}^2\,\omega_e^2\,\mathrm{e}^{\frac{\pi\,R}{3\,L\,n_{pp}\,\omega_e}}\right)}\right)}{\left(L^2\,{n_{pp}}^2\,\omega_e^2 + R^2\right)} \\
&+ \frac{K_E^2\,R\,\omega_e\,\sin\left(\theta_{ef} + \frac{5\,\pi}{6}\right)\,\left(\frac{\pi\,\cos\left(\theta_{ef}\right)}{6} - \frac{3\,\sin\left(\theta_{ef}\right)}{8} + \frac{\sqrt{3}\,\cos\left(\theta_{ef}\right)}{8} + \frac{\pi\,\sqrt{3}\,\sin\left(\theta_{ef}\right)}{6}\right)}{\left(L^2\,{n_{pp}}^2\,\omega_e^2 + R^2\right)} \\
&+ \frac{K_E^2\,L\,n_{pp}\,\omega_e^2\,\cos\left(\theta_{ef} + \frac{5\,\pi}{6}\right)^2}{4\,\left(L^2\,{n_{pp}}^2\,\omega_e^2 + R^2\right)} \\
&+ \frac{K_E^2\,R\,\omega_e\,\cos\left(\theta_{ef} + \frac{11\,\pi}{6}\right)\,\left(\frac{3\,\cos\left(\theta_{ef}\right)}{8} - \frac{\pi\,\sin\left(\theta_{ef}\right)}{6} + \frac{\sqrt{3}\,\sin\left(\theta_{ef}\right)}{8}\right)}{\left(L^2\,{n_{pp}}^2\,\omega_e^2 + R^2\right)} \ldots
\end{aligned}$$

$$\cdots + \frac{K_E^2\, R\, \omega_e\, \sin\left(\theta_{ef} + \frac{11\,\pi}{6}\right) \left(\frac{\pi\, \cos\left(\theta_{ef}\right)}{6} - \frac{3\, \sin\left(\theta_{ef}\right)}{8} + \frac{\sqrt{3}\, \cos\left(\theta_{ef}\right)}{8}\right)}{\left(L^2\, {n_{pp}}^2\, \omega_e^2 + R^2\right)}$$

$$- \frac{\sqrt{3}\, K_E^2\, R\, \omega_e \left(\frac{\sin\left(\theta_{ef}\right)^2}{4} - \frac{\theta_{ef}\, \sqrt{3}}{4} + \frac{\sqrt{3}\, \sin\left(2\,\theta_{ef}\right)}{8}\right)}{2\, \left(L^2\, {n_{pp}}^2\, \omega_e^2 + R^2\right)}$$

$$- \frac{\sqrt{3}\, K_E^2\, L\, n_{pp}\, \omega_e^2 \left(\frac{\theta_{ef}}{4} + \frac{\pi}{6} - \frac{\sin\left(2\,\theta_{ef}\right)}{4} + \frac{\sqrt{3}}{8}\right)}{\left(L^2\, {n_{pp}}^2\, \omega_e^2 + R^2\right)}$$

$$- \frac{\sqrt{3}\, K_E^2\, L\, n_{pp}\, \omega_e^2 \left(\frac{\theta_{ef}}{2} + \frac{\pi}{6} - \frac{\sin\left(2\,\theta_{ef} + \frac{5\,\pi}{3}\right)}{4}\right)}{2\, \left(L^2\, {n_{pp}}^2\, \omega_e^2 + R^2\right)}$$

$$- \frac{K_E^2\, L\, n_{pp}\, \omega_e^2\, \cos\left(\theta_{ef} + \frac{11\,\pi}{6}\right) \left(\frac{\left(2\, L^2\, {n_{pp}}^2\, \omega_e^2\, \sin\left(\theta_{ef}\right) - 2\, L\, R\, n_{pp}\, \omega_e\, \cos\left(\theta_{ef}\right)\right)}{\left(2\, L^2\, {n_{pp}}^2\, \omega_e^2 + 2\, R^2\right)}\right)}{\left(L^2\, {n_{pp}}^2\, \omega_e^2 + R^2\right)}$$

$$- \frac{K_E^2\, L\, n_{pp}\, \omega_e^2\, \cos\left(\theta_{ef} + \frac{11\,\pi}{6}\right) \left(- \frac{\left(L^2\, {n_{pp}}^2\, \omega_e^2\, \sin\left(\theta_{ef}\right) - L\, R\, n_{pp}\, \omega_e\, \cos\left(\theta_{ef}\right) + \sqrt{3}\, L^2\, {n_{pp}}^2\, \omega_e^2\, \cos\left(\theta_{ef}\right) + \sqrt{3}\, L\, R\, n_{pp}\, \omega_e\, \sin\left(\theta_{ef}\right)\right)}{\left(2\, R^2\, \mathrm{e}^{\frac{\pi\, R}{3\, L\, n_{pp}\, \omega_e}} + 2\, L^2\, {n_{pp}}^2\, \omega_e^2\, \mathrm{e}^{\frac{\pi\, R}{3\, L\, n_{pp}\, \omega_e}}\right)}\right)}{\left(L^2\, {n_{pp}}^2\, \omega_e^2 + R^2\right)}$$

$$+ \frac{\sqrt{3}\, K_E^2\, L\, n_{pp}\, \omega_e^2 \left(- \frac{\sqrt{3}\sin\left(\theta_{ef}\right)^2}{4} + \frac{\theta_{ef}}{4} + \frac{\sin\left(2\,\theta_{ef}\right)}{8}\right)}{2\, \left(L^2\, {n_{pp}}^2\, \omega_e^2 + R^2\right)}$$

$$- \frac{K_E^2\, L\, n_{pp}\, \omega_e^2\, \cos\left(\theta_{ef} + \frac{5\,\pi}{6}\right) \left(\frac{\pi\, \cos\left(\theta_{ef}\right)}{6} - \frac{3\, \sin\left(\theta_{ef}\right)}{8} + \frac{\sqrt{3}\, \cos\left(\theta_{ef}\right)}{8} + \frac{\pi\, \sqrt{3}\, \sin\left(\theta_{ef}\right)}{6}\right)}{\left(L^2\, {n_{pp}}^2\, \omega_e^2 + R^2\right)}$$

$$+ \frac{K_E^2\, L\, n_{pp}\, \omega_e^2\, \sin\left(\theta_{ef} + \frac{5\,\pi}{6}\right) \left(\frac{3\, \cos\left(\theta_{ef}\right)}{8} - \frac{\pi\, \sin\left(\theta_{ef}\right)}{6} + \frac{\sqrt{3}\, \sin\left(\theta_{ef}\right)}{8} + \frac{\pi\, \sqrt{3}\, \cos\left(\theta_{ef}\right)}{6}\right)}{\left(L^2\, {n_{pp}}^2\, \omega_e^2 + R^2\right)}$$

$$- \frac{K_E^2\, L\, n_{pp}\, \omega_e^2\, \cos\left(\theta_{ef} + \frac{11\,\pi}{6}\right) \left(\frac{\pi\, \cos\left(\theta_{ef}\right)}{6} - \frac{3\, \sin\left(\theta_{ef}\right)}{8} + \frac{\sqrt{3}\, \cos\left(\theta_{ef}\right)}{8}\right)}{\left(L^2\, {n_{pp}}^2\, \omega_e^2 + R^2\right)}$$

$$+ \frac{\sqrt{3}\, K_E^2\, L\, n_{pp}\, \omega_e^2 \left(R \left(L\, n_{pp}\, \omega_e - L\, n_{pp}\, \omega_e\, \mathrm{e}^{-\frac{\left(\pi\, R + 3\, \theta_{ef}\, R\right)}{3\, L\, n_{pp}\, \omega_e}}\, \sin\left(\theta_{ef} + \frac{5\,\pi}{6}\right)\right) - L^2\, {n_{pp}}^2\, \omega_e^2\, \mathrm{e}^{-\frac{\left(\pi\, R + 3\, \theta_{ef}\, R\right)}{3\, L\, n_{pp}\, \omega_e}}\, \cos\left(\theta_{ef} + \frac{5\,\pi}{6}\right)\right)}{2\, {\left(L^2\, {n_{pp}}^2\, \omega_e^2 + R^2\right)}^2}$$

$$+ \frac{K_E^2\, L\, n_{pp}\, \omega_e^2\, \sin\left(\theta_{ef} + \frac{11\,\pi}{6}\right) \left(\frac{3\, \cos\left(\theta_{ef}\right)}{8} - \frac{\pi\, \sin\left(\theta_{ef}\right)}{6} + \frac{\sqrt{3}\, \sin\left(\theta_{ef}\right)}{8}\right)}{\left(L^2\, {n_{pp}}^2\, \omega_e^2 + R^2\right)}$$

$$+ \frac{K_E^2\, L\, n_{pp}\, \omega_e^2\, \cos\left(\theta_{ef} + \frac{5\,\pi}{6}\right) \left(R \left(L\, n_{pp}\, \omega_e\, \sin\left(\theta_{ef} + \frac{\pi}{6}\right) - L\, n_{pp}\, \omega_e\, \mathrm{e}^{-\frac{2\,\pi\, R}{3\, L\, n_{pp}\, \omega_e}}\, \sin\left(\theta_{ef} + \frac{5\,\pi}{6}\right)\right)\right)}{{\left(L^2\, {n_{pp}}^2\, \omega_e^2 + R^2\right)}^2}$$

$$+ \frac{K_E^2\, L\, n_{pp}\, \omega_e^2\, \cos\left(\theta_{ef} + \frac{5\,\pi}{6}\right) \left(L^2\, {n_{pp}}^2\, \omega_e^2\, \cos\left(\theta_{ef} + \frac{\pi}{6}\right) - L^2\, {n_{pp}}^2\, \omega_e^2\, \mathrm{e}^{-\frac{2\,\pi\, R}{3\, L\, n_{pp}\, \omega_e}}\, \cos\left(\theta_{ef} + \frac{5\,\pi}{6}\right)\right)}{{\left(L^2\, {n_{pp}}^2\, \omega_e^2 + R^2\right)}^2}$$

$$+ \frac{\sqrt{3}\, K_E^2\, L\, n_{pp}\, \omega_e^2 \left(\frac{L\, n_{pp}\, \omega_e \left(\sqrt{3}\, L\, n_{pp}\, \omega_e - 2\, L\, n_{pp}\, \omega_e\, \mathrm{e}^{-\frac{\left(2\,\pi\, R + 3\, \theta_{ef}\, R\right)}{3\, L\, n_{pp}\, \omega_e}}\, \cos\left(\theta_{ef} + \frac{5\,\pi}{6}\right)\right)}{2}\right)}{{\left(L^2\, {n_{pp}}^2\, \omega_e^2 + R^2\right)}^2}$$

$$+ \frac{\sqrt{3}\, K_E^2\, L\, n_{pp}\, \omega_e^2 \left(- \frac{L\, R\, n_{pp}\, \omega_e \left(2\, \mathrm{e}^{-\frac{\left(2\,\pi\, R + 3\, \theta_{ef}\, R\right)}{3\, L\, n_{pp}\, \omega_e}}\, \sin\left(\theta_{ef} + \frac{5\,\pi}{6}\right) - 1\right)}{2}\right)}{{\left(L^2\, {n_{pp}}^2\, \omega_e^2 + R^2\right)}^2}$$

$$+ \frac{\sqrt{3}\, K_E^2\, L\, n_{pp}\, \omega_e^2 \left(\sqrt{3}\, L^2\, {n_{pp}}^2\, \omega_e^2 - R \left(L\, n_{pp}\, \omega_e - 2\, L\, n_{pp}\, \omega_e\, \mathrm{e}^{-\frac{\theta_{ef}\, R}{L\, n_{pp}\, \omega_e}}\, \sin\left(\theta_{ef} + \frac{5\,\pi}{6}\right)\right)\right)}{2\, \left(2\, L^2\, {n_{pp}}^2\, \omega_e^2 + 2\, R^2\right) \left(L^2\, {n_{pp}}^2\, \omega_e^2 + R^2\right)} \cdots$$

$$\cdots + \frac{\sqrt{3}\,K_E^2\,L\,n_{pp}\,\omega_e^2\,\left(2\,L^2\,{n_{pp}}^2\,\omega_e^2\,\mathrm{e}^{-\frac{\theta_{ef}\,R}{L\,n_{pp}\,\omega_e}}\,\cos\left(\theta_{ef}+\frac{5\,\pi}{6}\right)\right)}{2\,\left(2\,L^2\,{n_{pp}}^2\,\omega_e^2+2\,R^2\right)\,\left(L^2\,{n_{pp}}^2\,\omega_e^2+R^2\right)}\Bigg)$$

The expression for the first current peak $\widehat{I_1}$ is:

$$\begin{aligned}
\widehat{I_1} = {} & \frac{4\,V\,\left(\frac{1}{R}-\frac{\mathrm{e}^{-\frac{\pi\,R}{3\,L\,n_{pp}\,\omega_e}}}{R}\right)}{3} - \frac{V\,\left(\frac{1}{R}-\frac{\mathrm{e}^{\frac{R\,\left(\theta_{ef}-\frac{\pi}{3}\right)}{L\,n_{pp}\,\omega_e}}}{R}\right)}{3} \\
& - \frac{K_E\,\omega_e\,\left(\frac{\left(\frac{R}{2}+\frac{\sqrt{3}\,L\,n_{pp}\,\omega_e}{2}\right)}{\left(L^2\,{n_{pp}}^2\,\omega_e^2+R^2\right)}-\frac{R\,\mathrm{e}^{-\frac{\pi\,R}{3\,L\,n_{pp}\,\omega_e}}}{\left(L^2\,{n_{pp}}^2\,\omega_e^2+R^2\right)}\right)}{2} \\
& + \frac{K_E\,\omega_e\,\cos\left(\theta_{ef}+\frac{5\,\pi}{6}\right)\,\left(\frac{\left(R\,\sin\left(\theta_{ef}-\frac{\pi}{3}\right)+L\,n_{pp}\,\omega_e\,\cos\left(\theta_{ef}-\frac{\pi}{3}\right)\right)}{\left(L^2\,{n_{pp}}^2\,\omega_e^2+R^2\right)}-\frac{L\,n_{pp}\,\omega_e\,\mathrm{e}^{\frac{R\,\left(\theta_{ef}-\frac{\pi}{3}\right)}{L\,n_{pp}\,\omega_e}}}{\left(L^2\,{n_{pp}}^2\,\omega_e^2+R^2\right)}\right)}{2} \\
& - \frac{K_E\,\omega_e\,\sin\left(\theta_{ef}+\frac{5\,\pi}{6}\right)\,\left(\frac{\left(R\,\cos\left(\theta_{ef}-\frac{\pi}{3}\right)-L\,n_{pp}\,\omega_e\,\sin\left(\theta_{ef}-\frac{\pi}{3}\right)\right)}{\left(L^2\,{n_{pp}}^2\,\omega_e^2+R^2\right)}-\frac{R\,\mathrm{e}^{\frac{R\,\left(\theta_{ef}-\frac{\pi}{3}\right)}{L\,n_{pp}\,\omega_e}}}{\left(L^2\,{n_{pp}}^2\,\omega_e^2+R^2\right)}\right)}{2} \\
& - \frac{\sqrt{3}\,K_E\,\omega_e\,\left(\frac{\left(\frac{\sqrt{3}\,R}{2}-\frac{L\,n_{pp}\,\omega_e}{2}\right)}{\left(L^2\,{n_{pp}}^2\,\omega_e^2+R^2\right)}+\frac{L\,n_{pp}\,\omega_e\,\mathrm{e}^{-\frac{\pi\,R}{3\,L\,n_{pp}\,\omega_e}}}{\left(L^2\,{n_{pp}}^2\,\omega_e^2+R^2\right)}\right)}{2}
\end{aligned} \tag{A.3}$$

The expression for the second current peak $\widehat{I}_2$ is:

$$
\begin{aligned}
\widehat{I}_2 = {} & \frac{4\,V\,\left(\frac{1}{R}-\frac{\mathrm{e}^{-\frac{2\,\pi\,R}{3\,L\,n_{pp}\,\omega_e}}}{R}\right)}{3}-\frac{V\,\left(\frac{1}{R}-\frac{\mathrm{e}^{-\frac{\pi\,R}{3\,L\,n_{pp}\,\omega_e}}}{R}\right)}{3}+\frac{V\,\left(\frac{1}{R}-\frac{\mathrm{e}^{\frac{R\,\left(\theta_{ef}-\frac{\pi}{3}\right)}{L\,n_{pp}\,\omega_e}}}{R}\right)}{3} \\
& -\frac{V\,\left(\frac{1}{R}-\frac{\mathrm{e}^{\frac{R\,\left(\theta_{ef}-\frac{2\,\pi}{3}\right)}{L\,n_{pp}\,\omega_e}}}{R}\right)}{3} \\
& +\frac{K_E\,\omega_e\,\left(\frac{\left(\frac{R}{2}-\frac{\sqrt{3}\,L\,n_{pp}\,\omega_e}{2}\right)}{\left(L^2\,{n_{pp}}^2\,\omega_e^2+R^2\right)}+\frac{R\,\mathrm{e}^{-\frac{2\,\pi\,R}{3\,L\,n_{pp}\,\omega_e}}}{\left(L^2\,{n_{pp}}^2\,\omega_e^2+R^2\right)}\right)}{2} \\
& -\frac{K_E\,\omega_e\,\left(\frac{\left(\frac{R}{2}+\frac{\sqrt{3}\,L\,n_{pp}\,\omega_e}{2}\right)}{\left(L^2\,{n_{pp}}^2\,\omega_e^2+R^2\right)}-\frac{R\,\mathrm{e}^{-\frac{\pi\,R}{3\,L\,n_{pp}\,\omega_e}}}{\left(L^2\,{n_{pp}}^2\,\omega_e^2+R^2\right)}\right)}{4} \\
& +\frac{K_E\,\omega_e\,\cos\left(\theta_{ef}+\frac{5\,\pi}{6}\right)\,\left(\frac{\left(R\,\sin\left(\theta_{ef}-\frac{2\,\pi}{3}\right)+L\,n_{pp}\,\omega_e\,\cos\left(\theta_{ef}-\frac{2\,\pi}{3}\right)\right)}{\left(L^2\,{n_{pp}}^2\,\omega_e^2+R^2\right)}-\frac{L\,n_{pp}\,\omega_e\,\mathrm{e}^{\frac{R\,\left(\theta_{ef}-\frac{2\,\pi}{3}\right)}{L\,n_{pp}\,\omega_e}}}{\left(L^2\,{n_{pp}}^2\,\omega_e^2+R^2\right)}\right)}{2} \\
& +\frac{K_E\,\omega_e\,\cos\left(\theta_{ef}+\frac{11\,\pi}{6}\right)\,\left(\frac{\left(R\,\sin\left(\theta_{ef}-\frac{\pi}{3}\right)+L\,n_{pp}\,\omega_e\,\cos\left(\theta_{ef}-\frac{\pi}{3}\right)\right)}{\left(L^2\,{n_{pp}}^2\,\omega_e^2+R^2\right)}-\frac{L\,n_{pp}\,\omega_e\,\mathrm{e}^{\frac{R\,\left(\theta_{ef}-\frac{\pi}{3}\right)}{L\,n_{pp}\,\omega_e}}}{\left(L^2\,{n_{pp}}^2\,\omega_e^2+R^2\right)}\right)}{2} \\
& -\frac{K_E\,\omega_e\,\sin\left(\theta_{ef}+\frac{5\,\pi}{6}\right)\,\left(\frac{\left(R\,\cos\left(\theta_{ef}-\frac{2\,\pi}{3}\right)-L\,n_{pp}\,\omega_e\,\sin\left(\theta_{ef}-\frac{2\,\pi}{3}\right)\right)}{\left(L^2\,{n_{pp}}^2\,\omega_e^2+R^2\right)}-\frac{R\,\mathrm{e}^{\frac{R\,\left(\theta_{ef}-\frac{2\,\pi}{3}\right)}{L\,n_{pp}\,\omega_e}}}{\left(L^2\,{n_{pp}}^2\,\omega_e^2+R^2\right)}\right)}{2} \\
& -\frac{K_E\,\omega_e\,\sin\left(\theta_{ef}+\frac{11\,\pi}{6}\right)\,\left(\frac{\left(R\,\cos\left(\theta_{ef}-\frac{\pi}{3}\right)-L\,n_{pp}\,\omega_e\,\sin\left(\theta_{ef}-\frac{\pi}{3}\right)\right)}{\left(L^2\,{n_{pp}}^2\,\omega_e^2+R^2\right)}-\frac{R\,\mathrm{e}^{\frac{R\,\left(\theta_{ef}-\frac{\pi}{3}\right)}{L\,n_{pp}\,\omega_e}}}{\left(L^2\,{n_{pp}}^2\,\omega_e^2+R^2\right)}\right)}{2} \\
& -\frac{\sqrt{3}\,K_E\,\omega_e\,\left(\frac{\left(\frac{\sqrt{3}\,R}{2}-\frac{L\,n_{pp}\,\omega_e}{2}\right)}{\left(L^2\,{n_{pp}}^2\,\omega_e^2+R^2\right)}+\frac{L\,n_{pp}\,\omega_e\,\mathrm{e}^{-\frac{\pi\,R}{3\,L\,n_{pp}\,\omega_e}}}{\left(L^2\,{n_{pp}}^2\,\omega_e^2+R^2\right)}\right)}{4} \\
& -\frac{\sqrt{3}\,K_E\,\omega_e\,\left(\frac{\left(\frac{\sqrt{3}\,R}{2}+\frac{L\,n_{pp}\,\omega_e}{2}\right)}{\left(L^2\,{n_{pp}}^2\,\omega_e^2+R^2\right)}+\frac{L\,n_{pp}\,\omega_e\,\mathrm{e}^{-\frac{2\,\pi\,R}{3\,L\,n_{pp}\,\omega_e}}}{\left(L^2\,{n_{pp}}^2\,\omega_e^2+R^2\right)}\right)}{2}
\end{aligned}
\tag{A.4}
$$

Appendix B

Computationally efficient model power loss

A computationally efficient motor model is presented in Section 3.5, along with related equations in Appendix A. The average of the squared current is calculated using the approximation of a rectangular current waveform. This is justified in this appendix by reference to simulation results for the five sample motors presented in Appendix H.

Whilst the power loss for the computationally efficient model may be estimated using the average current, as shown in Equation 3.29, it may also be calculated through a piecewise linear approximation of the current waveform. Considering half a six-step switching cycle, for example switching intervals I, II and III in Figure 3.8, the current waveform may be approximated as a triangular rise, three trapezoids, and a triangular fall. This approximation is shown by the dashed line in Figure B.1, compared to the solid line – which is the square of the current shown in Figure 3.8.

The calculation of this approximation requires a measure of the current after commutation ends $I_{\theta_{ef}}$ and the peak current $\widehat{I}_1$. The second of these is available within the model, and the first may be calculated using *MuPad* in a similar manner to the rest of the model. Assuming linearity between these points the average of the square current can be calculated as

$$\overline{I^2} = \frac{1}{3}\left(I_{\theta_{ef}}^2 + \widehat{I}_1{}^2\right) \tag{B.1}$$

based on addition of the areas under the triangles and trapezoids. Although the commutation angle θ_{ef} is available for this calculation, it is not required as it cancels during simplification.

Power loss has been calculated by running the efficient model alongside the full model, to steady-state, at a number of different load torques and for a fixed voltage. The results for the *McLennan* machine are shown in Figure B.2. These are calculated for a fixed temperature of 95 °C at 24 V, and have corresponding speed-torque curves

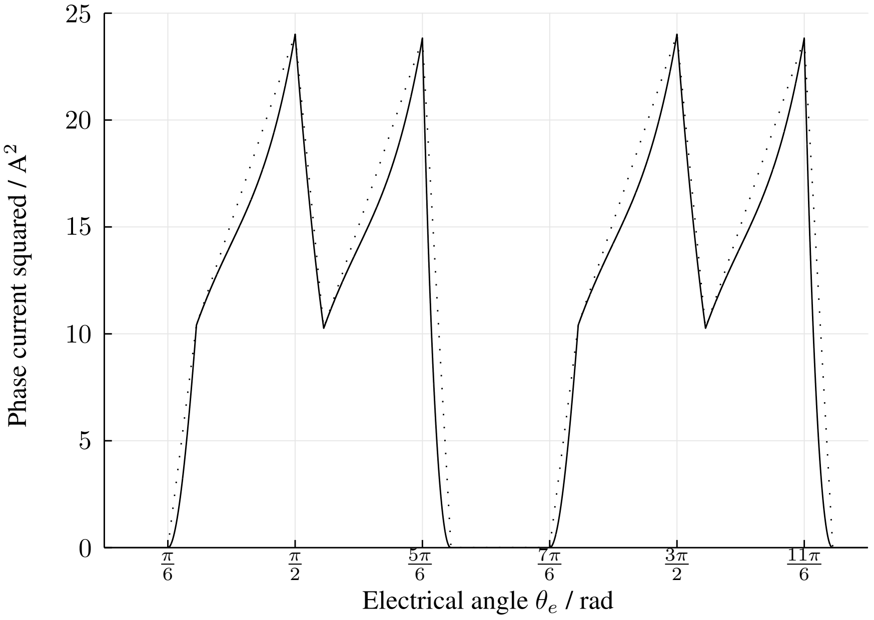

Figure B.1: Squared current in phase during commutation (solid), and a piecewise linear approximation (dashed)

similar to those in Section 5.2. It shows very similar performance between the models, with errors typically being seen at high torques. Average current measurement becomes noisy for the full model as the machine approaches stall torque, due to the large switching interval at very low speeds.

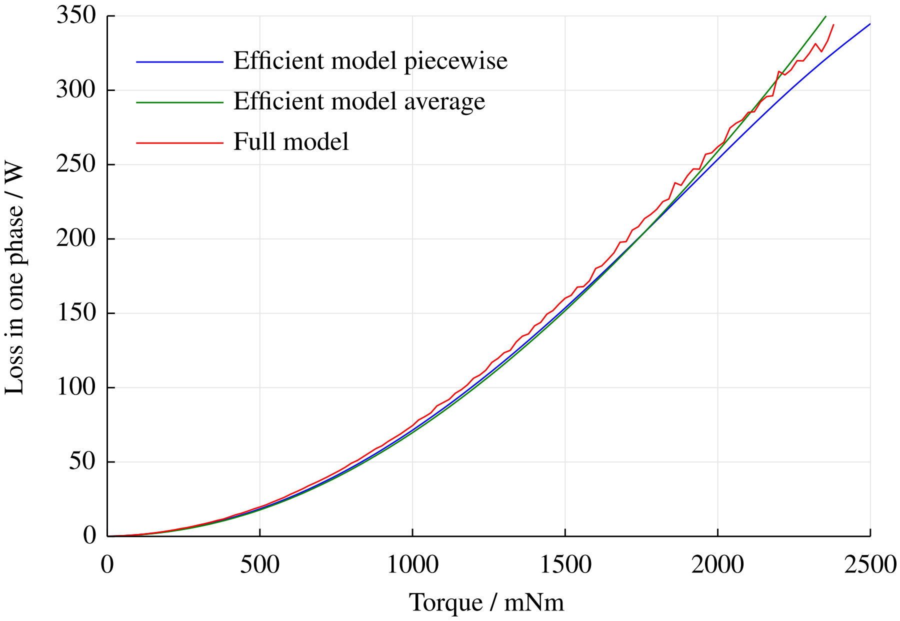

Figure B.2: Joule losses calculated by different models for the *McLennan* motor

Equivalent results for the *Maxon* EC-Flat and EC-Max motors are shown in Figures B.3 and B.4. A minor improvement in performance is seen at low torque and high speed by using the piecewise approximation in the efficient model, giving very similar performance to the full model; however this approximation also produces an underestimate of power loss as torque is increased. This effect occurs only close to stall torque for most of the sample motors, but is significant for a large part of the performance envelope for the *Maxon* EC-Max machine.

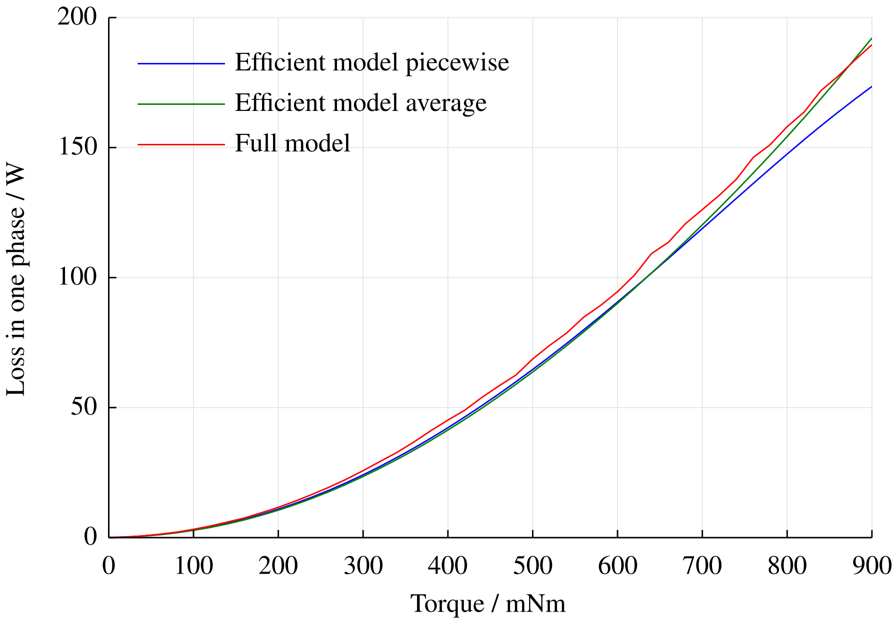

Figure B.3: Joule losses calculated by different models for the *Maxon* EC-Flat motor

The underestimate occurs when the commutation period is a small proportion of the switching period and there is a continued nonlinear current rise after this point – the linear approximation cannot include this rise. The low pole-pair number and electrical time constant of the EC-Max machine emphasises this effect. An example of this effect on the squared current waveform is shown in Figure B.5. The extent of this impact on the EC-Max results in Figure B.4 makes the piecewise approximation unreliable for use in this work.

The error in the average current approximation is typically below 10 %; being an underestimate at low torque and an overestimate at high torque. Performance of this approximation is similar across different voltages and temperature ranges. This is therefore the favoured approach for determining power loss in the computationally efficient model.

An alternative approach would be to compute power loss using the full model for a range of operating voltages and torques, and store this as a lookup table for use in the efficient model. A similar approach has been proposed in the literature for precomputing the commutation angle [169, 170]. Although this would provide the highest fidelity solution, it would also be the least flexible; it has therefore not been pursued in this work .

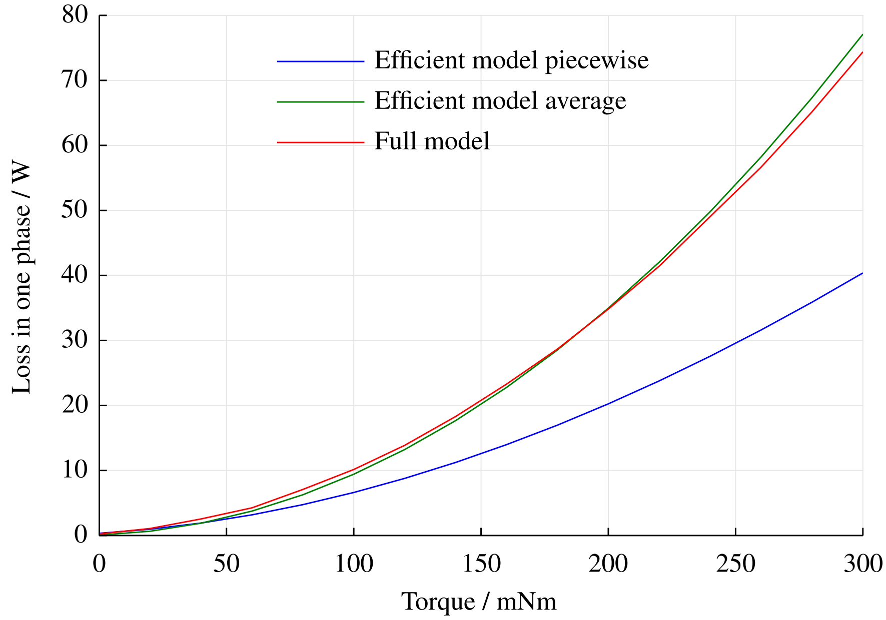

Figure B.4: Joule losses calculated by different models for the *Maxon* EC-Max motor

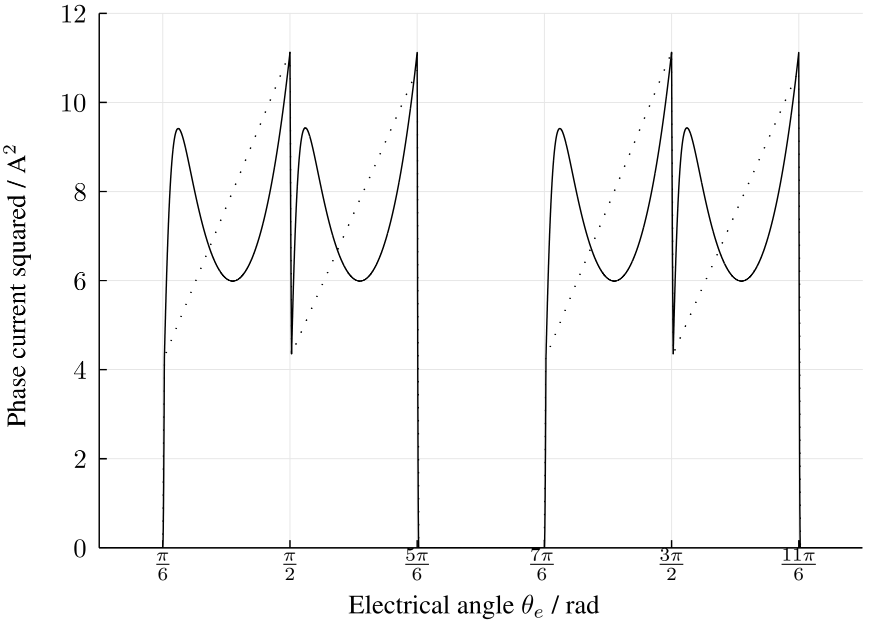

Figure B.5: Squared current in phase during commutation (solid), and the piecewise linear approximation (dashed), for the EC-Max machine

Appendix C

Actuator models in *Matlab Simulink*

C.1 Introduction

This appendix provides details of the *Simulink* implementation of the mathematical models outlined in Chapter 3. This is presented as images of the *Simulink* block diagrams, with commentary and references to the mathematical details in Chapter 3 as required. Although some familiarity with *Simulink* will be beneficial, care has been taken during layout to aid understanding. Several layers of subsystems are used to simplify layout, as indicated in the figure captions. In some cases 'masks' are used to pass parameters between system levels, including some dynamic masking in order to swap subsystem depending on mask selections – this allows for code reuse during model fidelity changes – where this technique is used it is noted in the text.

C.2 Motor model

The motor model has a mask for parameter input and selection between the full and computationally efficient winding models, and for inclusion of the thermal model or not. Beneath the mask the motor model is shown in Figure C.1. The 'noThermalModel' and 'windingsSimple' blocks automatically switch, depending on the mask selections, to 'thermalModel' and 'windingsComplete' blocks respectively. Where the full model is selected, connections for torque, current, power loss, voltage and winding temperature will represent 3×1 vector signals. Hall signals are always a 3×1 vector signal.

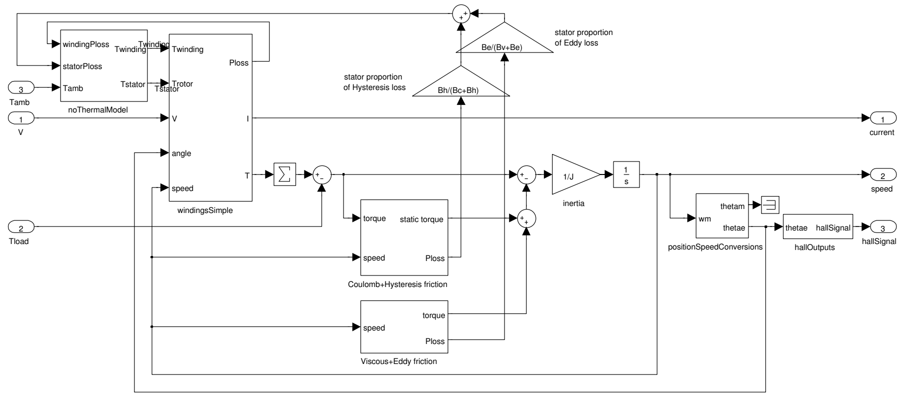

Figure C.1: *Simulink* interconnection of the motor equations

C.2.1 Full three-phase model

Implementation of the full three-phase motor model is via an intermediate level, shown in Figure C.2. This implements the ‘balance compensation’ which includes Equations 3.8 and 3.9, shown in Figures C.3 and C.4. The angular offsets used in Equation 3.4 are also introduced.

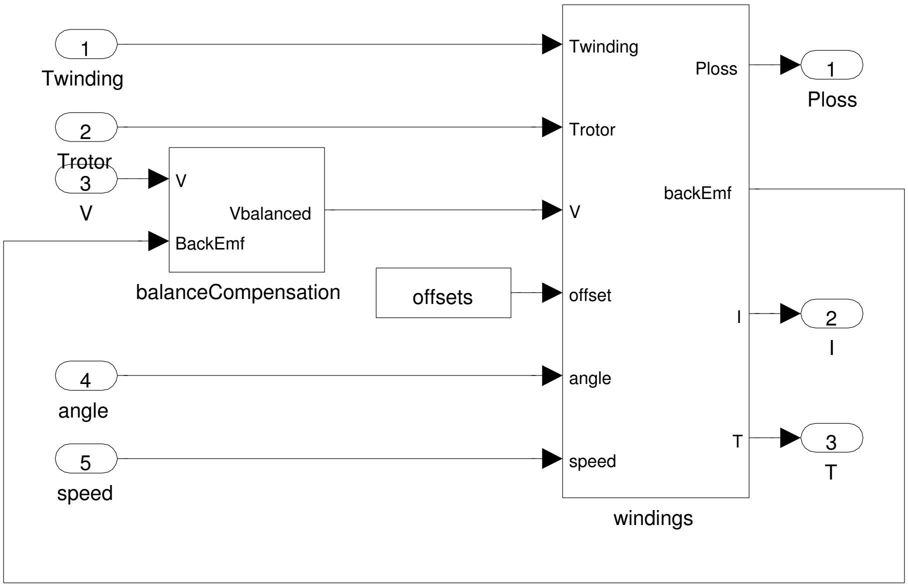

Figure C.2: *Simulink* windingsComplete intermediate level

The full motor electrical equations are implemented as shown in Figure C.5. This includes the electromagnetic Equations 3.2 and 3.5, alongside the variation of resistance and back-EMF constant with temperature, Equations 3.18 and 3.19, and the power loss in the winding, given by Equation 3.20. As some the inputs to this subsystem are vector signals, three-phase equations will handled automatically by *Simulink*.

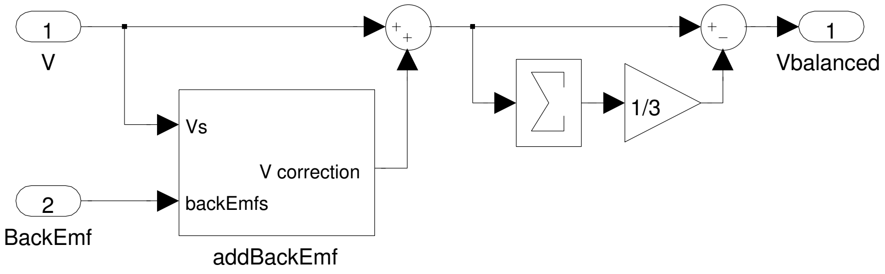

Figure C.3: *Simulink* windingsComplete/balanceCompensation implementing Equation 3.8

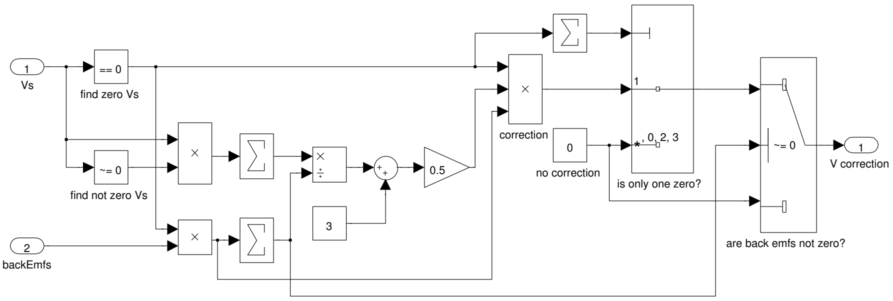

Figure C.4: *Simulink* windingsComplete/balanceCompensation/addBackEmf implementing Equation 3.9

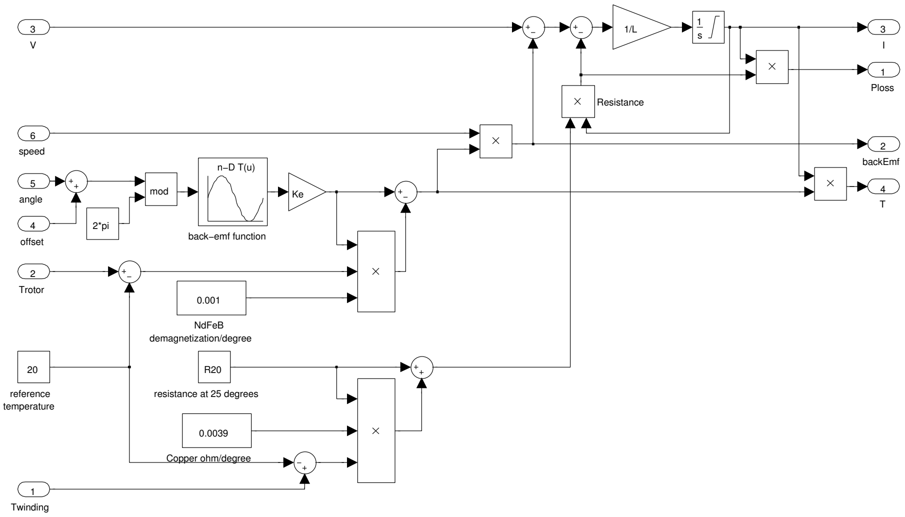

Figure C.5: *Simulink* windingsComplete/windings implementing Equation 3.8

C.2.2 Computationally efficient model

Implementation of the computationally efficient model is shown in Figure C.6. This includes the same temperature variation and power loss equations as used in the full model, however the analytic equations for calculating current and torque presented in Appendix A are used. Beneath the ‘currentTorque’ subsystem is the commutation angle tracking and *Matlab* equation calls shown in Figure 3.9. All signals within this are scalar, representing average values.

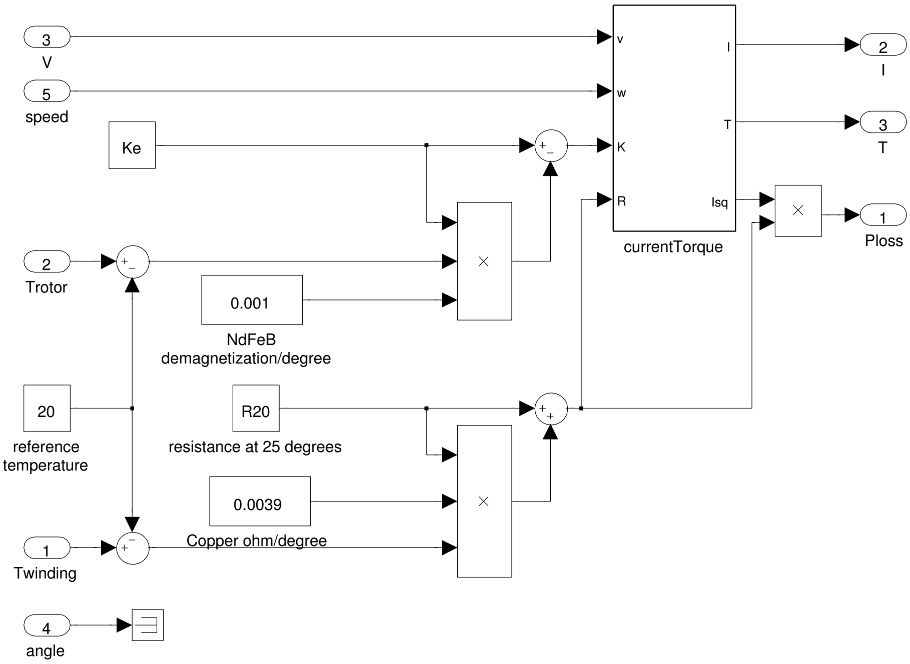

Figure C.6: *Simulink* windingsSimple – computationally efficient model implementation

C.2.3 Thermal model

Where a thermal model is not used, the ambient temperature is used as the winding and rotor temperatures, shown in Figure C.7. If the thermal model is selected then calculation is split into winding and stator temperatures (Figure C.8), shown in Figures C.9 and C.10, and implementing Equations 3.22 and 3.23, respectively. If the full model is used then the winding power loss and temperatures will be 3×1 vector signals, otherwise they are scalar. The 'sum of 3 windings' multiplier in Figure C.8 is set to compensate for this in the thermal model, depending on the motor model selected.

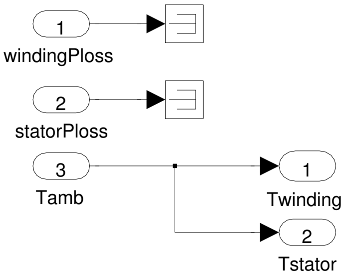

Figure C.7: *Simulink* noThermalModel – use of ambient temperature

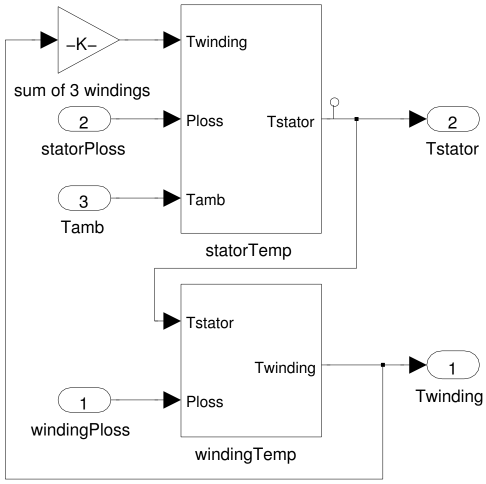

Figure C.8: *Simulink* thermalModel

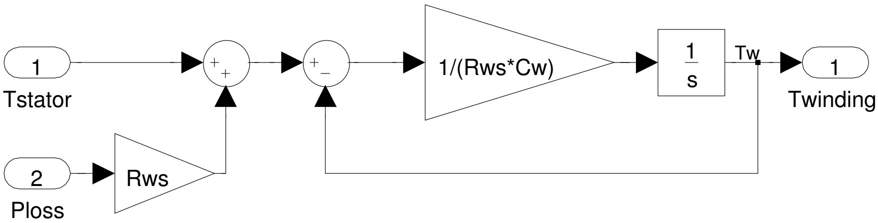

Figure C.9: *Simulink* thermalModel/windingTemp implementing Equation 3.22

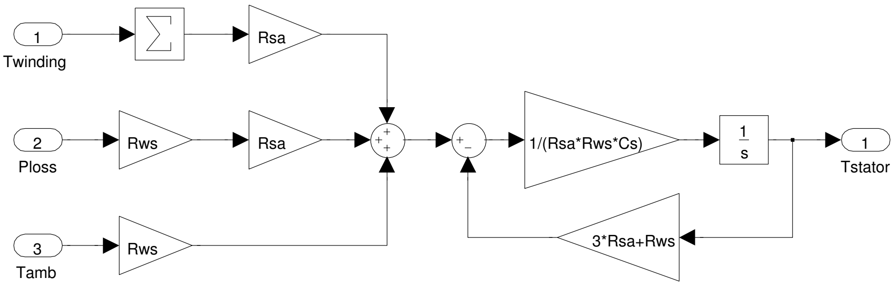

Figure C.10: *Simulink* thermalModel/statorTemp implementing Equation 3.23

C.2.4 Loss modelling

The frictional losses and iron losses have been combined within the *Simulink* model. Coulomb friction and hysteresis loss, defined in Equations 3.36 and 3.13 respectively, is included as shown in Figure C.11. Similarly, viscous friction and eddy current loss, defined by Equations 3.34 and 3.15, are included in Figure C.12. Power loss calculated in these subsystems is separated in the top level motor system (Figure C.1), such that only iron losses contribute to heating in the thermal model.

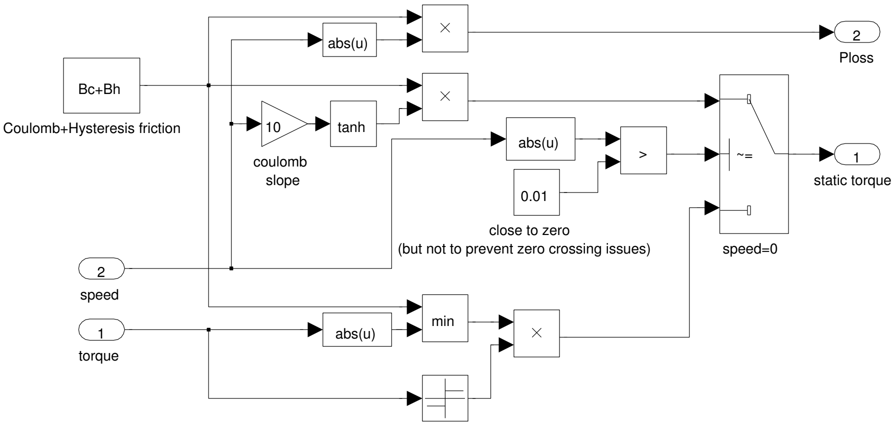

Figure C.11: *Simulink* Coulomb+Hysteresis friction implementing Equations 3.36 and 3.13

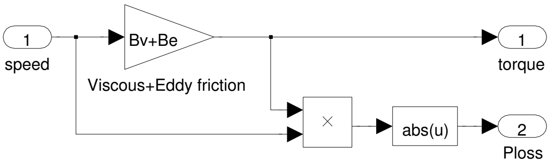

Figure C.12: *Simulink* Viscous+Eddy friction implementing Equations 3.34 and 3.15

C.2.5 Motor mechanics

Electrical torque, load torque and torques due to friction and iron loss are combined and converted to a motor speed using the specified inertia, according to Equations 3.17 and 3.38, as shown in Figure C.1. This is a mechanical shaft speed, but is converted to an electrical position based on the specified number of magnet pole pairs, for use in the electromagnetic model and for calculation of the hall sensor output, as shown in Figure C.13.

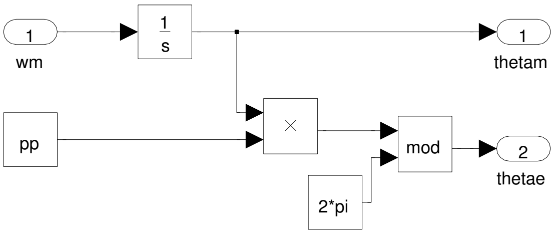

Figure C.13: *Simulink* positionSpeedConversions converting from mechanical speed to electrical position

C.2.6 Hall sensor output

The output of hall sensors within the motor is simulated based on the electrical position as shown in Figure C.14, where the ‘hallSignals’ lookup table is as specified by Table 3.4, and the sector calculation is as shown in Figure C.15.

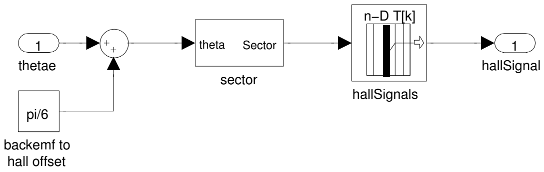

Figure C.14: *Simulink* hallOutputs converting from electrical position to hall sensor signals

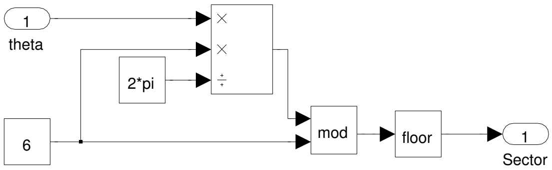

Figure C.15: *Simulink* hallOutputs/sector quantising the electrical position

C.3 Drive power electronics model

The drive power electronics model is shown in Figure C.16. This accepts a 3×1 vector of phase currents, supplied by the motor model, and a 3×1 vector of switch states, encoded as either 1, -1 or 0, as described in Section 3.4 and Table 3.5. The scalar voltage supplied to it should be half the DC link voltage.

Switch signals to drive this half-bridge model may be generated using the system shown in Figure C.17, as described in Section 3.4.2. This includes subsystems to interpret the hall signals, PWM signal generation and a mechanism for limiting the current.

Figure C.18 shows a conversion process that might typically be handled by an interrupt routine in a brushless motor microcontroller, implemented in *Simulink*. Hall signal vectors, supplied by the motor model, are converted into a quantised sector labelled as an incremental decimal sequence. This numeric sector is then passed to a lookup table to determine the half-bridge switch requests. The lookup table may differ for forward or reverse direction requests, depending whether a unipolar or bipolar switching scheme is used. The lookup tables may be modified to implement different switching schemes, as shown in Table 2.1.

This subsystem also calculates a position measurement based on the hall signals, as shown in Figure C.19. This is based on the change in the numeric sector calculated above, with provision for when the numeric sector wraps upwards and downwards.

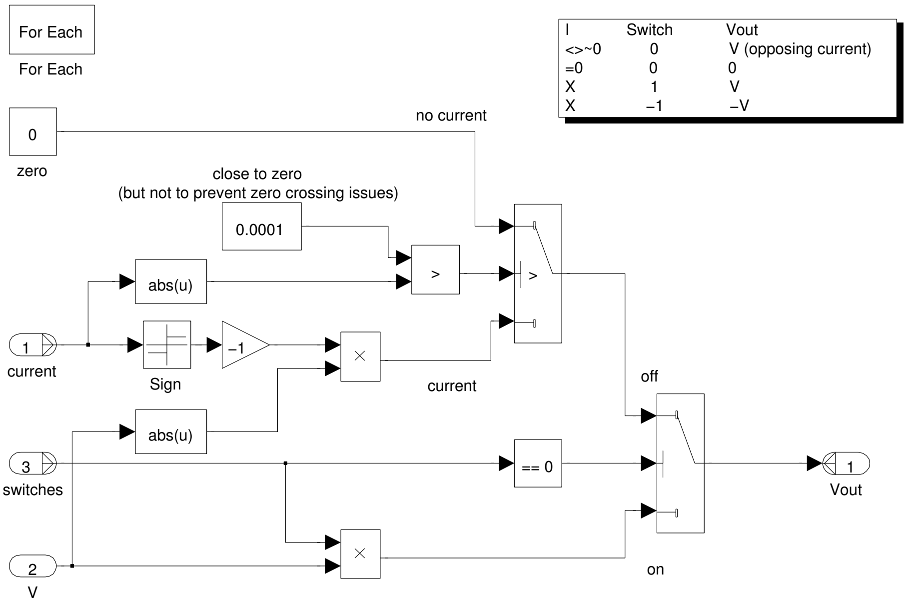

Figure C.16: *Simulink* half-bridge model implementing Table 3.5

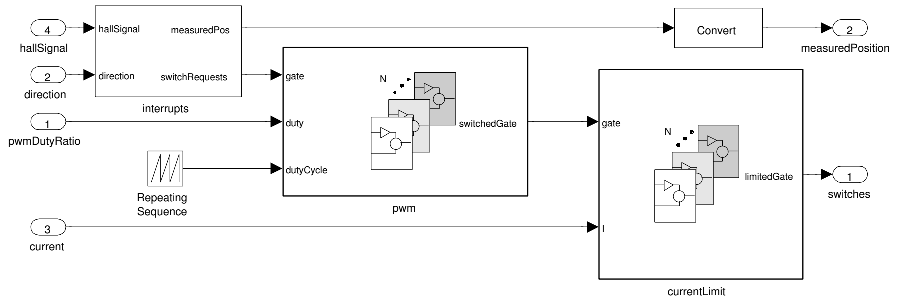

Figure C.17: *Simulink* switch signal generation

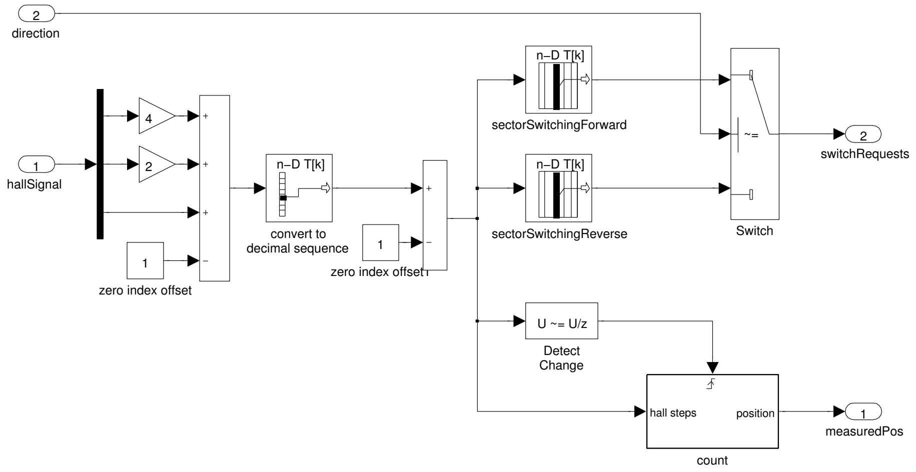

Figure C.18: *Simulink* switch/interrupts to process hall signals

The count of hall sensor changes is converted to an electrical angular position. This is not required for commutation, but is available to the simulation for the implementation of position control schemes or similar. Conversion to a mechanical position, taking into account the number of pole-pairs and any transmission scaling, must be handled externally.

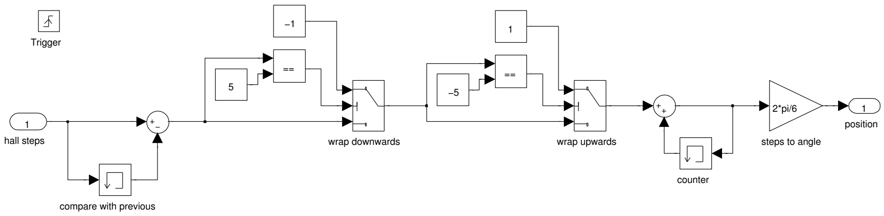

Figure C.19: *Simulink* switch/interrupts/count to calculate position based on hall signals

PWM switching and current control modulate the switch requests to the half-bridge, as shown in Figures C.20 and C.21. PWM is based on the duty ratio and set up for complementary switching; minor modification to the internal logic of this block can change it to independent switching. Current in the motor phases is monitored and the switch output disabled during overcurrent.

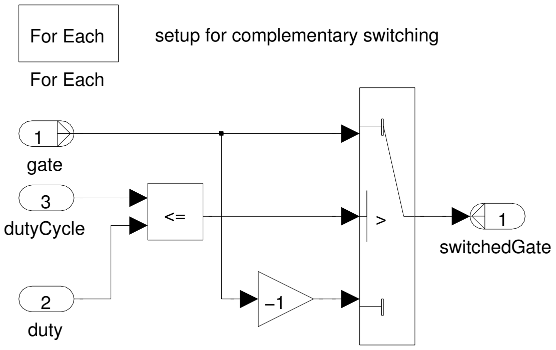

Figure C.20: *Simulink* switch/pwm to modulate the switch signals to the half-bridge based on duty ratio

C.4 General mechanical model

As outlined in Section 3.7 the *Simulink* implementation of the general mechanical model is shown in Figure C.22. This accepts an input speed and a load force and returns a load speed and a force on the input. It may be used to model either linear or rotational components. Power loss in the mechanics is also calculated, although it has not been used within this work. Component parameters are handled through a system mask, which also allows the backlash to be included or excluded from the model.

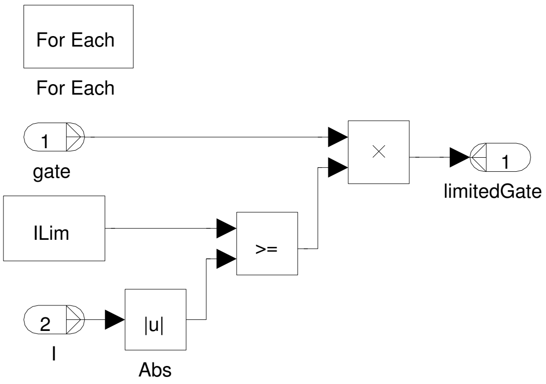

Figure C.21: *Simulink* switch/currentLimit to modulate the switch signals to the half-bridge to limit current

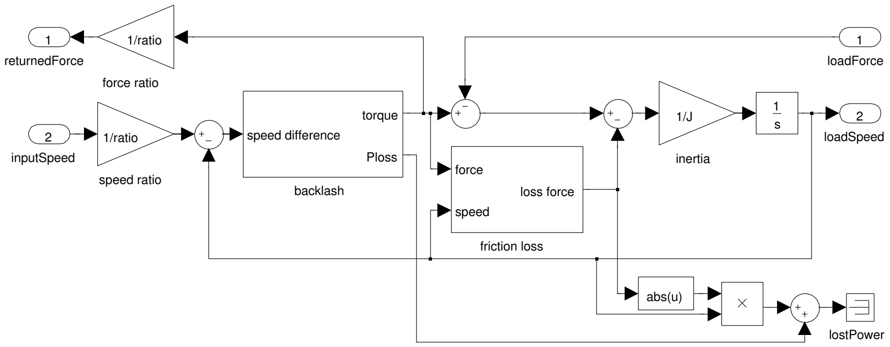

Figure C.22: *Simulink* general mechanical model construction

Equations 3.30 and 3.38 are shown in the top-level system. Frictional losses are calculated in the subsystems shown in Figures C.23 and C.24, implementing Equations 3.34, 3.36 and 3.37.

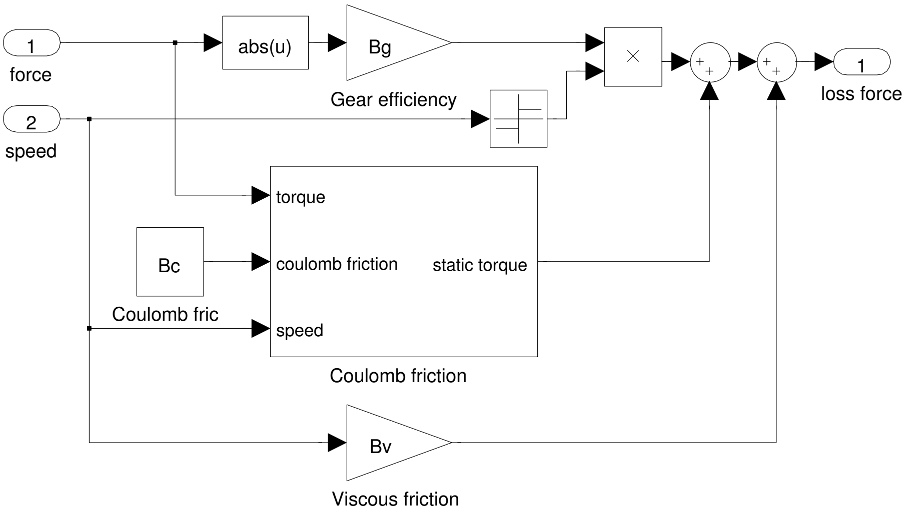

Figure C.23: *Simulink* friction loss in the general mechanical model

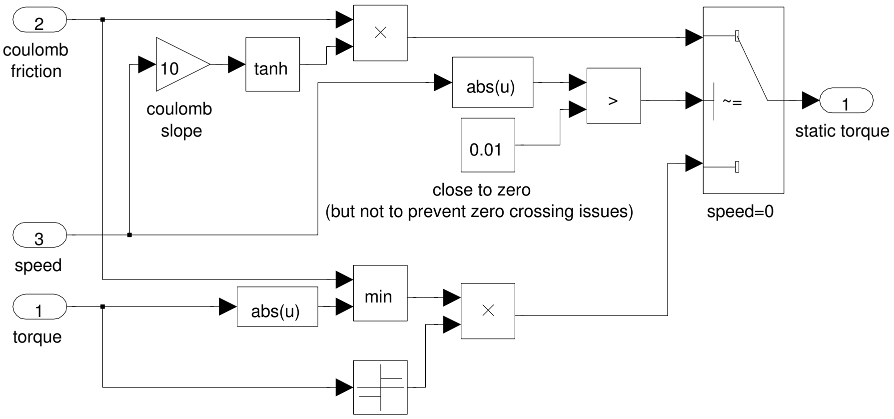

Figure C.24: *Simulink* Coulomb friction loss in the general mechanical model

Backlash will be included if switched on in the mask, as shown in Figures C.25 and C.26. This implements Equations 3.31, 3.32 and 3.33. Where backlash is not used it is replaced by the system shown in Figure C.27.

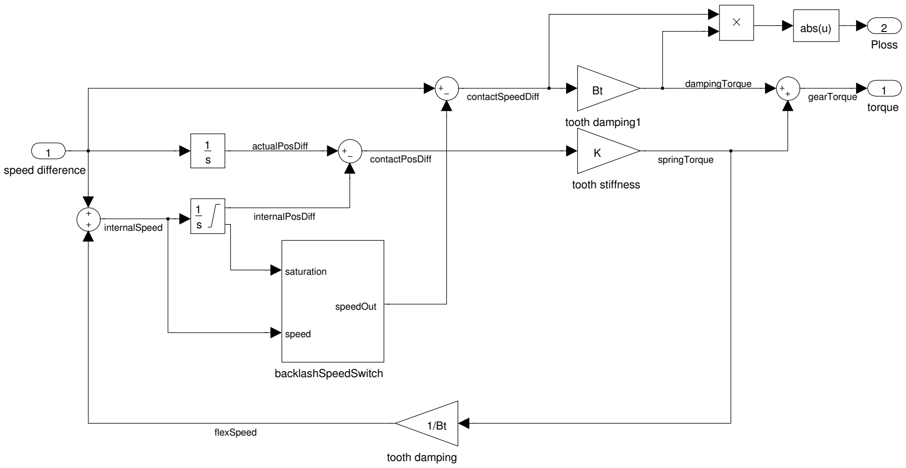

Figure C.25: *Simulink* backlash in the general mechanical model

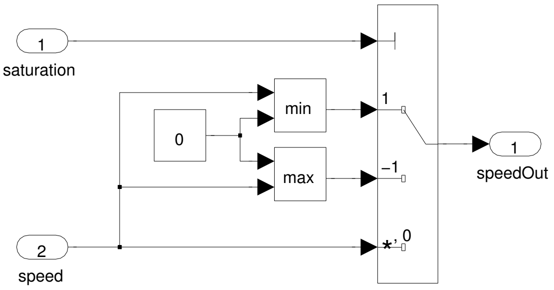

Figure C.26: *Simulink* backlash/backlashSpeedSwitch in the general mechanical model

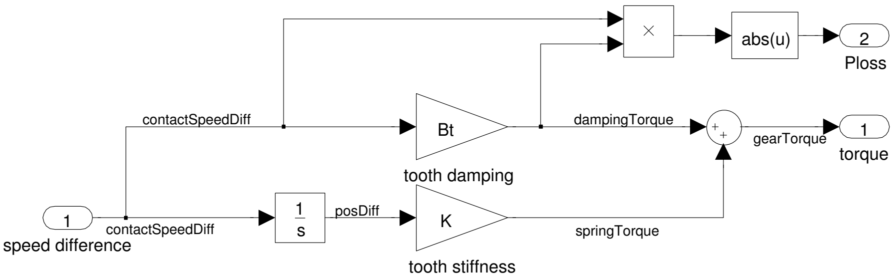

Figure C.27: *Simulink* not using backlash in the general mechanical model

C.5 Control scheme model

The *Simulink* implementation of the control scheme outlined in Section 3.6 and shown in Figure 3.10 is shown in Figure C.28. This also includes instances of the full motor model, the drive power electronics model (including the half bridge and the switching signals), and two instances of the general mechanical model.

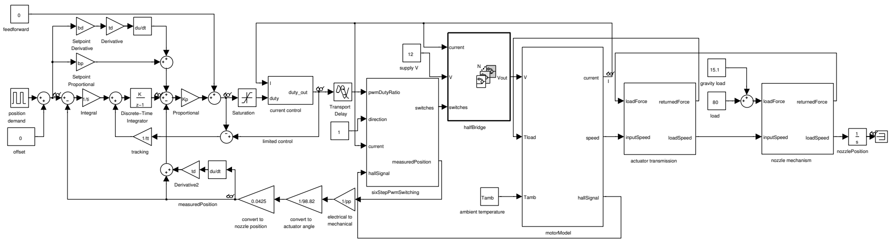

Figure C.28: *Simulink* full actuator model including control loop implementation

A similar implementation is shown in Figure C.29, but using the computationally efficient version of the motor model. In this case the switching and half bridge are not required; however, the interrupt subsystem from the switching is used to decode the hall signals. It is this model that is used to generate the results in Section 6.9.

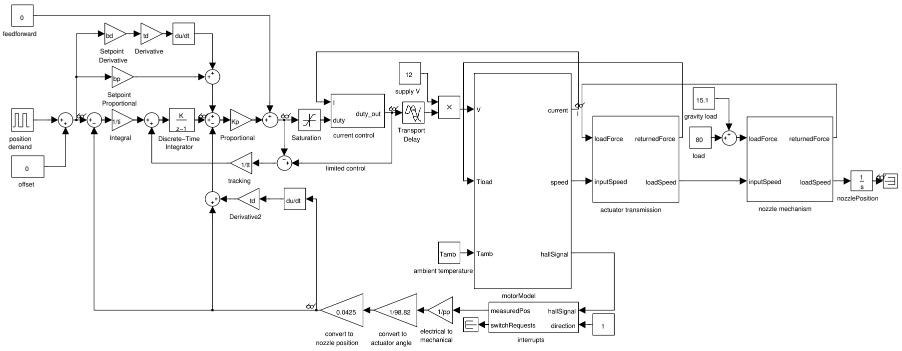

Figure C.29: *Simulink* efficient actuator model including control loop implementation

C.6 Hardware model and code

Code for the *Microchip* dsPIC chip used to drive the motors and actuator tested in this work was autogenerated from *Simulink* using the *Simulink coder* toolset. The control system to drive the actuator tested in Section 6.9 is shown in Figure C.30.

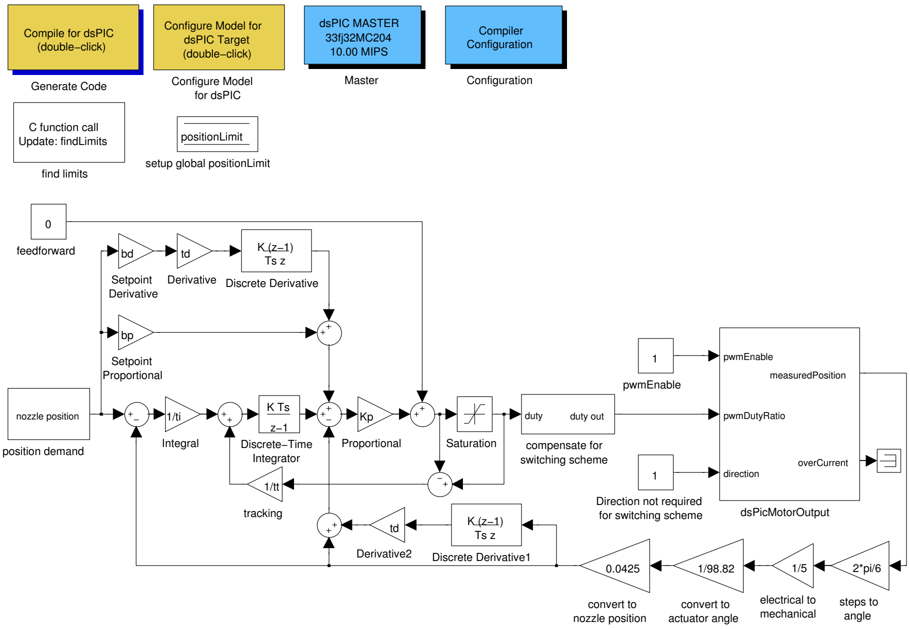

Figure C.30: *Simulink* diagram for autogeneration of *Microchip* code used in actuator testing

Within ‘position demand’ several different command signals may be selected depending on button presses on the development board. Outputs to the motor are handled within ‘dsPicMotorOutput’ by the blockset.

Separate functions to implement the startup routine and to commutate the motor were written in Microchip C. This was required as the initial startup ‘find limits’ is only run once, and the commutation is driven by hall sensor interrupts. Both of these types of function are difficult to implement directly in *Simulink*.

C.7 Simulation settings

Simulation results presented in Chapters 4 and 6 were generated from model simulation in *Simulink*. It was necessary to modify the model settings according to the model being implemented to adjust simulation fidelity. Brief detail of the solvers and settings used is provided in Table C.1. These were iteratively adjusted to provide minimal simulation time without compromising output fidelity. The computationally efficient model simulates fast enough that the compilation time required for each run outweighs the marginal improvement in simulation time produced by using the *Simulink* ‘Accelerator’ mode.

Table C.1: Model simulation settings

Motor model	Simulation type	Solver	Relative tolerance	Zero-crossing algorithm
Efficient model	Normal	ode23s (stiff/Mod. Rosenbrock)	10^{-7}	Nonadaptive
Full model, without PWM	Accelerator	ode23s (stiff/Mod. Rosenbrock)	10^{-5}	Adaptive
Full model, with PWM	Accelerator	ode23s (stiff/Mod. Rosenbrock)	10^{-8}	Adaptive
SimScape model	Accelerator	ode15s (stiff/NDF)	10^{-4}	Adaptive

Appendix D

Acausal actuator modelling

The models presented in Chapter 3 and Appendix C have been developed based on a mathematical description of the physical systems. This allows a high level of control over the model fidelity and detail. Some care is required in the implementation of the equations to ensure that connectivity between sub-system interfaces is maintained, as shown in Figure 3.12. The requirement for multiple ports on a system is due to the requirement for causality in *Simulink*. For example, the mechanical model of the transmission must be driven by a speed signal from the motor, and returns a load on the motor.

Tools are available to simplify the modelling process; these often provide predefined abstract sub-system models, which are allowed to determine their own causality. Such tools are often referred to as 'acausal' modelling packages. Within an acausal modelling tool mechanical systems can be connected together with no regard for, for example, which system is supplying torque or speed; their connection represents the more intuitive physical connection between the systems. The interaction between systems is solved by the modelling package during simulation. This more intuitive physical approach can allow models to be developed more quickly, however a designer may ultimately have less control over the underlying behaviour of the model. This type of model may also simulate more slowly, due to equations being solved repeatedly at each time-step.

Examples of acausal modelling tools include *Modelica*, *PLECS* and *SimScape*; the latter two are available as plugins for *Simulink*. Equivalent models to those shown in Appendix C, constructed using *SimScape* and its sub-packages, are detailed below. These models have been constructed to perform similarly to the models developed in Chapter 3.

D.1 *SimScape* motor model

An equivalent model of the actuator has been developed, as shown in Figure D.1. A *SimPowerSystems* block to represent the motor has been used. This allows user specification of the motor parameters (resistance, inductance, back-EMF, etc) and interfaces three phases of *SimScape* electrical connections to a single mechanical output. Iron losses and motor friction are included in this block.

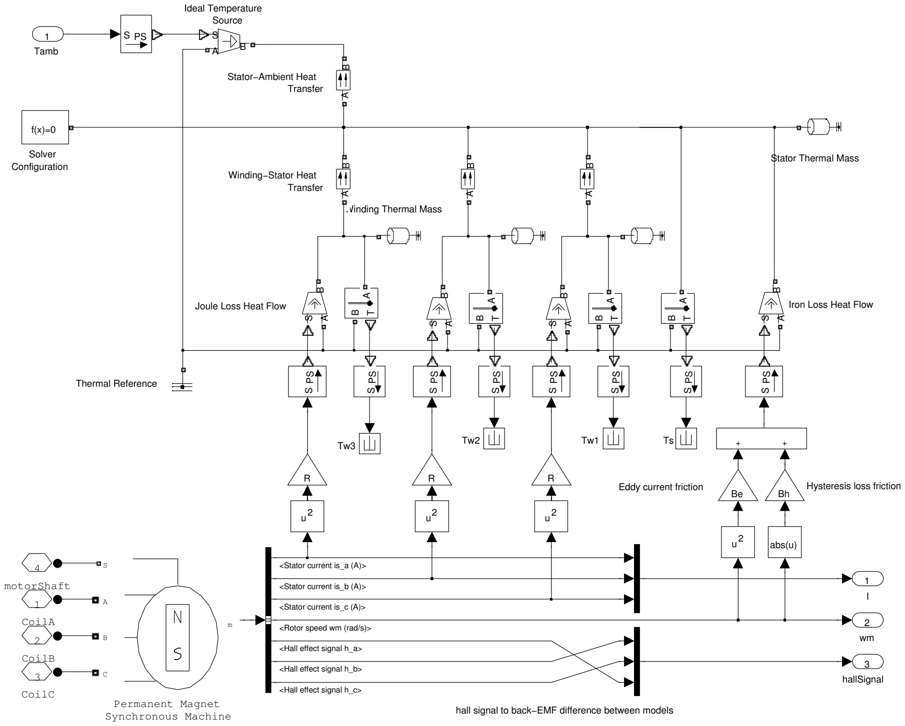

Figure D.1: *SimScape* motor model

Unfortunately the motor resistance and back-EMF are fixed parameters and cannot be varied during the simulation, therefore no direct temperature influence on them can be included. *SimScape* thermal modelling blocks have been used to represent the same thermal model shown in Figure 3.7. The power loss inputs have been calculated separately as they are not returned from the motor block.

D.2 *SimScape* drive power electronics model

A *SimPowerSystems* inverter block has been used to model the drive electronics, as shown in Figure D.2. This takes regular *Simulink* switching commands and a electrical supply voltage and returns three phase electrical connections to the motor. Switching time and losses due the power electronic components are included in this block.

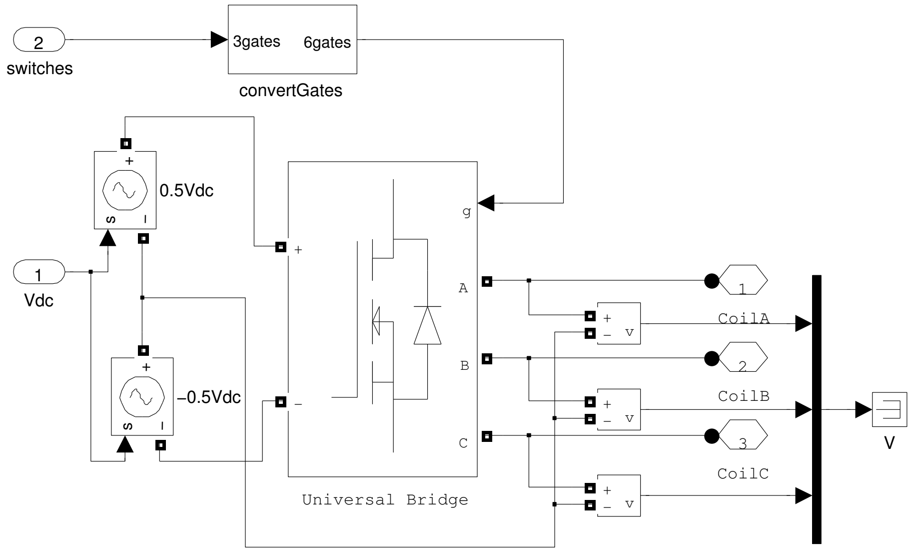

Figure D.2: *SimScape* half-bridge model

D.3 *SimScape* general mechanical model

A gear train model has been built equivalent to Figure 3.11, but using *SimDriveline* components, as shown in Figure D.3. This includes an ideal gear, backlash, stiffness, inertia and friction components.

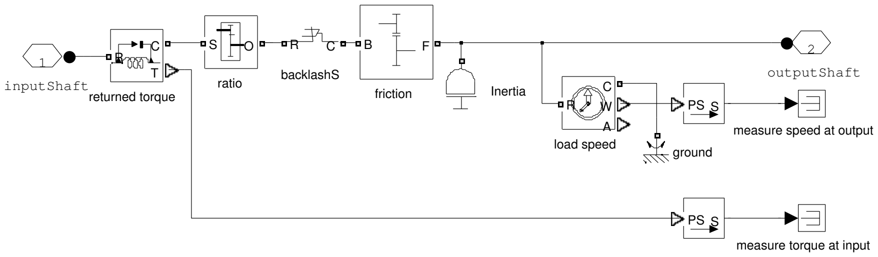

Figure D.3: *SimScape* mechanical model

Appendix E

Alternative thermal models

During the course of this work several different options for motor thermal modelling were investigated. The aim was to produce accurate model results, using minimal parameters, and whilst representing the independent temperatures of the stator, rotor and windings. This appendix details two thermal circuit models that were tested to try to achieve this. Unfortunately issues in the parameterisation and accuracy of these models were found, leading to the thermal model outlined in Section 3.3. This does not separate out the rotor temperature in the same manner as the models in this appendix, but was found to provide similar accuracy using a simpler model.

E.1 7-parameter model with stator-to-rotor connection

This is similar to the four-parameter model outlined in Section 3.3, however it separates the rotor temperature from the stator temperature as an extra component. This is connected as shown in Figure E.1. Alongside the parameters in the four-parameter model, there is an additional thermal resistance between the stator and the rotor R_{sr}, the rotor has a thermal capacitance C_r, and the rotor can transfer heat to ambient, via thermal resistance R_{ra}.

The temperature of each winding (T_{w_1}, T_{w_2}, T_{w_3}) may be calculated from

$$T_{w_1} = \frac{R_{ws}P_{w_1} + T_s}{R_{ws}C_w s + 1} \tag{E.1}$$

where T_s is the temperature of the stator, given by

$$T_s = \frac{R_{ws}R_{sr}R_{sa}P_s + R_{sr}R_{sa}(T_{w_1} + T_{w_2} + T_{w_3}) + R_{ws}R_{sa}T_r + R_{ws}R_{sr}T_{amb}}{R_{ws}R_{sr}R_{sa}C_s s + 3R_{sr}R_{sa} + R_{ws}R_{sa} + R_{ws}R_{sr}} \tag{E.2}$$

where T_{amb} is the ambient temperature surrounding the motor and T_r is the temperature of the rotor, given by

$$T_r = \frac{R_{sr}T_{amb} + R_{ra}T_s}{R_{ra}R_{sr}C_r s + R_{sr} + R_{ra}} \tag{E.3}$$

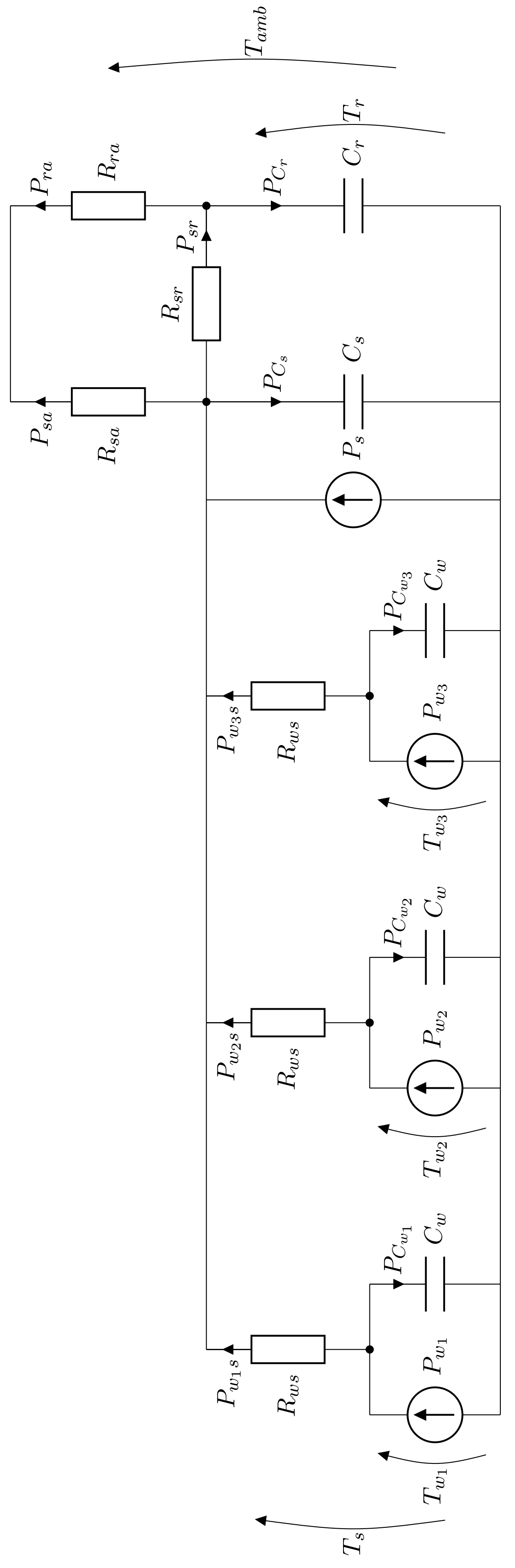

Figure E.1: A lumped 7-parameter motor thermal network model with stator-to-rotor connection

The parameterisation required for this model is more involved than for the 4 parameter model. The tests outlined in Chapter 4 were used, however the optional calculation of stator thermal resistance to ambient described in Section 4.4 becomes essential in order to uniquely determine all the parameters. Alternatively one or more resistance values may be estimated, along with the capacitances, by simulation within a gradient descent process as described in the static torque parameterisation test.

Using the available parameterisation data, this model was found to produce considerable variation in parameter values for the sample motor test set. During gradient descent parameter fitting it was common for capacitance parameters to tend to zero, due to the rotor transient temperature often being similar to the stator transient, but with different steady-state values.

Additionally, in some circumstances it is possible for the rotor temperature to exceed the stator temperature, particularly where the stator-to-ambient resistance is low. This is seen for the actuator static torque test in Figure 6.7. Due to the model only allowing heat transmission to the rotor via the stator, this situation cannot be achieved in simulation. For these reasons this model is not considered appropriate.

E.2 7-parameter model with winding-to-rotor connections

An alternative 7-parameter model did not connect the stator directly to the rotor, but connected the windings to the rotor via thermally resistive connections $\mathcal{R}_{wr}$, as shown in Figure E.2. In this case the temperature of each winding $\mathcal{T}_{w_1}, \mathcal{T}_{w_2}, \mathcal{T}_{w_3}$ may be calculated from

$$\boldsymbol{\mathcal{T}_w} = \frac{\mathcal{R}_{wr}\mathcal{R}_{ws}\boldsymbol{P_w} + \mathcal{T}_s\mathcal{R}_{wr} + \mathcal{T}_r\mathcal{R}_{ws}}{\mathcal{R}_{wr}\mathcal{R}_{ws}\mathcal{C}_w s + \mathcal{R}_{wr} + \mathcal{R}_{ws}} \tag{E.4}$$

where $\mathcal{T}_s$ is the temperature of the stator, given by

$$\mathcal{T}_s = \frac{\mathcal{R}_{ws}\mathcal{R}_{sa}P_s + \mathcal{R}_{sa}(\mathcal{T}_{w_1} + \mathcal{T}_{w_2} + \mathcal{T}_{w_3}) + \mathcal{R}_{ws}\mathcal{T}_{amb}}{\mathcal{R}_{ws}\mathcal{R}_{sa}\mathcal{C}_s s + 3\mathcal{R}_{sa} + \mathcal{R}_{ws}} \tag{E.5}$$

where $\mathcal{T}_{amb}$ is the ambient temperature surrounding the motor and $\mathcal{T}_r$ is the temperature of the rotor, given by:

$$\mathcal{T}_r = \frac{\mathcal{R}_{ra}(\mathcal{T}_{w_1} + \mathcal{T}_{w_2} + \mathcal{T}_{w_3}) + \mathcal{R}_{wr}\mathcal{T}_{amb}}{\mathcal{R}_{ra}\mathcal{R}_{wr}\mathcal{C}_r s + 3\mathcal{R}_{ra} + \mathcal{R}_{wr}} \tag{E.6}$$

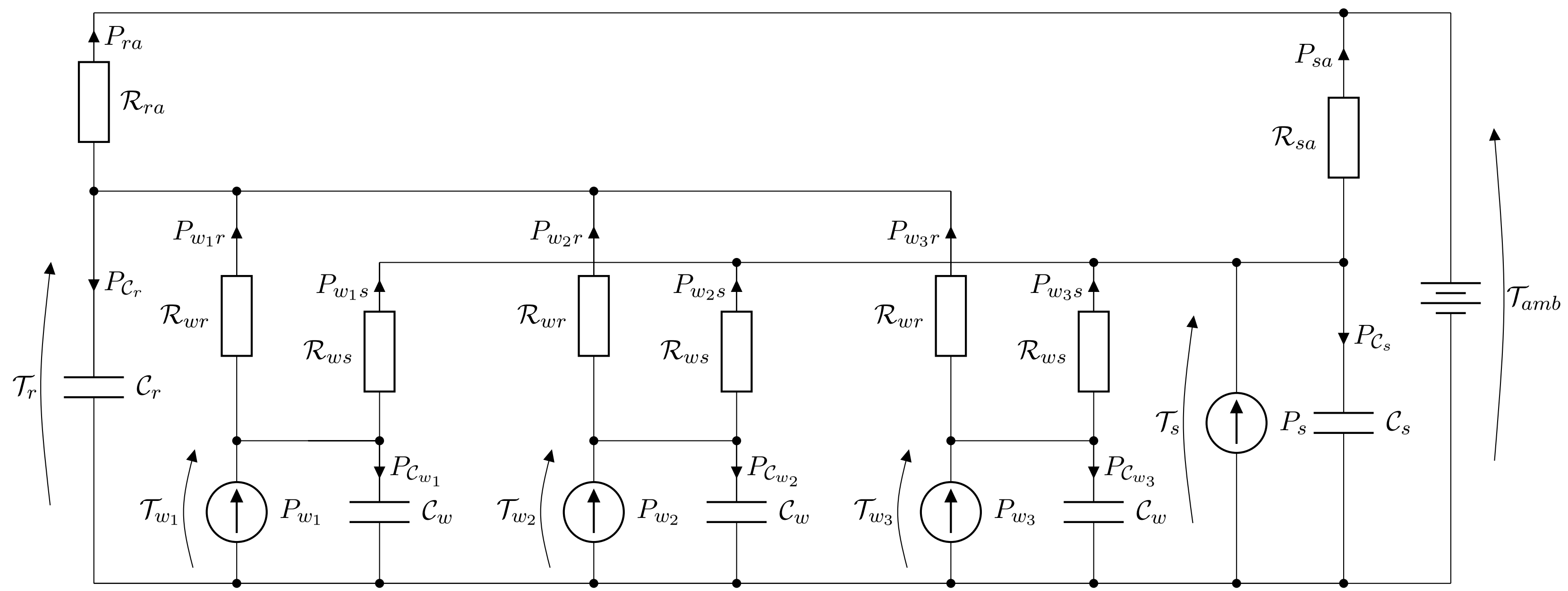

Figure E.2: A lumped 7 parameter motor thermal network model with winding-to-rotor connections

This model attempted to address the issues with the previous model by allowing heat transmission directly from the windings to the rotor. Again, this model is over-specified for the limited data available from the parameterisation tests, and therefore some parameters must be specified through calculation or estimated by fitting simulations to the test results.

Although the model was capable of allowing a hotter rotor than stator, and could be made to produce a close fit to the parameterisation test results, the parameter values required to produce a close fit were not realistic; frequently the rotor-to-ambient resistance would be significantly smaller than the stator-to-ambient resistance – which would not be expected for an internal rotor machine with a poor thermal connection along its shaft. The capacitances estimated by fitting this model were also unrepresentative of the motor size and materials for a number of the sample motors.

Although the static torque test proposed within Section 4.4 provides rotor temperature measurements, it is concluded that using these to parameterise a low-order thermal model poses significant problems. The four-parameter thermal model given in Section 3.3 is straightforward to parameterise, and has been shown to provide reasonable results without representing the rotor as a separate component. As discussed in Section 2.6, other research into higher-order thermal models is available in the literature.

Appendix F

Testrig development

A testrig has been designed, procured and constructed to allow a range of accurate measurements to be taken. The design has a test motor directly coupled to a load machine, an encoder and a torque sensor to take measurements during operation. An image of the new testrig is given in Figure 4.1 and key aspects of the design are detailed below.

The design of the testrig, with a direct coupling from a the test motor to a load machine mounted through a torque sensor, allows a wide range of different tests to be performed under various operating conditions. The shaft lock, test machine and torque sensor are all designed to be easily removable.

As the test machine is not connected through a speed reducing gearbox, as it is likely to be in a full actuator, the load inertia is expected to be considerably larger. This is not a problem for the parameterisation or validation tests performed in this chapter as the same inertia is used in the models being compared; although it should be noted that the frequency responses shown in Section 5 include this large testrig inertia.

F.1 Driver electronics

Accurate representation of driver electronics is an important step in producing a high fidelity models of motor performance and designing an improved overall system. The testrig is used to investigate several different driver algorithms, including both variations in commutation method and switching schemes within individual methods. The driver used is a *Microchip* Programmable Integrated Circuit (PIC) (chip *dsPIC33FJ32MC204*) in conjunction with a *Microchip* motor control development board (*dsPICDEM MCLV*). This allows for a flexible and adaptable approach to driving the motor.

In order to allow rapid development of driver code, and also to provide commonality between the simulations and the actual tests, a specialist *Simulink* blockset has been used in conjunction with *Matlab Real-Time Workshop* facilities to auto-generate driver PIC code direct from the models. *Simulink* models have been modified such that they can be auto-coded into PIC code. This software-in-the-loop type approach is increasingly being used in industry to reduce development time, ensure commonality, and fit in with model based design practices [1].

F.2 Load machine

A brushed DC motor (*Maxon RE40*) is used to provide a variable load to the test motor. This uses a 24 V nominal supply and is rated at 150 W. It has a single pole-pair rotor winding and 13 commutation segments. This provides a relatively smooth torque profile during rotation.

F.3 Load machine power supply

A bipolar power supply (*Kepco BOP 36-12M-LD*) is used to control the load machine winding current on the testrig; this allows it to either source or sink power to the test motor, smoothly transitioning between the positive and negative quadrants of voltage and current operation. This is especially important in providing representative conditions for testing actuator motors, in which a load torque acts against the motor whilst it responds to changing position demands.

Constant current in the load machine provides a constant load torque. It is also possible to control the current to follow an input voltage profile supplied by a signal generator.

F.4 Torque sensor

A reaction torque sensor (*Futek TFF325* 50in-oz or 12in-lb) is used to measure the torque between the load machine and test motor. Using a reaction sensor avoids taking measurements from a rotating shaft and allows for a rigid connection between the test and load machines. Torque sensors with different limits and accuracies may be swapped to allow accurate measurement over a large range of torques.

F.5 Position encoder

A quadrature encoder (*British Encoder 15T 50-SF 0500-NC-OC-V1*) on the shaft of the load machine provides accurate measurement of shaft position. The output of this is viewed and logged on an oscilloscope via a counter (*US Digital EDAC2*) which converts the digital encoder signal into an analogue position signal. The 2-channel 500 pulse-per-revolution encoder provides a position resolution of $0.36°$.

F.6 Locked shaft adjuster

A facility to lock the shaft of the load machine is included in the testrig; this allows the test motor to torque directly against the torque sensor. The locked position can be finely adjusted relative to the test motor body.

F.7 Test motor mounting

In order to test motors with different mounting methods on the same testrig, a universal mount for the motor body is used, with an adapter interfacing between the testrig and the motor. A different adapter is used for each motor, with adapters all having the same connection onto the testrig. The adapter is made of a thermally insulating plastic to ensure that significant heat is not conducted to the testrig during thermal tests.

F.8 Coupling

A bellows type coupling (*ABSSAC HMB1*) is used to connect the test and load machine shafts. Different couplings are used depending on the test motor shaft diameter. This type of coupling allows a reasonable mismatch in radial, axial and angular alignment between machines (to allow for manufacturing/fitting tolerances), whilst maintaining a high coupling stiffness and relatively low moment of inertia.

F.9 Oscilloscope

Short duration signals have been recorded using an oscilloscope (*Lecroy Waverunner LT354*) and appropriate voltage probes or current clamps (*Chauvin Arnoux E3N*).

F.10 Datalogging

Long duration testing, such as thermal analysis, has been performed by logging results to a Personal Computer (PC) via a multimeter (*Keithley 2701*).

F.11 Testrig parameters

Using tests outlined in Chapter 4 the following parameters have been measured or calculated for the testrig.

The inertia is the combination of the load machine rotor (given in its datasheet as $0.0142\,\mathrm{g\,m^2}$), the coupling (given in its datasheet as $0.0006\,\mathrm{g\,m^2}$), the interface piece attaching the encoder (estimated to be $0.0077\,\mathrm{g\,m^2}$ from its dimensions and material) and the rotating part of the encoder (assumed light enough to be negligible).

Coulomb friction from starting torque tests was found to be in the range $3.9\,\mathrm{mN\,m}$ to $5.4\,\mathrm{mN\,m}$. Testrig load machine back-EMF was found to be almost identical to the datasheet value and constant for all speeds tested. A summary of the important parameters extracted for the testrig is given in Table F.1. Typical error levels are also indicated; these are due to variation between tests, rather than due to errors in the regression fit. Regression fit errors are typically below $1\,\%$ for the spin-down test results.

Table F.1: Testrig parameters

Back-EMF constant K_E	30.2		$\mathrm{mV\,s\,rad^{-1}}$
Inertia J	22.5		$\mathrm{mg\,m^2}$
Coulomb friction B_c	7.6	± 0.5	$\mathrm{mN\,m}$
Viscous friction B_v	24	± 1	$\mathrm{\mu N\,m\,s\,rad^{-1}}$

Appendix G

Switching scheme analysis

As reviewed in Section 2.4.3, a number of different options exist for switching the drive power electronics in order to regulate the voltage/current. This appendix draws upon the review of the literature, supported by experimental and simulated results, to assess the differences between switching schemes and suggest their suitability for actuator control. It is assumed that voltage control is used to switch a standard three-phase half-bridge driver – alternative current control options are discussed in Section 2.4.4.

Table 2.1 summarises the schemes investigated in this appendix, although schemes B and D are not simulated explicitly as they differ from schemes A and C only in the sequence of commutation. The distinction between schemes A1 and A2, and C1 and C2, is also neglected, as the difference between holding high side and low side continuously is not important to the discussion. Due to schemes C and D requiring PWM switching of both high and low side switches in a complementary manner, there is no possibility of using lower specification devices on one side of the bridge. The difference between the two is therefore arbitrary. Schemes A1, C1, E, F, G and H are discussed in detail. Initial considerations when comparing schemes are the application requirements for: bidirectional power flow, current ripple, positioning/speed control performance and static torque.

Power return to the supply during forward drive operation is an inherent feature of some switching schemes during open-loop operation; however for a standard closed-loop control scheme there is potential for this to occur, regardless of the switching scheme. This is due to the control attempting to decelerate the motor on overshoot of a new set point, by driving against the rotating inertia, and also possibly the load force. Where the position change is in the same direction as the load force, some active braking may be required even without a position overshoot. If it is absolutely unacceptable to return power to the supply then significant steps will be need to be taken within the control scheme or the power electronics to ensure this does not occur.

Current ripple produces torque ripple, affecting actuator motion; it may also impact upon the supply. Neither current nor torque ripple is expected be a significant issue for a turbocharger actuator; the automotive battery should be robust and provide reasonable buffering for any ripple, and the smoothness of motion and any induced vibration are not a significant problems for positioning control.

The primary factor in determining an optimal switching scheme for a turbocharger actuator is determined to be the positioning performance provided. A secondary consideration is what schemes are supported in the chosen hardware. In order to answer these questions several schemes have been implemented in both simulation and physical hardware to evaluate their performance.

The models outlined in Chapter 3 do not provide a high fidelity representation of the power electronics used for switching. For this reason the acausal *SimScape* model presented in Appendix D is used for switching scheme evaluation. This has specific MOSFET models with an on-state resistance that is representative of the chips used in the *Microchip* development board – *FBQ55N10* MOSFETs with an on-state resistance of $21\,\mathrm{m}\Omega$).

The *dsPIC33FJ32MC204* chip used for testing only allows a single PWM counter for all switches and the MOSFET chips on the *dsPICDEM MCLV* board are driven directly from the chip signals. This means that schemes requiring complementary switching with high side and low side switching synchronised between legs (schemes F and H from Table 2.1), cannot be implemented using this chip and hardware combination; these have therefore been assessed only through simulation. A variant of scheme F, subsequently referred to as F′, is implemented in hardware, however it behaves differently to F, and more similarly to schemes A and C.

The relationship between duty ratio and effective output voltage varies between switching schemes, with some introducing significant nonlinearities. This might be alleviated by using a compensator, however this is not an ideal solution. The effective output voltage is plotted against the input PWM duty cycle of several switching schemes in Figure G.1. The effective voltage is estimated based on the steady-state open-loop speed and the back-EMF constant. As there is no load (except for frictional losses) it is assumed that the current is small and therefore the voltage drop across the winding resistance is negligible. As these plots are the result of testing using the testrig and the *MMT* sample motor they inherently exhibit some measurement noise. Note that in this and all subsequent analysis the duty ratio has been considered in the range -1 to 1, where negative duties correspond to reverse direction. Schemes E to H have the duty ratio rescaled from the range 0 to 1 for comparison, where less than 0.5 indicates a reverse direction.

It can be seen from Figure G.1 that schemes A1, C1 and F′ all provide a relatively linear relationship between duty and effective voltage, whereas schemes E and G display significant nonlinearities at low duty ratios. This is due to discontinuous phase current within the duty cycle. The extent of this nonlinearity is therefore determined by the resistance and inductance of the motor coils and the load torque. At increased loads the increased average current will mean the system is more likely to

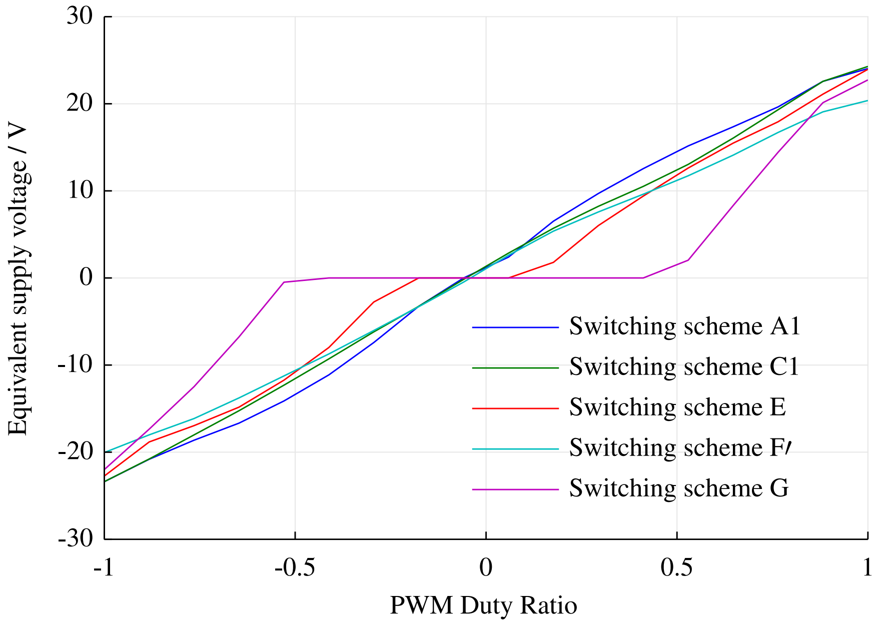

Figure G.1: Effective voltage provided by the duty ratio of different switching schemes

be operating in a continuous current mode, reducing this nonlinearity; however for closed-loop control, with a varying load torque, continuous current operation cannot be guaranteed. This nonlinear effect makes accurate control at low duty ratios difficult, leading to large overshoots and steady-state error in step responses; therefore these schemes are not considered to be suitable for positioning control.

The implementation of schemes A1, C1 and F′ is shown in Figures G.2, G.3 and G.4 in terms of their PWM switching within a single commutation period, as well as the current in the motor phase during switching. These results were taken for continuous speed operation with an effective duty ratio of 30 %. The solid blue line results were measured from the *MMT* motor on the testrig and the red dashed lines were simulated using the *SimScape* model. The slight difference in duty ratio is due to manual setting accuracy using a potentiometer on the hardware and is not a significant aspect of the results.

These results not only show a reasonable agreement between the simulation and the test results, they also highlight differences between the switching schemes. The phase current magnitudes differ slightly, likely due to unmodelled aspects of the real system, for example the inclusion of sense resistors for current monitoring.

Figure G.4 also shows how the implemented scheme F′ differs from the proposed scheme F. The switching of the high sides of phases 1 and 3 occur simultaneously, rather than in complement. This means that, like in schemes A to D, currents circulate in the high or low side of the half-bridge, rather than forcing a reverse voltage across the phase. This gives the slow current decay seen in all the examples.

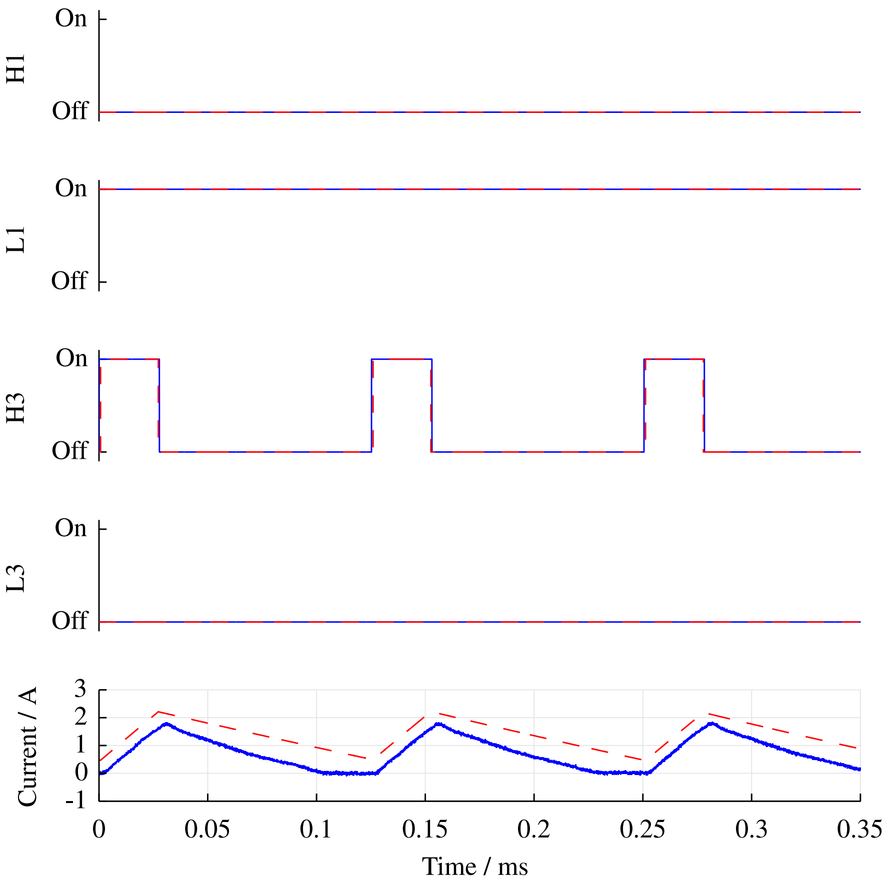

Figure G.2: Switching signals to the active phases of the half-bridge and phase current during a single step of scheme A1

The schemes differ in what happens when the current falls to zero in the phase – discontinuous current. In scheme A1 the current is recirculating in the L1 switch and the L3 diode. Once it reaches zero there is still a back-EMF voltage, as the motor is still rotating, however unless this exceeds the supply voltage (unlikely under normal operation) diodes L1 and H2 are still reverse bias and will not conduct. In scheme C1 the current is recirculating in the L1 switch and L3 diode as it falls, and it can continue to fall through zero to give a negative current in the L1 diode and L3 switch – producing a decelerating torque on the motor. Similarly in the F′ scheme, the falling current is initially circulating in the L1 switch and L3 diode, and then halfway though it changes to circulate in the H1 diode and H3 switch. Again current is able to fall below zero and decelerate the motor, in this case circulating in the H1 switch and H3 diode, dissipating power in the motor winding resistance.

This difference is important when the step response of the motor is investigated, as shown in Figure G.5. This compares the step response of the *MMT* motor operating with the three different switching schemes, with no load torque applied. The loop is

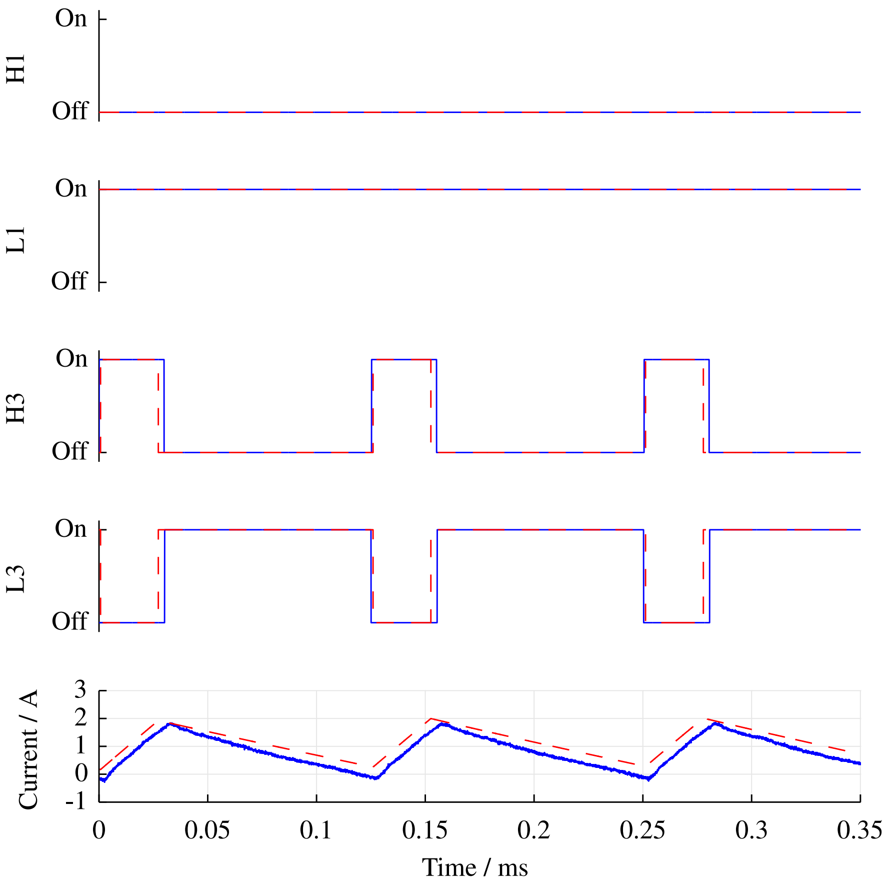

Figure G.3: Switching signals to the active phases of the half-bridge and phase current during a single step of scheme C1

closed with a simple proportional controller with a gain of 0.1 (where the error signal is measured in radians). The solid lines show results measured from the testrig and the dashed lines are simulated using the *SimScape* model. Three results are shown for each testrig case to show the variability.

The reduced performance of scheme A1 is obvious in terms of reduced damping (leading to larger overshoot and more prolonged oscillation). This is due to currents being unable to reverse and decelerate the motor during discontinuous operation (low duty switching). The results for scheme F' are slightly better than those for C1, due to the recirculation being split between the top and bottom of the half-bridge.

The simulation step results are very similar to the testrig results, with comparable overshoots and settling times (the overshoot is marginally larger and the settling time slightly shorter in the simulation). The same differences between switching schemes are also shown for the A1 scheme, although the C1 and F' schemes are very similar under simulation. Transient results are unchanged when a load torque is applied to the system, however steady-state errors are also introduced.

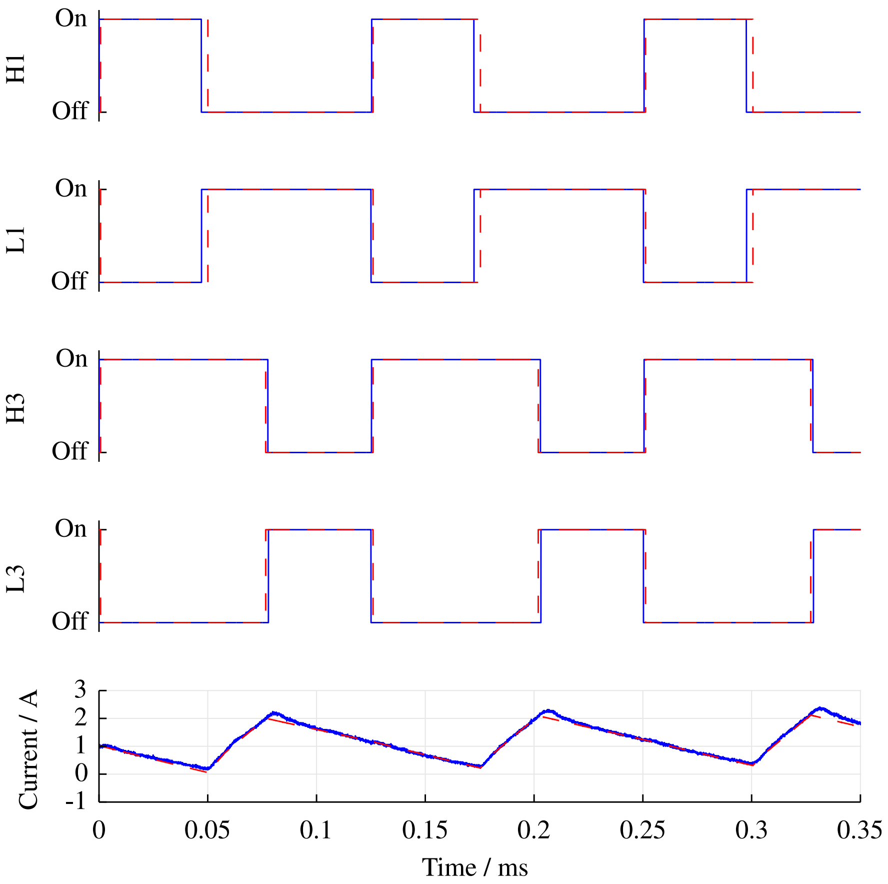

Figure G.4: Switching signals to the active phases of the half-bridge and phase current during a single step of scheme F′

Due to scheme F′ providing the best performance in these tests, it is this scheme that is used throughout this work. It is also the recommended switching scheme for position control using hardware that does not allow separate PWM counters for different half-bridge legs, although scheme C1 is almost as good and may provide a simpler implementation. Further performance improvements may be possible if independent PWM counters were available. A true scheme F switching strategy is shown through simulation only in Figure G.6.

As expected, this shows a considerably larger current ripple, as well as significant periods of negative current. The effect of this switching scheme on the position step response is shown in Figure G.7 compared against the previously simulated schemes. This shows a very similar response to that of the C1 and F′ schemes, with slightly increased overshoot.

Further improvements might be made to scheme F if a ‘centre-aligned’ or ‘symmetric’ PWM mode is available in the device, as scheme H can be used. This should reduce current ripple considerably, although switching losses in the electronics may

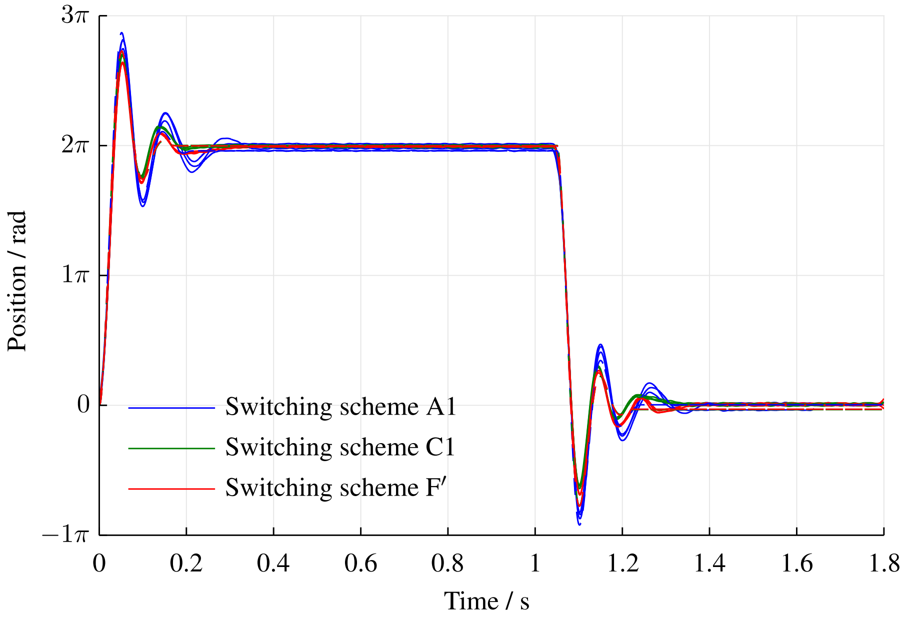

Figure G.5: Step response of different switching schemes

increase slightly. This is not expected to significantly improve step-response performance. Therefore schemes C or F′ remain the favoured options.

Scheme B is expected to suffer from the same issues as scheme A in recirculating currents through the diodes and is therefore not optimal. Scheme D differs by the PWM leg changing at every step. This means that there is no possibility of ‘over-current’ during commutation, as the current is being controlled by the current sense resistor in the half-bridge at all times. The only downside of this is a very slight increase in the number of switching instances – due to the non PWM switch changing every 60° electrical rather than every 120°; therefore scheme D is suggested over scheme C.

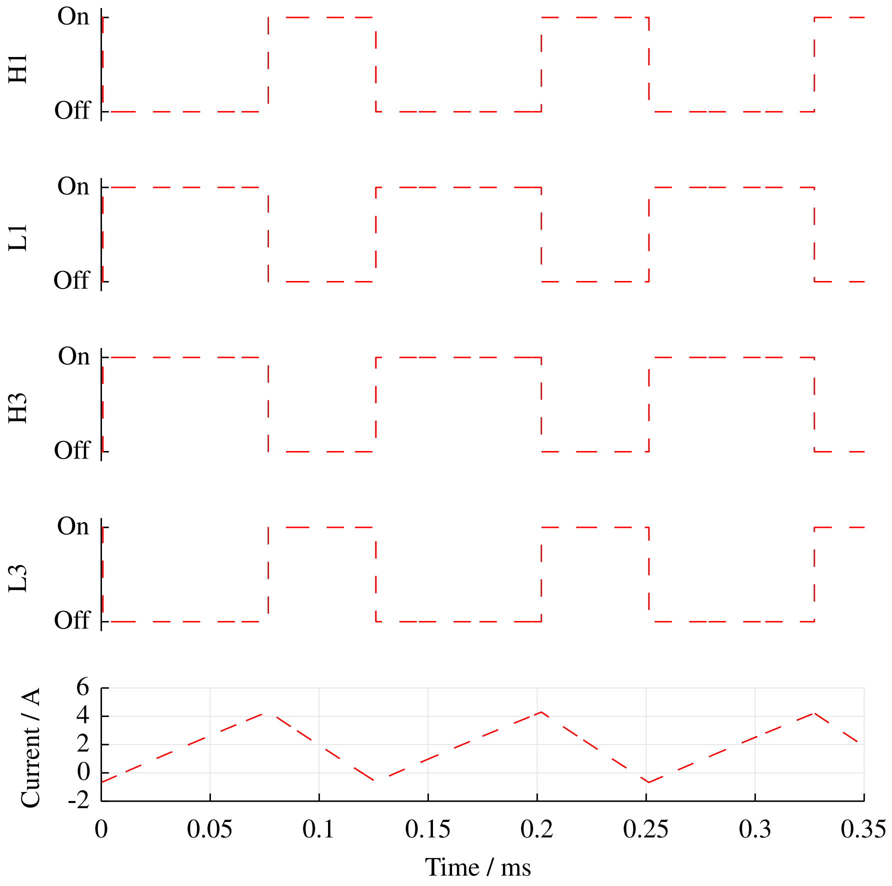

Figure G.6: Switching signals to the active phases of the half-bridge and phase current during a single step of scheme F

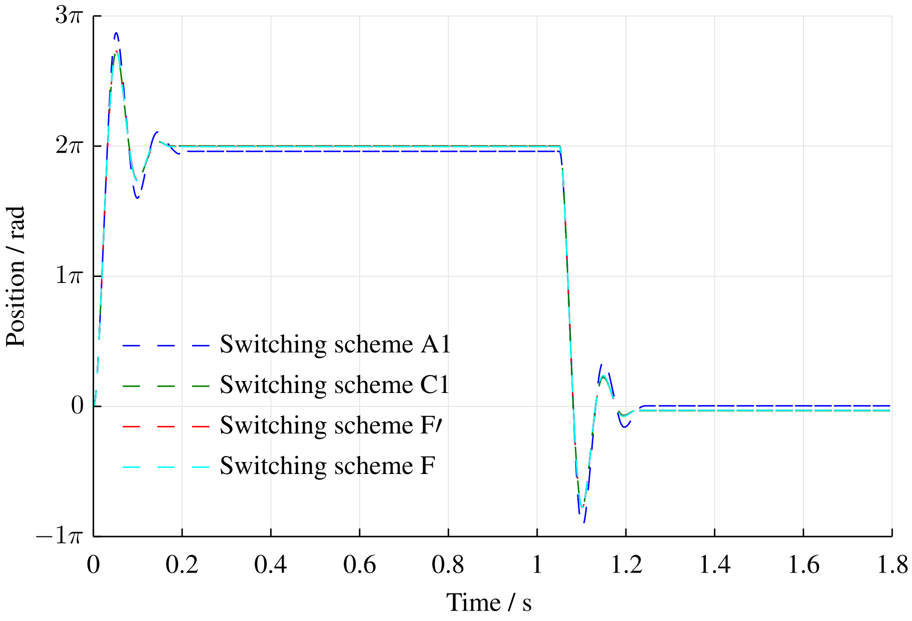

Figure G.7: Step response of different simulated switching schemes

A summary of the relative advantages and disadvantages of the switching schemes and design decisions addressed in this section are presented in Table G.1. Further studies may be required to determine the optimal scheme for a particular set of requirements.

Table G.1: Switching scheme performance summary

	Advantages	Disadvantages
PWM Scheme A	Linear relationship between duty and voltage	Unable to decelerate motor during discontinuous operation
PWM Scheme B		Unable to decelerate motor during discontinuous operation
PWM Scheme C	Linear relationship between duty and voltage	Cannot use lower specification switching devices on one side of the half-bridge
PWM Scheme D	No possibility of ‘overcurrent’ during commutation	Cannot use lower specification switching devices on one side of the half-bridge, slight increase in switching instances
PWM Scheme E		Nonlinear relationship between duty and voltage
PWM Scheme F		Increased current ripple
PWM Scheme F'	Linear relationship between duty and voltage, recirculation split between high and low sides of half-bridge	
PWM Scheme G		Nonlinear relationship between duty and voltage
PWM Scheme H	Reduced current ripple	Slight increase in switching losses, requires centre aligned mode

Appendix H

Sample motors

Five different motors, selected from four different manufacturers, were tested, all producing around 80 W output power and designed to operate from a 24 V supply. They show a variation in rotor pole numbers, stator structure and internal/external rotor designs. The main purpose of these motors is to validate the motor models, rather than to consider them as candidates for the application.

The *MMT* 50-2L motor [230] is representative of the motor used in current *Cummins* actuator designs. The two *Maxon* motors [48] are of very different designs, one being an external rotor machine and therefore achieving a very compact package but having a higher inertia, and the other having a toothless stator (and therefore no cogging torque) and a single pole-pair rotor. The *McLennan* motor [231] is a lower specification machine that may not be representative of current machines, but is nevertheless useful for validation. The *Moog* motor [232] is a more expensive and high performance machine.

All sample motors have a thermocouple thermally bonded to the external casing. For the external rotor machine the thermocouple is placed on the stator mounting face. The *MMT* machine has *PT100* resistance temperature sensors embedded in two of its coils. The *Moog* and *McLennan* machines have thermocouples in their coils, bonded and embedded respectively. All the motors are three-phase Y-connected, have an approximately sinusoidal back-EMF (see Section 4.1) and have three hall-effect sensors for commutation.

Details of the sample motor dimensions and masses, and rated performance, as provided in their datasheets, are given in Tables H.1 and H.3 respectively. A summary of the motor parameters is given in Tables H.2 and H.4. These show both the datasheet parameters and the parameters measured in Section 4.1. Single phase values have been given, in keeping with the manner in which they are used in the motor models. Appropriate scaling has been performed to obtain these values, where testing has measured a phase-to-phase value, or this is how it is specified in the datasheet. Blanks in the datasheet rows indicate that data was not available from the manufacturer for certain parameters. Thermal capacitance datasheet values were calculated based on thermal resistance and thermal time constants supplied by the manufacturer.

The final row in Tables H.2 and H.4 provides an indication of the typical measurement error encountered in obtaining the measured values. This has been estimated either based on several measurements being taken, or on the accuracy of the measurement process. It does not necessarily reflect the error in the regression fit used to obtain the results, as repeatability was found to be the cause of greater variation.

Table H.1: Sample motor dimensions

	Mass / g	Length / mm	Diameter / mm
MMT 50-2L	485	54	50
Maxon EC-Flat 45	141	27	45
Maxon EC-max 40	460	58	40
McLennan BM05-3 SQ		95	57
Moog BN17-25AA-02	385	64	43

Table H.2: Sample motor thermal parameters

	Thermal resistance winding-stator $\mathcal{R}_{ws}$ / $\mathrm{K\,W^{-1}}$	Thermal resistance stator-ambient $\mathcal{R}_{sa}$ / $\mathrm{K\,W^{-1}}$	Thermal capacitance winding $\mathcal{C}_w$ / $\mathrm{J\,K^{-1}}$	Thermal capacitance stator $\mathcal{C}_s$ / $\mathrm{J\,K^{-1}}$
MMT 50-2L	4.87	3.56	8.3	320
Datasheet	6	4.3	7.0	372
Maxon EC-Flat 45	10.19	8.49	4.9	60
Datasheet	4.3	3.1	7.2	50
Maxon EC-max 40	2.35	8.32	7.6	170
Datasheet	0.54	4.63	7.0	229
McLennan BM05-3 SQ	1.00	3.67	8.0	450
Datasheet				
Moog BN17-25AA-02	1.09	5.89	7.0	250
Datasheet		2.18		
Measurement error	±0.2	±0.2	±1	±40

Table H.3: Sample motor rated values

	Rated torque / $\mathrm{mN\,m}$	Rated current / A	Rated speed / $\mathrm{rad\,s^{-1}}$	No load current / A	No load speed / $\mathrm{rad\,s^{-1}}$	Peak stall torque / $\mathrm{mN\,m}$	Continuous stall torque / $\mathrm{mN\,m}$
MMT 50-2L	140		688.7		1089.1	730	165
Maxon EC-Flat 45	128	3.21	508.9	0.234	639.8	1150	112
Maxon EC-max 40	89	3.12	683.8	0.292	841.9	497	84
McLennan BM05-3 SQ	320		230.4		345.6	980	390
Moog BN17-25AA-02	107	5.57	723.0		1003.4	459	141

Table H.4: Sample motor electrical and mechanical parameters

	Back-EMF constant K_E / $\mathrm{mV\,s\,rad^{-1}}$	Torque constant K_T / $\mathrm{mN\,m\,A^{-1}}$	Winding terminal resistance R / Ω	Winding terminal inductance L / mH	Rotor inertia J / $\mathrm{mg\,m^2}$	Pole pairs n_{pp}	Coulomb friction B_c / $\mathrm{mN\,m}$	Viscous friction B_v / $\mathrm{\mu N\,m\,s\,rad^{-1}}$	Hysteresis constant B_h / $\mathrm{mN\,m}$	Eddy current constant B_e / $\mathrm{\mu N\,m\,s\,rad^{-1}}$
MMT 50-2L	13.6	12.4	0.13	0.145		5	0	10.6	4.4	2.4
Datasheet	11.8	11.8	0.10	0.150	12.50	5	4			
Maxon EC-Flat 45	21.7	20.1	0.30	0.163		8	0	8.5	2.4	0.5
Datasheet	21.3	21.3	0.30	0.232	18.10	8				
Maxon EC-max 40	17.3	15.9	0.68	0.096		1	0	5.0	1.0	0
Datasheet	16.2	16.2	0.68	0.093	5.12	1				
McLennan BM05-3 SQ	30.9	28.3	0.16	0.550		2	0	16.4	8.4	1.6
Datasheet	48.5	48.5	0.39		17.2	2				
Moog BN17-25AA-02	14.1	12.9	0.29	0.312		2	0	6.0	1.2	1.0
Datasheet	13.3	13.3	0.30	0.324	3.40	2				
Measurement error	±0.2	±0.2	±0.001	±0.005		0	±0.5	±1	±1	±2